UNIVERSITY OF SOUTHAMPTON

FACULTY OF ENGINEERING AND THE ENVIRONMENT

National Centre for Advanced Tribology at Southampton (nCATS)

White Structure Flaking Failure In Bearings Under Rolling Contact Fatigue

by

Martin-Halfdan Evans

Thesis for the degree of Doctor of Philosophy

July 2013

UNIVERSITY OF SOUTHAMPTON

ABSTRACT

FACULTY OF ENGINEERING AND THE ENVIRONMENT

Tribology

Thesis for the degree of Doctor of Philosophy

WHITE STRUCTURE FLAKING FAILURE IN BEARINGS UNDER ROLLING CONTACT FATIGUE

Martin-Halfdan Evans

White structure flaking (WSF) as a premature wear failure mode in steel rolling element bearings is caused by white etching cracks (WECs) and perhaps butterflies formed in the ~1 mm zone beneath the contact surface under rolling contact fatigue (RCF). WECs are branching crack systems typically several millimetres in length that have a microstructural change called 'white etching area' (WEA) associated with the crack. Butterflies are smaller cracks initiating at material defects and impurities that form WEA wings that revolve around their initiators. Hydrogen diffusion into the bearing steel during service and transient operating conditions have been suggested as drivers of white etching features (butterflies, WEA and WECs). However the initiation and propagation mechanisms as well as the thresholds for WEC formation are not well understood. This is due to the difficulties of creating WECs repeatedly under laboratory conditions and the lack of a method established for mapping WECs in detail or 3-dimensions as typically only limited metallographic analyses are conducted over several cross-sections.

A series of RCF tests have been conducted in this study to investigate the formation drivers and formation mechanisms of WECs using a two-roller RCF machine. WECs were successfully created in hydrogen charged 100Cr6 martensitic steel rollers under low-moderate concentrations of diffusible hydrogen (~1 ppm) and service realistic loading conditions (P_{max} 1.5 – 2 GPa). However, only butterflies were formed under transient conditions with non-hydrogen charged rollers. One such butterfly was analysed in detail to further understanding of crack formation mechanisms and carbide dissolution as part of the WEA microstructural change. Based on the evidence obtained from the SEM, FIB tomography and STEM/TEM analysis, a void/cavity coalescence theory for initial butterfly crack formation and iron-chromium carbide dissolution as part of the WEA formation mechanism is proposed.

Metallography was extensively used in this project to view cross-sections of the wear zones subject to RCF. A metallographic serial sectioning technique was established to quantitatively map wear zones for the first time. Mapping WECs in their entirety and 3D modelling revealed the 3-dimensional morphology and orientation of WECs and maximised detection of possible WEC initiators.

This study has for the first time quantitatively investigated the influence of diffusible hydrogen, load and rolling cycles on white etching feature formation and the thresholds of formation. The hydrogen-charged tests showed that the formation of butterflies was independent of the concentration of diffusible hydrogen with the test parameters used, but dependent on contact pressure and number of rolling cycles up to a threshold. WEC formation thresholds were found at certain values of the concentration of diffusible hydrogen, contact pressure and number of rolling cycles. Extensive serial sectioning and 3D modelling of WECs also demonstrated that the orientation of WECs differed depending on the sectioning direction. It was found that the vast majority of WECs were contained in the subsurface wear zone and did not make any

connection with the surface, thus dismissing surface initiation. The WECs often interacted with inclusions that were judged to be crack initiators and evidence was found that butterfly cracks could propagate to form WECs. The white etching features initiated predominately at short sulfide type inclusions, small globular manganese sulfide-oxide inclusions and small globular oxide inclusions. Therefore strong evidence was observed for a subsurface initiation mechanism of WECs from non-metallic inclusions.

A comparison of the WEC formations in the hydrogen charged two-roller tests was made with serial sectioning investigations of WEC formation in wind turbine gearbox bearings obtained from the field and those tested on a large-scale transient test rig (non-hydrogen charged). This was performed to understand if a difference in the WEC initiation and propagation mechanism occurs under the differing conditions. The comparison showed correlation between the WEC formation mechanisms as a high number of inclusions interacted with the WECs that were judged to be crack initiators and small/short sized inclusions predominated as the crack initiators. Therefore based on the serial sectioning analysis across various test specimens and bearings it is proposed that *one* mechanism of WEC formation is due to multiple linking of extended butterflies or small WECs in the subsurface to form larger WEC networks that eventually propagate to the surface resulting in WSF. The data also suggests that steel cleanliness standards analysing inclusion density (as opposed to maximum inclusion lengths) are more relevant in understanding butterfly/WEC initiation. However steel cleanliness standards used should record inclusions that are only a couple of micrometer’s in length/diameter.

Contents

List of Tables

List of Figures

List of accompanying materials

Chapter 5

Video 5.3.1
Video showing all the slices from the FIB tomography of a butterfly wing.

Video 5.3.2
Video showing 360 degrees rotation of the 3-D model of a butterfly wing.

Chapter 6

Video 6.4.1
Video showing all the slices from the FIB tomography of an inclusion-WEC interaction.

Video 6.4.2
Video showing 360 degrees rotation of the 3-D model of the inclusion-WEC interaction. The 3-D model is formed from 2D segmentation of the inclusions and crack portion from the FIB tomography. The WEA portion was not segmented or modelled.

Video 6.4.3
Video showing all the 2D crack + WEA segmentations from the serial sectioning process of WEC-9.

Video 6.4.4
Video showing an orthoslice sweep of the 2D crack + WEA segmentations from the serial sectioning process of WEC-9 in-situ with the 3-D model. The orthoslices are in the circumferential plane (the plane of material removal during serial sectioning).

Video 6.4.5
Video showing 360 degrees rotation of the 3-D model of WEC-9.

Video 6.4.6
Video showing a virtual orthoslice sweep of the 3-D model of WEC-9 in the axial plane (the plane perpendicular to the plane of material removal during serial sectioning).

Declaration of authorship

I, Martin-Halfdan Evans, declare that the thesis entitled '*White Structure Flaking In Bearings Under Rolling Contact Fatigue*' and the work presented in the thesis are both my own, and have been generated by me as the result of my own original research. I confirm that:

- this work was done wholly or mainly while in candidature for a research degree at this University;
- where any part of this thesis has previously been submitted for a degree or any other qualification at this University or any other institution, this has been clearly stated;
- where I have consulted the published work of others, this is always clearly attributed;
- where I have quoted from the work of others, the source is always given. With the exception of such quotations, this thesis is entirely my own work;
- I have acknowledged all main sources of help;
- where the thesis is based on work done by myself jointly with others, I have made clear exactly what was done by others and what I have contributed myself. See acknowledgements.
- parts of this work have been published and these publications are listed on the following page.

Signed:…………………………

Date: 27th July 2013

Publications and Awards

Journal publications

- M.-H. Evans, White structure flaking (WSF) in wind turbine gearbox bearings: effects of 'butterflies' and white etching cracks (WEC), *Materials Science and Technology*, 28 (2012) 3-22.
- M.-H. Evans, J.C. Walker, C. Ma, L. Wang, R.J.K. Wood, A FIB/TEM study of butterfly crack formation and white etching area (WEA) microstructural changes under rolling contact fatigue in 100Cr6 bearing steel, *Materials Science and Engineering A*, 570 (2013) 127-134.
- M.-H. Evans, A.D. Richardson, L. Wang, R.J.K. Wood, Serial sectioning investigation of butterfly and white etching crack (WEC) formation in wind turbine gearbox bearings, *Wear*, 302 (2013) 1573-1582.
- M.-H. Evans, A.D. Richardson, L. Wang, R.J.K. Wood, Effect of hydrogen on butterfly and white etching crack (WEC) formation under rolling contact fatigue (RCF), *Wear*, (2013), In Press, http://dx.doi.org/10.1016/j.wear.2013.03.008
- M.-H. Evans, L. Wang, H. Jones, R.J.K. Wood, White etching crack (WEC) investigation by serial sectioning, focused ion beam and 3-D crack modelling, *Tribology International*, (2013), In Press, http://dx.doi.org/10.1016/j.triboint.2013.03.022
- R.J.K. Wood, A.S. Bahaj, S.R. Turnock, L. Wang, M.-H. Evans, Tribological design constraints of marine renewable energy systems, *Philosophical Transactions of the Royal Society A*, 368 (2010) 4807-4827.

Awards

2013 **Platinum Poster Prize, Society of Tribologists and Lubrication Engineers (STLE)**
1st place poster prize at the STLE 2013 Annual Meeting.
2013 **Thomas Andrew Common Award Grant, Institute of Mechanical Engineers (IMechE)**
Award grant for international conference attendance.
2012 **Tribology Bronze Medal, Institute of Mechanical Engineers (IMechE)**
Award made annually to an early career scientist/engineer less than 30 years of age.
2012 **Dowson Prize, 39th Leeds-Lyon Symposium on Tribology, Shell Global Solutions**
Award made every two years for the best student journal paper and presentation.
2012 **Innovation in Tribology Prize, Institute of Physics (IOP)**
Annual prize for research demonstrating an innovative approach to tribology.
2011 **Materials Literature Review Prize, Institute of Materials, Minerals and Mining (IOM^3)**
Winning review paper in the national MST journal competition.
2010 **Mission of Tribology Award, Institute of Mechanical Engineers (IMechE)**
One award made per year at the annual conference for the best presentation.

Nomenclature

a	Semimajor axis of the contact ellipse [m]
b	Semiminor axis of the contact ellipse [m]
C	Dynamic load rating which is defined as the load which will give a life of 10^6 revolutions of the inner race
C_i	Global cleanliness index
E	Elastic Modulus [Pa]
E'	Reduced Young's Modulus [Pa]
F	Force of friction exerted by each surface on the other, acting parallel to the surface in a direction opposite to the net applied force [N]
G	Dimensionless material parameter $\alpha E'$
h	Asperity height [m]
$h_{central}$	Central film thickness [m]
h_{min}	Minimum oil-film thickness [m]
H	Hardness [Pa]
i_{total}	Total index for each inclusion type
i_{mean}	Mean index for each inclusion type
k	Ellipticity parameter [a/b]
k_{kappa}	Viscosity ratio (kappa value)
k_0, k_1, k_2, k_3, k_4, k_5	Contact coefficients which are determined by equations and charts
ΔK_{Th}	Fatigue threshold stress intensity [MPa $m^{1/2}$]
K_{1c}	Fracture toughness [MPa $m^{1/2}$]
L_{10} life	L_{10} is the expected life of 90% of similar bearings under similar operating conditions
n	Empirical load life exponent
N	Normal force exerted by each surface on the other, acting perpendicular (normal) to the surface [N]
P	Contact pressure (Hertzian stress) [Pa]
P_{eq}	Equivalent radial load [N]
P_{max}	Maximum contact pressure (Hertzian stress) [Pa]
R'	Reduced radius of curvature [m]
R_{bx}	Radius of curvature of body 'B' in the 'x' direction [m]
R_{by}	Radius of curvature of body 'B' in the 'y' direction [m]
R_x	Reduced radii of curvature in x-direction [m]
R_y	Reduced radii of curvature in y-direction [m]
R_a	Arithmetic average of the roughness profile [m]
R_{ax}	Radius of curvature of body 'A' in the 'x' direction [m]
R_{ay}	Radius of curvature of body 'A' in the 'y' direction [m]
R_{a1}	Arithmetic average of the roughness profile of body 'A' [m]
R_{a2}	Arithmetic average of the roughness profile of body 'B' [m]
$R_{p0.2}$	Yield strength [MPa]
R_q	Root mean squared roughness [m]
$R_{q,1}$, $R_{q,2}$	Root mean squared roughness of body 'A' and body 'B' [m]
t	Direction of travel for contacting surface
u	Mean lubricant entrainment speed [m/s]
U	Dimensionless speed parameter $u\eta_0/(E'R)$
U1, U2	Surface speed of test rollers [m/s]
v	Operating viscosity of the lubricant [mm^2/s]
v_1	Rated viscosity depending on the bearing mean diameter and rotational speed [mm^2/s]
V	Sliding velocity [m/s]
W	Dimensionless load parameter $w/(E'R^2)$
x_o	Position where τ_o acts in the x-direction (i.e. y=0) [m]
z	Depth below contact surface (z, radial direction) [m]
z_{max}	Depth under the surface where the maximum unidirectional shear stress acts [m]
z_o	Depth under the surface where the maximum orthogonal shear stress acts [m]
α	Pressure–viscosity coefficient [Pa^{-1}]

δ	Total deflection at the centre of the contact (i.e. $\delta = \delta_A + \delta_B$; where '$\delta_A$' and '$\delta_B$' are the maximum deflections of body 'A' and 'B', respectively) [m]
η_0	Viscosity at atmospheric pressure of lubricant [Pa s]
λ	Lambda ratio: the parameter characterising the ratio of the minimum film thickness to the composite surface roughness
μ	Friction (or traction) coefficient
ν	Poisons ratio
σ	Residual stress [Pa]
σ_{xx}, σ_{yy}, σ_{zz}	Principal stress components where x represents the over-rolling direction, y the width and z the depth (also σ_1, σ_2, σ_3)
σ_{yield}	Yield strength of material [Pa]
σ_e	Fictitious equivalent stress for the multi-axial stress state [Pa]
τ	Unidirectional shear stress acting at ±45° below the centre of the contact [Pa]
τ_{max}	Maximum unidirectional shear stress acting at ±45° below the centre of the contact at depth z_{max} (principle shear stress) [Pa]
τ_o	Orthogonal shear stresses acting parallel and normal to the surface below the contact surface (also τ_{zy}, τ_{yz}) [Pa]
$\tau_{o,max}$	Maximum orthogonal shear stress acting parallel and normal to the surface below the contact at depth z_o [Pa]
ϕ	Angle between the plane containing the minimum principle radius of curvature of body 'A' and the plane containing the minimum principle radius of curvature of body 'B' [rads]

Acknowledgements

This PhD project has been fully funded by **Vestas Wind Systems**. I wish to thank the following past and present employees who have steered and assisted the project in numerous ways: Christian Højerslev, Ole Lund Jensen, Marie Syndergaard, Morten Haastrup, Cecilie Laursen, Jörg Wadehn, Sverrir Gunnarsson, Jochen Baum, Corina Münch, WenFei Wu, Andrea Redolfi and Robert Rowntree.

Ling Wang and Robert Wood, as supervisors you are the most instrumental people in this project. The freedom you have given me to steer the project and cooperate with others has enabled me to strive for success and I sincerely thank you for this. I am very grateful for your continuous support throughout.

John Walker, thank you for your interest in butterflies! With your skill and perseverance we got there in the end and it was worth it. Your involvement from start to end in all aspects of that piece of research was instrumental. For that reason I wish to extend a special thanks to you.

Alex Richardson, you have played a significant role in this research. I sincerely thank you for your dedication and perseverance in the face of tedium. I hope you enjoy your future PhD as much as I have enjoyed mine.

A special thanks also goes to Terry Harvey for many hours spent advising, assisting in the practical aspects of the project and revising papers. You have been there to support me when there was no one else and I hugely appreciate that. Your willingness to help on all aspects of the project has aided me more than you realise.

I would like to thank Richard Pargeter and Sally Day at TWI for enabling access to the thermal desorption analysis machine and for your advice on the experiments. Mark Gee, I also thank you for allowing access to the FIB at NPL. Mike Lewis, you have been a supporter of this work from early on. I thank you for sharing your experiences from ESR Technology on steel cleanliness and butterfly formations. George Plint, you have always been more than willing to advise on operational aspects of the TE-74S two-roller testing and tribology in general. I therefore wish to thank you and your co-workers for your support in this project. Jens Grønbæk, thank you for your support and manufacturing our test samples to a very high quality at your company Strecon AS.

Thanks goes to the Southampton Nanofabrication Centre for access to the Focused Ion Beam (FIB) and Scanning Transmission Electron Microscopy (STEM) in this work.

A thank you also goes to the following people at the University of Southampton who have assisted in various ways during this project: Richard Boardman, Samuel Keyes, Steve Pilcher, Dave Beckett, Daniel Bull, Nicola Symmonds, Chao Ma, Stefano Neodo, Daniel Sutton, Chris Williams, John Walker, Shuncai Wang, Brian Mellor, Philippa Reed, Jurgita Zekonyte, Richard Cook and Sue Berger.

Thank you to my fellow past and present colleagues who have made my time at Southampton immensely enjoyable as well as best friends from Bournemouth, you know who you are. Thank you for your friendship and support, it means the world to me.

Bente and Søren Stær, thank you for hosting me and making my time very enjoyable in Aarhus numerous times over the last three years when visiting Vestas R&D headquarters.

Foremost I would like to thank my fiancée Warinthorn Kiadtikornthaweeyot. It is without a doubt in my mind that your immense support, understanding and patience over the last 3 years has allowed me to have more than my fair share of success from this PhD. I wish you equal success in finishing your PhD and I look forward to continuing our life together for the foreseeable future in Thailand!

Mum and dad, the vast amount of time and energy you have invested supporting me has not gone unnoticed or unappreciated. I owe no small part of the PhD to you. I hope you have enjoyed witnessing the journey as much as I have enjoyed travelling it!

Contributions to the work:

- The FIB process presented in chapters 3, 5 and 6 was directed by myself but operated by Dr. John Walker (nCATS) and Dr. Ken Mingard (NPL) and Ms. Helen Jones (NPL). All analysis and interpretation of data was conducted by myself.
- The STEM/TEM work presented in chapters 3, 5 and 6 was guided and partly operated by myself but also Dr. John Walker (nCATS) and Ms. Chao Ma (nCATS).
- The serial sectioning work presented in chapters 4, 5 and 6 was designed and prepared by myself. A significant part of the actual serial sectioning process was conducted by myself and a large portion was also conducted by Mr. Alex Richardson (nCATS) under my direction as part of a summer internship to support the PhD project. All data analysis and interpretation was conducted by myself.
- The steel elemental analysis and steel cleanliness analysis was carried out at the Dr. Sommer Werkstofftechnik GmbH lab. The X-ray diffraction analysis was conducted by Stresstech.
- The hydrogen concentration analysis experiments were designed and executed by myself and the actual thermal desorption analysis was conducted by Ms. Sally Day (TWI) under my direction.
- The large-scale transient testing of high-speed gearbox bearings presented in chapter 7 was partly designed by myself but was operated and executed by colleagues within Vestas.

1. Introduction

1.1 Project overview

It is well established that the average service life of multi-MW wind turbine gearboxes is approximately 5 years rather than the desired 20+ years. The high failure rates of wind turbine gearboxes are resulting in a higher cost for wind energy, since it costs between £0.1 – 0.3m (2010 costing) to replace a gearbox.

Rolling element bearing failures account for the majority of gearbox failures, with a large proportion being attributed to a premature failure mode called *White Structure Flaking (WSF)*, thought to be due to environmental effects and transient operating conditions not fully understood. The formation of so-called *butterflies* and *white etching cracks* (WEC) are known causes of premature failures generated by rolling element contacts. However the formation of WECs are especially not well understood which has limited the development of solutions for WSF.

1.2 Aims & objectives of the project

The aims of the project were to conduct systematic rolling contact fatigue (RCF) testing and advanced microstructural analysis of test samples and wind turbine gearbox bearings to investigate the formation drivers and formation mechanisms of WSF.

The main objectives of this project are listed below:

- To carry out a comprehensive literature survey on the WSF failure mode to clarify the considerable confusion in the field concerning what the suggested formation drivers and formation mechanisms are and what further research is required to address the unknowns. This informs test equipment, test conditions, methodology and post-test analysis.
- To develop laboratory test programmes that enable reproduction of butterflies and WECs repeatedly under conditions realistic to wind turbine gearbox bearing operation.
- To investigate tribological drivers and formation mechanisms of butterflies and WECs. Key variables for investigation: load, slip, rolling cycles and concentration of diffusible hydrogen.
- Use metallographic analysis techniques coupled with advanced microstructural analysis techniques (FIB and STEM/TEM) to characterise butterflies/WECs and their formation mechanisms in both test samples and wind turbine gearbox bearings.
- To elucidate initiation and propagation mechanisms of WECs to inform design of potential solutions.

1.3 Thesis structure

Fig. 1.3.1 shows the main workflow of the thesis.

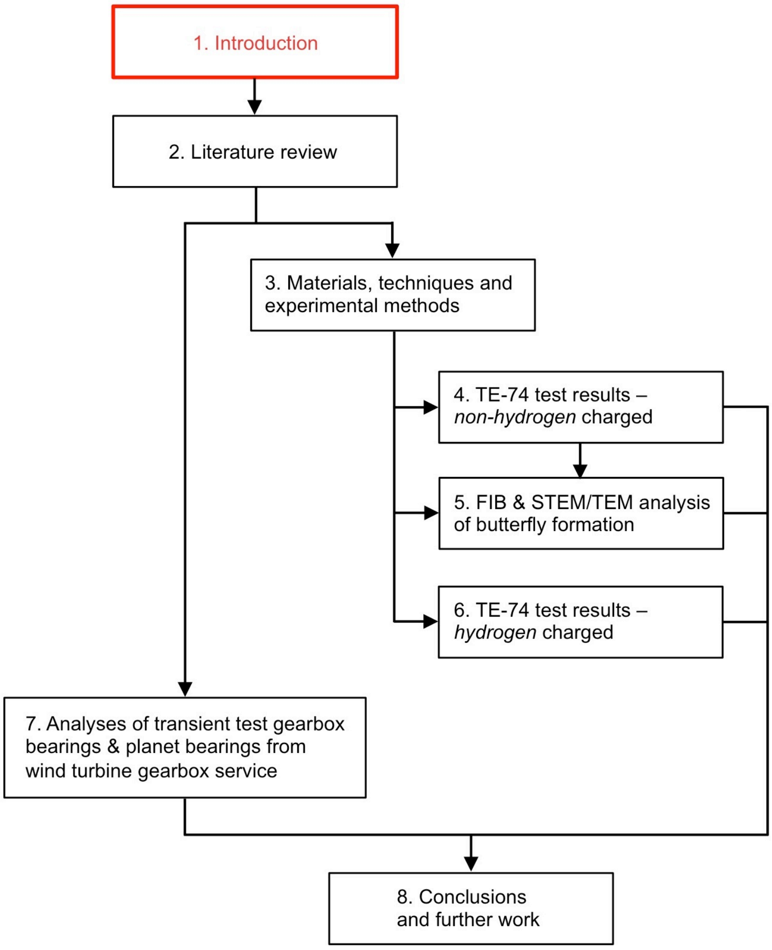

Figure 1.3.1: Thesis work flow chart.

Chapter 2 – Literature review

Chapter 2 overviews the fundamentals in bearing technology, tribology, materials and rolling contact fatigue relevant to this project. Following this a collation and discussion of the previous literature regarding butterflies and WECs is made with a focus on formation drivers and formation mechanisms. Emphasis is made at the end concerning the testing strategies used in the aim of enabling WEC formation in lab testing.

Chapter 3 – Materials, techniques and experimental methods

Chapter 3 presents the materials, experimental methods and analysis techniques utilised in this project. The details of the analysis used to characterise the steel used to manufacture the TE-74S test rollers is presented. Later the process used to conduct metallographic analysis is detailed, followed by the advanced microstructural analysis and modelling techniques utilised.

Chapter 4 – TE-74S test results - non-hydrogen charged

Chapter 5 presents a brief overview of the test results and analysis conducted concerning the TE-74S two-roller *non-hydrogen* charged tests. A major output concerning microstructural analysis of butterfly formation in one of these tests is presented in chapter 5.

Chapter 5 – FIB & STEM/TEM analysis of butterfly formation

Chapter 5 provides a detailed microstructural characterisation investigation of butterfly crack formation from testing in chapter 4. SEM, FIB tomography, 3D modelling and TEM/STEM analysis techniques are used to determine crack initiation and carbide dissolution as part of the WEA microstructural change formation.

Chapter 6 – TE-74S test results - *hydrogen charged*

Chapter 6 presents the main experimental outputs of the project concerning the *hydrogen charged* TE-74S two-roller testing. The influence of contact pressure, rolling cycles and concentration of diffusible hydrogen on butterfly and WEC formation is quantified by a serial sectioning metallography technique. Advanced analysis techniques and 3D modelling is used to help elucidate WEC initiation and propagation mechanisms.

Chapter 7 – Analysis of transient test gearbox bearings & planet bearings from wind turbine gearbox service

Chapter 7 is an important chapter that details results from transient gearbox bearing testing on the project sponsors test rig and serial sectioning metallographic analysis of these test bearings and bearings from wind turbine gearbox bearing service. The work has been conducted to compare the formation mechanisms of WECs in these large-scale bearings with the smaller hydrogen-charged lab tests details in chapter 6.

Chapter 8 – Conclusions and further work

Chapter 8 presents the main novelties and conclusions from this project. Further work is also suggested.

Appendix

The appendix details the calculations used for determining the maximum contact pressures and shear stresses during rolling contact in the 26v52 mm test rollers.

2. Literature review

2.1 Introduction

This chapter presents an overview of the WSF premature bearing failures that occur in wind turbine gearboxes and other applications. The tribological conditions in bearing operation and a general background on rolling contact fatigue are given. The review then concentrates on the specific damage features associated with WSF, namely butterflies and white etching cracks (WECs). The tribological drivers of WSF and possible prevention measures that have been investigated so far are discussed. The chapter concludes with suggestions of areas that need to be investigated with research studies and finally strategies to enable WEC formation in lab testing. Fig. 2.1.1 shows the thesis work flow chart.

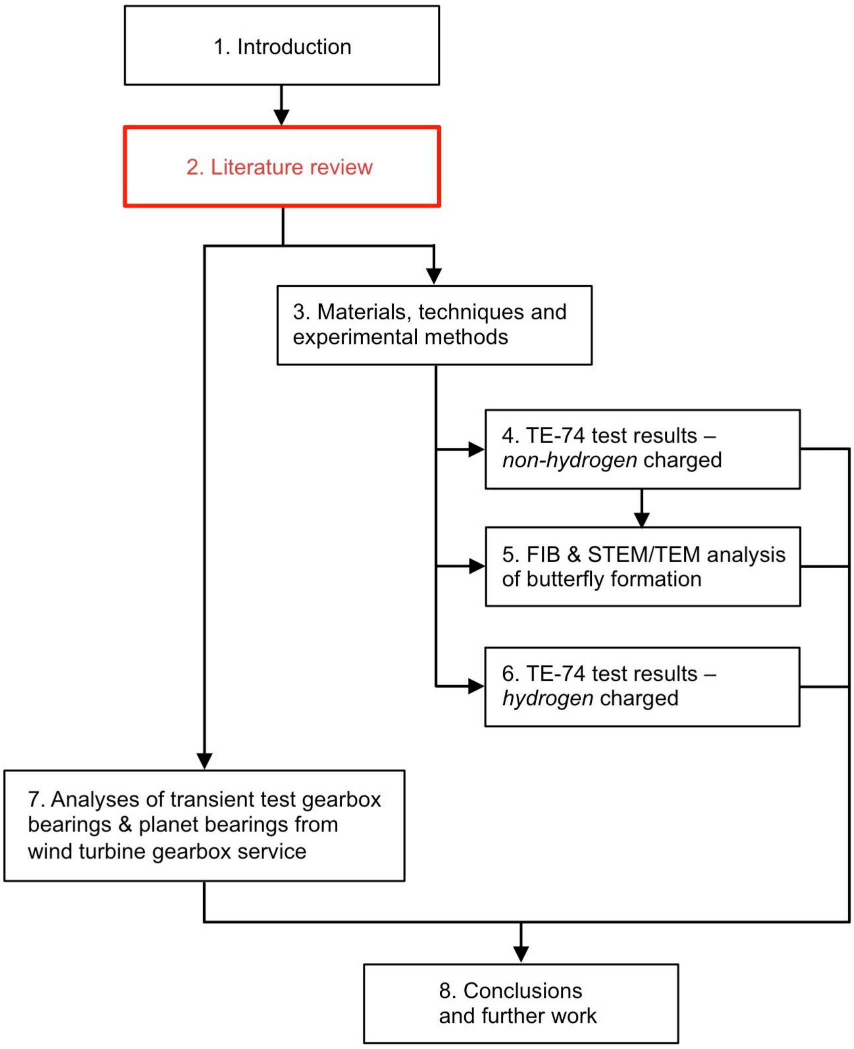

Figure 2.1.1: Thesis work flow chart.

2.2 Overview of gearbox bearings & their failure modes

2.2.1 Introduction

The wind energy industry is experiencing an increasing interest from governments worldwide as they aim to meet their ambitious renewable energy targets. However it is well established that the actual service life of wind turbine gearboxes is often well below the desired 20 years. Wind turbine gearboxes tend to fail predominately at several critical bearing locations, by the modes of micropitting, smearing and white structure flaking (WSF) [1]. The *'L_{10} life'* of a bearing characterises the rolling contact fatigue (RCF) life of a bearing for a given operating condition at which statistically 90% of bearings survive. Normal RCF failures typically exceed the L_{10} life and eventually fail by spalling failure (flaking of the steel surface), which is unavoidable and will always occur in bearings. Micro-pitting is a surface initiated fatigue flaking failure caused by moderate roller/raceway sliding, breakdown of the oil film and through contamination by hard particles [1]. Micropitting occurs in both bearings and gear teeth [2]. Smearing typically occurs in high-speed bearings where gross sliding causes metal-to-metal contact and subsequent material transfer across contact surfaces [1]. Premature bearing failures in the form of WSF are another type of spalling (Fig. 2.2.1), which differs from the conventional subsurface slow material decay caused by RCF.

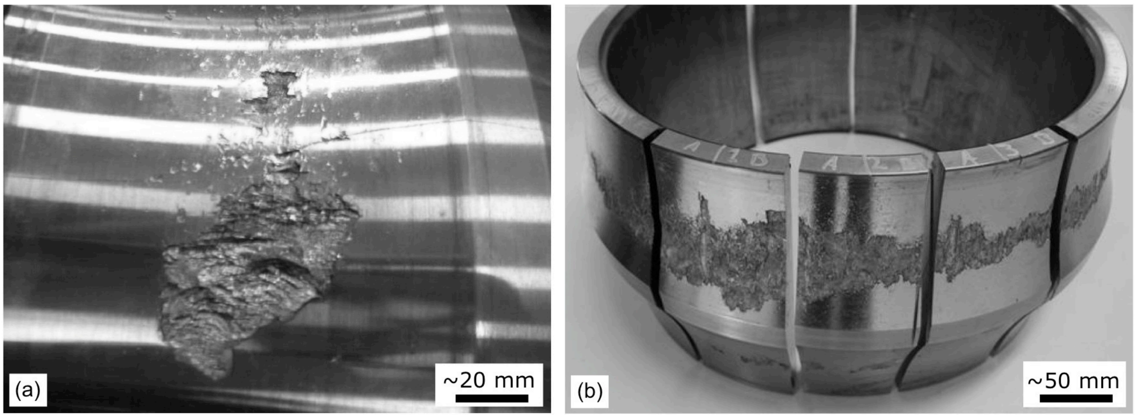

Figure 2.2.1: Optical microscopy images of material removal by white structure flaking (WSF) on wind turbine bearing inner raceways. (a) Double row spherical roller bearing inner ring. (b) Double row spherical roller bearing inner ring from a planetary stage.

The WSF type of flaking is not reserved to any one type of bearing. It is found to be unpredictable and has been observed to occur at as little as 1% of L_{10} life [3], but more commonly at 5 – 20% of L_{10} life [4-6]. WSF is associated with a microstructural change in bearing steels that is usually called *white etching area* (WEA) and *white etching cracks* (WECs)

(Fig. 2.2.2). WEA gains its name from the white appearance of the altered microstructure after being etched in Nital solution (~2% Nitric acid in ethanol) and viewed under reflected light. WEA/WECs formed in the ~1 mm zone beneath the contact surfaces lead to WSF. WSF has also been related to butterflies due to butterfly wings consisting of WEA. Butterflies are cracks with microstructural changes induced around stress raisers (typically non-metallic inclusions) under highly localised subsurface shear stresses forming a butterfly shape.

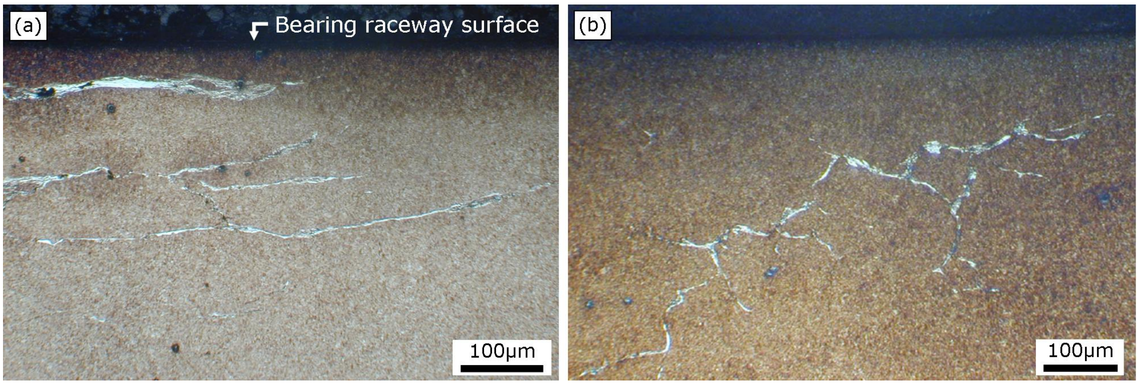

Figure 2.2.2: Optical microscopy images of axial sections through wind turbine inner ring bearing raceways showing WECs. (a) Parallel WEC. (b) Branching network WEC. Both sections from a double-row spherical roller bearing made from 100CrMo7-3 bainite steel. Oil lubricated during operation. Ref [7].

White etching phenomena occur in many applications; on hard turned surfaces [8-10], rail track surfaces [11-15], as adiabatic shear bands (ASB) in ordnance and machining processes [16, 17], and in rolling element bearings as white etching bands (WEB) [18-21], butterflies and WECs. The steel type varies widely between these applications; white etching layers (WEL) from hard turning [9, 10], ASB, WEB and butterflies/WECs have been found in standard bearing steel AISI-52100/100Cr6 for example, which has been used for over 100 years. Rail steels are typically pearlitic steels (0.65 – 0.8 wt.% C) or bainitic steel (0.2 – 0.55 wt.% C) with manganese additions [11, 12, 15]. Surface WEL from hard turning are typically a few microns deep, with hardness of 900 – 1200 HV [9, 10], whereas WEL on rail tracks form at the surface to a depth of ~100 μm with a hardness of ~1200 HV [11].

In bearing steels, white etching area (WEA) formation as butterflies and WECs occur in martensitically through hardened steel [22-39], bainite steel [22], case-hardened steel [25, 40-42], high chromium steel [5, 31, 34, 35, 43], tungsten tool steel [40], high speed tool steel [30], graphite steel [26] and steel containing no carbides [23]. WEA consists of almost equiaxed nano-ferrite grains 10 – 100 nm in diameter [22, 25-29, 37, 39, 44, 45]. WEA has often been observed with a lack of carbides, which has been suggested to be due to deformation, break-up and dissolution of the carbides [21, 23, 26-28, 39, 45, 46] and are cited to be supersaturated with carbon to varying wt.%'s [41, 42]. WEA typically has hardness 30 – 50% higher than the matrix

[25, 28, 39].

WEAs were reported in literature several decades ago [18, 23, 30, 39, 40], but it was not until just over a decade ago that WECs started to be widely reported [1, 4-6, 22, 26, 29, 31-38, 40-43, 47-58]. WECs has many synonyms; white structure, white etching area (WEA), white-banded flaking, irregular white etching area (irWEA), unusual microstructural change (UMC), bright etched regions (BER), exfoliation, peculiar microstructural change, flaking at early stage, white etching constituent (also WEC), subsurface-initiated flaking, white etching bands, white layers, brittle flaking and hydrogen embrittlement. WEA microstructural change occurs in wind turbine gearbox & main bearings [1, 6, 47], hydrogen fuel cell system bearings [37, 54, 57], marine POD drive bearings, paper machine bearings, automotive alternator, electromagnetic clutch, inclusion pulley, air-conditioner compressor, water pump & driveline transmission bearings [41, 43, 50, 53, 56, 57], rolling members of torodial CVT [59], aircraft turbine bearings [40], crane lifting devices [6] and gears [39]. However despite these failures having been observed for two decades in various industries, their formation mechanisms and preventative solutions against them are not well understood, especially in wind turbine gearbox bearings.

2.2.2 Wind turbine gearboxes

Most wind turbines have a horizontal axis with a drive train incorporating a gearbox with ~15 bearings to step-up the ~15 – 35 rpm rotor input to ~1500 – 1800 rpm output (50 – 60 Hz) for AC generation (Fig. 2.2.3). The gearbox oil used to lubricate bearings and gears is part of a circulatory system (contained on most turbines wholly within the nacelle) that regulates oil temperature and filtering of contaminates. Most wind turbines use just one type of lubricant inside their gearboxes. In older models the gears dipped into an oil sump at the bottom of the gearbox, though this is becoming obsolete in multi-MW wind turbines that operate with dry sump at normal conditions. Lubricants have to work for both gear tooth contact and bearings; therefore additives are not designed specifically for bearings. The oil sump is also where heavier particles such as debris and contaminants collect, subsequently being filtered out. The lubricant, usually oil, is guided to the bearings by pipes to ensure they have a feed of oil at all times.

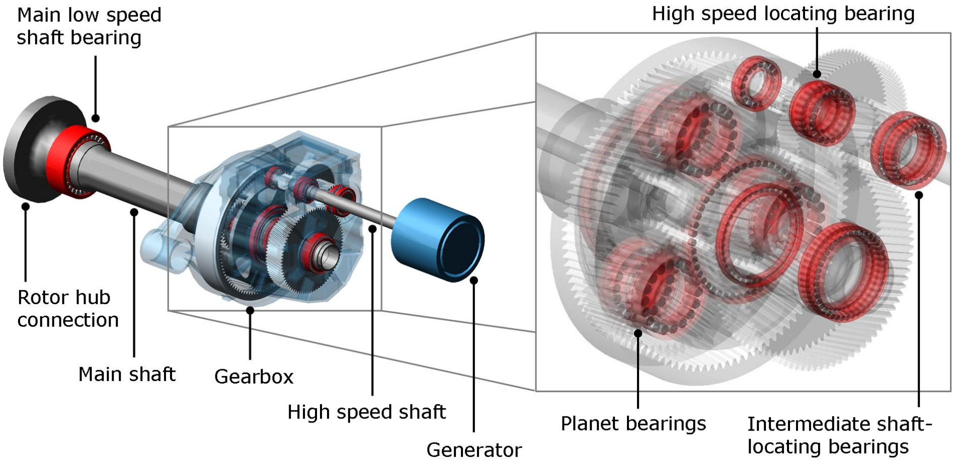

Figure 2.2.3: Typical gearbox configuration for wind turbines above 500 kW. The first stage of the gearbox is a planetary system that uses either spur or helical gears, where the sun pinion drives a parallel low-speed shaft, driving an intermediate stage, which in turn drives the high-speed shaft. The low- to high-speed shafts use helical gears and these types of gearboxes use approximately fifteen bearings. Wind turbine CAD model constructed from Ref [60].

2.2.3 Gearbox bearings

Most wind turbine gearboxes contain approximately 15 bearings as shown in Fig. 2.2.3. It is suggested by major wind turbine original equipment manufacturers (OEMs) that ~60 – 85% of gearbox failures are caused by bearing failures. It is further proposed that ~70 – 90% of these bearing failures are attributed to WSF.

A double row rolling element bearing is shown in Fig. 2.2.4a. A rolling element bearing consists of four components; inner race, outer race, rolling elements and cage.

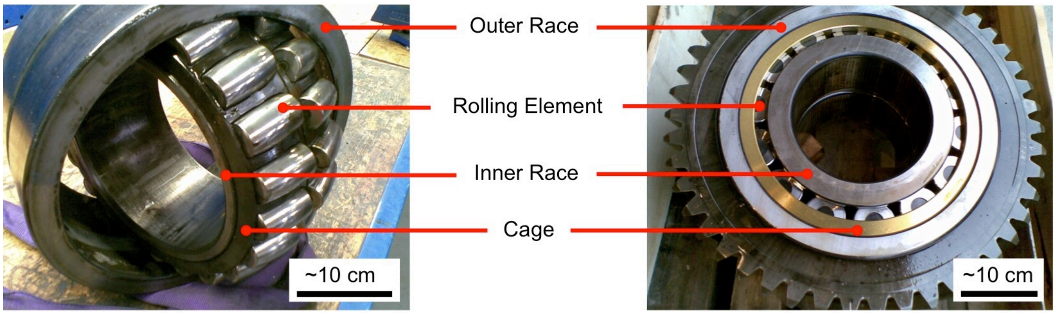

Figure 2.2.4: (a) Double row spherical rolling element bearing overview. (b) Planetary bearing system for wind turbine gearbox.

The inner raceway is usually coupled onto a shaft with an interference fit and is the driven component. The contact surfaces of the inner and outer ring as well as the elements are precision finished to give moderately low surface roughness, the importance of which is explained in following sections. The operation of rolling element bearings is complex due to numerous stresses operating, friction, surface deformation and wear. These are addressed in the following sections. To separate the contact surfaces during motion, rolling element bearings require lubrication to operate. The lubricant amount, type and cleanliness are essential factors. An elasto-hydrodynamic (EHD) film is desired between rolling contact surfaces to enable the bearing to operate and prevent metal-to-metal contact. Other desired features of the oil are to minimise friction, corrosion, wear, heat build-up, contamination and bearing noise. Problems are introduced by surface and subsurface defects, very high or low operating temperature, low speeds, incorrect installation (such as misalignment) and contamination. Both high loads and debris entrainment can cause excess clearances in the bearings. There are also concerns across certain parts of the system with stray electrical currents leading to wear and micropitting of bearings due to electro-corrosion mechanisms. These are discussed in later sections.

Bearing manufacturers follow international bearing rating standards, International Standards Office (ISO 281:2007) [61]; however each manufacturer uses proprietary design life assessments which can introduce large differences in actual calculated bearing life. The scale-up issue is also important, as most bearing life calculations are based on comparatively small bearings. Gearbox manufacturers rely on bearing manufacturers for the bearing life assessment and commercial sensitivities often make this a less than transparent process [62]. In addition, the bearing manufacturers may not have full information about the severe tribological conditions and complex loading conditions the gearbox experiences, such as unpredictable loads beyond the bearing mounting location (e.g. housing deformations). This results in bearings that are unable to sustain the operation conditions. It would seem that a greater level of collaboration between bearing manufactures, gearbox manufactures and wind turbine OEMs is required to help design gearboxes and bearings that can survive the intended 20-year lifetime.

2.2.4 Operating conditions and tribological problems

Despite manufacturers keeping to international standards for wind turbine gearbox manufacture (ISO 81400-4:2005 [63]) and standards concerning maintenance specifications based upon an expected gearbox lifetime of twenty years (ANSI/AGMA/AWEA 6006-A03, [64]), this does not currently result in gearboxes reaching their designed life time. Gearboxes often fail prematurely within 0.5 – 11 years of operation [47, 65-70] at critical bearing locations such as the planet bearings, intermediate shaft-locating bearings and high speed locating bearings [47, 62] (see Fig. 2.2.3). Total gearbox replacement including installation and downtime can cost up to £300,000 [67, 71] resulting in a higher cost for wind energy.

The high rate of growth in wind turbine size and capacity is resulting in increasingly extreme operating conditions, requiring more challenging designs. Optimising the basic design of gearboxes is problematic, as these have to be validated in gearbox test rigs and field trials before the design is qualified. This takes years to complete and the outcome is less than certain, especially on the long term as gearbox trials are not able to simulate long term longevity. In addition to concerns about basic design, the bearings in gearboxes are forced to incorporate materials which are already inadequate [72] (see bearing steel section).

Gearbox bearing failures are typically caused by the severe tribological environments and dynamic multi-axial loads faced [1, 73, 74]. For example gearbox oil often overheats in service, contamination by particles and moisture is frequent and wind turbines are used all over the world in varying climates. One oil lubricates both gear and bearing contacts throughout widely differing speed and load operating conditions, leading to bearings often running in mixed and boundary lubrication regimes. Gearbox oils are often not completely changed for long durations between 25,000 – 50,000 operating hours [75], although online filtration is used and often oils are topped up with additives. As the automotive industry has been operating for a much longer time, additive packages are often applied from this sector to the wind turbine industry. This may result in the lubricant additive chemistry perhaps not being optimised for their intended purpose.

An ever fluctuating torque is characteristic from the turbulent nature of wind (where for large wind turbines this variation is relatively fast compared to rotational speed), resulting in accommodating drive-train movement. Hence planet bearings for example are misaligned a number of times during a single revolution [65]. Gearbox bearings in general are subjected to various transients during operation such as wind gust loading, misalignment (i.e. excessive axial movement), sliding in-between elements and race, inertia forces, braking loads, torque reversals from electrical grid fluctuations and severe vibrations [76-78]. Premature engagement of the wind turbine to the electrical grid results in accelerations and decelerations, overloading and instantaneous torque reversals. Wind turbines can typically experience ~3000 start-up's/year with ~5 torque oscillations at each start, resulting in ~15,000 overloads/year [72]. Torque reversals can indirectly relocate load zones on bearings and impact loading on sliding and misaligned elements cause peak stresses at certain element contact points [1]. Wind turbines also suffer tribological and loading problems during idling or long standstills either prior to electrical grid connection or during service.

The essence of the problem is that severe transient and tribological operating conditions in wind turbine gearbox bearings are not fully understood and thus bearings are not designed to sustain them.

2.2.5 Bearing steel

Martensitic and bainitic through-hardened bearing steels

To survive the thermomechanical loads in service, bearing steels must have high fatigue resistance against alternating shear stresses (obtained by good steel cleanliness and high hardness), resistance to wear, high elastic limit to prevent excessive deformation under load, and good dimensional stability [30, 31, 79]. Tempering temperatures of common through-hardened bearing steels such as AISI-52100 steel (~160 – 200 °C), as well as many case-carburised and carbo-nitrided steels, are well above the typical operating temperatures (90 °C max) of wind turbine gearboxes (although oil flash temperatures will be significantly higher). With the relatively low cost of through hardened steels, this make them suitable for most bearing applications. Carbo-nitrided and case-carburised steels are typically more expensive and are used when through hardened steels are not appropriate.

The majority of bearings are manufactured from through-hardening steels. These steels are classed as (hyper)eutectoid-type steel when containing more than 0.8% carbon by weight and contain less than 5% by weight of total alloying elements. Various grades are available depending on the application. The American Iron and Steel Institute (AISI) 52100 martensitic high carbon chromium bearing steel (100Cr6) is used in most wind turbine gearbox bearings, and has therefore been used for the RCF testing in this study and will be focused on in this section. The chemical composition and mechanical properties of martensitic AISI 52100/100Cr6 steel in the tempered condition are shown in Table 2.2.1 and Table 2.2.2 respectively.

Table 2.2.1: The chemical composition (wt.%) limits for AISI 52100, 100Cr6, EN31, JIS-SUJ2 steels.

C	Mn	Si	P	S	Cr	Mo	Fe
0.98–1.10	0.25–0.45	0.15–0.35	0.025max	0.025max	1.30–1.60	0.00–0.10	balance

Table 2.2.2: Mechanical properties of AISI 52100, 100Cr6, EN31, JIS-SUJ2 steels [80, 81].

Ultimate tensile strength [MPa]	Yield strength, $R_{p0.2}$ [MPa]	Fatigue threshold stress intensity ΔK_{Th} [MPa $m^{1/2}$]	Fracture toughness K_{1c} [MPa $m^{1/2}$]	Vickers hardness HV	Elastic modulus E GPa
2150 – 2450	1400 – 2200	4.5	18	750 – 850	190 – 210

The process of manufacturing 100Cr6 steel is as follows; austenitisation, quenching and tempering. During austenitisation, the plain carbon steel is heated to ~850 °C for ~15 minutes changing the steel to face centred cubic (FCC) crystal structure in solid solution, so that the austenite is formed. Subsequently rapid quenching in oil or water baths take place, to a temperature that forms a martensite structure that is body centred tetragonal (BCT) in supersaturated solid solution (if the carbon content exceeds solubility in ferrite, 0.02 wt.% at 723 °C). In the present condition, the martensitic plain carbon steel is very hard and strong, but lacks toughness and is limited by its susceptibility to small material flaws, thereby becoming brittle. Therefore a further heat treatment, tempering, is required to give toughness. During tempering the as-quenched martensite is raised to certain temperatures and held for specific durations. It is customary to divide the process into different temperature stages, although it should be understood that there is overlap between neighbouring stages [79, 82].

For bearing applications discussed in this study, 100Cr6 steel is tempered at ~180 °C for 1 – 2 hours, or a double temper process of 2X 1-hour, to give a tough but also hard (~60 HRC) microstructure. The resultant microstructure is very complex which contains six constituents: tempered martensite, retained austenite, ferrite + cementite (from decomposition of retained austenite), metastable ε-carbides (temper carbides), cementite and undissolved carbides (from austenitization) [79, 83]. The microstructure of tempered martensite before over-rolling mainly shows very thin (0.1 – 1 μm width) martensite needles with a high dislocation density [84]. 100Cr6 steel typically contains approximately 7 – 15 vol.% retained austenite [19, 84, 85], and it contains 3 – 5% vol.% of $(Fe,Cr)_3C$ type carbides that does not dissolve during the austenitising treatment preceding hardening [81, 85]. In addition, there are always non-metallic inclusions present with a variety of compositions and morphologies.

Bainitic steel: the formation of bainitic steel, another type of through hardened steel, is achieved by a process called 'austempering', where the steel is quenched and held in a molten salt bath through the bainite transformation temperatures (~500 – 250 °C) and then moderately cooled [82]. There are various advantages that can be gained by use of bainitic steels rather than martensitic. These advantages are less harsh quenching, which results in less rapid volume changes and therefore less induced distortion and potential for cracking in the steel when compared to martensitic steels. Use of bainitic steels is thus easier for larger bearings, where rapid quenching can be difficult and large potential for cracking and distortion is possible.

An explanation of the manufacturing techniques and resultant properties of 100Cr6 steel can be found in Harris & Kotzalas [81], which reveals the difficulty in manufacturing steel to certain quality standards and indirectly highlights where steel could differ in microstructural terms within the same grade.

Steel cleanliness

Various elements are used during the manufacture to aid the process and make machining after manufacture easier. These elements can combine with other elements such as oxygen or the alloying elements in the steel to create non-metallic inclusions. These can be evenly distributed throughout the steel or segregated into bands or areas depending on manufacturing. Upon subsequent rolling deformation of the steel to make bearing rings for example, the inclusions tend to elongate in the plane perpendicular to rolling. Therefore inclusions can range in aspect ratio (i.e. globular or elongated) and range in length from ~1 – 500 µm depending on the inclusion composition [81, 86]. Typical inclusion compositions are: elongated manganese sulfides (with or without oxide encapsulation), aluminates as bands and stringers, elongated silicates, globular oxides (pure or in combination with Al, Ca, Mg, etc.) and titanium carbo-nitrides. See the ISO 4967-B steel cleanliness standard [87] for further description and examples of these inclusions.

Steel cleanliness refers to the number, type and size of non-metallic inclusions in the steel introduced during the manufacturing process. Various standards are typically used to assess the cleanliness of bearing steels. These typically assess the maximum size of inclusions by statistical methods and also the density of inclusions [87, 88]. In all cases, actual cross-sections of the steel need to be analysed with optical microscopy. Inclusions viewed in the cross sections are recorded and compared to pre-determined charts in the standards to categorise the inclusions via their composition and size. A minimum area of analysis is required in the standards to ensure a representative analysis of the steels cleanliness is conducted. Steel cleanliness measurements are however time consuming and therefore expensive. The use of software packages linked to microscopes for automatic detection and categorising of inclusions has decreased costs, however the costs are still prohibitive. It is for this reason that wind turbine OEMs and gearbox manufacturers often do not have a clear understanding of the cleanliness of the bearing steels being used.

Non-metallic inclusions are typically detrimental to RCF life. Non-metallic inclusions, voids, microcracks and carbide stringers can act as crack initiation points. Thus steel manufacturers aim to minimise the number and severity of inclusions in steel. With the increased cleanliness of steels, normal subsurface rolling contact initiated spalling from defects has decreased in occurrence, i.e. a 10X life improvement from reducing oxygen content in steel from ~30 ppm down to 5 ppm [58, 89]. In addition Murakami, et al. [90] found that super clean steels show a significant improvement in RCF life. It was found that with super clean steels, small inhomogeneities in the microstructure, rather than inclusions, have a greater effect on fatigue life. However special steels have at present extremely small production capacity, far short of supplying the steel tonnage required for the wind industry. The maximum size of inclusions in steel has a large influence to rolling contact fatigue life. Murakami, et al. [91] have shown by a fracture mechanic type approach that fatigue life is inversely proportional to the square-root of the size of inclusions ($\sqrt{\text{area}}$ parameter model). The $\sqrt{\text{area}}$ parameter model however does not take directly into account the orientation, morphology and location of the inclusions, which is discussed in the butterfly initiation section 2.4.2.

2.3 Fundamentals of rolling contact fatigue tribology

In the following sections, a brief overview of rolling contact fatigue tribology is presented. The cyclic contact stresses from over-rolling and the typical progression to fatigue failures are described with the aid of images of failed bearings from service. Loads acting between rolling elements are transmitted through very small areas of contact. The effective area supporting the load rapidly increases with depth below the surface, thus the high compressive stress the surface experiences does not continue far below the surface. Hence bulk failure of rolling elements is not a concern, but failures of the surface and near surface are. Therefore in the following sections only surface stresses and stresses occurring in the near surface are considered [81].

2.3.1 Stresses induced in rolling contact

RCF is very different from classical fatigue as the material is cyclically loaded, thus each portion of material experiences different shear stresses during the load cycle. Rolling contact eventually results in either surface or subsurface cracking due to the alternating contact stresses that occur during over-rolling. RCF occurs in a small volume of stressed material as the contact stress field is highly localised. Elastic contact deformations of the surface also occur under the high pressures typically experienced in rolling element bearings contacts. Typical contact pressures are in the order of one to few gigapascals, however pressures at asperity-asperity contact are significantly higher [92].

In 1896 Hertz [93] developed the classical solution to local stress and deformation of two elastic bodies, which was considered at the time to contact at a single point (which cannot exist without causing gross yielding or failure of the material at the surface) and is called Hertz or Hertzian stresses. Hertz reasoned that instead of a point or line contact, a small contact area must form causing load to be distributed over the surface, alleviating the condition of infinite stress associated with a single point of contact.

Theoretically two types of contact condition exist in rolling element bearings; point or line contact, which occur from the ball or roller respectively. When loaded the point contact becomes elliptical and the line contact becomes rectangular. Fig. 2.3.1 illustrates the surface compressive stress distribution for elliptical contact.

The state of stress in non-conformal contacts where RCF occurs is complex and multiaxial. The classical description of a non-conformal contact is the ball-on-flat. When two bodies contact each other in rolling contact, if the contacting bodies are smooth, loaded below the elastic limit and are not subjected to any tractive forces, then the stress field near the contact is governed by that of the Hertz pressure distribution.

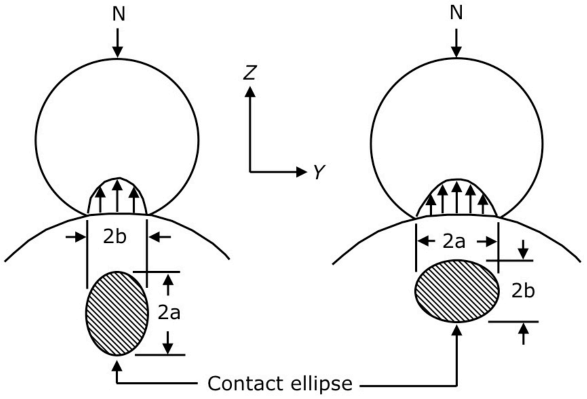

Figure 2.3.1: Surface compressive stress distribution for point contact. N is the force applied in the radial direction z, a and b are the semimajor and semiminor axes of the projected elliptical area of contact. Adapted from Ref [81].

Although rolling element bearing contact surfaces are not perfectly smooth and are lubricated, if oil film thickness is large compared to roughness then Hertzian theory for determining contact pressure and subsurface stresses is still applicable with reasonable accuracy [83]. Actual contacts are rough and thus the stress field is more complex than a simple Hertzian type approach, as peak contact pressure will be experienced at raised asperities [92, 94].

A hydrostatic stress component, derived from the load-induced three-dimensional stress field in each Hertzian contact load cycle, is also present in non-conformal contacts. This is absent in classical tension-compression or bending fatigue [95].

Contact stresses are compressive in three axes with differing values (principal stress components σ_{xx}, σ_{yy}, σ_{zz}, where x represents the over-rolling direction, y the width and z the depth). These constantly change in direction during a stress cycle resulting in the planes of maximum shear stress also changing [95]. It is well established that two types of shear stresses are present in the subsurface of rolling element contacts; the orthogonal shear stress (τ_o) acting parallel and normal to the contact surface, and the unidirectional shear stress (τ) acting at an angle of ±45° to the surface. These differ in magnitude and position depending on the contact parameter, i.e. ranging from point to line contacts (line contact example shown in Fig. 2.3.2). The Lundberg-Palmgren theory [96] for bearing life ratings is based on 2X maximum orthogonal shear stress ($\tau_{o,max}$) as the stress initiating material fatigue. For rolling contact in steels with Poisson's ratio of $\nu = 0.3$, the maximum amplitude of orthogonal shear stress ($\tau_{o,max}$) acts at depths from 0.35z/b (point contact) to 0.5z/b (line contact) at positions of ~±0.87y/b. For static Hertzian contacts (and therefore also rolling contact at any one point in time), the maximum amplitude of unidirectional shear stress (τ_{max}) acts at depths from 0.48z/a (point contact) to 0.78z/b (line contact) at positions of 0y/b (centre of the contact). The maximum magnitude of the unidirectional shear stress is approximately constant across point to line contacts at $\tau_{max} = \sim 0.3\ P_{max}$ (where P_{max} is the maximum contact pressure).

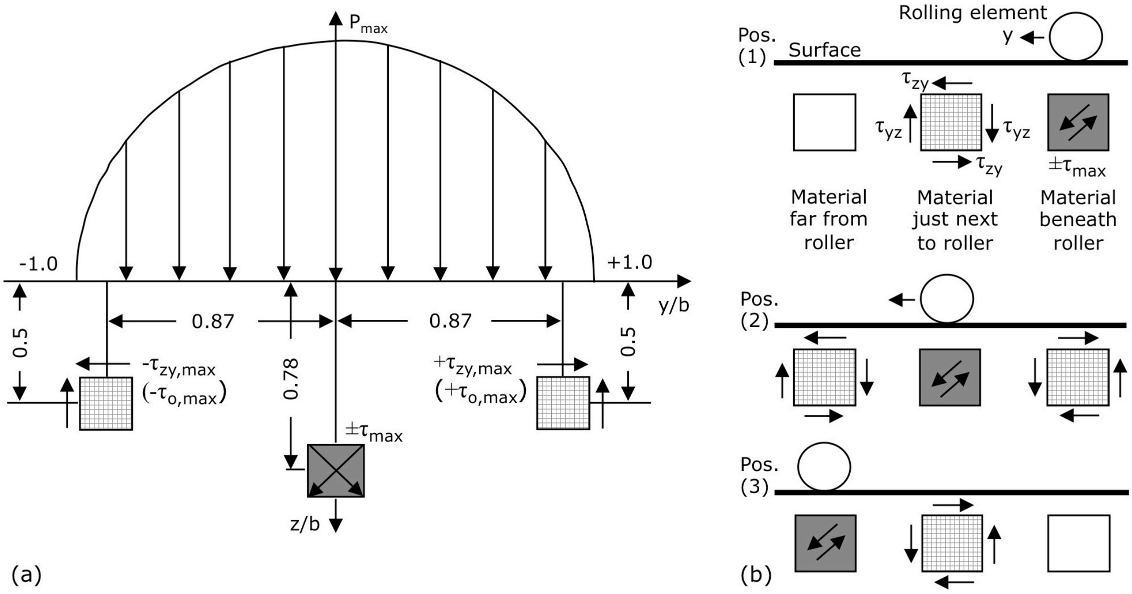

Figure 2.3.2: Line contact shear stresses present in the material subsurface relative to Hertzian maximum contact pressure P_{max}, where b is the semi-width of the contact geometry in the rolling direction. (a) Line contact maximum stressing according to orthogonal shear stress ($\tau_{o,max}$) occurs at a depth of 0.5b and at a distance of y=±0.87b from the centre of the contact area, which acts parallel and normal to the raceway, alternating in sign. The stress from unidirectional shear stress (τ_{max}) acts at a depth of 0.78b and in the centre of the contact area, forming an angle of ±45° with the tangent of the raceway. (b) Two dimensional illustration of cyclic nature of subsurface shear stresses at one depth with three rolling element positions. Assumes steel with a poisson's ratio of 0.3 and no friction in the contact. Adapted from Ref [18] and Ref [97] respectively. See permission [2.1].

It is not thought that subsurface cracks develop at the instant of largest calculated material stressing in the load cycle, as this coincides when hydrostatic pressure is at a maximum. Rather cracks are proposed to develop at the relief phase of the load cycle (P=max changing to P=0) when hydrostatic pressure is at its lowest [18, 24].

Many researchers consider the distortion energy hypothesis (von Mises) and unidirectional shear stress acting at 0.7 – 0.78b to be the most robust ways of characterising RCF [18]. Thus the magnitude and predicted depth at which cracks may initiate varies depending on the theory used. In the following a summary of the von Mises and Tresca criterion are given [98, 99]. The von Mises' yield criterion (1913) states that yielding is dependent on a function of all three values of principle stresses (σ_1, σ_2, σ_3), rather than being dependent on any particular normal stress or shear stress. Pure hydrostatic pressure does not cause yielding in a continuous solid, therefore the hydrostatic stress component of a multi-axial stress state does not influence the stress at which yielding occurs. As the criterion is based on differences of normal stress, it is therefore independent of hydrostatic stress. According to von Mises, the fictitious equivalent stress for the multi-axial stress state is calculated by Eq. 2.3.1 as shown:

$$\sigma_e = \frac{1}{\sqrt{2}}\left[(\sigma_1 - \sigma_2)^2 + (\sigma_2 - \sigma_3)^2 + (\sigma_3 - \sigma_1)^2\right]^{1/2} \tag{2.3.1}$$

The principle stresses are by convention arranged so that $\sigma_1 \geq \sigma_2 \geq \sigma_3$. The von Mises equation predicts that yielding will occur if the differences in stresses (right hand side of the equation) exceed the yield stress in uniaxial tension (σ_{yield}). Hencky (1924) gave the criterion physical understanding, by assuming that yielding occurs when a critical value of distortion energy is exceeded. The distortion energy is the part of the total strain energy per unit volume that induces not a change in volume, but a change in shape of the material.

The von Mises criterion can be approximately interpreted by the hypothesis of maximum shear stress, where from this Tresca equivalent stress can be derived. The Tresca criterion assumes that yielding occurs when the maximum shear stress (τ_{max}) reaches the value of the shear stress in the uniaxial-tension test. This is relevant as yield in ductile materials is usually caused by slippage of crystal planes along the maximum shear stress direction. The maximum shear stress is given by Eq. 2.3.2:

$$\tau_{\max} = \frac{\sigma_1 - \sigma_3}{2} \tag{2.3.2}$$

where σ_1 is the largest and σ_3 the smallest principle stress. The principle shear stress for the elliptical contact in this study has a maximum value of 0.33 P_{max} at a depth of $z = 0.64b$ (see Appendix). Then by Tresca and von Mises criterion, yield in the elliptical contact will approximately initiate at the point according to Eq. 2.3.3:

$$(P_{\max})_{yield} = \sim 1.6\sigma_{yield} \tag{2.3.3}$$

If the yield stress of the material is exceeded by the maximum value of any of the above stress measures, then slip along crystallographic planes (slip planes) occur and the inelastic deformations may lead to crack initiation and propagation under the cyclic stressing. Experimentally cracks have been observed to form at various depths, hence the exact stress criterion governing crack initiation is not yet clear [95]. WECs form in a large range of depths (0 – 1.5 mm) and are also often observed to propagate into the depth direction. The location of WECs often does not correspond to the depths of calculated maximum shear stresses; hence it is likely that a combination of the various shear stresses drive WEC initiation and propagation.

Other factors affecting the overall stress state are hoop stresses (generally tensile) in bearing rings from interference fits. Hoop stresses may become particularly important for martensitic bearing rings, as these tend to have slightly tensile residual stresses in the near contact surface from manufacture. When both the residual tensile stress and imposed tensile stress from interference fits are combined, a high state of tensile stress could be present. Hoop stresses reduce fatigue life in general [100, 101] and may also be important in controlling the propagation mode of WECs in particular. This is because a high tensile stress state could cause a subsurface propagated WEC to open-up to form a hairline crack connecting to the surface. This may not occur with bainitic or case-carburised steels as their inherent compressive residual stresses from manufacture may significantly or completely negate any imposed tensile hoop stresses from interference fits.

When a surface is subjected to pure rolling contact the highest shear stress exists in the subsurface. However when a surface is subjected to pure sliding contact the highest shear stress exists at the surface (Fig. 2.3.3). All bearings in operation will experience a certain degree of slip between contacting elements when in operation, therefore the level of maximum subsurface stressing will be raised towards the surface during operation depending on traction level. Friction (traction) coefficient, μ is defined in Eq. 2.3.4:

$$\mu = \frac{F}{N} \tag{2.3.4}$$

where;

N Normal force exerted by each surface on the other, acting normal to the surface [N].
F Force of friction exerted by each surface on the other, acting parallel to the surface in a direction perpendicular to the normal applied force [N].

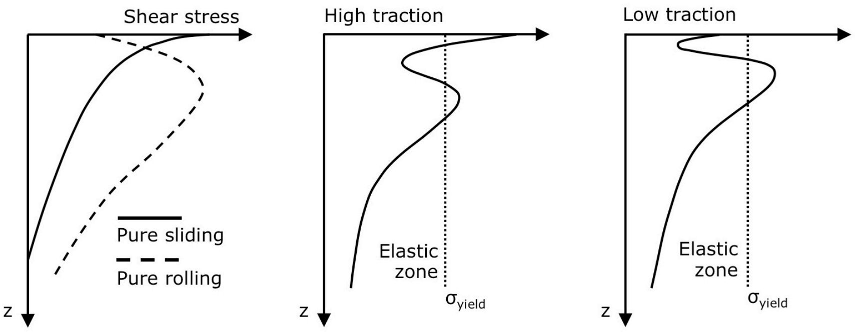

Figure 2.3.3: (a) The shear stress as a function of the depth, z. (b) Surface shear stress is higher than subsurface shear stress (at depth where initiation of cracks may occur from inclusions) thus the surface initiated spall will result before subsurface. (c) Surface shear stress is lower than the subsurface shear stress (at depth where initiation of cracks may occur from inclusions), thus yielding and crack initiation will occur in the subsurface.

2.3.2 Surface and subsurface fatigue

Rolling contact fatigue in rolling bearings is unavoidable. RCF is evident in many different ways that result in failure. There are two types of mechanisms for material spall from a raceway; 1) surface initiated from asperity contact or surface defects resulting in micropitting and flaking, 2) subsurface initiated from shear stresses induced in rolling contact causing crack initiation and propagation to the surface and spalling. These are competing mechanisms and the final mechanism is dependent on factors such as surface quality, lubricant cleanliness, material quality, etc. [95].

It has been proposed that if a rolling element bearing is correctly loaded, lubricated (without ingress of contamination) and installed (i.e. with appropriate alignment), then the main mode of failure is subsurface material fatigue (e.g. cracks initiating at material defects and non-metallic inclusions) [95]. Voskamp [102], Olver [83], Vegter and Slycke [32] and Sadeghi, et al. [95] have presented overviews of the mechanisms in rolling contact fatigue and these are discussed in the next sections.

Residual stresses

It is well established that when steel is subjected to over-rolling with moderate to high contact stresses, the material undergoes local structural transformation (explained in section 2.2.6) and experiences changes in the residual-stress pattern [19, 85, 102-104]. This occurs by micro deformation as the yield strength of the material is locally exceeded by the von Mises equivalent stress that represents the triaxial stress field during rolling contact. Changes in the macro residual stresses indicates plastification (local yielding) and changes in the XRD peak width indicates material aging (defect accumulation). The physical broadening of an X-ray diffraction (XRD) line is related to the microstructural condition of the material by size and strain influences [105] therefore the peak width represents a measuring quantity for material alterations and densities of crystal defects [106]. A reduction in line broadening by plastic deformation indicates a decrease in lattice distortion. Residual stress formation and the beginning of plastification conform to the von Mises energy distortion hypothesis, whereas RCF material aging and damage evolution that results in a XRD peak width reduction corresponds to the alternating orthogonal shear stress (τ_o) [106]. The peak width is expressed as the full width at half maximum (FWHM) value. The austenite phase volume fraction is a sensitive measure of microstructural alterations in the steel matrix (see Fig. 2.3.5) [104] and is therefore useful for further characterisation of material aging.

If the contact pressure and number of rolling cycles is sufficient, the retained austenite in through-hardened steels decomposes, resulting in a volume change that generates internal stresses. The local plastic deformation in the subsurface involves material flow in a direction parallel to the contact surface (e.g. perpendicular to the direction of the largest load induced stress). The material flow which predominately occurs in the axial direction causes a development of a compressive residual stress in the axial direction (see Fig. 2.3.4) [102]. This is because the subsurface volume constrains the lateral expansion of the surface region. The development of a compressive residual stress in the circumferential direction occurs by a similar mechanism. A tensile residual stress development in the normal direction to the surface may also develop because of reduction in the thickness of the plastically deformed subsurface region due to axial material flow [102].

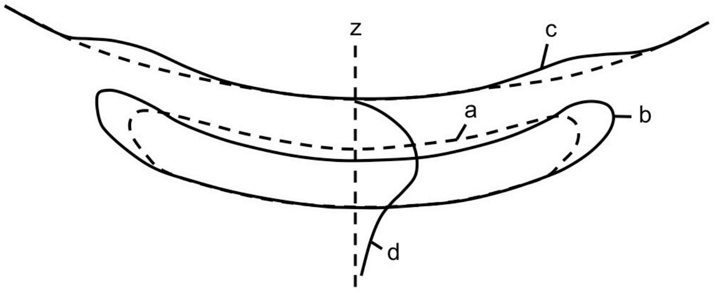

Figure 2.3.4: Schematic illustration of the micro-plastic flow in the axial direction in a small region beneath the rolling contact surface. The volume stressed above the yield limit (see contour 'a') changes its form (see contour 'b') causing an elevation of the surface in the rolling track at locations indicated by 'c' and 'a' radial component of residual stress (i.e. perpendicular to the rolling track surface) that is of tensile nature and which exhibits a depth profile as illustrated by the curve 'd' for depths beneath the bottom of the groove. Adapted from Ref [104].

Residual stress determinations are based on the measurement of strain and are later converted to stresses according to elasticity theory. Residual stresses can be measured based on line-shift analyses. By combining these analysis methods with grinding or electropolishing material removal techniques, a distribution of the residual stresses and FWHM values below the contact surface through the stressed volume can be gained (see Fig. 2.3.5) [104]. In most cases in RCF, the development of residual stress is similar in the circumferential and axial directions [104] with a maximum deviation of 20 – 30% [106], therefore it has been common in literature to only report residual stresses in the circumferential direction.

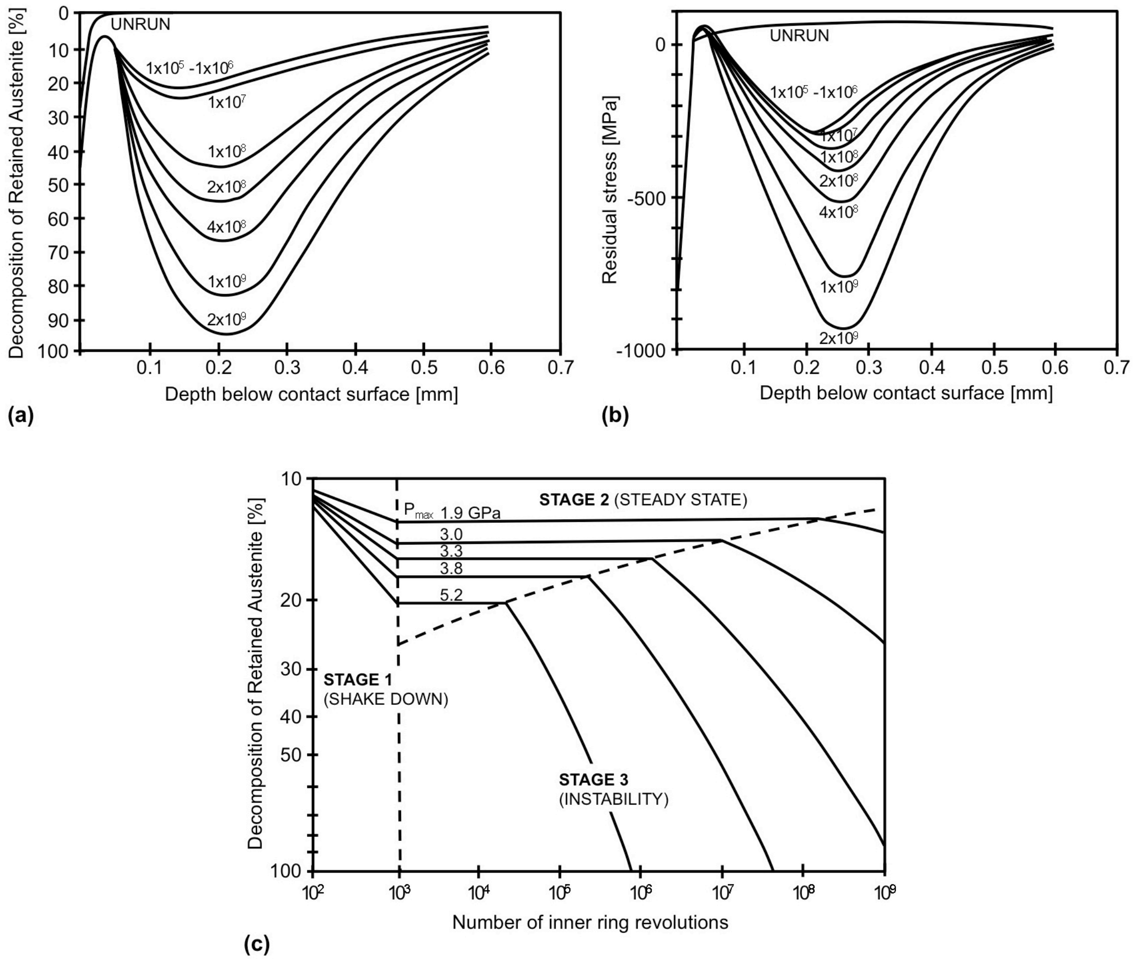

Figure 2.3.5: (a) and (b) shows the percentage decomposition of retained austenite and development of circumferential residual stress respectively versus the depth below the contact surface in the inner rings of tested 6309 DGBB bearings. The test conditions were as follows: P_{max} of 3.3 GPa, operating temperature of 53 ºC, inner ring rotational speed of 6000 rpm. (c) Retained austenite decomposition versus number of inner ring revolutions for different maximum contact pressures. Measurements taken at 0.2 mm below the centre of the ball track in a 6309 DGBB inner ring raceway. The test conditions were as follows: operating temperature of 53 ºC, inner ring rotational speed of 6000 rpm. The solid lines represent the material response to rolling contact loading during shake-down, steady-state and instability stages. Adapted from Ref [104].

The magnitude of the applied load is important; an increase in residual stress usually occurs for an increase in Hertzian contact pressure and there exists thresholds below which no residual stress forms [19, 104, 107] (see Fig. 2.3.5). The magnitude of residual stress increases with amount of stress cycles towards a maximum value [19, 106].

Crack initiation and growth in the subsurface of rolling contact bodies are promoted by the presence of a tensile residual stress and counteracted by the presence of compressive residual stress (perpendicular to the crack) [85]. Therefore the state of residual stresses in specimens/bearings prior to and during rolling contact is important because compressive residual stresses in the near surface zone (0 – 0.5 mm) can retard crack propagation, as opposed to tensile stresses and hoop stresses which can cause vertical crack propagation [83].

Subsurface initiated spalling

Subsurface originated spalling is the most common mode of failure in bearings which have smooth surfaces and operate with elastohydrodynamic lubrication (EHD) conditions (explained in the next section). Bearings have a limited life because of probability of subsurface initiated fatigue spall. Subsurface initiated spall is strongly influenced by the steel microstructure, which is inherently inhomogeneous due to the presence of defects and anisotropic properties. Hence spalling lives of an identical batch of bearings, which are subjected to the same load, speed, lubrication and environmental conditions show a degree of scatter. RCF leads to metallic particles flaking from the contact surfaces, by the process of subsurface crack initiation, link-up and propagation to the surface. Cracks are mostly likely to initiate at material inhomogeneities (e.g. non-metallic inclusions) at approximately the depth of maximum shear stresses. Factors accelerating this are smooth surfaces, high densities and sizes of non-metallic inclusions and absence of surface shear. The probability of fatigue spalls has been reduced over the last couple of decades due to the advancements in cleanliness in bearing steels. Spall formation occurs through several distinct cracks and has been observed by metallographic examinations of spalled sections.

The subsurface evolution of RCF material degradation leading to a fatigue spall involves a three-stage process: (I) shakedown, (II) steady-state elastic response and (III) instability [95, 102].

Stage (I) shakedown occurs normally before $10^4 - 10^5$ cycles (0.1 – 1% of total bearing life depending on the bearing). During the shakedown stage small-scale obstacle-controlled dislocation glide (micro yielding) takes place [32]. Yielding leads to the generation of large amounts of crystal defects, such as dislocations and vacancies and a range of vacancy carbon clusters [32]. Residual stress develops, in addition work hardening and transformation of retained austenite to martensite causes an increase in the material strengthening and microyield stress [95]. The yielding mechanism decreases gradually through work hardening and ultimately ends [32]. A higher initial load applied during this stage results in a higher saturation level of work hardening which leads to an extended fatigue life overall from the modification of material response in stages (II) and (III) [95].

In stage (II) no fatigue damage is thought to occur as the cyclic response is elastic [95]. The length of this stage is a function of maximum stress, material characteristics and temperature (where it is thought it is very temperature sensitive). Maintaining the stage (II) elastic response for the longest time possible is critical for extending bearing life. It is thought that stability of the finely dispersed carbides in tempered martensite is important for extending stage (II). Microstructural changes by microplastic deformation compromises the ability of maintaining an elastic response, which leads to localised damage and increase in probability for crack initiation and fatigue failure. Microplastic deformation occurs at microstructural discontinuities (inclusions, carbide clusters etc.) from the resultant stress exceeding the local microyield threshold at that fatigue cycle leading to crack initiation. Other factors affecting the ability to maintain an elastic response during RCF are physical parameters (applied stress, temperature and stress cycle number), material parameters (steel alloy type, heat treatment, residual stress and work hardening during run-in) and chemical influences (hydrogen embrittlement, etc.).

The stage (III) steady-state fatigue damage stage subsequently takes place. In this stage, the micro-plastic damage accumulates at a rate several orders of magnitude slower than in the shakedown stage and is thus only evident with extensive numbers of rolling cycles [32]. This stage is distinguished by a decrease in yield stress from material softening, which leads to an increase in subsurface volume which is deformed plastically [95]. Vegter and Slycke [32] proposed that the slow damage rate is controlled by climb controlled dislocation glide (a cyclic creep-like damage mechanism). This damage mechanism describes that a gliding dislocation, which may have become trapped by an obstacle, is only able to resume its glide motion by becoming free from the obstacle, through stepwise climb of the dislocation segment around the obstacle. The climb process is thus controlled by iron self-diffusion, as the process entails local rearrangement of the matrix atoms around the dislocation core. Vegter and Slycke [32] explained that hardened bearing steels exhibit high fatigue resistance as the dislocation climb and fatigue damage mechanism are slow due to the number of vacancy exchanges being few at low temperatures. Sadeghi, et al. [95] noted that radial tensile stresses and texture development promote growth of cracks parallel to the rolling surface.

Voskamp [102] produced a schematic representation of the three stages in the material response in the subsurface volume at a depth where the equivalent von Mises stress is approximately maximal (see Fig. 2.3.5 and Fig. 2.3.6).

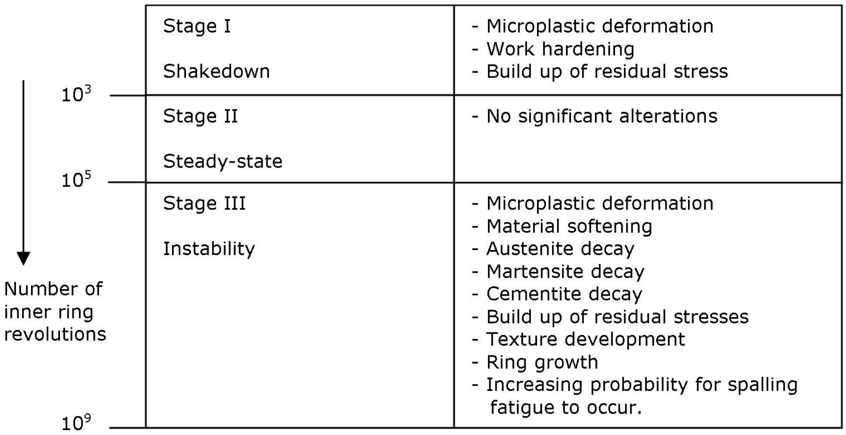

Stage I Shakedown	- Microplastic deformation - Work hardening - Build up of residual stress
Stage II Steady-state	- No significant alterations
Stage III Instability	- Microplastic deformation - Material softening - Austenite decay - Martensite decay - Cementite decay - Build up of residual stresses - Texture development - Ring growth - Increasing probability for spalling fatigue to occur.

Figure 2.3.6: Schematic representation of the three stages in the material response in the subsurface volume at a depth where the equivalent von Mises stress is approximately maximal. Adapted from Ref [102]. See permission [2.2].

Surface initiated spalling

Surface initiated pitting is common in gears where significant sliding occurs between contacting surfaces and occurs when surface irregularities (dents, scratches etc.) are present [95]. Cracks initiate at these surface defects from the local stress concentrations these create and propagate at shallow angles (15 – 30° to the surface). The cracks branch up towards the surface again when a critical length is reached, removing surface material to form a pit. In the presence of hoop stress the cracking may extend beyond the surface into the bulk of the steel.

Micropitting is widespread in wind turbine gearboxes. It reduces gear accuracy and may escalate into other more severe failure modes such as macropitting, scuffing or bending fatigue [108]. Micropitting is characterised by numerous small pits that are normally accompanied by extensive cracking [83]. Micropitting is often seen in hard steels that have been ground and operate with the lubrication film being too thin compared to the height of the surface roughness (e.g. boundary lubrication). Thus it is thought that the mechanism for micropitting is associated with the asperity stress field [92].

2.3.3 Lubrication regimes

Lubrication is achieved by an oil film between two contacting surfaces that move relative to one another. These oil films can have a thickness ranging from a few nanometers to hundreds of microns. The most important property of a lubricant is the viscosity, which is the fluids ability to resist motion. Increasing the viscosity will increase the load bearing capacity, though increasing the viscosity does not necessarily constitute to a good lubricant. Viscosity however is not constant and varies with pressure and especially temperature. The chemistry, additive package and interface conditions all determine if the lubricant is correct for its application [92]. The thickness of the oil film determines the (fluid) lubrication regime, which are listed below:

1. Boundary lubrication ($h \ll R_a$) – two surfaces are mostly in contact, even with fluid present.
2. Mixed lubrication ($h \sim R_a$) – two surfaces are partly separated, partly in contact.
3. Elastohydrodynamic lubrication (EHD) – two surfaces are separated by a thin fluid film.
4. Hydrodynamic lubrication ($h > R_a$) – two surfaces are separated by a fluid film.

The lambda ratio, λ the parameter characterising the ratio of the minimum film thickness to the composite surface roughness is defined by the Eq. 2.3.5:

$$\lambda = \frac{h_{\min}}{\sqrt{R_{q1}^2 + R_{q2}^2}} \tag{2.3.5}$$

where,
h_{min} Minimum film thickness [m]
R_{q1} RMS roughness of body '1' [m]
R_{q2} RMS roughness of body '2' [m]

The lubrication regime depends on the oil film thickness, which depends on the oil viscosity, load applied and the speed which the two contact surfaces moves relative to one another. The Stribeck curve displays how these factors affect the friction losses and how this corresponds to the lubrication regime. The Stribeck curve is a plot of the friction as it relates to viscosity, speed and load (see Fig. 2.3.7) [92, 109].

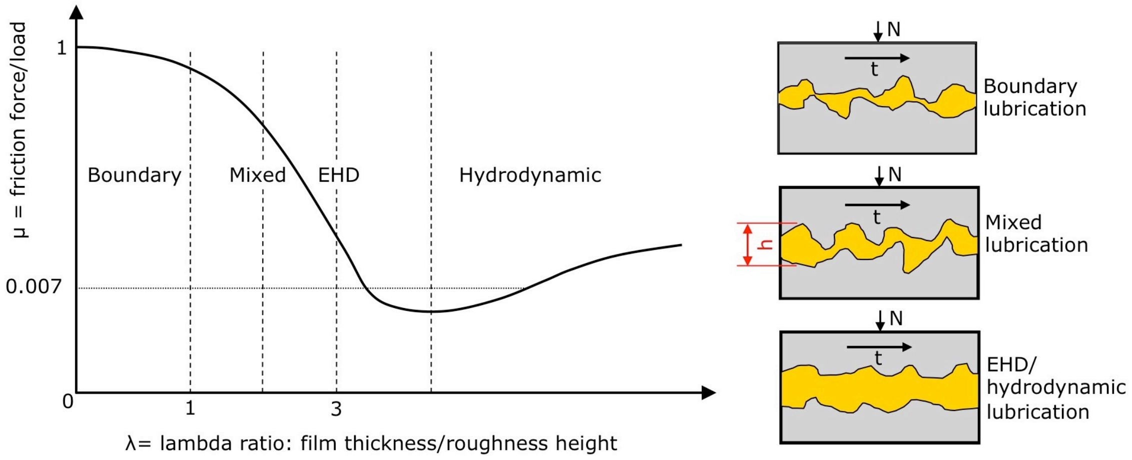

Figure 2.3.7: Stribeck curve plotting coefficient of friction (μ) and lambda ratio (λ). Not to scale. Graphical representations of asperity contact in each regime is shown, where h represents the asperity height, N the normal load applied and t the direction of travel.

Stribeck curve:

Boundary lubrication (λ<1) has limited fluid in the interface and a high amount of asperity contact, which results in high friction. Boundary lubrication occurs when the oil film is approximately equal thickness to the surface roughness. This is undesirable from the increased friction, energy loss, wear and material damage. Bearings will experience boundary lubrication during start-up, shutdown and low speed operation. Lubricants and additives (AW, EP) are used to minimise the detrimental effects [92].

Mixed lubrication (~1<λ<1.5) occurs as the speed and viscosity increases, or the load decreases, resulting in the surfaces starting to separate. This film is thin but increasingly supports load and is marked by a friction drop because of decreasing surface contact. The fluid film thickness is greater than the surface roughness, but only marginally, resulting in little asperity contact. The asperities which do contact each other can form small nonconformal contacts (explained below) leading to EHD, where this effect is termed micro-EHD [92].

Elastohydrodynamic lubrication (~$1.5<\lambda<3$) is the lubrication regime (EHD) that is desired during a bearings operation. EHD pressures are high enough to increase the oil viscosity up to 10^8 times that of ambient conditions so a semi-solid lubricant results. This enables an extremely thin oil film to form, supporting the load and enabling smooth, reliable operation. A thick fluid film, low friction and no wear are characteristic of hydrodynamic lubrication, however this generally occurs at conformal contacts. Nonconformal contact may produce pressures in excess of the deformation limit, thus temporarily deforming the steel surface, which also affects the fluid viscosity [92].

Hydrodynamic lubrication ($\lambda>3$) film is formed when the geometry, surface motion and fluid viscosity combine to increase the fluid sufficiently to support the load. This occurs as the surfaces continue to separate as the speed or viscosity increases until a point where there is no surface contact. The change is associated with the drop of friction coefficient to its minimum and no wear, as there is no contact between surfaces. The friction does however eventually increase with increasing lambda ratio due to fluid drag on the moving surfaces. As the speed or viscosity increases a thicker oil film results and the fluid drag increases [92].

A schematic of the pressure distribution in an idealised rolling contact with smooth surfaces can be seen below in Fig. 2.3.8. When oil is present between two contacting surfaces, the pressure profile is changed from that at dry Hertzian contact [92]. The changes in pressure are experienced to the greatest extent at the inlet and outlet regions of the contact. Because the oil film and rolling slightly enlarge the contact area, at the inlet the hydrodynamic pressure is lower than that at dry Hertzian contact. Here the lubricant thickness is defined as the central film thickness, $h_{central}$. The lubricant experiences a rise in viscosity when it enters into the contact, followed by a drop back to ambient viscosity at the exit of the contact. A constriction is therefore formed to maintain continuity of flow and compensate from the viscosity drop at the exit. A large pressure peak is generated just before the constriction, which is normally larger than the maximum Hertzian contact pressure, this effect decreasing as lubrication starvation and hence dry contact conditions are approached. Here the oil film thickness is denoted as h_{min}, the minimum oil film thickness experienced in the contact. The EHD pressure distribution at high contact pressures is similar to an elliptical profile generated according to Hertzian conditions, as the elastic deformation dominates, though at higher speeds the hydrodynamic effects dominate, resulting in displacement of the pressure peak towards the centre of the contact [92].

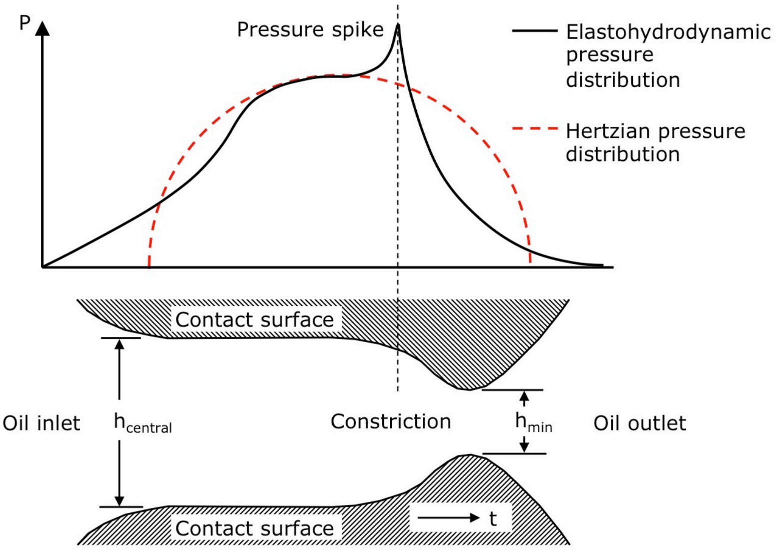

Figure 2.3.8: Hydrodynamic pressure distribution in an elastohydrodynamic contact; $h_{central}$ is the central film thickness and h_{min} is the minimum film thickness. Adapted from Ref [92].

With wind turbine start-up and shutdown, boundary lubrication will occur in all gearbox rolling element bearings (low speeds causes a thin film). The lubrication regime will stay boundary or mixed in slow-speed and planet bearings. The lubrication regime in intermediate and high-speed bearings will make a transmission to elastohydrodynamic lubrication as the speed increases to normal operating conditions. Rolling element bearings will suffer considerable friction and wear during start-up and shutdown.

2.3.4 Bearing life ratings

Fatigue in the material has been selected as the criteria for bearing life, as this is how it will eventually fail if it is properly lubricated, properly mounted and aligned, kept free of abrasives, moisture and corrosive reagents and not overloaded [81]. It is desirable to use just one rating method for rolling bearings. Since it is possible in any given rolling bearing application to have combinations of line and point contact, Lundberg & Palmgren [110] estimated the fatigue from Eq. 2.3.6.

$$L_{10} = \left(\frac{C}{P_{eq}} \right)^{n} .10^{6}\, rev \qquad (2.3.6)$$

Where C is the dynamic load rating which is defined as the load, which will give a life of 10^6 revolutions of the inner race. P_{eq} is the equivalent radial load [N], n is the load life exponent, which is empirically found to be n=3 for ball bearings and n=10/3 for roller bearings. L_{10} is the expected life of 90% of similar bearings under similar operating conditions. When the equivalent radial load equals the C rating, the L_{10} life will be 10^6 revolutions. The Lundberg-Palmgren theory suffers from several limitations, therefore modification factors to Eq. 2.3.6 now exist to include life factors such as reliability, material and operating conditions [95]. As inclusions and inhomogeneities exist in the microstructure, bearing lives show a degree of scatter, where bearing life can be plotted as a Weibull distribution [81]. Life to failure is a function of stressed volume, where a higher stressed volume equates to a higher number of material weak points. Hence even for the same applied load, the probability of failure increases. Therefore larger bearings have a higher probability for failure than smaller bearings.

2.3.5 Microstructural alterations from over-rolling

Microstructural alterations induced by rolling contact were first reported by Jones [111]. These microstructural alterations are described visually by their etch response to nital (a dilute mixture of nitric acid (2 – 3 vol.%) and ethanol). When the microstructure in 100Cr6 bearing steel experiences rolling contact fatigue, the microstructural changes observed are known as dark etching region (DER), butterflies that possibly lead to white etching cracks (WECs) and finally white etching bands (WEBs). These features depend on the magnitude of applied shear stress and number of rolling cycles. Dark etching region (DER) appears ‘dark’ under reflected light and conversely white etching area (WEA) in butterflies/WECs and white etching bands (WEBs) appears ‘white’. Etching is the corrosive attack of a microstructure in the presence of material defects and phases, such as grain boundaries, carbides, cracks and dislocations. The etchant attacks regions of local anodes, whereas cathodes are not attacked. An explanation for why the WEA resists etching is that the surrounding matrix acts as a cathodic protector. In this case the subgrain boundaries of dislocation networks (see Fig. 2.4.7 in section 2.4) are not preferentially attacked by the etchant as they have a lower boundary energy compared to the carbides in the matrix, as small carbides have a large interfacial energy [112]. WEA appears ‘white’ as visible light reflects off the relatively smooth surface that resists etching, compared with the surrounding matrix which has etched to a rougher surface causing diffuse reflection.

If the material is subjected to a level of stressing so that the yield point is locally exceeded, the material plastically deforms. Slip motions in the microstructure of a rolling element bearing can often be found. It is typical that the slip marks are located orthogonal to each other and form an angle of approximately 45° with the surface [18]. Swahn, et al. [21] chronologically characterised regions of microstructural alterations and their orientation to the contact surface; DER, DER+(30° white etching bands) and DER+(30° & 80° white etching bands) shown in Fig. 2.3.9:

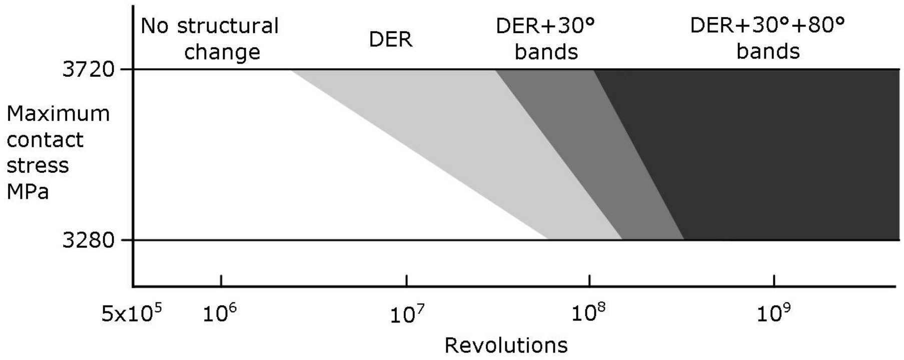

Figure 2.3.9: Microstructural alterations as a function of stress level and number of inner-ring revolutions. Adapted from Ref [21]. See permission [2.3].

DERs will form depending on the magnitude of the load and number of rolling cycles [39, 113]. Fig. 2.3.10 shows an example of a DER microstructural alteration that is located in a region just below the contact surface at depths corresponding to highest magnitude shear stresses. DERs are zones where slip motions have occurred in the microstructure [81, 102]. The DER occurs due to the migration of carbon atoms on a micro-scale towards heavily dislocated regions that are caused by microplastic deformation during RCF. The process is associated with the rejection of excess carbon from the cubic martensite [104]. DER consists of a ferritic phase containing a non-homogeneously distributed excess carbon content (which is equivalent to that of the initial martensite) mixed with residual parent martensite [81]. This indicates that martensite decays by a stress-induced process [21]. With increased numbers of slip motions the DERs become visually darker. The position and visual darkness of the DER zone reveals information about the heaviest stressing which has occurred subsurface. Typically the upper boundary is sharp whilst the lower one is diffuse.

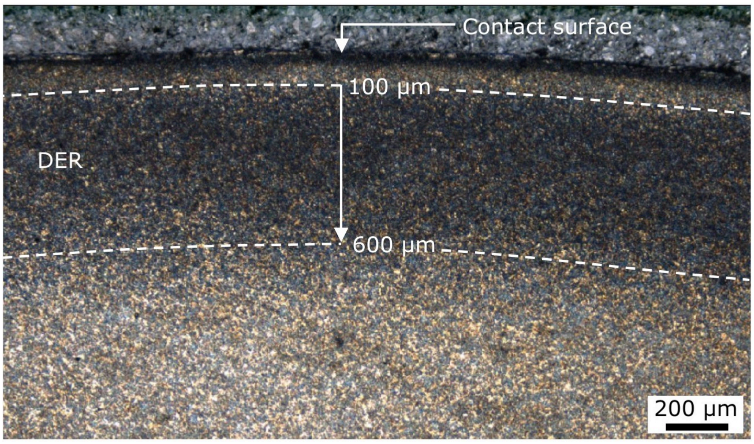

Figure 2.3.10: Circumferential cross-section of a RCF tested roller etched with Nital 2%. The DER that has formed from 100 – 600 µm below the contact surface is evident.

DER in AISI 52100 steel was shown to appear at 5 x 10^6 – 5 x 10^7 cycles under maximum contact pressures of 3.72 – 3.28 GPa respectively [21]. The findings of Schlicht, et al. [18]

agreed with this, with DER appearing in AISI 52100 steel at 10^6 – 10^9 cycles under maximum contact pressures of 3.5 – 2.7 GPa respectively. This shows the trend for DER to form at a slower rate at reduced contact pressures and applies over a large range of cycles. DER has been shown to develop in a zone of approximately 0.15 – 0.65 mm depth below the contact surface [23].

Butterflies and WECs may form in the subsurface of the steel and are extensively discussed in the next section of the report.

Further over-rolling causes WEBs to form within the DER after a large number of cycles by the formation of a new ferrite phase [81, 102]. Initially WEBs form at ~30° with the surface tangent and with further over-rolling at ~80° (see Fig. 2.3.11c). 30° WEBs are disk-shaped regions of ferrite (~0.1 – 0.5 μm thick) and are sandwiched between carbide-rich layers (Fig. 2.3.11b). 80° WEBs shown in Fig. 2.3.11c penetrate the previously formed 30° (flat) WEBs and are considerably larger and thicker disk-shaped regions (~10 μm thick) consisting of severely plastically deformed ferrite [81]. The structural changes indicate a pronounced decay of martensite. Schlicht, et al. [18] found formation times can be from 10^8 – 10^{11} cycles under maximum contact pressures of 4.0 – 2.5 GPa respectively. Details on the formation mechanism of WEBs are reported by Voskamp, et al. [19] and Polonsky & Keer [20].

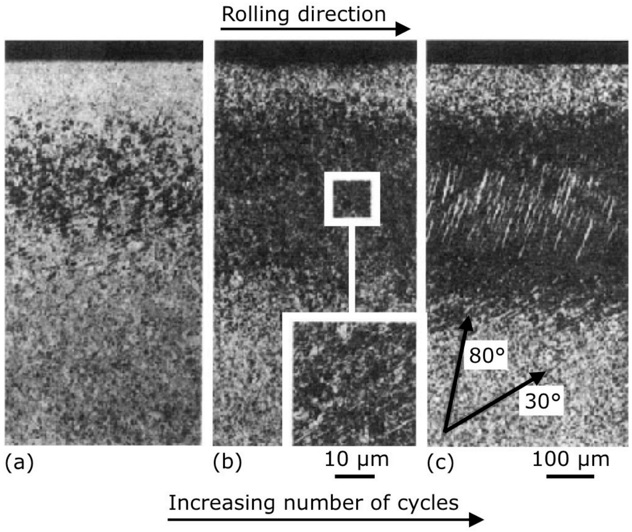

Figure 2.3.11: Optical microscopy images of structural changes in 6309 deep-groove ball bearing inner rings (circumferential sections). (a) DER in early stage. (b) Fully developed DER + (30° bands). (c) DER + (30° + 80° bands). Adapted from Ref [21]. See permission [2.3].

2.4 Butterflies and WEA/WECs

2.4.1 Overview

In the following sections the microstructural damage features focused on in this study are separated into butterflies and WEA/WECs. The formation mechanisms and characteristics cited in literature are discussed. Since the WEA microstructural change is the same or very similar between both phenomena, the discussion regarding WEA formation mechanisms is combined.

2.4.2 Butterflies

Butterfly overview

Butterfly formation under rolling contact fatigue has been studied over the last half century [18, 23-25, 27, 28, 39, 44, 45, 114-120]. Butterflies form in steels due to cyclic shear stresses induced during RCF which become locally high at material imperfections (i.e. non-metallic inclusion stress raisers) causing plastic deformation and initiating cracks and microstructural changes (WEA) at these locations (Fig. 2.4.1).

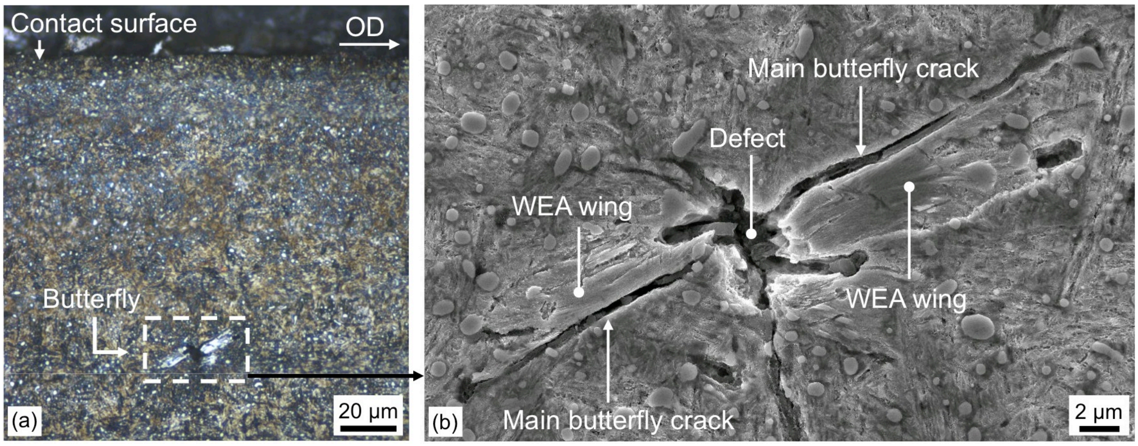

Figure 2.4.1: Images showing typical butterfly formation. Circumferential sections are shown and the microstructure has been etched with 2% Nital. (a) Optical image. (b) SEM image.

Butterflies form below the contact surface to depths of ~1.5 mm [22, 23] and the sizes are found to range from approximately 10 µm to over 100 µm (wing tip to wing tip). Butterflies sometimes only form a single wing. Butterflies form at shallower depths in earlier periods of over-rolling and at increasingly deeper depths with further over-rolling, increasing temperature and increasing contact pressure [24]. The cracks and microstructural changes are three-dimensional structures that sweep around their initiator [23, 27, 39]. The cracks are found lying predominately at 30 – 50° (and 130 – 150°) to the direction of over-rolling [23-28, 39, 44], thus unidirectional shear stress (τ_{max}) acting at ±45° may be significant to their formation.

The butterfly wing WEA is cited as consisting of equiaxed nano-ferrite grains of ~10 – 100 nm diameter [22, 24-28, 39, 45] or lamella like grains up to 300 nm equivalent diameter [28]. In one study it was found that smaller grains (10 – 50 nm) were present close to the main crack, and larger grains (50 – 100 nm) close to the butterfly boundary [27].

Spalling/flaking of the contact surface can originate subsurface by butterfly cracking initiated at defects which can form crack networks linking to the surface [120]. Butterflies are also cited [22] as potentially being an initiator of WECs. However, despite the similarities between butterflies and WEA/WECs, both the links between them and their relation with WSF are still unknown and unproven.

Butterfly initiation

Butterflies initiate at defects such as non-metallic inclusions, voids [26, 27], micro-cracks [23, 26], grain boundaries [40], large carbides [25, 39, 40], carbide stringers and porosity [24]. Differences in elastic modulus, coefficient of thermal expansion (CTE), size, shape, adhesion property and coherence between material imperfections and the steel matrix are considered to be the controlling parameters for butterfly initiation [23-25, 39, 84, 115, 121-123].

For current bearing steels, sulfides, sulfide + oxides, oxides and titanium-carbonitrides are typically present [22], where butterflies preferentially form at oxides [23, 81]. High quality bearing steels contain less than 10 ppm oxygen and therefore have few pure oxide inclusions [124, 125], but do contain sulfides + oxide inclusions.

Microstructurally altered material adjacent to Al_2O_3 inclusions after rolling contact has been reported [28] (see Fig. 2.4.2) and has also been observed by TEM around carbides [39]. This offers evidence that the debonding of inclusions from the matrix and high stresses induced at the interface of inclusions or carbides with the matrix induces plastic deformation and breakdown of the locally surrounding microstructure.

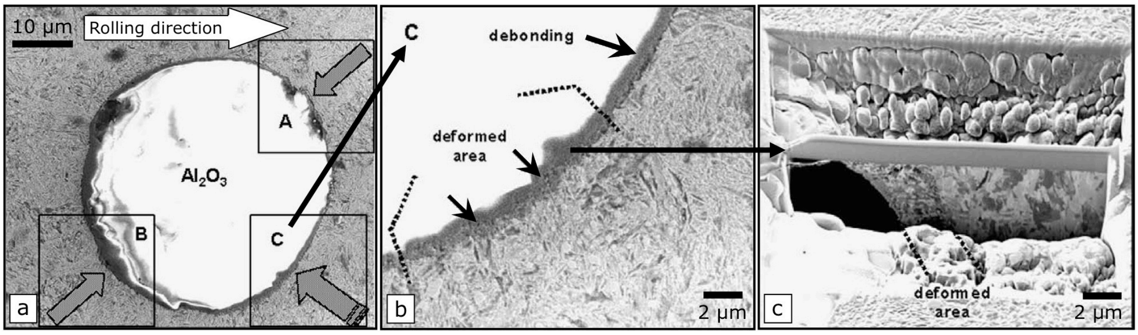

Figure 2.4.2: (a) SEM image of Al$_2$O$_3$ inclusion debonded at areas ‘A’ and ‘B’. Area ‘C’ presents the region with deformed material at the inclusion/steel interface. (b) SEM image of detail ‘C’ showing the deformed interface region. (c) FIB cross section of the lamella containing deformed region of fine granular structure along the inclusion interface. Depth = 400 µm, contact pressure = 2.6 GPa. Adapted from Ref [28]. See permission [2.4].

Synchrotron X-ray micro-tomography revealed that the orientation of inclusions with their associated cavities (gap between inclusion and matrix) influences the zone of material stressing [84], where the presence of cavities may control the severity of inclusions [126, 127]. Hashimoto, et al. [127] showed that closing Al$_2$O$_3$ inclusion/matrix cavities in JIS-SUJ2 steel by Hot Isostatic Pressing extended RCF crack initiation life. Calcium additions acting as de-oxidisers in bearing steels have detrimental affects [114], e.g. oxide inclusion composition affects butterfly formation and RCF life in the order of increasing severity as follows; SiO$_2$-Al$_2$O$_3$, Al$_2$O$_3$ and Al$_2$O$_3$-CaO [114, 126]. Different inclusions will have different coefficients of thermal expansion (CTE) compared with typical bearing steel microstructures. Inclusions such as MnS will have larger CTEs than Al$_2$O$_3$ which will have smaller CTE’s. Compressive and tensile stresses are thus induced around the MnS and oxide inclusions respectively [123]. A tensile residual stress also exists at sulfides + oxides where the oxide part makes contact with the matrix [120, 123]. From a fracture mechanics approach, crack initiation and short crack growth from inclusions/butterflies can be explained by Mode I loading [120]. The induced residual tensile stresses around inclusions are cited to enable initial crack growth relatively easily when combined with the overall cyclic shear stress field from rolling contact. The induced residual tensile stresses will eventually reduce to zero with distance from the inclusion. In low temperature tempered (<400 °C) bearing steels, cracks can initiate around non-metallic inclusions without externally applied stress [128] which could be pre-requisites for butterfly formation.

Referring to Table 2.4.1, preferential butterfly formation at oxide parts of inclusions is due to the inclusion being hard and brittle, often displaying an incoherent interface with the matrix and debonding [24, 114, 122]. Softer, more ductile inclusions such as sulfides have a semi-coherent interface with the steel matrix and can encapsulate non-metallic particles so they do not act as stress concentrators [39, 81, 114, 119]. Sulfides rarely initiate butterflies according to older literature [23, 39, 114], on the other hand in recent literature MnS inclusions are said to initiate most butterflies [118]. Hence the adhesion property and coherence between the inclusion and steel matrix is thought to be important in controlling the severity of the inclusion type [23, 25, 28, 39, 114, 121].

Table 2.4.1: Young's modulus E, and hardness H, of typical inclusions found in 100Cr6 are shown. Young's modulus of 100Cr6 steel is 210 GPa with hardness 8 GPa.

	Al oxide	**TiN**	**Spinel**	**CaAlO (I)**	**CaAlO (II)**	**MnS**
E (GPa)	375	380	279	195	126	103
H (GPa)	32.2	21.5	26.6	18.2	9.6	3.4

Composition of calcium aluminate I is $(Al_2O_3)_6$-(CaO) and calcium aluminate II is $(Al_2O_3)_2$-(CaO). Adapted from Ref [115]. See permission [2.5].

Butterfly formation & propagation

The elastic modulus differences, differing CTE and the weak interfacial energy between the inclusion and matrix generate tensile and shear stresses in the locally surrounding matrix [18, 39, 114, 116]. This causes deformation and crack initiation/propagation in the direction of the unidirectional shear stress, τ (e.g. ~45°), perhaps due the latter shear stresses influence [18, 115, 117]. Butterfly wings typically increase in length with over-rolling [22] to a threshold. With increased amounts of over-rolling the frequency of butterfly formations and size of the zone in which they generate increase [23]. However their growth can be suppressed in these same areas by the formation of DER (damage by slip motions having occurred by plastic deformation) which reduces the stress concentration hence suppressing microcrack formation [23, 116].

From a fracture mechanics approach, after initial short crack growth from inclusions/butterflies by Mode I loading, further growth of the cracks from the high cyclic shear stress field would then be governed by Mode II/III shear loading if the Mode II/III threshold stress intensity factor was exceeded [120].

It is contested whether the microcrack forming at a defect occurs prior to WEA microstructural change [18, 23, 25, 26, 39, 115, 117] or whether crack and wing form cooperatively [24], as is why WEA only forms at one side of the cracks. As WEA is harder than the matrix, cracks may nucleate within prior formed WEA to relax localised stress during cycling, as it cannot plastically yield like the surrounding matrix [39]. Cracks may nucleate when a critical density of dislocations is reached [115], though this does not relate to other observations [23, 27, 28, 44, 116].

Another observation is that secondary microcracks [28] and voids [18, 27, 29, 44, 116] which lead to formation of cavities and pores [24, 27, 28] are present in the WEA. It has been cited that the decohesion of defects/inclusions from the matrix lead to the nucleation of voids that can lead to formation of these cavities [27, 129]. Under continued straining, it is suggested that the cavities grow and coalesce into a central crack propagating away from the defect into the matrix along localised shear planes at 45° with respect to the contact surface [98].

The butterfly formation mechanism may differ between inclusion types. Recently Grabulov et al. [24] suggest cooperative growth of WEA wing and crack when initiating at hard oxide type inclusions. It is proposed that the initial nano-meter scale rubbing between the debonded oxide inclusion and the matrix induces local shear damage accumulation and gradual material transfer across the gap onto the inclusion surface. It is suggested that the initial gap then moves out into the steel matrix progressively from material transfer across crack faces and evolves into the main butterfly crack [24]. On the other hand for soft MnS inclusions, Brückner, et al. [118] proposes that butterflies form first by the inclusion cracking though its length due to the cyclic stressing. Subsequently the crack is proposed to extend into the matrix with cooperative WEA formation in the same way as that of oxide inclusions described previously.

Butterflies could be classed into two categories; 1) those that do not propagate significantly and thus not causing failure, and 2) those that do propagate to a length that is critical, forming into cracks in the traditional sense or WECs. Factors which could control whether butterflies are propagating or not are explored in later sections, however in general they can be thought of as stress transients above crack propagation thresholds (i.e. cracks repeatedly growing small amounts from higher than usual loading) and other influences which reduce thresholds for crack propagation such as weakening effect of hydrogen.

Fig. 2.4.3 shows a summary of butterfly characteristics and formation conditions identified from literature.

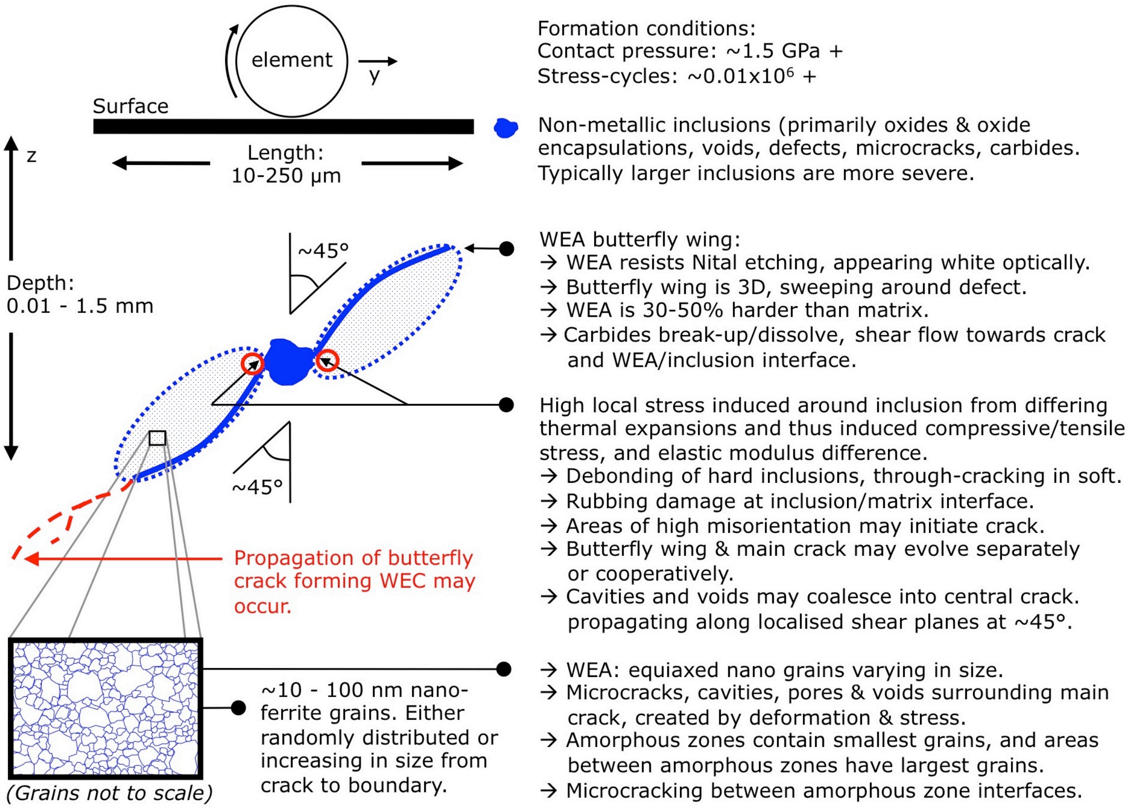

Figure 2.4.3: Butterfly characteristics and formation summary diagram. Over-rolling plane of element across race is designated as (y). Schematic is not to scale.

2.4.3 WEA/WECs

WEA/WEC overview

WECs do not form in directions specific to any maximum shear stress, forming in parallel or branching type crack systems, with cracks typically following the WEA-matrix boundary or passing through the WEA (Fig. 2.4.4). Larger WEA/WECs are typically several millimetres+ in length when viewed as cross-sections, however much smaller WECs can form. WECs form to depths up to ~1.5 mm below the contact surface. The WEA is also found to be similar to that in butterfly wings being nano-crystalline.

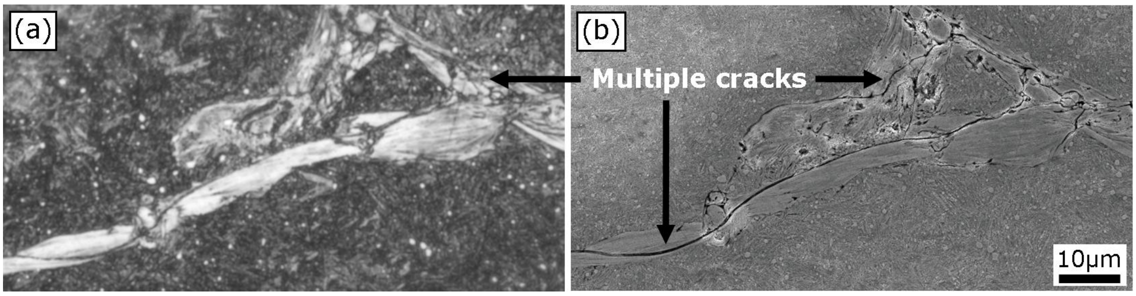

Figure 2.4.4: Optical image (a) and SEM image (b) of multiple cracks passing through a WEA/WEC in a wind turbine gearbox planet bearing. Sample etched with Nital 2%.

WEA/WEC initiation, formation and propagation

Previous WSF investigations have typically been based on a small number of metallographic analyses. Therefore the mechanisms of WEC initiation and propagation, e.g. whether WECs are initiated from surface cracks [37, 106], from inclusions or butterflies in the subsurface [22, 32, 37], or by adiabatic shear banding from impact events [70] are not confirmed (see Fig. 2.4.5). This is partly due to the difficulties of repeatedly creating WEA/WECs under laboratory conditions. The mechanical and environmental thresholds for WECs to form are also not well understood.

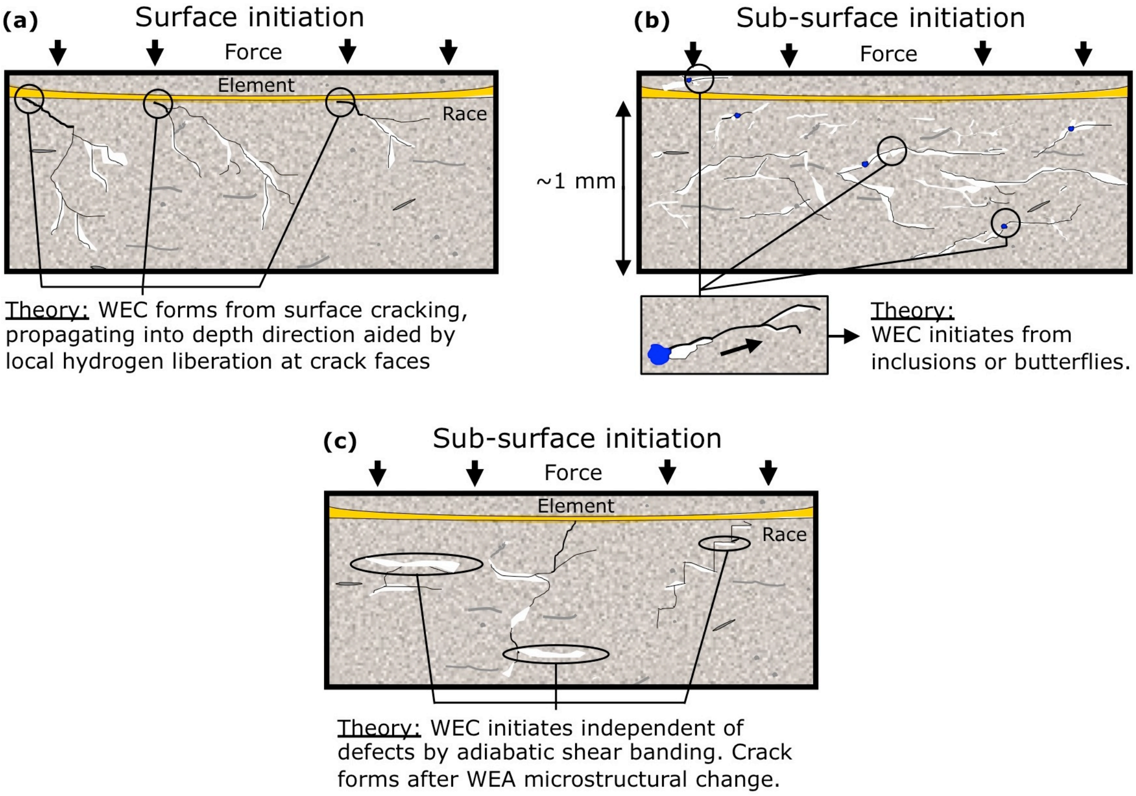

Figure 2.4.5: Mechanisms of WEC initiation and formation suggested in literature.

WEC formation has mostly been attributed to hydrogen embrittlement [4, 5, 29, 31-37, 42, 43, 50-54, 56, 124] with little mechanistic theories suggested. Some researchers supposed that microcracks and subsequent WEA formation generate everywhere just below the raceway eventually uniting to result in flaking [26, 38]. Others proposed that propagating cracks subsequently develop into WECs by the nano-crystalline microstructural change forming as a consequence of material transfer by rubbing crack faces [32]. Gegner [130] suggested that spontaneous brittle fracture on the bearing raceway surface occurs as a consequence of frictional tensile stresses arising during operation. Gegner proposed that subsequently the lubricant enters the cracks and a corrosion fatigue cracking mechanism prevails due to hydrogen being locally released at the crack tip. Becker [25] and Gegner [106] proposed that local material aging and embrittlement is manifested by the formation of a dark etching region (DER) locally around the WECs that is sometimes observed when etching with nital or picral. It is proposed that the local DER around the WECs is the precursor to WEA formation. On the other hand Luckyx [70] suggested that WEA/WECs are initiated by adiabatic shear banding as a consequence of impact loads during bearing operation. Luckyx postulated that longitudinal and shear waves from the impact loading propagate the crack in the horizontal and depth direction respectively in a step-wise manner. In another study two types of WECs were found to occur [42] depending on if the WECs were formed at early or late stage in the RCF life of the bearing. Other studies found thin lined-microstructures only observable by SEM consisting of ultra-fine grained microstructures which were thought to be the early formation of WECs [37]. Large radial cracks on wind turbine gearbox bearing raceways transverse to the direction of rolling have frequently been observed in connection with WECs and WSF areas [106, 131]. WECs have been shown to link to these radial through cracks, however the relationship between radial cracks and WECs has not been established.

Further research is clearly required to clarify mechanisms of WEC initiation and propagation. More than one mechanism of WEC initiation and propagation is feasible and the mechanisms may differ between bearing types, steel grades and industrial application.

2.4.4 WEA microstructural change

It appears that WEA microstructural change in butterfly wings and that associated with WECs are essentially the same. Diffraction patterns show WEA to be a body-centered cubic (BCC) nanocrystalline ferrite structure [25, 27-29, 48] in 100Cr6 steel. Due to the temper carbide dissolution, M_3C carbide dissolution and matrix degradation, the WEA is cited to be supersaturated with carbon in solid solution containing ~1 wt.% carbon [24] with a high dislocation density (estimated as $\sim 10^{16} - 10^{17}$ m^{-2} [27]). The hardness of the WEA is found to be about 30 – 50% higher than that of the matrix [25, 28, 39] which can be explained by the Hall-Petch relationship [39] and the dispersion of very fine cementite particles which has been observed inside WEA (see Fig. 2.4.6) [25, 28, 39]. WEA inside butterfly wings were also found to have no preferential crystallographic orientation when analysed by EBSD [28].

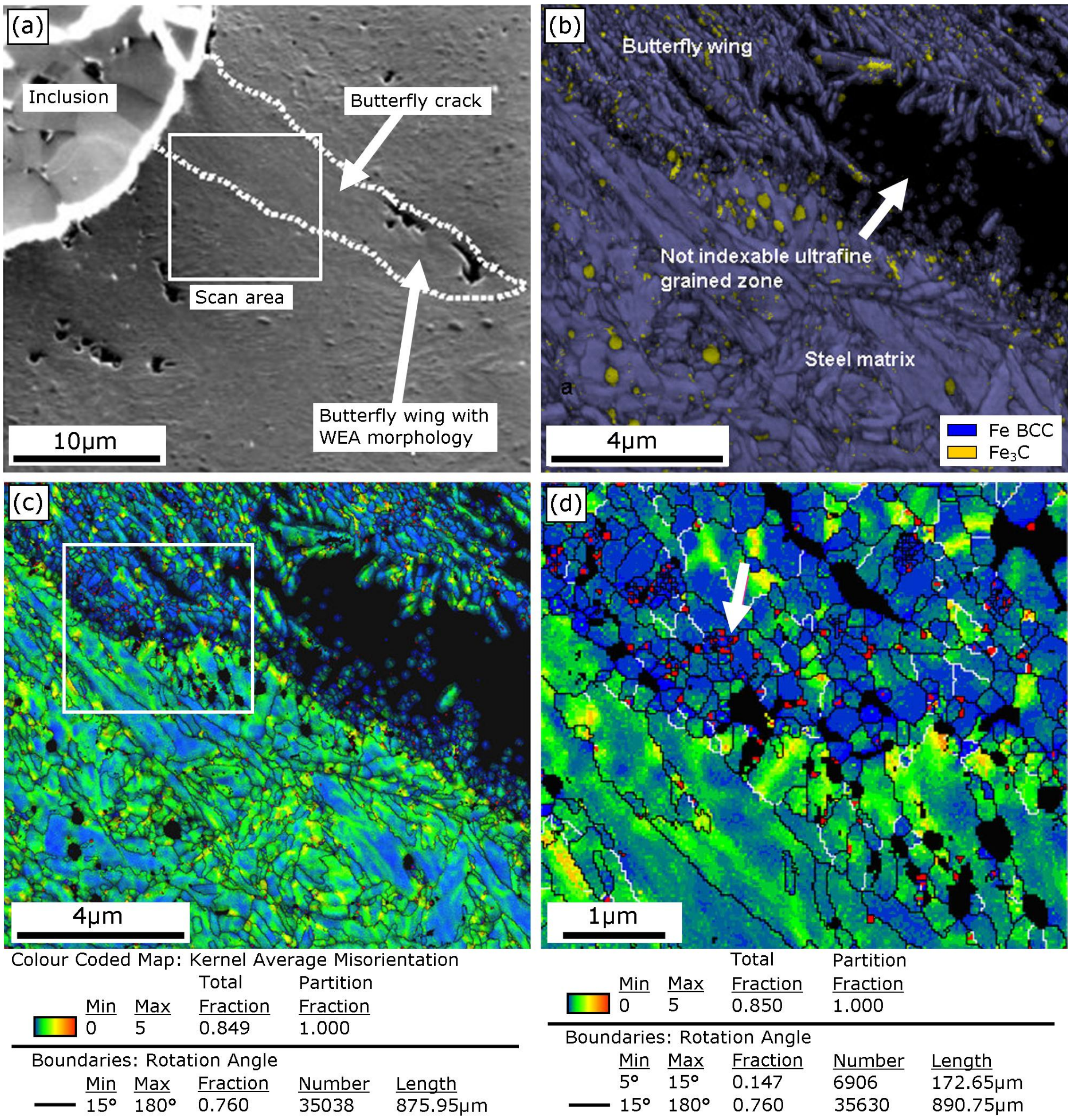

Figure 2.4.6: (a) SEM image of a butterfly wing around inclusion. The marked area (containing the steel matrix and the butterfly wing) marks the EBSD investigation location. (b) Automatic crystal orientation mapping: combined image quality (IQ) and phase map showing the fine granular WEA and black unindexable area with grain diameter <50 nm, also displaying martensite (blue) and carbide (yellow) phases. (c) Colour coded kernel average misorientation (KAM) map displaying higher local misorientation in martensite matrix than in the butterfly wing. (d) Detailed view from (c) consisting of fine grains with very low KAM inside the volume (blue) with a jump transition to the highest KAM next to the grain boundaries (red). Often such regions are situated next to the carbides (black). Adapted from Ref [28]. See permission [2.4].

Since carbon has poor solubility in ferrite (~0.005 wt.% at ambient temperatures), carbon must be accommodated by lattice defects such as vacancies, vacancy-carbon complexes, dislocation cores forming Cottrell atmospheres and the large grain boundary area [24, 46, 132]. A high dislocation density is not observed within the nano-ferrite grains themselves [44] due to their small size, thus it is suggested that dislocations are mostly accommodated at grain boundaries (dislocation networks) [44] where enrichment of carbon at grain boundaries will occur as dislocations migrate from grain interiors to grain boundaries transporting carbon atoms. It is suggested that carbon will also be accommodated by migration to WEA borders to precipitate as lenticular carbides [23, 44, 46] which is consistent with pressure raising the activity level of carbon.

It has been suggested that dislocation generation and movement (glide) from the interface of the defect-matrix [39, 115] lead to repeated interaction between dislocations and carbide precipitates. This is suggested to cause temper carbide dissolution and spherical M_3C carbide elongation, deformation, break-up and dissolution [21, 23, 25, 27, 29, 39, 41, 45, 46]. However in the case of butterflies it has been contested that dislocations sweeping the entire wing is correct, as in hard steels there are many obstacles (carbide precipitates, high density of dislocations, vacancy clusters, etc.) strongly limiting average dislocation glide during each stress cycle [24]. Spherical carbide dissolution in WEA adjacent to larger RCF cracks has been observed previously by TEM [25], however spherical carbide dissolution and how this relates to the WEA microstructural change in the butterfly wings is not well understood.

WEA in butterflies and WECs have been observed to contain amorphous-like regions [27, 29], the amorphous-like regions containing the smallest grains and areas in between amorphous-like regions containing larger grains. Microcracking was found at the interface of the amorphous-like/granular regions and WEA/matrix. Micro-voids formed at the interface of retained austenite/martensite and spheroidised carbide/martensite [29].

Referring to white etching phenomena in other applications than rolling element bearings, white etching layers (WEL) on rail steel surfaces and hard turning consist of a nano-grained microstructures. These areas are also associated with carbide dissolution and are suggested to be supersaturated with carbon. Concerning WELs in hard turning applications, plastic deformation or thermal transformation is cited as the formation mechanism [8, 9]. In rail track applications, high temperatures by sliding and cyclic plastic deformation are cited as formation mechanisms [14, 133]. However in rail steels, reaustenitisation temperatures of 600 °C do not occur [14] as surface temperatures rapidly decrease with depth from the contact surface [13]. The decomposition of carbides and formation of nano-crystalline microstructures also occur in high pressure torsion [133], ball drop & laser heating [134], ball milling [135, 136] and heavily drawn pearlitic steels [132, 137-139]. In all these applications, the mechanisms for nano-grained microstructures, carbon dissolution and carbon distribution are not fully understood [140].

A number of mechanisms for grain refinement forming butterflies under RCF in rolling element bearings have been proposed over the past years [25, 27, 28, 39, 44]. Reversing rolling direction after a period of over-rolling has been shown to form a second pair of butterfly wings in the symmetric orientation [114]. A thermally activated process for butterfly WEA formation cited in earlier works has been refuted due to the inconsistency of the microstructural features in butterflies with a thermal mechanism [25, 39, 114]. These inconsistencies refer to that carbides in the untransformed martensite adjacent to the WEA ferrite phase show no evidence of tempering (there is no size or density gradient near the WEA ferrite). In addition the sharp boundaries between the WEA and the untransformed matrix are inconsistent with a thermal mechanism, as a gradient of structures would be expected in the later [25]. Martin, et al. [44] suggested a polygonisation mechanism (the generation of sub-grains by clustering of dislocations in networks, see Fig. 2.4.7) for the formation of nano-ferrite grains in WEAs. Österlund, et al. [39] proposed that successive grain nucleation takes place at the stress concentration zone at the interface of inclusion-matrix. It is proposed that these grains subsequently work harden by plastic deformation, this redistributing the stress concentration zone to generate more dislocations at the front boundary of the grain refinement. The process was suggested to repeat with each new layer of grains extending out into the matrix to form the butterfly wing. Grabulov, et al. [27] refuted dynamic recrystallisation forming the WEA grain refinement in butterflies due to a lack of time in the RCF stress cycle and lack of sufficient heat generation during RCF [27]. A low-temperature recrystallisation process taking place over a longer time period in-between stress events was proposed for butterflies [27, 28]. The theory states that as plastic deformation results in a high density of dislocations and crystal point defects (the later stabilised by carbon in the solid solutions) [141], that there was no need to thermally activate the formation of vacancies as their mobility was invoked during normal operation.

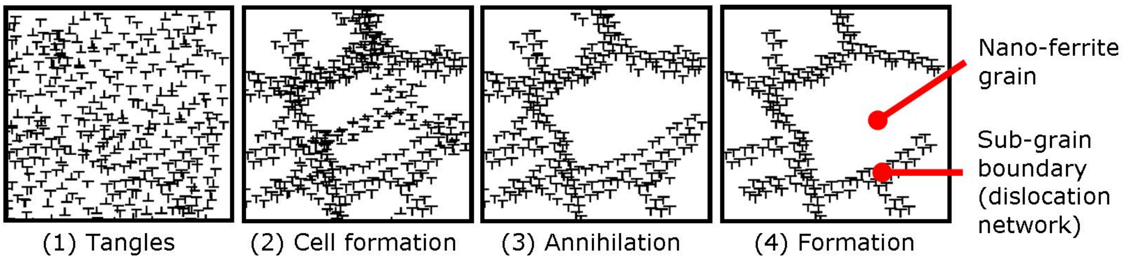

Figure 2.4.7: Polygonisation: the generation of sub-grains by clustering of dislocations in networks. Adapted from Ref [142]. See permission [2.6].

However for the microstructural change associated with WECs, fewer mechanisms have been proposed. It has been suggested that the WEA occurs from rubbing crack faces and subsequent material transfer between the cracks [32]. In summary for butterflies it has been suggested that the high stresses alone in the near vicinity of inclusions, or cracks, are the drivers for the grain refinement [25, 39]. In addition it is generally believed that the structural breakdown of the original matrix by plastic deformation and dislocation movement to form a BCC ferrite nano-crystalline microstructure is a gradual process [25, 27, 28, 39].

2.4.5 Butterfly and WEC formation thresholds

Butterflies

To the authors knowledge there are only a few studies that have reported on the thresholds for butterfly formation.

Lund [22] conducted RCF experiments on spherical ball bearings, which when moderately loaded, produced contact pressures from 4.9 GPa to 0 GPa in the outer ring of the bearing. It was found for maximum contact pressures of 2.25 GPa to 4.9 GPa that the predicted orthogonal shear stress ($\tau_{o,max}$) threshold for butterfly formations was 400 MPa.

It was reported by Brucker, et al. [118] that the threshold maximum contact pressure for butterfly formations in medium and large sized bearings is ~1.4 GPa. Takemura, et al. [143] found that the threshold maximum contact pressure for butterfly formations was 1.3 GPa for ‘dirtier’ 100Cr6 steel and 2 GPa for ‘cleaner’ 100Cr6 steel, but no information on magnitudes of shear stresses can be obtained.

Grabulov [24] conducted RCF experiments on powder metallurgically produced 100Cr6 steel with artificially introduced Al_2O_3 inclusions of ~45 μm diameter. Tests were conducted using a maximum contact pressure of 2.6 GPa. It was found that butterflies always formed at a depth corresponding to predicted orthogonal shear stress magnitude of ~450 MPa, but that butterflies predominately formed at depths corresponding to predicted orthogonal shear stress magnitudes of 575 – 600 MPa (z_o depth = 63 μm). As the predicted orthogonal shear stress reduced below 450 MPa at deeper depths, butterflies tended not to form. However, it must be noted that large Al_2O_3 inclusions can not be thought to be fully representative of inclusions found in normal 100Cr6 steel, therefore the threshold stresses for butterfly formations at these inclusions in Grabulov’s experiments can be thought to be lower than for typical 100Cr6 steel.

In summary a conservative estimate of the threshold orthogonal shear stress for butterfly formation is ~400 – 500 MPa. This assumes that the steel does not contain diffusible hydrogen, as this will lower the stress thresholds for crack formation (see section 2.4.6).

WEA/WECs

Contact pressures used to create WEA/WECs in laboratory range between 3 – 5.6 GPa in the WSF RCF tests [5, 26, 29, 31-33, 37, 38, 42, 43] with rolling cycles of 10^5 – 10^8. Wind turbine gearbox bearing raceways would typically experience a contact pressure between 1 – 2 GPa during normal operation. However transients in service could result in much higher contact pressures intermittently, these perhaps providing critical stresses in excess of thresholds to continue crack propagation. Maximum contact pressure and number of rolling cycles are however not the only driving variables in WSF, as highlighted in the next section.

2.4.6 WSF formation drivers

Overview

In the following section each formation driver that could contribute towards WSF in wind turbine gearbox bearings is identified and discussed. These are split into seven sections: i) hydrogen, ii) lubricant chemistry, iii) water, iv) slip/traction, v) corrosion/standstills, vi) electricity, vii) loading/impact events and vii) vibration/bending/hoop stress. Two types of drivers for WSF have been suggested; one being the transient operating conditions in wind turbines or automotive devices [1] and the other being hydrogen release and diffusion into bearing steel (sourced from the lubricating oil or water contamination) [43]. Typical methods for white etching feature (butterfly and WEA/WEC) creation in laboratory involve either mechanically accelerating the RCF by introducing transient conditions, or chemically by introducing hydrogen into steel to accelerate WSF. Transient conditions include rapid acceleration-deceleration to force slip in the rolling contacts, high slip ratio, spin slip, vibrations induced through belt drives, rapid loading-unloading, etc. Hydrogen has been introduced into steels by using special oils that promote hydrogen release and diffusion into steel, applying electrical currents across contacting surfaces, adding water in lubricants, running RCF tests in hydrogen gas atmospheres or hydrogen charging steels prior to RCF testing.

Influence of hydrogen

Hydrogen is often cited as a root cause or accelerator of WSF [4, 5, 29, 31-38, 42, 43, 49-56]. Hydrogen in its natural state is diatomic molecular gas, H_2. This molecule is too large to enter steel and must therefore be dissociated into single atoms/ions to enter the steel. Sources of hydrogen are dissociation from water and degradation of organic lubricants. Hydrogen has previously been found to diffuse into steel during RCF tests [5, 42, 43, 50, 51] at concentrations between about 0.1 – 4.2 ppm [42, 43, 51]. For this reason, to replicate this diffusion of hydrogen into the steel during RCF, hydrogen charging on test specimens/bearings has been used in various WSF studies. Two mechanisms for hydrogen entering steel during rolling contact have been suggested (see Fig. 2.4.8): 1) through surface cracks where lubricant or water enters surface cracks allowing release of hydrogen ions by tribochemical reactions at the nascent surfaces at crack tips [106]. Aging reactions of lubricants releasing hydrogen during WEC growth has been observed by chemical analysis on preparatively opened fracture surfaces. During the fractographic investigations of WECs, sulphur, phosphorous and zinc were found near crack tips which indicates the reactions of additives containing these elements inside the cracks [106]. 2) through wear induced nascent surfaces where hydrogen is generated by tribochemical reactions of water and decomposition of lubricants through catalytic reactions [51]. However the regenerative passivating protective layer formed on the steel surfaces prevents diffusion of hydrogen into the steel in normal circumstances. Therefore hydrogen ions released absorb by wear induced nascent surfaces and recombine with electrons to form atomic hydrogen [56]. The second mechanism is suggested to be able to drive or accelerate WSF, where the amount of hydrogen that penetrates into steel is proportional to the wear on the steel [51]. When water is present, hydrogen mainly derives from the oil and not water [144].

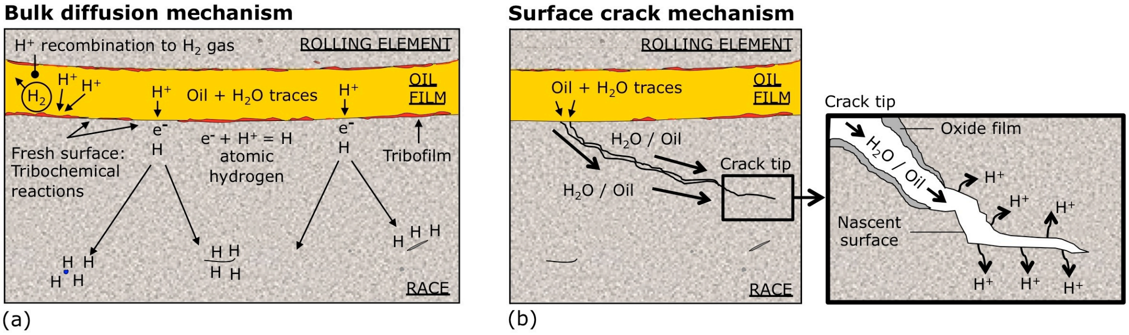

Figure 2.4.8: Schematic of hydrogen entry mechanisms. A rolling element and race lubricated with oil (or grease) that contains hydrogen radicals and/or water contamination. (a) Hydrogen ions (H^+) combine with electrons (e^-) at nascent steel surfaces to form atomic hydrogen (H). (b) Lubricant or water enters surface cracks allowing release of hydrogen ions by tribochemical reactions at the nascent surfaces at crack tips.

Hydrogen pre-charging samples [5, 32, 37, 38, 42, 43, 128, 144-149] or testing in hydrogen gas environments [31, 33, 36, 145] has been used to study hydrogen influence on fatigue life by RCF, tensile [128, 146], tension-compression [147, 150, 151], pure sliding & rolling rotating-bending [146] and cyclic torsion [149] experiments. In the latter, slip bands and microstructural changes only occurred in specimens charged with hydrogen. In general a decrease in fatigue life and strength occurs with hydrogen charging and under rolling contact loading conditions specimens/bearings tend to fail from WSF. Average hydrogen concentrations have been measured by thermal desorption analysis using mass spectroscopy and gas chromatograph analysers. Samples are often frozen immediately after testing with dry ice or liquid nitrogen to stop hydrogen escaping [37, 38, 42]. In studies using hydrogen charging to create WSF the concentration of diffusible hydrogen in samples have been measured as between about 0.5 –

10+ ppm [32, 37, 38, 42, 43, 152]. However these values are not readily comparable between studies due to uncertainties and experimental factors when performing hydrogen measurements.

As an interstitial solute, hydrogen remains in mono-atomic form retaining its mobility in high strength steels [147]. After entering steel, hydrogen (either from manufacturing processes or lubricant/water during bearing operation) can exist in steel in two forms, i.e. mobile/diffusible or non-mobile. Diffusible hydrogen refers to hydrogen able to maintain its mobility or hydrogen that is trapped in weak reversible traps, while non-mobile refers to hydrogen trapped at irreversible traps [150, 153-155]. Any diffusible hydrogen in the steel introduced during the manufacturing process would be mostly lost due to tempering or aging of the steel prior to the bearings operation. Examples of traps are grain boundaries, dislocations, carbides, non-metallic inclusions, voids, retained austenite, etc. [150, 153, 156-160]. Traps are also classified as attractive, physical or a combination of both, where attractive traps attract hydrogen by forces due to electrical fields, stress fields and temperature gradients, and physical traps are defined as those in which hydrogen is trapped by the result of mobile hydrogen's random walk [161]. Stress fields are introduced by microstructural defects such as grain boundaries, inclusions, dislocations and crack tips. Autoradiography showed hydrogen trapping to predominately occur at martensite matrix-carbide and carbide-carbide interfaces in AISI-440C steel [128] and the trapping to vary depending on the type of inclusion [157]. Hydrogen was inhomogeneously distributed at defects in the matrix surrounding MnS (Fig. 2.4.9a), at boundary layers between the Cr-carbide and matrix (Fig. 2.4.9b) and intensely localised at defects in the boundary layers surrounding Al_2O_3 (Fig. 2.4.7c). This was attributed to the differing CTE's when cooling during quenching and thus compressive stress fields around MnS and tensile around Al_2O_3 and Cr-carbide.

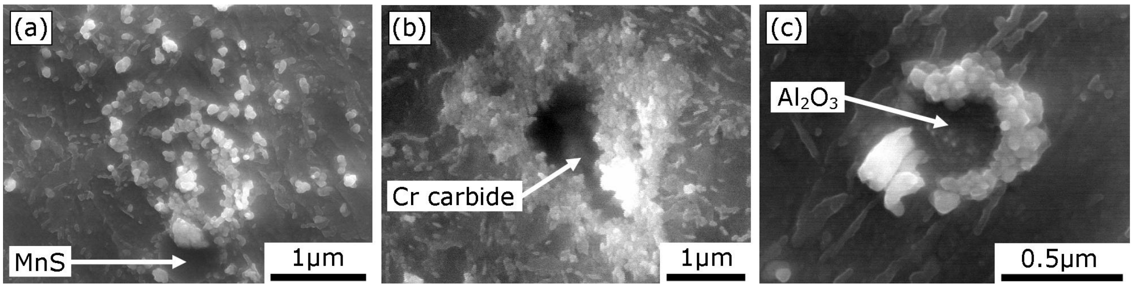

Figure 2.4.9: FE-SEM image of the autoradiograph around MnS and Al_2O_3 inclusions and Cr-carbide in JIS-SCM440 tempered martensitic steel (0.4 wt.%C, 0.21 wt.%Si, 0.79 wt.%Mn, 1.2 wt.%Cr, 0.21 wt.%Mo). Bright white spots are Ag grains (hydrogen atoms) corresponding to locations of tritium. (a) MnS: Ag grains appear on cementite particles precipitated in high angle boundaries such as block, packet and prior austenite grain boundaries but not in the matrix, indicating cementite particles acting as traps around the inclusion. (b) Cr-carbide: Ag grains accumulated at the boundary layers between Cr-carbide and matrix. (c) Al_2O_3: Ag grains accumulated at the boundary layers of the matrix surrounding the inclusion with no widely distributed Ag grains. Adapted from Ref [157]. See permission [2.7].

The presence of diffusible hydrogen in bearing steel is detrimental to the steel's mechanical properties due to hydrogen embrittlement. Several theories have been offered in an attempt to explain hydrogen's detrimental effect on the steels properties, such as hydrogen-enhanced decohesion (HEDE) [162], hydrogen-enhanced localised plasticity (HELP) [163] and recently hydrogen enhanced strain induced vacancy (HESIV) [154] theories. However, no consensus has been reached yet and hydrogen embrittlement theories do not fully explain the effects of hydrogen in bearing steels [164]. Vegter & Slycke [32] suggest that with hydrogen's formation enhancement of vacancies, this enhances the dislocation climb-controlled damage process [149] which with hydrogen's attraction to point defects results in a self-generating damage localisation process. Generally hydrogen's role in the steel would be to enhance slip deformation and localisation of plasticity at the fatigue crack tip [149, 151] and to decrease mode I/II stress limits for crack growth and propagation [120, 149].

Apart from the numerous studies that have shown that WSF occurs in steel with heightened concentrations of hydrogen, little is known about the relationships between hydrogen concentration and butterfly/WEA/WEC formation and whether any thresholds for formation exist. Previous studies by Uyama, et al. [37] on thrust washer ball bearings showed qualitatively that a difference in the size/amount of WEA/WECs occurred with differing concentrations of diffusible hydrogen. However little metallographic analysis was conducted to confirm or quantify their findings. Therefore the links between hydrogen embrittlement and WSF and the thresholds of WSF under hydrogen influence are not well understood.

Tribochemistry, lubrication and additives

Lubricants can be in the form of grease or oil, where wind turbine gearboxes mainly use oils with high viscosity (ISO-VG 220 – 320) at operating temperatures of 60 – 85 °C.

Wind turbine gearbox bearings often run in mixed and boundary lubrication regimes rather than elastohydrodynamic lubrication, which is the desired regime for bearings. This can result in high traction coefficients, metal-metal contact and asperity induced peak contact pressures and temperature flashes. Under rolling/sliding tribofilms form at contact surfaces with various morphologies and thicknesses depending on the lubrication and steel type, and tribomutation layers can form in a shallow zone below the contact surface [165, 166]. Tribofilm formation is predominately caused by reaction flash temperatures rather than reaction with nascent surfaces [167]. Tribofilms provide significant adhesion protection under severe plastic deformation and lubricant starvation [166] and provide a barrier to corrosion and hydrogen diffusion into steel if continuous and intact. Extreme pressure (EP) additives typically consist of sulphur, phosphorous or chlorine compounds, these chemically reacting at the steel surface under extreme pressure and temperature flashes. Tests on AISI-52100 steel showed phosphorus-enhanced films form first on nascent surfaces, then sulphur-enhanced films form under increased loads and temperatures to prevent metal-metal contact [168]. However, chemically active EP additives such as sulphur-phosphorous can be detrimental to RCF life [169], accelerating the progress of surface fatigue microcrack propagation when inside cracks with nascent surfaces [170]. In addition, anti-wear additives can produce an increase in friction and reduction in oil film thickness [171]. Sulphur additives in lubricants can prevent atomic hydrogen recombination to H_2 gas, thus enabling more hydrogen ions to combine with electrons to form atomic hydrogen [172] (see Fig. 2.4.8). Most lubricant compositions comprise of a rust preventative additive such as sulfonates that has been shown to increase the likelihood of WSF [43, 53, 54]. Rust preventatives 'keeping surfaces clean' accelerate WSF, whereas rust preventatives 'deactivating surfaces' can prevent WSF [43]. Additives such as oxidised iron powder [43], copper powder [43] and aluminium oxide [53] have been shown to accelerate WSF.

With regards to tribological preventative measures against WSF, it was found by Murakami, et al. [41] that during WSF rapid acceleration-deceleration and impact loading tests on greases in automotive bearings, grease giving extended life until WSF showed the following characteristics. i) Wider and shallower load zones, ii) resistance to impact load film breakdown, iii) lower repulsion coefficient, iv) lower maximum vibration level close to resonance (by a factor of 2X), and v) the grease containing an adhesive substance. These were cited to increase damping characteristics and hence reduction in peak and impact loads [41]. Fluorine based oils (e.g. PFPE) and fluorine based surface active agents that form raceway films have been suggested as partial preventers of water ingress and WSF [51, 54]. PFPE oils contain no hydrogen radicals and are therefore not a source of hydrogen [51]. It has been shown that isopropylaminoethanol additive condenses into surface microcracks along with water, capturing generated hydrogen ions sourced from the water and thus preventing hydrogen enhanced crack propagation [173]. Lubrication with increased heating stability, specifically synthetic ether [43] and Al metal powder increases WSF life [53]. The following additives have been found to either prevent hydrogen penetration or WSF in tests: i) $NaNO_2$ and K_2MoO_4 anodic corrosion inhibitors (which reduce anode reactions by oxidising steel, with adsorption and reaction of oxidising ions or dissolved oxygen) forming a metal oxide film [31, 51, 53]. ii) $ZnCO_3$ cathodic corrosion inhibitor (which decreases cathode reactions by formation of anti-corrosion films). iii) Rust preventatives/metal deactivators Naphthenate (e.g. Zn) [54], succinic acid derivative (metal DTC or DTP) [54] and organic metal salts (preferably Zn based) [54] which form a reactive film in a minute gap. However, merely reducing the occurrence of nascent steel surfaces by anti-wear additives does not reduce hydrogen penetration into steel [51]. In addition, phosphate additives forming a film which has a high anti-wear property to suppress generation of hydrogen are ineffective [31, 53] because of a lack of thermal activation to form a film [31].

Clearly damage in rolling element bearings that results in exposing nascent steel surfaces is detrimental, as these nascent surfaces can act as catalysts for tribochemical reactions or corrosion which could allow hydrogen to diffuse into the steel. It has been shown in numerous studies that the lubricant and especially additives used can strongly control whether WSF occurs and how quickly. Hence when designing RCF tests to enable creation of WSF it is very important to consider the lubricant and additives used.

Influence of water

WSF has been reproduced in tests by adding water to the lubricant [5], this either causing corrosion which enhances hydrogen diffusion into steel, formation of atomic hydrogen by creation of hydrogen peroxide [174] or formation of nascent surfaces which leads to hydrogen generation. A major contaminant in wind turbine gearboxes is water ingress [1] sourced from coolants and condensation [49]. As wind turbines slow down to standstill, they cool down and draw moisture from the air, i.e. as the gearbox breathes through seals and breathers, water can enter the gearbox. Another source of water is in-situ from the oxidative decomposition of oil [145]. Water attracts to surface microcracks, liberating hydrogen at nascent surfaces inside the crack [170]. Water transforms sulphur-phosphorous EP additives into acids, resulting in a corrosive acidic fluid environment [1, 170]. Small water globules pulled in-between contacting surfaces result in collapsed oil film strength and thus lost clearance, this causing impacts and rubbing of contact surfaces and nascent surface generation [1, 170].

Influence of contact slip and traction

There are two ways that slip could be a driver of WSF, firstly directly by creation of surface traction and shear stresses shifted closer to the surface and their damage influence [4, 29]. For example slip can result in high frictional energy input which rapidly accelerates surface fatigue and high traction coefficients, shifting the position of subsurface shear stresses closer to the surface and increasing their magnitude [116, 175] (see Fig. 2.4.10). This could increase probability of crack initiation at inclusions located in the near surface zone. Secondly, slip could indirectly be a driver of WSF by tribofilm damage and creation of nascent surfaces liberating hydrogen [51].

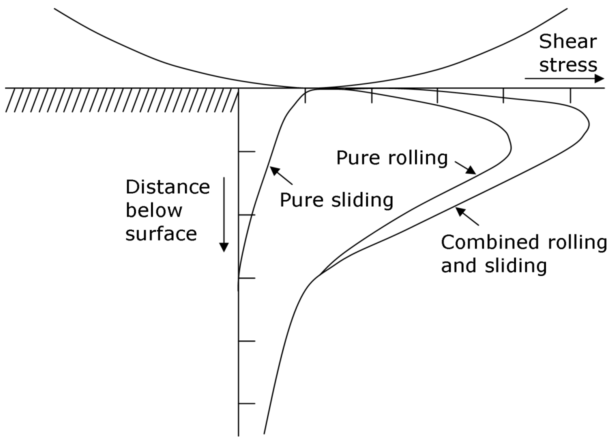

Figure 2.4.10: Shear stress distribution at and near two contacting surfaces under sliding-rolling conditions. Adapted from Ref [175]. See permission [2.8].

Slip is inevitable in rolling element bearings and occurs in operation at loads below the dynamic load rating, at misaligned rollers in unloaded zones due to low traction forces, as "Heathcoat slip" in rolling element bearings (especially spherical roller bearings) due to a geometrical constraint [1] and during transient events in transmissions, such as rapid accelerations-decelerations [176]. Simulations have shown that for spherical roller bearings in an intermediate shaft location of a wind turbine gearbox, moderate sliding (3 – 10% slip) at roller-raceway contacts in the unloaded zone occur continuously [176]. Extreme slip (~20 – 110% slip) occurs for low load and high speed conditions due to concomitant contact area reduction and traction loss at roller-raceway interfaces [176].

Slip to varying degrees is often used in rolling contact studies [4, 5, 29, 35, 41, 43, 48, 53, 54, 56, 165, 177] and it is often quoted as being essential in enabling the creation of WEA/WECs. It was found WSF only occurs at specific regions having the largest PVmax value (a product of contact pressure (P) and slip velocity (V), MPa.m/sec) in rolling element bearings due to these regions corresponding to the highest concentrations of hydrogen [4, 35]. Slip can also shear and heat the lubricant, reducing oil film thickness [178, 179] which may lead to wear and hydrogen liberation. However, a high slip ratio does not necessarily mean that shearing of contacting surfaces is high; it is the traction coefficient that influences the amount of shear induced in the contacting materials. Thus traction coefficient and lubricant regime should be key parameters in tribological experiments aiming to create WSF.

Influence of corrosion and standstill time

Fresh water, sea-water and salt contamination from offshore environments are possible in wind turbine gearboxes. Wind turbines also often experience long standstills and idling operation. Thus it is likely that corrosion occurs and fretting corrosion (small amplitude movements between the element and race by vibration for example) which can result in passivation films being removed and nascent steel surfaces being exposed to corrosion from the atmosphere. Corrosion as a mechanism of hydrogen liberation may be an indirect driver of WSF. Corrosion may also enable hydrogen enhanced diffusion to the subsurface of the steel at corrosion damage on the raceway surface and also corrosion within surface microcracks generated during operation [173].

Influence of electricity

Lightning strikes and stray currents could affect bearings in wind turbine gearboxes. Electricity may cause WSF indirectly by arcing damage by current on bearing surfaces which produces nascent surfaces and sites for hydrogen release [53], or by liberation of hydrogen from water contamination by electrolysis. Studies show that the larger the current (from 0.1 – 3 A) the earlier the occurrence of WSF [53] and that more wear occurs on the bearing ring at the electrically positive pole thereby corresponding to the location of WSF. Static electricity (several hundred-thousand volts) due to a belt driving the bearing assembly has been cited to indirectly cause WSF in automotive bearings. The static accumulates between contacting surfaces and subsequently discharges (spark) when metal-metal contact occurs (from oil film deterioration by static electricity during periods of excessive microslip or vibration) which liberates hydrogen from water in the lubricant [5]. Use of hybrid bearings (ceramic elements) and conductive lubrication (carbon black/nanotube additives) that prevent the static electricity discharge phenomenon between contacting surfaces that liberates hydrogen from water in the lubricant has been shown to prevent WSF in this application [5].

Influence of loading and impact events

WSF RCF tests have typically employed high constant maximum contact pressures between 3 – 5.6 GPa [5, 26, 29, 31-33, 37, 38, 42, 43]. Compared with the typical maximum contact pressures experienced by rolling element bearings in wind turbine gearboxes for example (P_{max} below 2 GPa), the mechanisms of damage formation leading to WSF formation at these high contact pressures may be different. This is due to factors such as crack initiation at material imperfections, development of residual stresses and material alterations.

Even though predicted loading in wind turbine gearbox bearings is a maximum of ~2 GPa, condition monitoring of loading in actual gearbox bearings may not have a high enough sampling rate to register instantaneous impact loads. Impact events are frequently experienced in wind turbine gearboxes; by wind gusts, braking, load reversals and generator/grid engagements and disengagements. In the unloaded zones of rolling element bearings, repeated impacts occur when elements are instantaneously loaded whilst in misaligned conditions along one or two contact points in the load profile [72]. Therefore contact stresses exceeding yield strength can be experienced. For example a 600 mm displacement of an intermediate shaft from a 1.5 MW gearbox resulting in severe misalignment [72] can produce a predicted transient raceway stress exceeding 3.1 GPa [1]. WECs in automotive belt driven bearings may be caused by collisions of rolling elements [57]. During rapid acceleration-deceleration testing, impact loads events at rates of 0.3 seconds have been found to occur which were attributed to the reduction in WSF life [41].

Vibration, bending stress and tensile hoop stress

Bending stress, tensile hoop stress and vibrations as mechanisms increasing maximum loads has been cited [41]. Severe vibrations [4, 5, 41, 43, 48, 53, 57] and resonance applied on a belt driving a bearing [41, 57] have also been induced to create WSF in RCF tests. Vibrations in wind turbines can occur from blades and blade revolution frequency, from grid connections, brake loads and nacelle deflections. Vibrations may influence oil film formation leading to formation of nascent surfaces, increasing of peak loads, or to disturb the kinematics of the rolling elements.

Summary of WSF formation drivers

There are many factors that could drive the formation of WECs. However it is apparent that many drivers directly relate to the influence of hydrogen. In addition several other mechanical drivers also indirectly aid hydrogen generation and diffusion making verification of other drivers difficult. A summary diagram showing the WSF formation drivers is shown in Fig. 2.4.11.

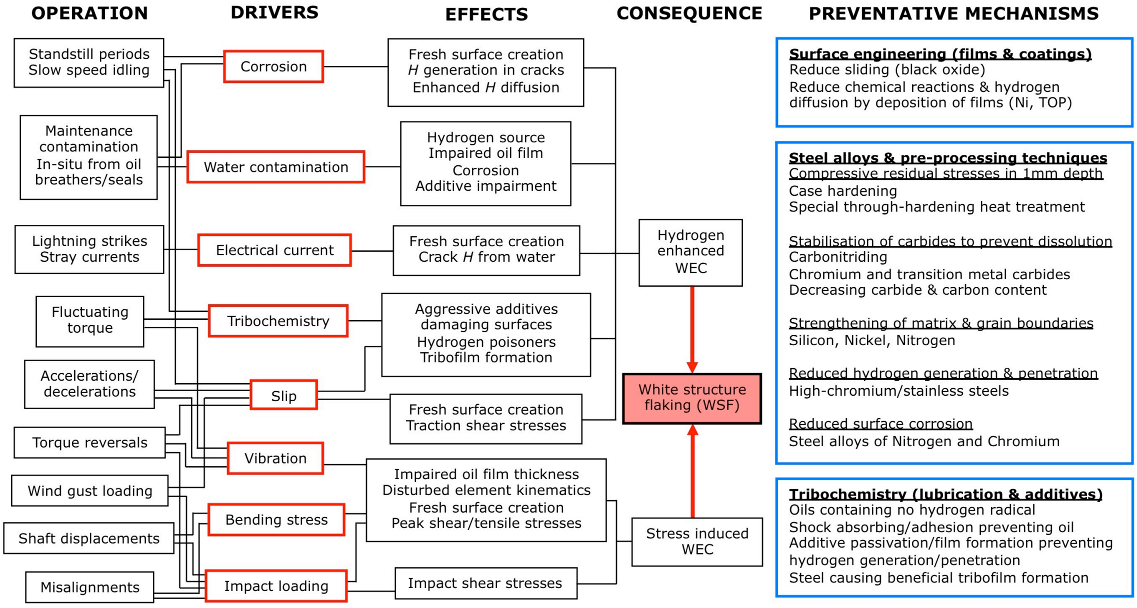

Figure 2.4.11: WSF formation driver summary in wind turbine gearboxes and possible solutions. *H* = hydrogen.

2.4.7 Potential bearing steel and coating solutions to WSF

In the following section, bearing steels and surface engineering are discussed in terms of their influence to preventing WSF. It is useful to understand potential solutions as these give key insights into the formation drivers.

Bearing steels combating WSF failure

Should WECs initiate at inclusions it is a logical solution to use super clean grades of steel to reduce the chance of crack initiation. However this has not been investigated to the author's knowledge. In through-hardened bearing steel, fatigue properties increase with degree of hot-working reduction [114], however it has been noted that heat treatment conditions do not significantly affect development of butterfly wing formations [22]. Compared to carburised steel, through-hardened steels have better dimensional stability and can sustain higher loads. This is because through hardened steels have lower quantities of retained austenite (austenite transforms to martensite under load with an associated volume increase) [116]. Residual stress induced from manufacture differ between martensitic, bainitic and case-hardened steels, which have tensile, compressive and high compressive residual stresses respectively from just below the surface to a depth of ~0.3 mm [49]. Subsurface compressive residual stresses in case-hardened steels are beneficial in retarding crack development by decreasing the effective applied stress [116] and are therefore used to negate tensile stresses in bearing rings that require tight interference fits [100, 101]. Carburised steel, which reduces bending stress in bearing outer rings due to compressive residual stresses [41], and carbonitrided steel [4] can increase WSF life. Impurity atoms interact with dislocations and grain boundaries, trapping vacancies thus decreasing vacancy diffusion. Since carbides have been shown to dissolve as part of WEA formation, replacing these with more stable carbonitrides, Cr-carbides [50] or transition metal carbides such as Mo [59] prolongs their decay. Additions of Si and Ni which strengthen the matrix and grain boundaries may also delay microstructural change [36]. AISI-52100 steel has been shown to be more susceptible to tribochemical wear than that of case-carburised steel. This is suggested to be due to AISI-52100 having a more coarse grain structure and spheroidal carbides typically an order of magnitude larger (~1 – 2 μm) compared to that of case-carburised steel (~0.1 – 0.5 μm) [165] (see Fig. 2.4.12).

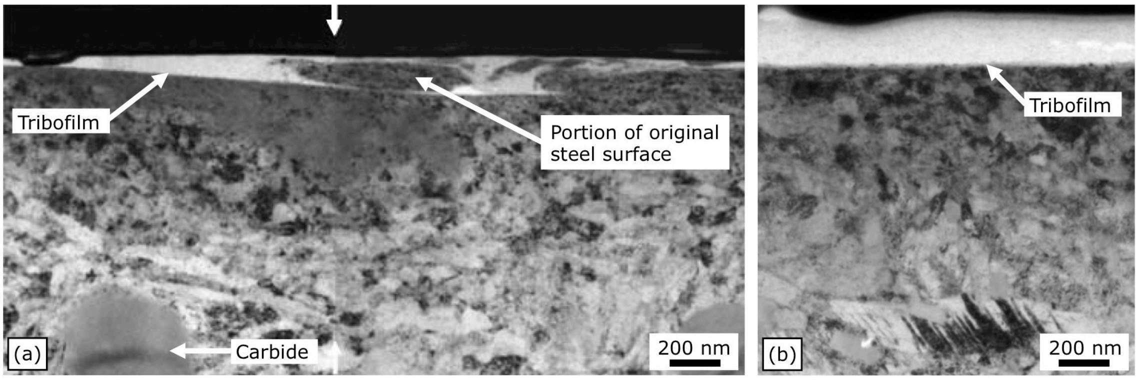

Figure 2.4.12: TEM images of cross-sections of the wear track, where the ball rolled across the horizon of the image. (a) AISI-52100 steel showing tribofilm with a non-uniform thickness and structure, cracking, tribofilm penetration into the surface and surface particle detachment. White arrow indicates where two images are spliced together. (b) AISI-3310 case-carburised steel (0.11wt.%C, 0.53wt.%Mn, 1.58wt.%Cr, 3.5wt.%Ni) showing uniform, thick and intact tribofilm of ~200nm thickness with a sharp smooth interface with the matrix. Adapted from Ref[165]. See permission [2.9].

Average carbon content in steels has been proposed to influence WSF. AISI-52100 has carbon content of 0.9 – 1.1 wt.%C, case-hardened steels 0.1 – 0.3 wt.%C (0.65 – 1.1 wt.%C in the case-hardened zone), whereas hardened steels containing 0.4 – 0.8 wt.%C supposedly show reduced occurrences of WEA/WECs [6, 23]. AISI-440C high-carbon martensitic stainless steel (1 wt.%C, 17 wt.%Cr) is typically used in mildly corrosive environments. However, compared to AISI-52100 the dynamic load bearing capacity of AISI-440C is lower and the steel contains coarse eutectic carbides which can act as crack initiators and chromium concentration sites [116, 180]. Martensitic stainless steel ES1 [50, 180] has a lower carbon and chromium content than AISI-440C to suppress eutectic carbides and has a comparable hardness to AISI-52100. ES1 is alloyed with nitrogen which forms carbonitrides, strengthens the matrix and provides corrosion resistance, all these factors enabling a 10X increased WSF life compared to AISI-52100 [50].

Martensitic stainless steel has a much lower hydrogen diffusivity rate than through-hardened steel due to high contents of chromium which provides a strong hydrogen trap and allows the formation of a passive film on its contact surface [4, 35]. Higher chromium content results in a higher number of Cr-carbide formations, but also higher levels of chromium in the matrix that mitigates the generation of nascent surfaces during severe slip events. This prevents hydrogen generation and diffusion due to the passive chromium layer formation on the contact surface [4, 50]. Recently a hydrogen failure resistant bearing steel has been conceived by a microstructure which combines a martensitic matrix in which fine cementite precipitates impart strength and V4C3 nano-scaled particles act as hydrogen traps [181].

Martensitic stainless steel exhibits a longer fatigue life under hydrogen testing [145], generally (but not always) increasing WSF life compared to AISI-52100 steel [4, 31, 43] by as much as 4X [50]. It has been shown that incremental increases in chromium content up to 13 wt.% can increase WSF life [4, 34, 35].

Compressive residual stresses from rolling contact are induced in the circumferential [102-104] and axial [102, 103] directions in the subsurface of rolling contact bodies if the load is sufficient. The absence of high residual stresses in low load operation may increase the likelihood of WEC formation.

As it stands, carbonitriding, low-carbon steel, high chromium steels and low-carbon stainless nitrogen alloy steels may offer extended life until WSF. Research into tribofilm formation, compressive residual stress development and the influence of carbide strengthening should be furthered as these could be important factors. It seems that the majority of potential bearing steel solutions offer protection from hydrogen diffusing into the steel.

Surface engineering combating WSF failure

A ~3 μm thick electroplated nickel film that diffuses into the raceway under rolling contact induced heat and stress [42] and highly dense pre-formed trioctyl phosphate (TOP) film [31] prolong time until WSF by ~5X [42] by prevention of hydrogen diffusion. Black oxide treatment on bearing contact surfaces prevents damage from smearing, increasing resistance to slippage and damage during alternating, low-load conditions. Black oxide is a mixed iron oxide produced in a dip solution, providing a soft 0.4 – 2 μm layer that increases lubrication film thickness, reduces traction coefficient and provides damping. Black oxide is highly resistant to bending and stress [182-184] and offers protection against detrimental surface reactions from aggressive lubricants. Although black oxide wears off in operation (months to several years), it typically prolongs WSF in wind turbine gearboxes [70]. However the preventative mechanisms are not fully understood and the long-term effects on gearbox components are unknown.

Summary of potential solutions to WSF

It is clear that there already exist some methods to prolong time until WSF occurs. However cost, limited supply or lack of trials has inhibited the introduction of these into the wind turbine industry. It is also apparent that many of the potential solutions suggest the mechanism of improvement is reduction in hydrogen diffusion into the bearing steel. This suggests that hydrogen is a root cause of WSF. A summary of possible solutions to WSF is given in Fig. 2.4.11.

2.5 Literature review conclusions

- Few systematic studies have been conducted with the aim of identifying tribological formation drivers of WSF. As a consequence the formation drivers of WECs are not well understood, not least due to the difficulties in reliably creating WECs in laboratory tests. A greater understanding of transient loading and tribological conditions faced in wind turbine gearbox bearings are required (e.g. impact loading, vibrations, slip) to better inform laboratory testing conditions.
- Approximately 75% of literature proposes hydrogen as a root cause of WSF. Hydrogen is suggested to diffuse into bearing steels either from local release inside cracks from aging of lubricants and water contamination or from bulk diffusion at nascent surfaces on the raceway. It can be seen from Fig. 2.4.9 that many stimuli to the tribological system have a possible consequence of hydrogen influence. This makes it difficult to separate the possibility of deleterious effects of hydrogen in testing from those of mechanical stress drivers. In addition many of the solutions suggest the mechanism of improvement is by the reduction of hydrogen diffusion into the bearing steel, which further indicates hydrogen as a root cause of WSF. However the concentration of diffusible hydrogen should be measured in wind turbine gearbox bearings from service, in-situ or immediately after operation, to deduce whether hydrogen does indeed diffuse into the gearbox bearings as suggested. It is clear that hydrogen within the microstructure lowers thresholds for crack initiation and propagation, however the initiation and propagation mechanisms of WECs as well as the thresholds for their formation under the influence of hydrogen are not yet established.
- Non-metallic inclusions and defects initiate butterflies, where inclusion size, morphology, orientation, adherence and composition determine severity. It is not known whether crack formation or WEA microstructural change occurs first or whether cooperative growth prevails. Moreover, whether there is a link between butterfly formations and WECs is not

well understood due to a lack of evidence to suggest that butterfly cracks could propagate to form WECs.

- Initiation mechanisms of WECs are contested and require clarification. Initiation of WECs by surface cracking, subsurface cracking at inclusions or initiation by impact event induced adiabatic shear banding are proposed. How the WECs then propagate to cause flaking is also not well understood.
- Grain refinement mechanisms forming WEA that consists of ultrafine ferrite grains of ~10 – 100 nm diameter that is super-saturated with carbon, by dislocation movement, carbide dissolution and recrystallisation are contested.
- Lubrication and additive selection can significantly accelerate or retard WSF, which is usually explained by deleterious effects from hydrogen influence. Additives either accelerate or decelerate corrosion, wear, electrical effects, tribochemical reactions and hydrogen generation/diffusion and can prevent surface damage from sliding, adhesion, vibration and shock loads.
- Steels containing reduced quantity of carbon and size of spherical carbides, case-hardened steels such as carbonitrided steels, high-chromium steels and low-carbon stainless nitrogen alloy steels show improved WSF life. Elements which strengthen the matrix and grain boundaries and beneficial compressive stresses may also prevent or prolong WSF. The mitigation of hydrogen influence by reduced wear, enhanced corrosion resistance, matrix strengthening and carbide stabilisation is cited; however the mechanisms for improved performance are not fully understood and solutions may be unacceptably expensive. Also steel cleanliness and how this relates to the WSF failure mode has not been firmly established.
- Surface engineering by the formation of protective films or surface coatings on contacting surfaces are cited to reduce hydrogen generation/diffusion and friction from slip and therefore improve WSF life. However often the preventative mechanisms and long term effects on components are unknown.

2.6 RCF testing strategy to create WSF

2.6.1 Introduction

In the following section, the WSF formation drivers that have been identified are overviewed in relation to incorporating these in to the RCF testing in chapter 3. The formation drivers are limited to the capabilities of the RCF test machine identified for use in this study.

2.6.2 Non-hydrogen charged testing

In the following a summary of the hypotheses behind why certain conditions were identified for use in testing is detailed. These were informed from gearbox operating conditions and literature.

Transient load

In the loaded zone of wind turbine gearbox bearings the maximum contact pressure that is experienced in normal operation is in the range of 1.5 – 2 GPa. However, it has been cited that a load of 3.1 GPa+ [1] could occur in service at certain overloading transients which have been recorded in wind turbine gearboxes in service [72]. A transient load has thus been identified for use in the testing to replicate transient loading events that are thought to occur during operation.

A transient load induces maximum shear stress at various depths rather than a constant load; therefore a higher number of material defects in the steel will be subjected to high magnitude shear stresses. This is important, as the volume of steel for the test samples is extremely small compared to wind turbine gearbox bearings. Therefore ‘shear stress scanning’ the steel will increase the probability of defects being included in a critical zone of stressing, e.g. a zone where stress is high enough to cause crack initiation/propagation. See Fig. 2.6.1 for a simplistic macro view of the stress field that ignores surface roughness and traction effects.

However it is important to consider how the load is applied. The test rig that has been identified for use in this study cannot apply ‘impact’ loads as the load is applied pneumatically. Therefore the load to be applied cannot be instantaneous, as it would take a few seconds to raise the load from 2 GPa to 5 GPa for example (dependant on contact geometry used).

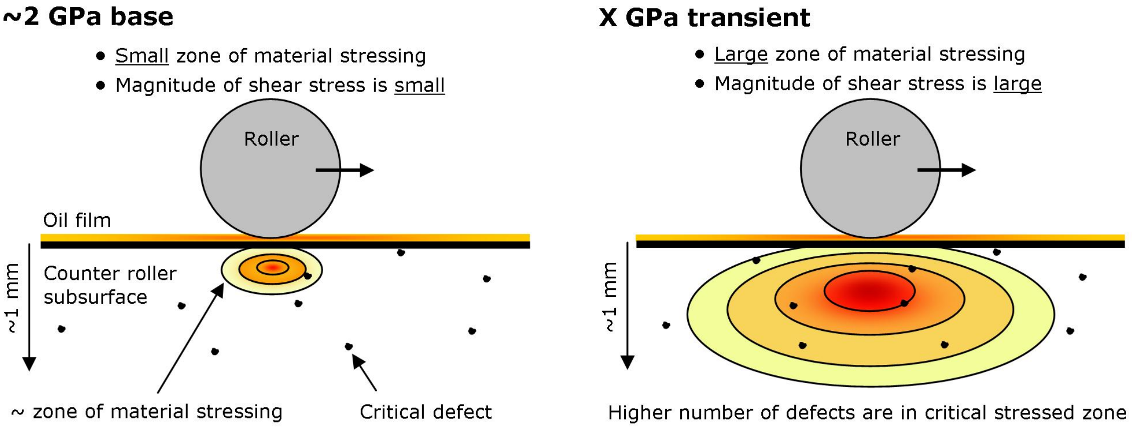

Figure 2.6.1: Hypothesis behind load transient driving butterfly and microcrack formation. The effect of roughness (asperity) induced micro-stress fields and traction is not considered. Rolling direction left to right.

Acceleration-deceleration transients and controlled slip

Acceleration-deceleration transients are known to occur in wind turbine gearbox bearings. For example in a 1.5 MW wind turbine, during premature engagement of the generator to the electrical grid, the generator forced the intermediate shaft to accelerate from 375 to 422 rpm in 2 seconds (126 rpm/second), which was 18 times faster than the average acceleration [72]. Estimation of slip in wind turbine gearbox spherical roller bearings during acceleration transients have been calculated [176]. Slip ranging between 30 – 110% were calculated to have been experienced at various points in the acceleration transient depending on the load applied to the bearing. In addition, simulations have shown that for spherical roller bearings in an intermediate shaft location of a wind turbine gearbox, moderate sliding (3 – 10% slip) at roller-raceway contacts in the unloaded zone occur continuously [176].

The test rig identified for use in this study can investigate acceleration-deceleration and controlled slip transients. The aim of this would be to cause slip, traction in the contact and shearing of the oil film, these possibly causing metal-to-metal contact, wear induced nascent surfaces and tribochemical reactions. Tribochemical reactions under boundary lubrication and at wear induced nascent surfaces may drive hydrogen to be disassociated from lubricants and consequently diffuse into the steel. See Fig. 2.6.2 for a local/micro-scale view of the effect of roughness and tribochemical interactions. Concerning high traction in the contact, this would raise the level of subsurface shear stress towards the surface and increase its magnitude. See Fig. 2.6.3 for a simplistic macro view of the stress field that ignores surface roughness. This may aid in formation and propagation of butterflies/WECs in a near surface zone.

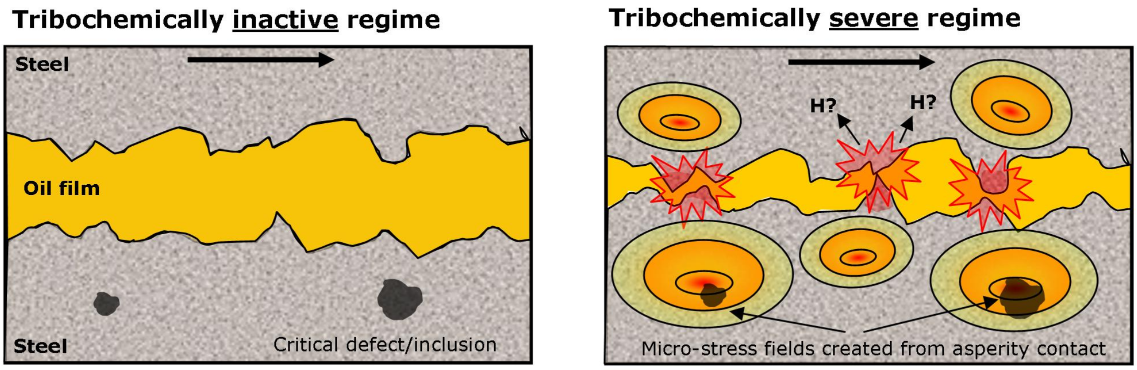

Figure 2.6.2: Hypothesis behind boundary lubrication regimes and wear induced nascent surfaces driving WEC formation.

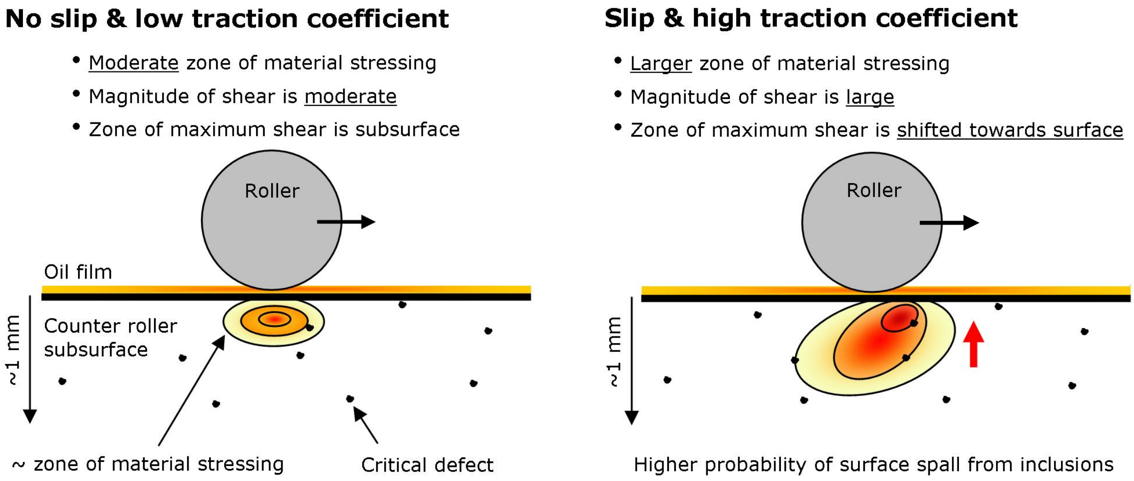

Figure 2.6.3: Hypothesis behind high traction driving butterfly and microcrack formation. The effect of roughness (asperity) induced micro-stress fields is not considered. Rolling and sliding direction left to right.

Number of rolling cycles

Since a bearing in a wind turbine gearbox is supposed to last ~150,000 hours (~20 years, i.e. the L_{10} life) and WSF typically occurs at ~1 – 20% of L_{10} life, it can be understood that WSF occurs from ~1500 – 30000 hours operating time [70]. This equates to ~0.5 – 5 years operation at 60% capacity (wind turbine running for 60% of time due to standstills, maintenance, low wind conditions, etc.). Table 2.6.1 details the estimated number of rolling cycles for wind turbine gearbox bearings for 0.5 – 5 years operation time at 60% capacity. As there are limitations on the speeds achievable in the RCF test machine and time restraints on rig usage not all wind turbine gearbox bearing lifetimes can be replicated in this study. Table 2.6.1 highlights the service lifetimes of wind turbine gearbox bearings that can be replicated with the test set-up used in this study. It can be seen that it is possible to replicate ~0.5 – 5 years operation in intermediate speed bearings. However it is not feasible to replicate high-speed bearing operation in lab in a reasonable time scale (~3 weeks), e.g. achieving ~2E8 – 1E9 cycles.

Initially the strategy for testing was decided to be use of moderate numbers of rolling cycles to determine if WSF failure occurs in a short time scale. If this were unsuccessful subsequent testing would use moderate numbers of rolling cycles combined with other severe tribological conditions or a higher number of rolling cycles to maximise the chance of WSF forming.

Table 2.6.1: Estimated revolutions for wind turbine gearbox bearings operating for 60% of time due to standstills, maintenance, low wind conditions, etc.

Bearing type	**~Speed [rpm]**	**~No. revolutions (operating 60% of the time)**			
		~0.5 years	**~1 years**	**~2 years**	**~5 years**
High speed	1500	2.4E8	4.7E8	9.5E8	2.4E9
	500	7.9E7	1.6E8	3.2E8	7.9E8
Intermediate	300	4.7E7	9.5E7	1.9E8	4.7E8
	200	3.2E7	6.3E7	1.3E8	3.2E8
	100	1.6E7	3.2E7	6.3E7	1.6E8

Green = achievable cycles in lab for ~3 week transient test.

Black = unachievable cycle numbers for a reasonable duration RCF test.

Lubricant base and additives

Poly-α-olefins (PAO) are common base oils in wind turbine gearboxes and have therefore been targeted for use in this study. PAO-4 has been specifically identified as it has low viscosity that allows boundary and mixed lubrication regimes to be achieved in lab under moderate loads, sliding conditions and oil temperatures.

Literature suggests sulphur components in additives, such as EP and anti-corrosion sulfonates, may accelerate WSF due to sulphur acting as a ‘hydrogen poisoner’ by stopping hydrogen recombination to H_2 gas instead keeping hydrogen in the form of atoms/ions that diffuse into the steel surface (see Figure 2.4.6) [43, 53, 54, 172]. Therefore various additives such as anti-wear (AW), extreme pressure (EP) and anti-corrosion sulfonates have been identified in the aim of creating WECs.

Oil inlet temperature

In wind turbine gearboxes typical oil temperature ranges between 60 – 85 °C, with a minimum of ~20 °C and maximum of ~90 °C depending on environmental conditions. Therefore oil inlet temperatures between 50 – 90 °C have been identified for the testing in this study. Use of higher oil temperatures in the tests would lower the viscosity of the oil and result in reduction of film thickness between contacting surfaces. Increasing oil temperature may also allow for increased additive activation and tribochemical reactions that may increase the chance of forming WECs.

2.6.3 Hydrogen charged testing

The strategy adopted in this study was to conduct the non-hydrogen charged testing first to determine if WSF could be reproduced. If this proved to be unsuccessful, a hydrogen-charging technique would be used to investigate the sensitivity of WEC formation under the influence of diffusible hydrogen.

The hydrogen charging process aims to replicate hydrogen diffusion into a bearing by the mechanism of bulk hydrogen diffusion at wear induced nascent surfaces. In this mechanism the hydrogen is generated by tribochemical reactions of water contamination and decomposition of hydrocarbon lubricants through catalytic reactions [51]. The hydrogen ions released absorb at wear induced nascent surfaces and recombine with electrons to form atomic hydrogen [51, 56].

The concentration of diffusible hydrogen in the test rollers prior to RCF testing can be quantified. It was intended that the testing is this study use low to moderate diffusible hydrogen concentrations compared with previous investigations and that the levels could be thought of as realistic to those that may occur during wind turbine gearbox bearing operation.

This page is intentionally left blank

3. Materials, techniques and experimental methods

3.1 Introduction

The materials, techniques and experimental methods used in this study are detailed in this section. Firstly an overview of the TE-74S RCF test machine is given followed by the test conditions used. The method of hydrogen charging and analysis of the concentration of diffusible hydrogen in the test rollers is also presented. Analyses conducted to characterise the steel used to manufacture the test rollers and analyses of the final test rollers themselves is detailed. Subsequent to RCF testing a number of analysis methods have been used to characterise damage features created. The procedure of metallographic analysis of the test rollers by standard methods and serial sectioning is first overviewed followed by a description of the further advanced analysis conducted by focused ion beam (FIB), transmission electron microscopy (STEM/TEM) and 3D crack reconstruction. The thesis work flow chart is shown in Fig. 3.1.1.

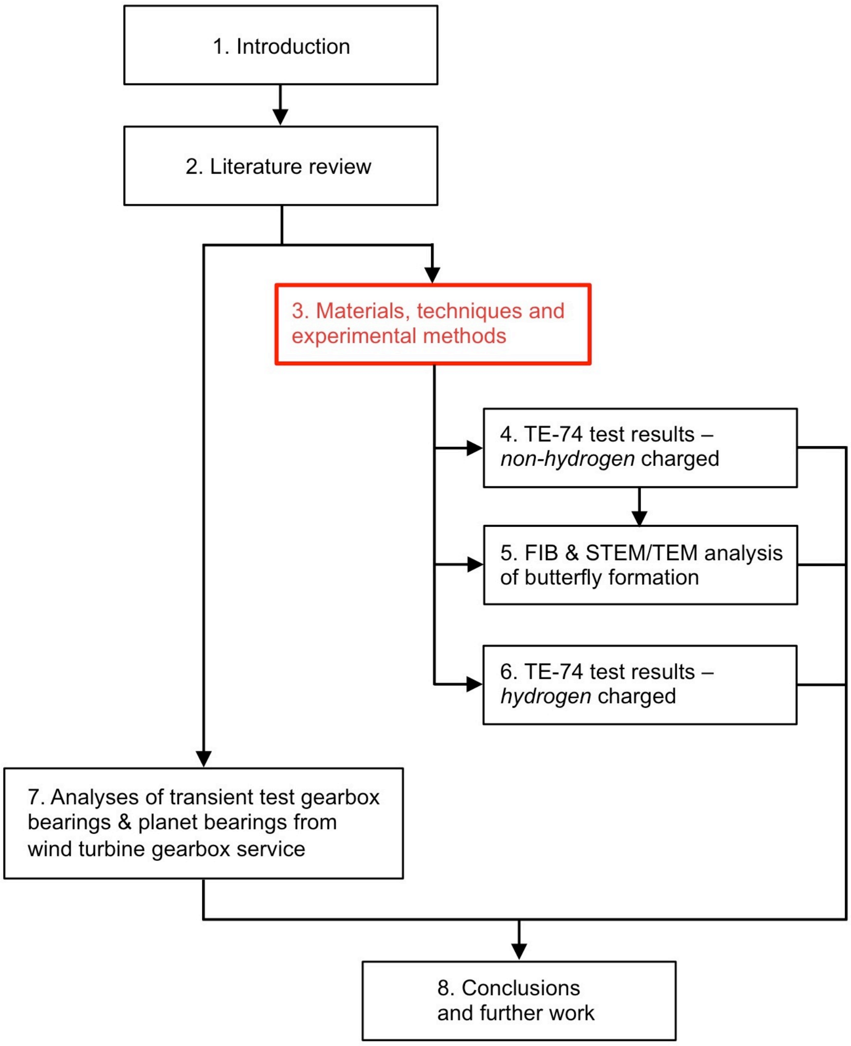

Figure 3.1.1: Thesis work flow chart.

3.2 TE-74S testing

3.2.1 TE-74S RCF test machine

The TE-74S two roller machine is a research machine for the study of wear and rolling contact fatigue of materials under conditions of pure rolling or rolling/sliding (0 – 100%), under point or line contact. This is a two motor machine with the test rollers simply supported through shafts between bearings. One of the motors provides the input power and the other absorbs the transmitted power. For control purposes, one drive is designated as master with the second drive deriving its speed set point, adjusted for the required slip ratio, from the master drive. The lower specimen shaft is carried in fixed bearings. The drive to the lower roller incorporates an in-line torque transducer for measuring the input torque to the system, thus the traction coefficient can be derived. Loading is achieved by a servo controlled pneumatic bellows actuator with force transducer feedback. A lubricant service module is fitted incorporating a sump tank with immersion heater (ambient up to 150 °C), delivery pump, scavenge pump and oil-to-water heat exchangers for cooling. The motors are A.C. powered by conventional vector drives allowing precise control of speed. The TE-74S (standard capacity) machine which this study uses incorporates two 5.5 kW motors (maximum master shaft speed 3000 rpm), a shaft centre distance of 40 mm and 12 kN loading system [185]. Fig. 3.2.1 shows the overall set-up of the TE-74S and Fig. 3.2.2 shows the test roller location in the load arm.

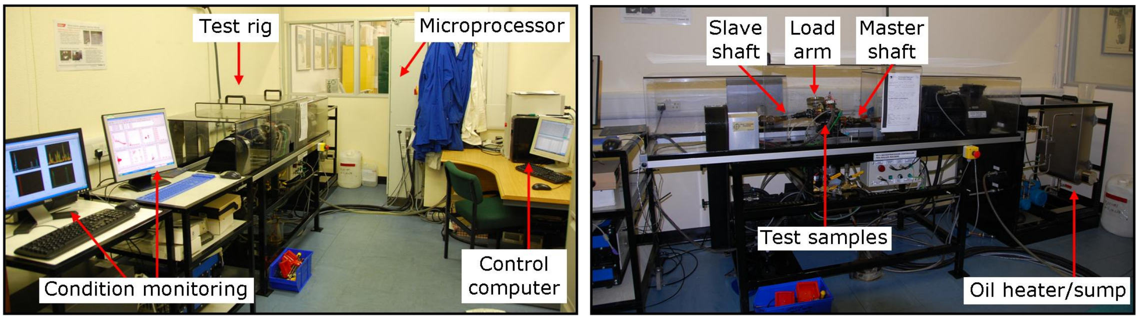

Figure 3.2.1: Overview of the TE-74S set-up.

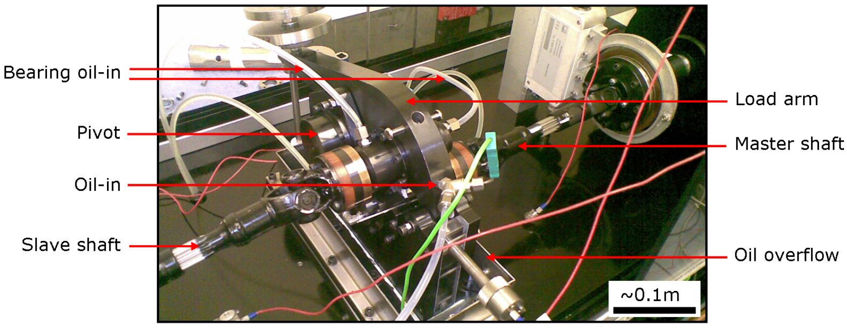

Figure 3.2.2: Close up view of the drive shafts and load arm. The rig is disassembled after each test and samples removed and replaced.

Various contact geometries are possible on the TE-74S depending on test requirements, e.g. if you desire one of the test rollers to be subjected to a higher number of rolling cycles and/or different contact geometrical conditions. In general two rollers are loaded against each other under controlled slide/roll conditions, while the lubricant oil is jetted at a constant rate flooding the contact. The oil is delivered on the entrainment side of the contact. The samples initially used in this study were 40v40 mm to enable rapid high load transients. A change in the design of the samples occurred after initial testing to 26v52 mm rollers crown-on-flat contact (see Fig. 3.2.3).

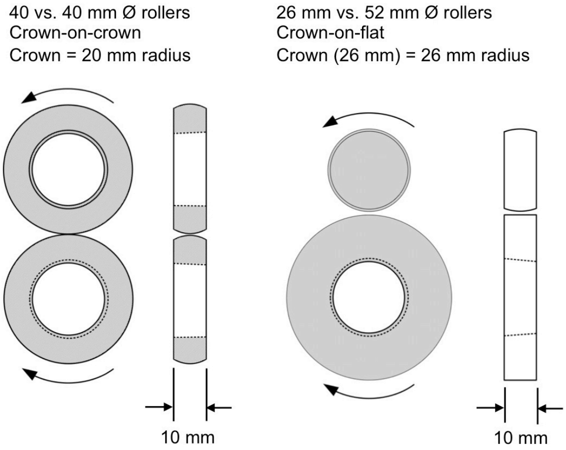

Figure 3.2.3: Sample geometries used in this study. Initially 40v40 mm samples were used. Later this changed to 26v52 mm.

A schematic of the TE-74S where the 26v52 mm rollers were used is shown in Fig. 3.2.4. In this case the upper roller (diameter 26 mm, 26 mm radius crown) has half the diameter of the lower (diameter 52 mm, flat) and each is driven independently. By using a 2:1 pulley on the shaft driving the 26 mm roller, pure rolling occurs in the contact with the smaller roller experiencing twice the number of stress cycles of the larger. This arrangement enables two stress cycle numbers to be achieved in a single RCF test.

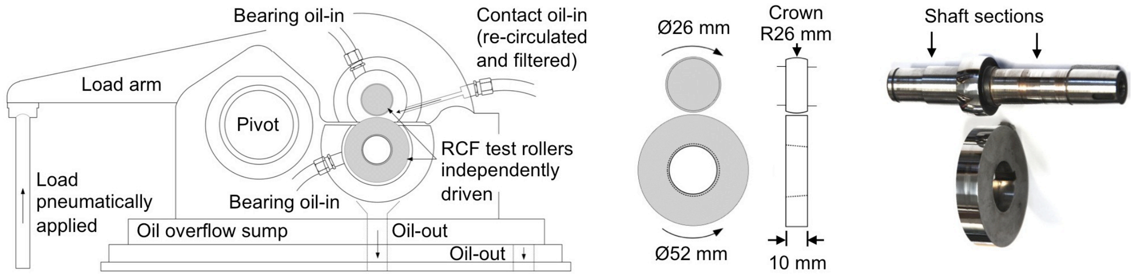

Figure 3.2.4: Plint TE-74S two-roller tribometer schematic showing 26v52 mm roller ratio used in the majority of RCF testing. See permissions [3.1] & [3.2].

The TE-74S has computer based sequence programmable control and data acquisition. This is provided by an integrated Serial Link Interface Module and Compend 2000 software running on a host PC. Data is stored to the hard disk in standard spread sheet compatible file formats. Tests are defined by a sequence of steps, each step containing set-point, data recording rates and alarm level information. Set-points may be adjusted by step change or ramp. The pre-programmed test sequence is followed unless interrupted by the operator or an alarm. Set-points may also be adjusted manually during testing [185]. Table 3.2.1 lists the TE-74S controlled and measured parameters.

Table 3.2.1: TE-74S controlled & measured parameters.

Controlled parameters	**Measured parameters**
Motor speed	Motor speed
Motor speed difference	Motor speed difference
Applied load	Applied load
Test fluid temperature	Transmitted torque
Test duration	Lubricant inlet temperature
	Test bath outlet temperature
	Vibration sensor output
	Electrical contact resistance

3.2.2 RCF testing phases and strategies to create WSF

The testing phases and strategies used in the aim of creating WSF in this study are overviewed in Fig. 3.2.5. In the following, the testing in each phase is detailed.

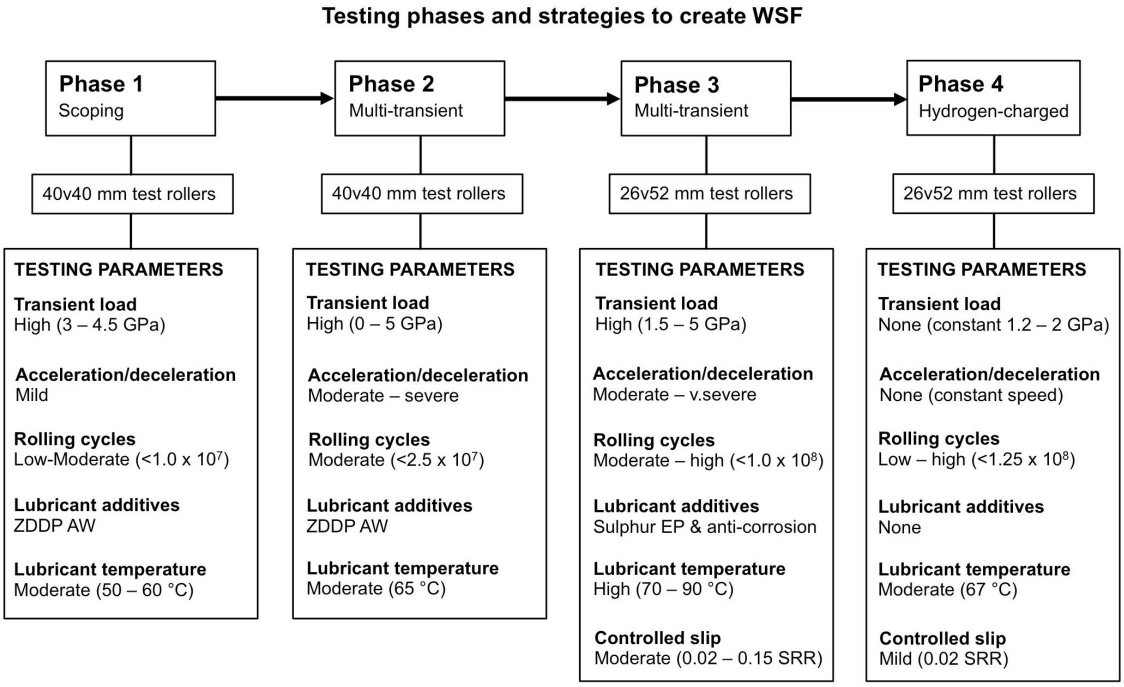

Figure 3.2.5: Testing phases and strategies used in the aim of creating WSF in this study.

3.2.3 Non-hydrogen charged RCF tests

Testing was conducted to investigate whether non-hydrogen charged tests would enable the formation of butterflies, WECs and WSF. The conditions used were constant high load, transient loading, rapid loading, slip and rapid acceleration-deceleration. The strategy behind use of these conditions is detailed in section 2.6 in chapter 2. These tests were aimed at replicating wind turbine transient conditions.

Overview

Phase 1 & 2: 10 tests were initially carried out using the original manufacturer's design of 40v40 mm rollers under a variety of conditions. These tests were exploratory experiments to scope the TE-74S's operating capabilities and feasibility of generating WECs.

Phase 3: Subsequently the roller design was changed to the 26v52 mm ratio due to a manufacturing flaw that was discovered with the 40v40 mm rollers (see chapter 4). 7 tests were conducted using a variety of severe conditions. Tests 1b – 5b used the smooth surface finish rollers and Tests 6b* and 7b* the rough surface finish rollers (see section 3.3).

A summary of the 17 non-hydrogen charged RCF tests is shown in Table 3.2.2. In tests 1a – 10a the slave speed/cycles concerns the upper 40 mm roller and in tests 1b – 7b the slave speed/cycles concerns the 26 mm roller.

Table 3.2.2: Non-hydrogen charged RCF tests.

Test	Test type	Pmax [GPa]	Slave speed [rpm]	Slave cycles [rpm]	Base oil	Additives	Oil temp [°C]
40v40 mm tests (Phase 1/2)							
1a	Speed transient	4	0 – 2970	5.9E6	PAO-4	ZDDP AW	52
2a	Load transient	3 – 4.5	2970	5.0E6	PAO-4	ZDDP AW	50
3a	Constant	3	2970	10.0E6	PAO-4	ZDDP AW	60
4a	Load transient	3 – 4	2970	10.0E6	PAO-4	ZDDP AW	60
5a	Constant	3	2970	10.0E6	PAO-4	ZDDP AW	60
6a	Load transient	3 – 4.5	2970	10.0E6	PAO-4	ZDDP AW	60
7a	Load/speed/slip transient	0 – 5	0 – 2970	9.8E6	PAO-4	ZDDP AW	65
8a	Load/speed/slip transient	0 – 5	0 – 2970	0.5E6	PAO-4	ZDDP AW	65
9a	Load/speed/slip transient	0 – 5	0 – 2970	25.0E6	PAO-4	ZDDP AW	65
10a	Load/speed/slip transient	0 – 5	0 – 2970	14.0E6	PAO-4	ZDDP AW	65
26v52 mm tests (Phase 3)							
1b	Load/speed/slip transient	2 – 5	0 – 6000	42.0E6	PAO-4	Sulphide EP	70/90^{+}
2b	Load/slip transient	2 – 5	6000	26.0E6	PAO-4	Sulphide EP	70
3b	Load transient	2 – 5	0 – 6000	75.0E6	PAO-4	Sulphide EP	70
4b	Constant slip	4	3000	25.0E6	PAO-4	Sulphide EP	77
5b	Constant slip	2	480	10.0E6	PAO-4	Mo EP/AW + Ca S	70
6b*	Load/speed/slip transient	1.2 – 4	200 – 5000	50.0E6	PAO-4	Mo EP/AW + Ca S	70
7b*	Speed/slip transient	2	100 – 6000	100.0E6	PAO	Mo EP/AW + Ba/Na/Ca S	90

PAO-4 base additives: Sulphide EP is type dialkyl polysulphide, Mo EP/AW is type molybdenum dithiocarbamate at 1 wt.%, Ca S is corrosion inhibitor calcium sulfonate at 2 wt.%.

PAO base additives: Mo EP/AW is type molybdenum dithiocarbamate, Ba/Na/Ca S is corrosion inhibitors barium, sodium and calcium sulfonate.

* Rough surface finish rollers.

+: The first 24 hours of the test used an inlet oil temperature of 90 °C, this being dropped to 70 °C for the remainder of the test.

Base oil and additives in tests 1a – 10a and 1b – 6b* supplied by Lubrizol.

RCF testing conditions

40v40 mm tests (phase 1 & 2): Fig. 3.2.6 highlights phase 1 & 2 testing and the detailed conditions used in these non-hydrogen charged 40v40 mm tests are shown in Table 3.2.3.

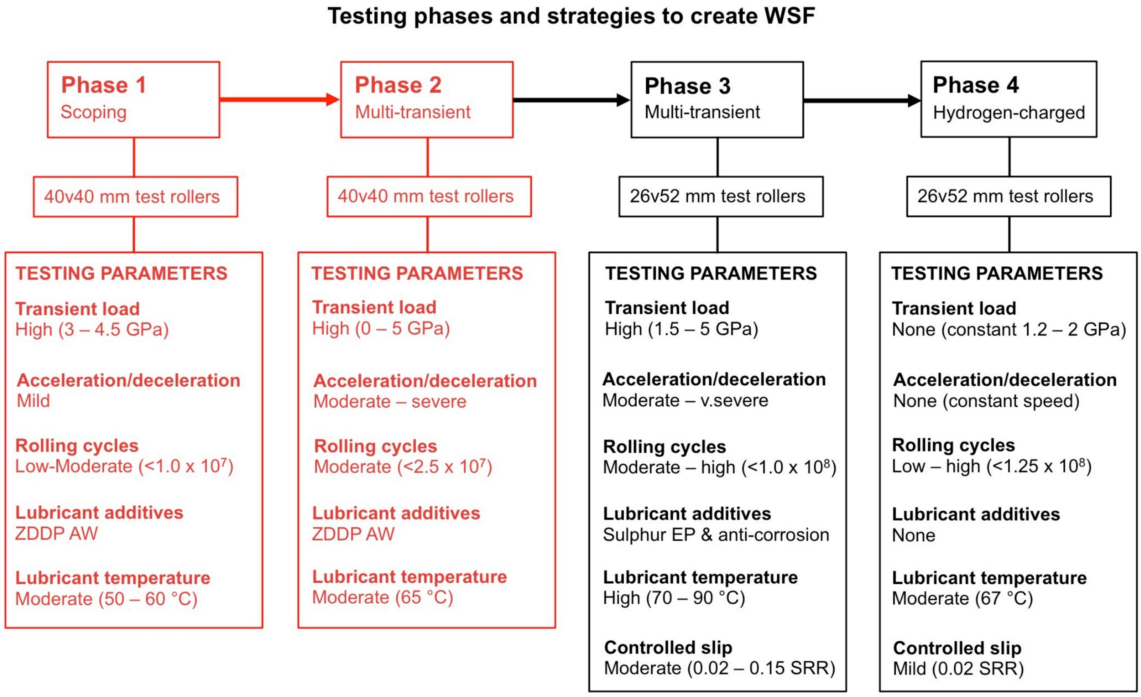

Figure 3.2.6: Phase 1 & 2 testing

Tests were either carried out under pure rolling conditions (slave shaft disengaged, tests 1 – 6) or transient conditions with slip in the contact (slave shaft engaged, tests 7a – 10a). In tests 7a – 10a uncontrolled slip occurred on the acceleration-deceleration transients. The lubricant used in the tests was PAO-4 base oil with ZDDP anti-wear (AW) additive and the inlet temperature varied between 50 – 65 °C. Tests 1a, 2a, 4a and 6a – 10a are looped to enable transient conditions. For example in test 10a, a whole transient cycle lasts 215 seconds (steps 2 – 11). The tests did not run continuously, only running during the daytime.

Table 3.2.3: Details of non-hydrogen charged 40v40 mm RCF tests.

♯	Step type	Next step	Step time [s]	P_{max} [GPa]	Speed [rpm]	Rolling cycles
40v40 mm – Test 1a						
1	Run-in	2	1800	3.0	2970	$5.9x10^6$
2	Base	3	300	4.0	2970	371 loops
3	Deceleration	4	25	4.0	0	38 hours
4	Standstill	5	10	4.0	0	
5	Acceleration	3	25	4.0	2970	
40v40 mm – Test 2a						
1	Run-in	2	1800	3.0	2970	$5.0x10^6$
2	Base	3	30	3.0	2970	2204 loops
3	Load transient	2	15	4.5	2970	28 hours
40v40 mm – Test 3a						
1	Run-in	2	1800	3.0	2970	$10x10^6$
2	Constant	-		3.0	2970	56 hours
40v40 mm – Test 4a						
1	Run-in	2	1800	3.0	2970	$10x10^6$
2	Base	3	300	3.0	2970	315 loops
3	Load transient	2	15	4.0	2970	28 hours
40v40 mm – Test 5a						
1	Run-in	2	1800	3.0	2970	$10x10^6$
2	Constant	-		3.0	2970	56 hours
40v40 mm – Test 6a						
1	Run-in	2	1800	3.0	2970	$10x10^6$
2	Base	3	30	3.0	2970	4450 loops
3	Load transient	2	15	4.5	2970	56 hours
40v40 mm – Test 7a						
1	Run-in	2	1800	3.0	2970	$9.8x10^6$
2	Low speed base	3	60	3.0	1500	1190 loops
3	Acceleration + load	4	5	5.0	2970	72 hours
4	Deceleration + load	5	5	3.0	1500	
5	Base	6	60	3.0	2970	
6	Deceleration	7	5	3.0	0	
7	Standstill	8	5	3.0	0	
8	Acceleration	9	5	3.0	2970	
9	Base	10	60	3.0	2970	
10	No load	11	5	0	2970	
11	Load transient	2	5	5.0	2970	
40v40 mm – Test 8a						
Same as Test 7						$0.5x10^6$ 50 loops 3.5 hours
40v40 mm – Test 9a						
Same as Test 7						$25x10^6$ 3050 loops 183 hours
40v40 mm – Test 10a						
1	Run-in	2	1800	1.5	2970	$14x10^6$
2	Low speed base	3	60	1.5	1500	1700 loops
3	Acceleration + load	4	5	5.0	2970	102 hours
4	Deceleration + load	5	5	1.5	1500	
5	Base	6	60	1.5	2970	
6	Deceleration	7	5	1.5	0	
7	Standstill	8	5	1.5	0	
8	Acceleration	9	5	1.5	2970	
9	Base	10	60	1.5	2970	
10	No load	11	5	0	2970	
11	Load transient	2	5	5.0	2970	

26v52 mm tests (phase 3): Fig. 3.2.7 highlights phase 3 testing and the detailed test conditions used in the non-hydrogen charged 26v52 mm tests are shown in Table 3.2.4.

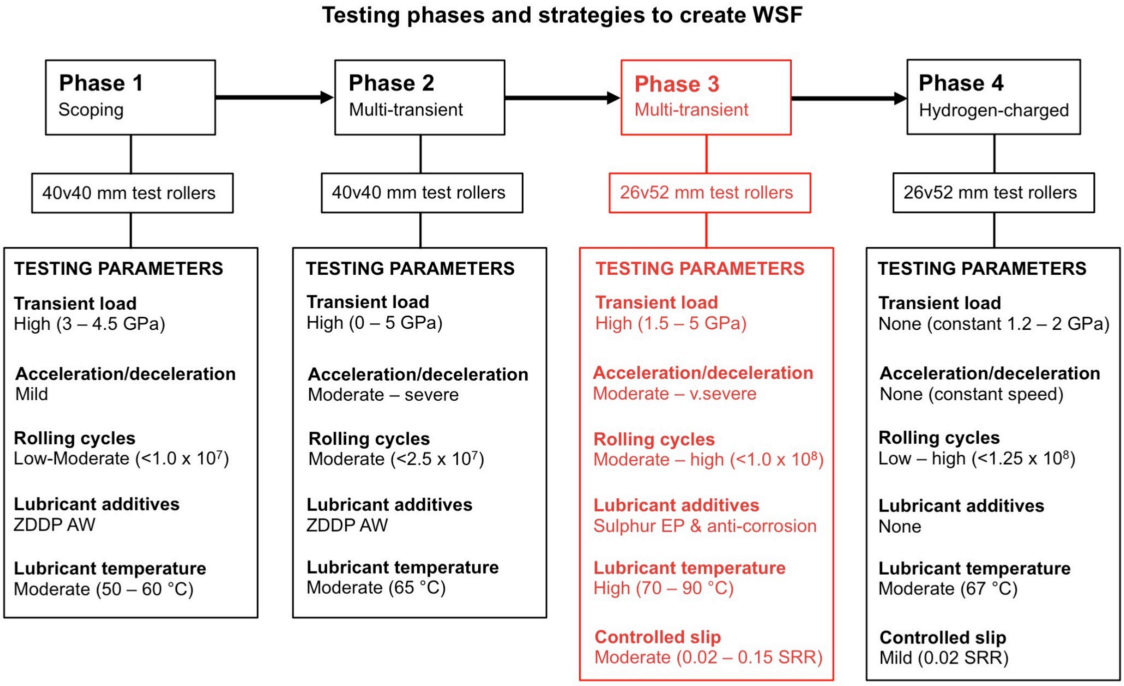

Figure 3.2.7: Phase 3 testing.

The base oil used in all the tests was PAO. Two different lubricant additives were used in the PAO-4 oil in tests 1b – 6b*, the first being a sulphide EP and the second being a mix of Mo EP/AW + corrosion inhibitor Ca S. The oil used in test 7b* was Total Transmission TI75W80 automotive gearbox oil. This oil is PAO based with additives Mo EP/AW + corrosion inhibitors Ba/Na/Ca S. The oil inlet temperatures varied between 70 – 90 °C depending on the test. Ramp time refers to the time taken to complete the parameter change in each step. CoF refers to the coefficient of friction recorded during the test where average and maximum values are detailed. Various degrees of traction between the rollers are experienced at different times in the test cycles. To enable a controlled slip portion in some of the tests, each roller is driven independently allowing for controlled slide-roll ratios. The SRR is calculated using Eq. (3.2.1).

$$SRR = 2(U1-U2)/(U1+U2) \tag{3.2.1}$$

U1 and U2 are the surface speeds of the two rollers (U1 = 26 mm roller, U2 = 52 mm roller) respectively. Stribeck calibration tests were performed to deduce the rotational speed and slip level where traction coefficient was highest. This information partly determined the testing conditions used. During the controlled slip portions in tests 1b, 2b and 4b the 26 mm roller experienced traction force in the opposite direction of rolling (positive slip), while the 52 mm roller experienced traction force in the direction of rolling (negative slip). On the other hand the opposite occurred in tests 5b – 7b. Tests 1b, 2b, 3b, 6b* and 7b* are looped to enable transient conditions. For example in test 1b, a whole transient cycle lasts 48.4 seconds (steps 2 – 8). Test 7b* is also looped, however two distinct programmes are utilised with a manual change over each day. In programme 1x – 4x the slave shaft is disengaged to allow high cycle speeds and accumulation of a large number of rolling cycles. In programme 1y – 4y the slave shaft is engaged to allow a slip portion. Programme 1y – 4y runs approximately 8 hours per day and programme 1x – 4x the remainder of the time. Time between the change over between programme (x) and (y) was less than 15 minutes. Tests 2b and 3b were ended prematurely from a slave shaft and oil feed pump failure respectively. Contrary to the 40v40 mm tests, the 26v52 mm tests ran continuously (apart from test 7b* with the 15 minute change overs between programme (x) and (y)).

Table 3.2.4: Details of non-hydrogen charged 26v52 mm RCF tests.

♯	Step type	Next step	Step time [s]	Ramp time [s]	P_{max} [GPa]	52 mm [rpm]	26 mm [rpm]	26 mm cycles	CoF – μ (avg), [max]
26v52 mm – Test 1b									
1	Run-in	2	1800	-	2.0	3000	6000	42x10^{6} cycles	-
2	Base	3	5	1	2.0	3000	6000	13250 loops	(0.02),[0.1]
3	Load transient	4	3.4	3	5.0	3000	6000	160 hours	[0.075]
4	Base	5	5	-	2.0	3000	6000		(0.02),[0.1]
5	Deceleration	6	10	5	2.0	0	0		[0.06]
6	Standstill	7	5	-	2.0	0	0		-
7	Acceleration	8	10	5	2.0	3000	6000		[0.08]
8	Slip (0.05 SRR)	2	10	1	2.0	2857	6000		(0.03)
26v52 mm – Test 2b									
1	Run-in	2	1800	-	2.0	3000	6000	26x10^{6} cycles	-
2	Base	3	5	1	2.0	3000	6000	14500 loops	(0.02)
3	Load transient	4	3.4	3	5.0	3000	6000	75 hours	[0.07]
4	Base	5	5	-	2.0	3000	6000		(0.02)
5	Slip (0.15 SRR)	2	5	1	2.0	2608	6000		[0.025]
26v52 mm – Test 3b									
1	Run-in	2	1800	-	2.0	3000	6000	75x10^{6} cycles	-
2	Base	3	15	-	2.0	3000	6000	41666 loops	(0.025)
3	Load transient	2	3	3	5.0	3000	6000	208 hours	[0.025]
26v52 mm – Test 4b									
1	Run-in	2	1800	-	2.0	1500	3000	26x10^{6} cycles	-
2	Slip (0.15 SRR)	-	-	-	4.0	1304	3000	12 hours	(0.004)
26v52 mm – Test 5b									
1	Run-in	2	1800	-	2.0	250	480	10x10^{6} cycles	
2	Slip (0.04 SRR)	-	-	-	2.0	250	480	336 hours	(0.08),[0.11]
26v52 mm – Test 6b*									
1	Run-in	2	1800	-	2.0	1500	3000	50x10^{6} cycles	-
2	Load	3	20	20	4.0	2500	5000	7500 loops	(0.015)
3	Base	4	40	1	2.0	2500	5000	229 hours	(0.02)
4	Deceleration	5	15	15	2.0	100	200		[0.1]
5	Slip (0.05 SRR)	6	15	1,1	1.5	100	190		[0.25]
6	Acceleration	7	15	15	2.0	2500	5000		(0.09)
7	Base	2	5	-	2.0	2500	5000		(0.02)
26v52 mm – Test 7b*									
1	Run-in	2a	1800	-	2.0	3000	6000	99x10^{6} cycles	-
1x	Base	3a	120	-	2.0	3000	6000	(x) 6260 loops	(0.015)
2x	Deceleration	4a	15	15	2.0	50	100	(y) 5904 loops	-
3x	Low speed	5a	60	-	2.0	50	100	610 hours	(0.01)
4x	Acceleration	2a	15	15	2.0	3000	6000		-
1y	Base	2b	60	-	2.0	1500	3000		(0.01)
2y	Deceleration	3b	15	15	2.0	53	100		-
3y	Slip (0.02 SRR)	4b	60	-	2.0	53	100		(0.08),[0.1]
4y	Acceleration	2b	15	15	2.0	1500	3000		-

Oil film thickness calculations

The minimum oil film thickness (h_{min}) between the rollers was calculated using Hamrock-Dowson viscous-elastic calculation [186], see Eq. (3.2.2).

$$h_{min} = 3.63U^{0.68}G^{0.49}W^{-0.073}(1 - e^{-0.68k}) \qquad (3.2.2)$$

where,

U: dimensionless speed parameter, $u\eta_0/(E'R)$
G: dimensionless material parameter, $\alpha E'$
W: dimensionless load parameter, $N/(E'R^2)$
u: mean lubricant entrainment speed [m/s]
η_0: viscosity at atmospheric pressure of lubricant [Pa s]
E': effective elastic modulus [Pa]
R': reduced radius of curvature [m]
α: pressure–viscosity coefficient [Pa^{-1}]
N: normal load [N]
k: ellipticity parameter, (a/b)
a: semi-major axis of the contact ellipse [m]
b: semi-minor axis of the contact ellipse [m]

The initial lambda ratio (λ) was then calculated using Eq. (3.2.3), where $R_{q,1}$ and $R_{q,2}$ are the rms roughness values of the two contact surfaces.

$$\lambda = h_{min} / (R_{q,1}^2 + R_{q,2}^2)^{1/2} \qquad (3.2.3)$$

PAO-4 oil tests: PAO-4 oil has viscosity of 4 cSt at 100°C and 16.8 cSt at 40°C, giving a viscosity index of 122 (~0.007 Pa s at 90 °C and ~0.012 Pa s at 70 °C). PAO-4 pressure viscosity coefficient, α = 12.8 GPa^{-1}. Table 3.2.5 and Table 3.2.6 show the calculated oil film thicknesses and lambda ratios at pure rolling conditions for the 40v40 mm and 26v52 mm tests respectively. A range of load and speeds are detailed to give an impression of the predicted lubrication regimes during the various testing conditions.

Table 3.2.5: 40v40 mm test oil film thickness calculations. Pure rolling, base oil PAO-4, oil temperature 60 °C.

Rotation speed (40 mm)	rpm	10	50	100	500	1500	3000
Linear velocity (40 mm)	m/s	0.02	0.10	0.21	1.05	3.14	6.22
Smooth surface finish							
P_{max} 3 GPa							
Minimum film thickness	µm	0.00	0.00	0.01	0.03	0.07	0.12
Lambda ratio, λ		0.11	0.33	0.52	1.56	3.30	5.30
P_{max} 5 GPa							
Minimum film thickness	µm	0.00	0.00	0.01	0.03	0.07	0.10
Lambda ratio, λ		0.10	0.30	0.47	1.40	3.00	4.72

Table 3.2.6: 26v52 mm test oil film thickness calculations. Pure rolling, base oil PAO-4, oil temperature 70 °C.

Rotation speed (26 mm)	rpm	100	500	1000	1500	3000	6000
Rotation speed (52 mm)	rpm	50	250	500	750	1500	3000
Linear velocity (26 mm)	m/s	0.14	0.68	1.36	2.04	4.08	8.17
Linear velocity (52 mm)	m/s	0.14	0.68	1.36	2.04	4.08	8.17
Smooth surface finish							
P_{max} 2 GPa							
Minimum film thickness	µm	0.01	0.04	0.06	0.08	0.16	0.22
Lambda ratio, λ		0.60	1.80	2.90	3.80	7.41	9.80
P_{max} 5 GPa							
Minimum film thickness	µm	0.01	0.03	0.05	0.07	0.13	0.18
Lambda ratio, λ		0.50	1.48	2.36	3.11	6.10	8.00
Rough surface finish							
P_{max} 2 GPa							
Minimum film thickness	µm	0.01	0.04	0.06	0.08	0.16	0.22
Lambda ratio, λ		0.08	0.22	0.36	0.47	0.92	1.21
P_{max} 5 GPa							
Minimum film thickness	µm	0.01	0.03	0.05	0.07	0.13	0.18
Lambda ratio, λ		0.06	0.18	0.30	0.40	0.75	1.00

It can be seen that for the 40v40 mm and 26v52 mm tests with a smooth surface finish that mixed lubrications regimes ($\lambda<3$) only occur when the rotational speed is below ~1000 rpm. EHD conditions will be experienced anything above this in pure rolling, thus the large majority of the tests are running in EHD for most of the test duration. Boundary lubrication ($\lambda<1$) will be experienced at the lower speed portions of acceleration/deceleration transients in tests. On the contrary with the 26v52 mm rollers with a rough surface finish, either a mixed/EHD or boundary lubrication regime occurs for the range of test speeds. Even though the contact surfaces will smooth during rolling contact, the 26v52 mm tests with a rough surface finish can be assumed to be more tribochemically active due to higher percentages of time spent in lubrication regimes where asperity contact occurs (boundary/mixed).

Total Transmission TI75W80 tests: Total Transmission TI75W80 oil has viscosity of 9.5 cSt at 100°C and 64 cSt at 40°C, giving a viscosity index of 124 (~0.018 Pa s at 90 °C). The pressure viscosity coefficient, α at 90 °C is ~8 GPa^{-1}. Table 3.2.7 show the calculated oil film thicknesses and lambda ratios at pure rolling conditions for 26v52 mm test 7b. The calculations show that boundary lubrication regimes are expected for the low-speed portions of the test and mixed/EHD regimes for the high-speed portions.

Table 3.2.7: 26v52 mm test oil film thickness calculations. Pure rolling, Total Transmission TI75W80, oil temperature 90 °C.

Rotation speed (26 mm)	rpm	100	500	1000	1500	3000	6000
Rotation speed (52 mm)	rpm	50	250	500	750	1500	3000
Linear velocity (26 mm)	m/s	0.14	0.68	1.36	2.04	4.08	8.17
Linear velocity (52 mm)	m/s	0.14	0.68	1.36	2.04	4.08	8.17
Rough surface finish							
P_{max} 2 GPa							
Minimum film thickness	µm	0.01	0.04	0.07	0.09	0.19	0.23
Lambda ratio, λ		0.08	0.23	0.38	0.50	1.08	1.27

Shear stress calculations

Since the shear stresses in the steel are important to RCF and WSF, the magnitudes and depths of the maximum subsurface orthogonal shear stress ($\tau_{o,max}$) and unidirectional shear stress (τ_{max}) under the maximum contact pressures of 1.2 – 5 GPa are calculated using the equations in references [96, 99, 187-189] for pure rolling conditions (see Table 3.2.8 and Appendix). These have been calculated for the 26v52 mm rollers only due to the 40v40 mm tests not having created butterfly/WEC damage features. The values are indicative only as traction in the contact can also affect the shear stresses and depth, e.g. the higher the traction the higher the magnitudes of the subsurface shear stresses and proximity to the contact surface.

Table 3.2.8: Theoretical shear stresses in the 26v52 mm rollers during RCF for pure rolling.

P_{max} [GPa]	**Normal load [N]**	**Semi-major axis [µm]**	**Semi-minor axis [µm]**	**τ_{max} [MPa]**	**Depth τ_{max} [µm]**	**$\tau_{o,max}$ [MPa]**	**Depth $\tau_{o,max}$ [µm]**
5.0	10390	1420	700	1650	446	1090	267
2.0	665	570	280	660	178	436	107
1.5	280	430	210	495	134	327	80
1.2	135	335	164	388	105	256	63

τ_max = maximum unidirectional shear stress acting at ± 45° with respect to the surface.

τo,max = maximum orthogonal shear stress acting parallel and normal with respect to the surface.

Assumes elastic bodies, no surface roughness and no traction in the contact.

3.2.4 Hydrogen charged RCF tests

Overview

A number of RCF tests with hydrogen charged rollers have been carried out in phase 4 of the testing as shown in Fig. 3.2.8. In the following, the procedure of hydrogen charging the test rollers, quantifying the concentration of diffusible hydrogen in the rollers and RCF test conditions used are detailed.

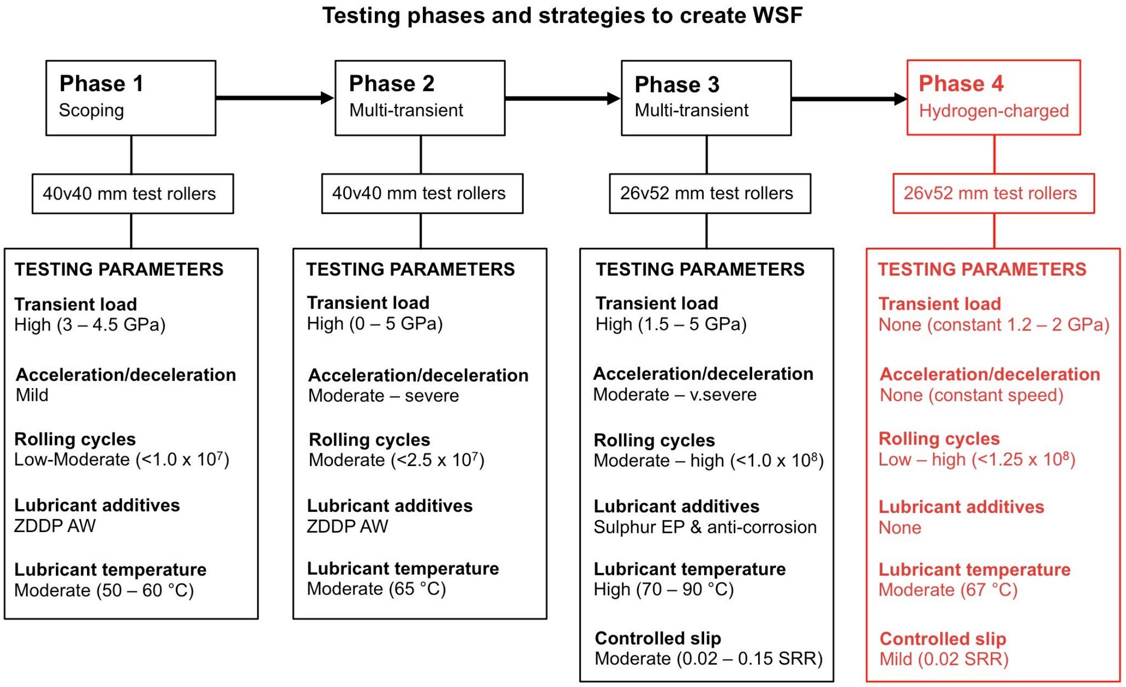

Figure 3.2.8: Phase 4 testing.

Hydrogen charging and diffusible hydrogen concentration analysis

The RCF test rollers were charged with hydrogen by immersion in aqueous solutions of NH_4SCN at 50 °C for 48 hours [37, 38, 149, 150, 190] prior to RCF testing. The concentration of diffusible hydrogen at the subsurface zone beneath the contact surface (1 mm depth) introduced by this process is expected to be near-uniform following simple calculations by Fick's laws, however local variation at non-metallic inclusions and microstructural discontinuities is possible [150, 153, 156-158]. To quantify the concentration of diffusible hydrogen in the rollers, thermal desorption analysis (TDA) has been carried out at 400 °C for 20 minutes. The temperature was restricted to 400 °C as WSF is believed to be related to the diffusible hydrogen in the steel [5, 32, 36, 42, 50, 53, 150, 152, 153, 190]. Hydrogen detection levels during measurements conducted in this study indicated that all diffusible hydrogen was removed within the sensitivity of the instrument in 20 minutes. During TDA over 20 minutes, a double-peaked profile of detected hydrogen was observed for all TDA experiments and this indicates how hydrogen is trapped (e.g. lattice or non-metallic inclusions) [150].

Since a large number of parameters can affect the TDA results on the concentration of hydrogen measured, strict measures have been taken to minimise errors. The important parameters are the heating method (rate, duration, upper temperature), geometry of specimens (surface exposed to charge medium), time to start of TDA (length of time samples are held at room temperature before TDA or before freezing), freezing method (LIN or dry ice), specimen surface preparation (removal of contaminants such as moisture, oxide layers and lubricant residue) and precision of TDA instruments (resolution, calibration and minimum hydrogen detection limits).

In this study, TDA was carried out on both model and real test rollers under various charging and effusion conditions. This is to determine the concentration of diffusible hydrogen and to explore links between this and the concentration of NH_4SCN for hydrogen charging as well as the effusion time. Model disc specimens were used as the majority of the hydrogen concentration measurement specimens to save cost. These were manufactured using the same steel as the actual test rollers, where the differences between the model and actual 26 mm test rollers are that the model specimens only have a 7 mm shaft length on a single side (as opposed to a full shaft on either side as shown in Fig. 3.2.4), and the model specimens have no crown. In all cases the surface area of specimens/rollers exposed to the charge medium was ~0.01 m^2. A few real RCF test rollers (prior and post RCF testing) were also analysed for comparison.

To prepare rollers for a RCF test, the rollers were ultrasonically cleaned after being removed from the NH_4SCN solution then the test surfaces were slightly buffed to remove the thin corrosion layer. The time lapsed between the finish of the charging and the start of RCF testing was approximately 1.5 hours.

For TDA, some specimens were immersed in LIN straight after charging and cleaning (i.e. 0 effusion hours). Other charged specimens are kept in test oil at 50 °C for various durations before being cleaned and immersed in LIN to evaluate how much hydrogen will effuse from the charged specimens over time. This is to simulate the concentration of diffusible hydrogen in the real test rollers during RCF testing. In general the time taken for specimens and test rollers to move from hydrogen charging/oil effusion to LIN immersion was ~15 minutes. A control model 26 mm specimen was also analysed without any hydrogen charging. The test rollers from two RCF tests (tests 8H and 9H) were also analysed post-test. This was conducted, as there are some differences in the RCF test conditions that could affect the concentration of diffusible hydrogen from that of the predictions gained from the model specimens. These post RCF test rollers were removed from the TE-74S test rig and immersed in LIN within 30 minutes of the test ending.

Both the model specimens and RCF test rollers were cut into smaller sections prior to TDA to fit into the analyser. To minimise hydrogen loss, the cutting process was kept at <20 seconds.

Prior to TDA all the sample surfaces were lightly blasted with Alumina grit for <30 seconds to remove contaminants and the oxide layer.

The TDA was performed using a Bruker G4 Phoenix DH utilizing the carrier gas hot extraction method. The analyser is equipped with a rapid infrared-heated clamshell furnace with a 30 mm diameter quartz tube as the specimen chamber. During heating the evolved hydrogen from the specimen is detected by a sensitive and long-term stable thermal conductivity detector (TCD). The minimum concentration of hydrogen measurable by the analyser is 0.05 ppm and the precision is ±0.05 ppm.

RCF testing conditions

A number of RCF tests with hydrogen charged rollers have been carried out. The lubricant used in the tests was PAO-4 base oil and the inlet temperature to the contact was 67 °C. Details of the RCF tests discussed are summarised in Table 3.2.9.

Table 3.2.9: Details of RCF tests (phase 4 testing).

Test	**26 mm [rpm]**	**52 mm [rpm]**	**SRR**	**Traction coefficient**	**P_{max} [GPa]**	**26 mm [cycles]**	**52 mm [cycles]**	**Time [h]**
20 wt.% NH_4SCN hydrogen charge								
1H	4000	2040	0.02	0.042	2.0	70 x 10^6	36 x 10^6	295
2H	4000	2000	0	0.008	2.0	50 x 10^6	25 x 10^6	208
3H	4000	2040	0.02	0.047	2.0	36 x 10^6	19 x 10^6	152
4H	4000	2000	0	0.009	2.0	7.5 x 10^6	3.8 x 10^6	31
5H	4000	2000	0	0.008	2.0	1.0 x 10^6	0.5 x 10^6	4.2
6H	4000	2000	0	0.022	1.5	50 x 10^6	25 x 10^6	208
7H	4000	2000	0	0.028	1.2	50 x 10^6	25 x 10^6	208
8 wt.% NH_4SCN hydrogen charge								
8H	4000	2000	0	0.008	2.0	50 x 10^6	25 x 10^6	208
5 wt.% NH_4SCN hydrogen charge								
9H	4000	2000	0	0.008	2.0	50 x 10^6	25 x 10^6	208
2.5 wt.% NH_4SCN hydrogen charge								
10H	4000	2000	0	0.008	2.0	125 x 10^6	65 x 10^6	465
1 wt.% NH_4SCN hydrogen charge								
11H	4000	2040	0.02	0.031	2.0	125 x 10^6	65 x 10^6	465
12H	4000	2000	0	0.007	2.0	50 x 10^6	25 x 10^6	208

See permission [3.1].

The traction coefficient is an average value recorded during the tests. The maximum contact pressure in the tests was maintained below 2 GPa. A controlled slide-to-roll ratio (SRR) of 0.02 was induced for two of the tests (tests 1H and 3H) to simulate slip occurring between rolling elements and the raceway in certain types of bearings. During tests 1H and 3H with slip in the contact, the 26 mm roller experiences traction force in the direction of rolling (negative slip), while the 52 mm roller experiences traction force in the opposite direction of rolling (positive slip). Compared with the pure rolling tests, these two tests have experienced higher traction between the contact. The minimum oil film thickness (h_{min}) between the rollers was calculated using Hamrock-Dowson viscous-elastic calculation [186], see section 3.2.3. Considering the variation in surface roughness of the rollers pre- and post- hydrogen charging (see section 3.3.3), the relevant minimum film thickness and initial lambda ratios are calculated under various contact pressures. Since the initial lambda ratios for all the tests was between 1.5 - 3.8, mixed/EHD lubrication is expected for all the hydrogen charged RCF tests conducted in this study (see Table 3.2.10). The magnitudes and depths of the maximum subsurface orthogonal shear stress ($\tau_{o,max}$) and unidirectional shear stress (τ_{max}) under the maximum contact pressures of 2 GPa, 1.5 GPa and 1.2 GPa are shown in Table 3.2.8).

Table 3.2.10: Minimum film thickness (h_{min}) and lambda ratio (λ) calculations for the RCF tests.

Parameter	**P_{max} = 2 GPa (1 wt.% – 20 wt.% charges)**	**P_{max} = 1.5 GPa (20 wt.% charge)**	**P_{max} = 1.2 GPa (20 wt.% charge)**
h_{min} [μm]	0.160	0.174	0.183
Lambda (λ)	1.5 – 1.8	1.5 – 3.1	1.9 – 3.8

3.3 Test roller material characterisation

3.3.1 TE-74S test roller steel type

The RCF test rollers were machined from standard 100Cr6 bearing steel bar that was austenitised at 850 ºC and quenched in oil, followed by 2X 1-hour tempering stages at 180 ºC. The chemical composition of the 26v52 mm roller steel had been determined using an optical emission spectrometer (measured by the Dr. Sommer Werkstofftechnik GmbH lab). The elements carbon and sulphur were determined using combustion analysis and the elements oxygen and hydrogen were determined using melting extraction analysis. The total residual (irreversibly trapped) hydrogen concentration in the rollers post manufacture and prior to hydrogen charging was 0.7 ppm (26 mm roller) and 0.6 ppm (52 mm roller), which are moderate levels for bearing steel. The results are shown in Table 3.3.1.

The microstructure consists of a homogeneous distribution of primary spherical carbides (M_3C) from austenitization and ε-carbides precipitated during tempering in a matrix of martensite. The 26v52 mm as-machined test rollers were analysed using X-ray diffraction analysis to determine the retained austenite content on a Bruker AXS D8 Advanced using MoK_α radiation. The measurements were taken at the core of the sample away from the contact surface. The X-ray diffraction analysis on the as-machined 26v52 mm test rollers revealed the retained austenite to be 15.8 wt.% in the 26 mm roller and 17.7 wt.% in the 52 mm roller. Four hardness measurements were made and averaged for each test roller to give 62.2 ± 0.7 HRC (26 mm roller) and 61.9 ± 0.7 HRC (52 mm roller) according to the DIN EN ISO 6508-1, method M2. These are comparable with bearing steels typically ranging from 58 – 62 HRC.

Table 3.3.1: Chemical composition of the test roller material, wt.%.

Roller	**C**	**Si**	**Mn**	**P**	**S**	**Cr**	**Mo**	**Al**	**Ca**	**Ti**	**O**
26 mm	1.02	0.30	0.30	0.013	0.005	1.45	0.03	0.036	0.0009	0.0015	0.0012
52 mm	1.05	0.29	0.37	0.017	0.008	1.54	0.01	0.028	0.0018	0.0014	0.0010

See permission [3.1] & [3.2] & [3.3].

3.3.2 TE-74S test roller steel cleanliness

The cleanliness of the steel used for the RCF test rollers was analysed by the Dr. Sommer Werkstofftechnik GmbH lab using ISO 4967-B and ASTM E2283-08 standards, which measure the density of inclusions and maximum inclusion lengths respectively.

In the ISO 4967-B standard [87], fields of view at magnifications of 100X with viewable areas of 0.5 mm^2 are compared to pre-determined charts in the standard and particular severity indexes given to the inclusions present. Titanium carbonitrides (Ti(C,N)) were also recorded in the steel as counts and the length of these inclusions grouped into bands for simplicity. As shown in Table 3.3.2 both rollers contain large numbers of sulfide type A inclusions, small numbers of globular oxide type D/DS & Ti(C,N) inclusions and very few aluminate type B & silicate type C inclusions. The global cleanliness index (C_i) was found to be 30.4 (26 mm roller) and 43.8 (52 mm roller) inferring that the 52 mm roller is about 44% dirtier than the 26 mm roller. However the type A fine inclusions have caused the higher C_i in the 52 mm roller. As the minimum inclusion size rating for recording of type A inclusions is 37 μm for index 0.5, any type A inclusions less than 37 μm length are not recorded. In the metallographic examination by serial sectioning conducted in this study it was observed that many short length sulfides with oxide encapsulation (Duplicates) existed in steel, hence there will have been many type A inclusions that were not recorded in the cleanliness standard.

Table 3.3.2: Steel cleanliness data based on the ISO 4967-B standard.

Field	**A**		**B**		**C**		**D**		**DS**	**Ti(C,N)**	
	Fine	Thick	Fine	Thick	Fine	Thick	Fine	Thick	Count	Length (μm)	Count
26 mm roller											
0.5	141	162	7	1	1	-	15	70	23	0-5	-
1	30	28	3	-	-	-	-	3	3	5-10	2
1.5	-	3	-	-	-	-	-	-	-	10-15	12
2	-	-	-	-	-	-	-	-	-	15-20	16
2.5	-	-	-	-	-	-	-	-	-	20-25	4
3	-	-	-	-	-	-	-	-	-	25-30	3
i_{total}	100.5	113.5	6.5	0.5	0.5	-	7.5	38	14.5	30-50	1
i_{mean}	0.058	0.066	0.004	0.000	0.000	-	0.004	0.022	0.008	50-150	1
No. fields = 1720, Area = 932 mm^2											
C_i, global cleanliness index = 30.4											
52 mm roller											
0.5	276	128	-	-	-	-	9	23	7	0-5	1
1	88	23	-	-	-	1	-	-	1	5-10	1
1.5	13	3	-	-	-	-	-	-	-	10-15	4
2	-	1	-	-	-	-	-	-	-	15-20	5
2.5	-	-	-	-	-	-	-	-	-	20-25	1
3	-	-	-	-	-	-	-	-	-	25-30	-
i_{total}	245.5	93.5	-	-	-	1	4.5	11.5	4.5	30-50	-
i_{mean}	0.157	0.060	-	-	-	0.000	0.003	0.007	0.003	50-150	-
No. fields = 1569, Area = 848 mm^2											
C_i, global cleanliness index = 43.8											

Group A (sulfide type), group B (aluminate type), group C (silicate type), group D (globular type, usually oxide), group DS (single globular type with diameter ≥ 13 μm) and group Ti(C,N) (titanium carbonitrides).

i_total = total index for each inclusion type.

i_mean = mean index for each inclusion type.

Ci, global cleanliness index, is calculated using the suggested weighting factor as described in the standard.

Ti(C,N) inclusions were also recorded and grouped in bands of inclusion lengths for simplicity, and were not included in the global cleanliness index.

See permission [3.1] & [3.2].

The ASTM 2283-08 standard [88] uses a methodology to statistically characterise the distribution of the largest indigenous non-metallic inclusions in steel specimens based upon quantitative metallographic measurements. Six sections from the steel of about 150 mm^2 are polished four times to give 24 measurements over an area of about 900 mm^2. The maximum inclusion length for each inclusion type is recorded for each field to give 24 data points. These data points can then be plotted on a graph of reduced variate from -2 to +3 (this corresponds to a probability range of inclusion lengths from 0.87% through 95%) versus maximum inclusion length. Estimation of the parameters of the extreme value distribution has been conducted by the maximum likelihood method. Statistical analysis has been used for non-exogenous inclusions only to predict the maximum inclusion length/diameter for a much larger area of steel (150,000 mm^2). The processed and simplified data from the ASTM E2283-08 standard can be viewed in Fig. 3.3.1.

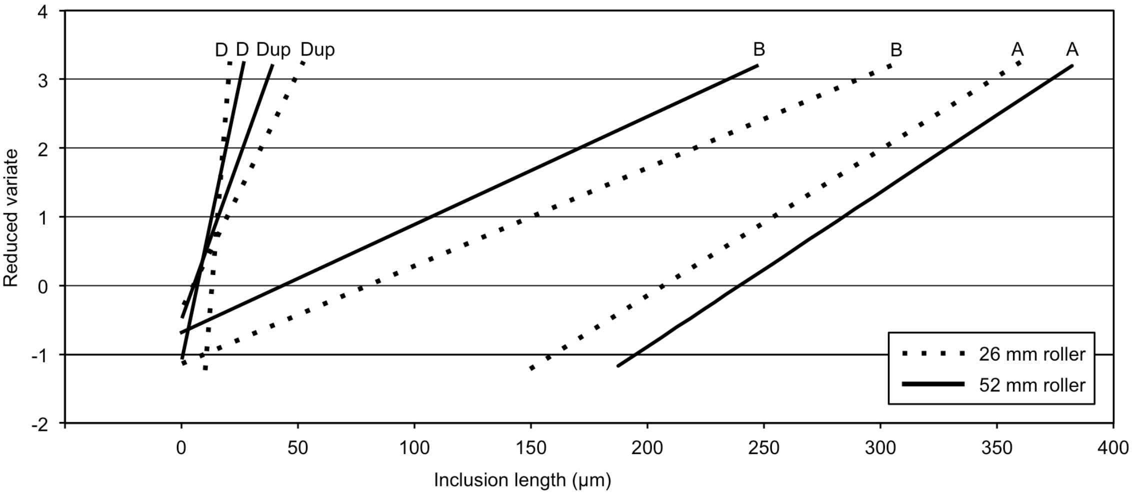

Figure 3.3.1: ASTM E2283-08 maximum inclusion length or diameter data for the 26 mm and 52 mm rollers. Only lines of best fit are shown with data points removed for clarity. Type A, B, D/DS and Duplicate (Dup) are displayed. Type Dup inclusion has one outlier at the position of maximum inclusion length for both rollers. See permission [3.2].

The graph plots the lines of best fit from the 24 maximum inclusion lengths recorded over the 24 fields. In some fields, no inclusions of a particular type were measured, these are designated values of zero as per the standard, hence the B, D and Dup lines of best fit in the graph meet the zero value on the x-axis. The Dup single maximum inclusion lengths were outliers in the data (see standard). Table 3.3.3 shows the ASTM E2283-08 maximum inclusion length estimations for non-exogenous inclusion types A, B and D/DS. The estimations of the maximum lengths of pure sulfide inclusions was ~500 µm, sulfide + oxide inclusions ~50 µm and diameter of globular oxide inclusions ~25 – 50 µm. SE is the standard error for any inclusion of length X.

Table 3.3.3: ASTM E2283-08 maximum inclusion length estimations for type A, B and D/DS.

Type	**L_{max} [µm]**		**SE(x) of L_{max}**		**Characteristic size of maximum inclusion**
	26 mm	52 mm	26 mm	52 mm	
A	531.93	547.40	56.25	52.78	No difference
B	567.87	484.09	84.00	75.61	No difference
D/DS	29.02	49.25	2.97	7.29	52 mm roller > 26 mm roller

See permission [3.2].

It is important to make a distinction in terms of probability for crack initiation at inclusions between large rolling element bearings that have extremely large volumes of steel subject to RCF and the test rollers used in this study that have relatively small steel volumes subject to RCF. This is because large bearings have a much higher probability of critical (size, composition, etc.) inclusions being located in highly stressed zones. The cleanliness of wind turbine gearbox bearings analysed with the ISO 4967-B standard are reported in chapter 7. The global cleanliness indexes (C_i) of two wind turbine gearbox bearings were found to be approximately 10 – 20, which is lower than that of the test roller steel in this study (C_i ~30 – 45). However there are limitations recording of small/short length inclusions, so this does not confirm that the wind turbine gearbox bearings are cleaner than the test roller steel. Because larger bearings have a much higher volume of steel under critical stresses, it is reasonable to suggest that crack initiation at inclusions is more likely to occur in larger bearings.

The direction in which the inclusion length is elongated (i.e., the hot deformation direction of the 100Cr6 bar which was used to manufacture the rollers) is in the axial direction for the test rollers (transverse to direction of travel). Bearings in wind turbine gearboxes can either have inclusion elongation in the axial direction (rings are hot deformed during production in the axial direction), in the circumferential direction (ring rolling hot deformation in the circumferential direction) or with no definitive elongation direction (deformation in both directions during different stages or manufacture). The difference in direction of inclusion elongation, and therefore whether the inclusion elongation is aligned in direction of travel, may be influential in crack initiation.

3.3.3 TE-74S test roller surface roughness

Surface roughness analysis was performed on the contact surfaces of the rollers using a Talysurf 120L profilometer. An evaluation length of 3 mm and a cut-off of 0.8 or 0.25 were selected depending on the roughness judged by an initial run. Measurements were taken in the direction of travel of the rollers.

Smooth surface finish rollers

The average surface roughness of the as-machined 40v40 mm smooth surface finish rollers was R_a 0.012 µm and R_q 0.015 µm. Table 3.3.4 shows the average roughness of the 26v52 mm smooth surface finish rollers in the as-machined condition prior to RCF testing.

Table 3.3.4: Surface roughness of the 26v52 mm smooth surface finish rollers.

Type	**Roughness (26 mm roller)**		**Roughness (52 mm roller)**	
	R_a [µm]	**R_q [µm]**	**R_a [µm]**	**R_q [µm]**
Pre RCF test	0.014	0.017	0.011	0.014

Rough surface finish rollers

Table 3.3.5 shows the average roughness of the rough surface finish rollers in the as-machined condition and the roughness ranges after the rollers were hydrogen charged. The range of surface roughnesses only reflects variability and not a relationship between differing concentrations of hydrogen charge.

It can be seen that for both rollers the surface roughness has reduced after hydrogen charging. This is thought to be due to smoothing of asperities from the hydrogen charging corrosion process and the formation of a corrosion layer that partially filled the valleys between asperities. Close examination of the roller surfaces showed that the hydrogen charging process did not introduce any surface cracking or degradation that could act as crack initiation points. Previous studies also showed that NH_4SCN hydrogen charging introduces minimal changes in surface condition [190] and that the reduction in fatigue life in RCF tests is due to the presence of diffusible hydrogen in the steel rather than a change in the surface condition [37].

Table 3.3.5: Surface roughness of the 26v52 mm rough surface finish rollers before and after hydrogen charging.

Type	Roughness (26 mm roller)		Roughness (52 mm roller)	
	R_a [µm]	**R_q [µm]**	**R_a [µm]**	**R_q [µm]**
Pre hydrogen charge	0.07	0.09	0.12	0.15
Post hydrogen charge	0.03 – 0.06	0.04 – 0.08	0.03 – 0.06	0.04 – 0.08

See permission [3.1].

3.3.4 TE-74S test roller residual stress analysis

Residual stress depth profiles measurements on the as-machined 26v52 mm rough surface finish rollers were taken to determine any near surface residual stresses present from heat treatment and surface finishing. These were measured using a thin tube collimator (Ø 0.6 mm) at the rollers center of contact. Measurements were also taken after RCF testing on certain 52 mm rollers at the center and edge of the wear track and these were measured using a polycapillary collimator (spot size ~0.3 mm). In both cases depth profiles were performed up to 0.3 mm depth. Measurements were performed by Stresstech using a Stresstech Oy XSTRESS3000 diffractometer and material removal was made by electropolishing.

The residual stress profiles on the as-machined 26v52 mm rough surface finish rollers are shown in Fig. 3.3.2. Full width half maximum (FWHM) values are also given. Both rollers have tensile residual stresses (negative values) immediately at the surface, however the 52 mm roller has higher magnitudes in both the circumferential and axial direction respectively, and remain high through depth. The residual stresses for both rollers then display minor fluctuations with depth.

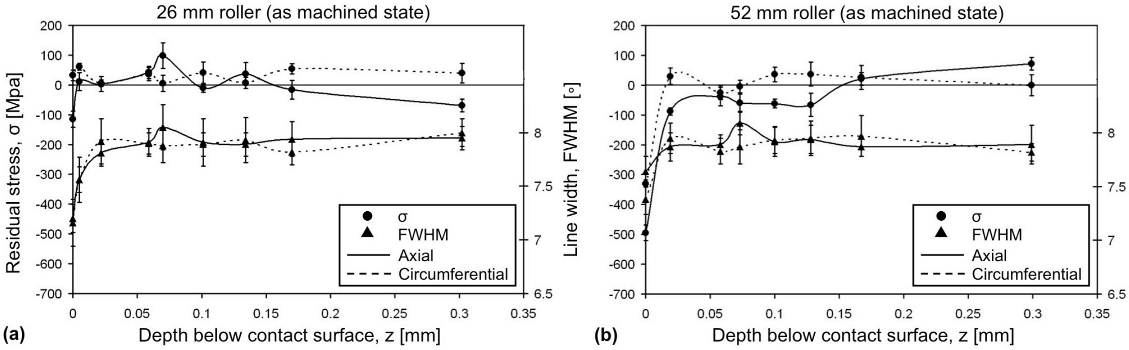

Figure 3.3.2: Residual stresses, σ and FWHM values in (a) the rough surface finish 26 mm rollers and (b) the rough surface finish 52 mm rollers in the as machined state. See permission [3.2].

3.4 Metallographic analysis

3.4.1 Introduction

Following RCF testing the rollers were cleaned and stored in a cool, dry place until required. Optical microscopy or SEM analysis of the wear tracks was used to determine surface damage features. Subsequently the rollers were cut using various methods to enable metallographic analysis. Cutting was performed on a circular disc-cutting machine using diamond cutting discs. There are two directions that can be used to examine the cross section of samples. These are either circumferentially or axially. When cutting a circumferential section, sections can be viewed either at the exact centre of the wear track or a position offset from the centre (see Fig. 3.4.1). It is assumed that the highest probability of subsurface damage occurs at the centre of contact and in small zones either side. When cutting an axial section, it does not make any consequence where the cut is made across the sample circumference, only that a fair representation of the roller is analysed (e.g. 1 section from each of the rollers four quadrants), in case any certain section of the steel has an increased number of non-metallic inclusions than other areas. Following cutting, test roller sections were mounted in bakelite to enable multiple automatic grinding, or to enable samples to be held by hand for manual grinding. Grinding and polishing was conducted using two different systems, either using SiC grit papers or diamond discs and suspensions. Struers Labo-Force 3 and Buehler Metaserv Motopol 8 polishing machines were used.

SiC grit paper grinding and polishing: Grinding using 120 grit grade was used to ensure samples were plane and that the correct area of interest was gained. Polishing was then performed using SiC grit grades 400, 800, 1200, 2500 and 4000 until a mirror finish was obtained.

Diamond grinding and polishing: Grinding was conducted on diamond grinding discs at 120 equivalent grit grade. Polishing was then performed on 1200 equivalent grit grade diamond grinding discs, followed by polishing with diamond suspensions at 9 μm and 3 μm on the specific pads and cloths.

After the polishing stage, samples were viewed by optical microscopy in the as-polished condition. Samples were then etched with nital (2% Nitric acid in ethanol) to reveal microstructural features, such as DER and WEA. A magnification of 200X was used to scan the area of interest, followed by 500/1000X magnifications to analyse any features in detail.

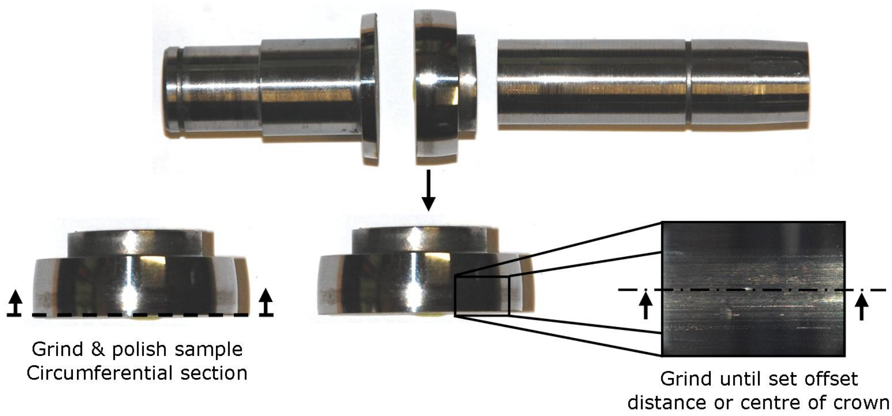

Figure 3.4.1: Example of circumferential cut in 26 mm roller.

3.4.2 Standard metallographic analysis

Standard metallographic analysis has been used as the first step for determining the formation of damage features in the test rollers. After each RCF test, small sections were cut from the rollers and these were then cut to expose a plane parallel to the direction of travel and hot mounted in 30 mm diameter bakelite resin mounts. By standard grinding and polishing, circumferential cross-sectional planes offset at distances of 0.5 mm and 0.25 mm and 0 mm from the centre of the wear track were analysed.

3.4.3 Serial sectioning analysis

To conduct an in-depth investigation of the formation of butterflies and WEA/WECs in the test rollers and map these subsurface damage features in 3D a serial sectioning process was used. The process involves fine grinding and polishing of sections of the rollers at ~3 μm or ~5 μm material removal intervals in the circumferential plane. Polished cross-section surfaces are etched with Nital 2% solution before being examined with optical microscopy and select features by SEM/EDS.

The serial sectioning procedure was established by macro indentation across the circumference of the steel bearing cross sections. The Vickers pyramid indent depth is ~1/7th of the length of the pyramid diagonal, therefore a process of imaging the indent, polishing, then subsequent imaging and measuring the change in diagonal length enables an accurate method for assessing material removal.

Sectioning in the circumferential direction gives a higher likelihood of observing inclusions interacting with the white etching features. This is because some inclusion types (e.g. sulfides) are elongated in the axial direction from manufacture. If sectioning in the axial direction, the length of sulfides inclusions in the direction of material removal may only be a few μm, hence inclusion-WEC interactions could be easily missed between slices. The Vickers indentation was also used on the exposed face of the cross section to provide reference markers to track white etching features over multiple slices. Optically imaging at set magnifications of 100X or 200X with tracking markers allowed for subsequent image alignment.

After each RCF test, small sections were cut from the rollers measuring approximately 15 mm chord length (see Fig. 4.3.2 and Fig. 4.3.3). These small roller sections were then cut to expose a plane parallel to the direction of travel and hot mounted in 30 mm diameter bakelite resin mounts. Two different serial sectioning analysis investigations have been conducted and these are explained in the following:

Full wear zone analysis: For the 52 mm roller section of test 3H the cross section cut was made circumferentially at a distance of about 0.1 mm from the edge of the wear track (see Fig. 3.4.2). At a plane still offset from the edge of the wear track, grinding at ~20 – 50 μm material removal intervals was begun to find the first viewable WECs outer most edge. As soon as the first WEC was viewed, the serial sectioning process at ~5 μm material removal intervals was begun to track the WECs orientation and location through the volume of the steel. Any further WECs that appeared were also mapped in the same way. The process continued until no WECs were visible which corresponded to about 300 slices.

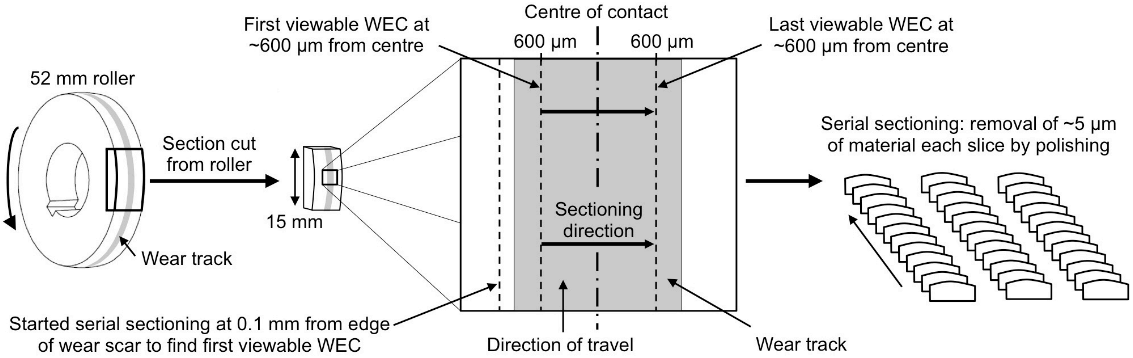

Figure 3.4.2: Full wear zone serial sectioning analysis. See permission [3.2].

Partial wear zone analysis: The length for polishing was either 300 µm or 100 µm offset from the centre of the wear track depending on the amount of white etching features observed (see Fig. 3.4.3). Multiple sections of the rollers from tests 9H – 11H have been analysed to check the uniformity of the white etching features formed around the whole test roller.

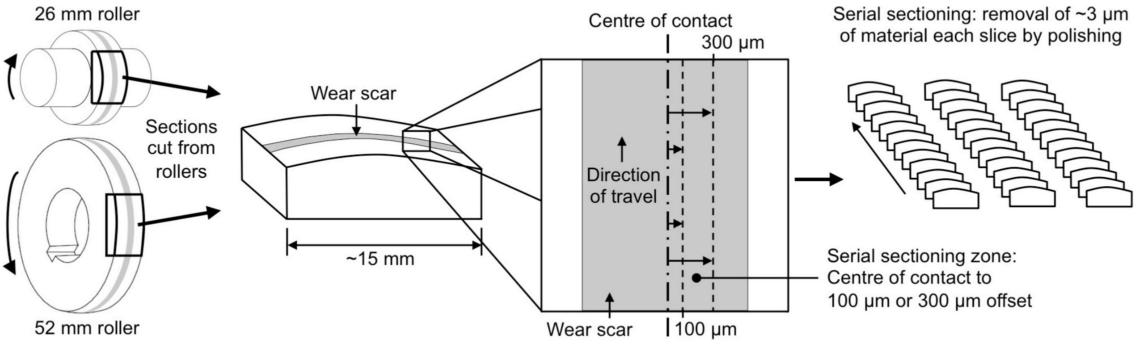

Figure 3.4.3: Partial wear zone serial sectioning analysis. See permission [3.1].

3.4.4 Optical microscopy

An Olympus BH2 microscope was used for the analysis in this study. Images were obtained with magnifications between 50X to 1000X. Manual aperture control was used.

3.4.5 Scanning electron microscopy and energy dispersive spectrography (EDS)

A JEOL JSM-6500F SEM has been used in this study as the next stage of microstructural characterisation after optical microscopy. The energy dispersive spectrography has been conducted using Oxford Inca 300 that is combined to the SEM system. An accelerating voltage of 15 kV was used.

3.5 Focused ion beam (FIB)

3.5.1 Introduction

Two different dual-beam FIB-SEM instruments have been used for in-depth microstructural analysis in this study. In a dual-beam FIB-SEM, both an electron column (SEM) and gallium ion column (FIB) are incorporated into the same machine. This allows cross-section sample preparation using the ion beam to mill material away normal to the surface whilst the electron beam enables viewing of the cross sectional face (see Fig. 3.5.1). An image can also be created using the secondary ions from the FIB source, which can give much greater contrast that the electron image. As the milling from the ion beam can be viewed in real-time by the electron beam, the ion milling can be stopped when the feature of interest is reached [191]. The slice and view technique has been used in this study to build up a sequence of images to model 3D crack reconstructions as detailed in section 3.7.

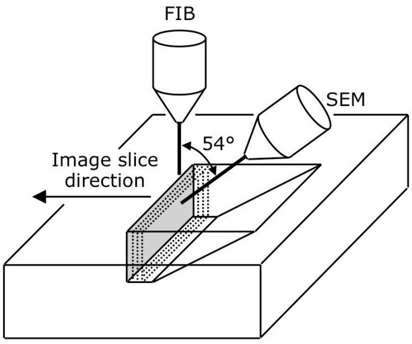

Figure 3.5.1: Schematic of a dual-beam FIB-SEM system.

3.5.2 FIB investigation 1: butterfly (chapter 5)

A Zeiss NVision 40 CrossBeam FIB was used to generate 3D tomographical images at a selected butterfly crack. The first step was deposition of a 1 μm thick layer of carbon for surface protection from ion damage when sputtering (Fig. 3.5.2a). The carbon layer was marked with fiducial markers for when image slices were subsequently aligned in a stack for 3D reconstruction (Fig. 3.5.2b). Material surrounding the butterfly was removed by milling at an accelerated voltage of 30 kV and a current of 3 nA. Slices from within the butterfly were subsequently sputtered at a lower beam current of 300 pA to expose the tip of the butterfly crack. Secondary electron images were taken at 54° to the specimen surface at regular intervals during sputtering, resulting in over 50 slices at approximately 350 nm slice thickness being captured up to the centre at the void (Fig. 3.5.2d). Gallium ion beam images were also captured at select locations.

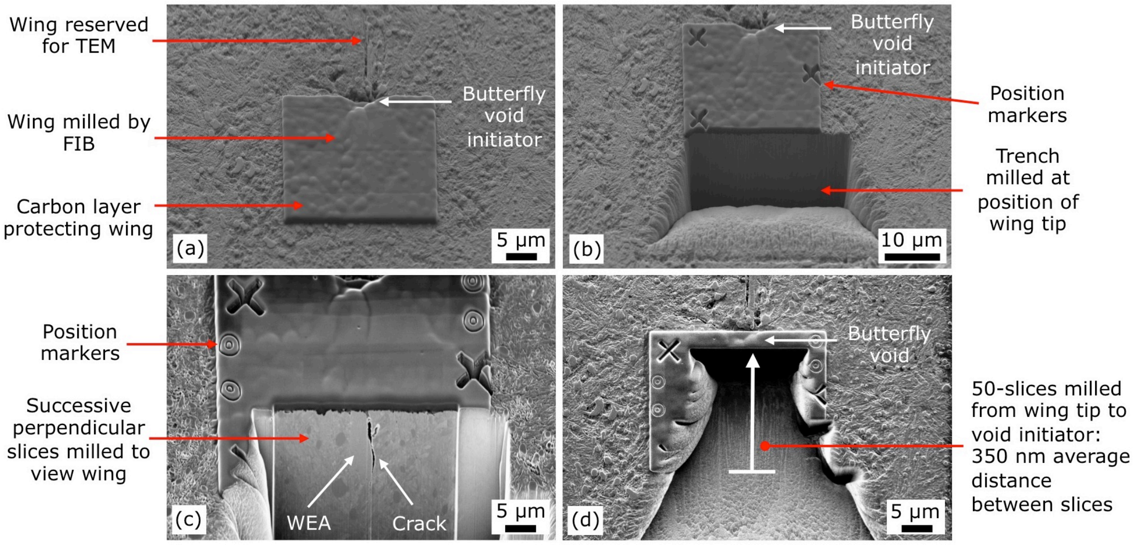

Figure 3.5.2: Process of FIB tomography. (a) 1 µm carbon deposition layer on the butterfly wing. (b) Milling of alignment markers and a trench. (c) Subsequent milling and imaging of slices. (d) 50 slices milled from butterfly tip to void centre, with an average 350 µm distance between slices.

FIB was also used to remove a cross-sectional lamella for TEM analysis from the remaining butterfly wing (Fig. 3.5.3). Deposition of a 1 µm thick layer of carbon for surface protection was again used. The lamella was attached to a copper grid with carbon deposition and final thinning of the lamella conducted using a beam current of 150 pA and 80 pA to give a thickness of ~50 – 100 nm.

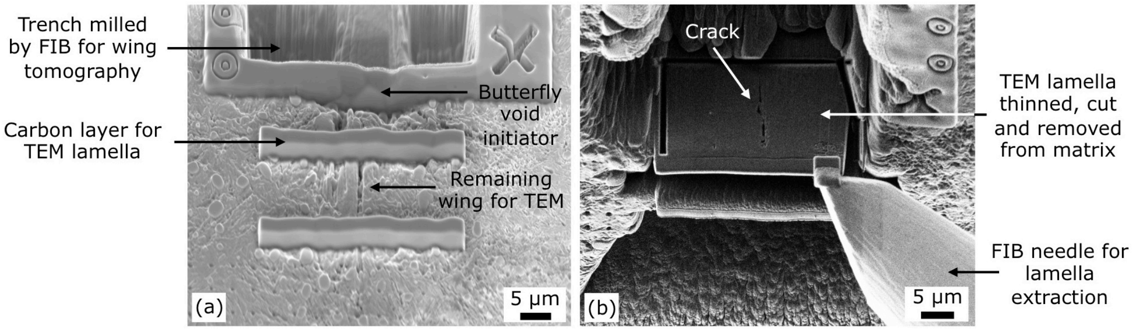

Figure 3.5.3: FIB process for TEM lamella removal. (a) Carbon deposition strips on butterfly wing. (b) Cutting and removal of the lamella for placement on a copper grid for TEM analysis.

3.5.3 FIB investigation 2: inclusion-WEC interaction (chapter 7)

A Zeiss Auriga 60 FIB-SEM was used to generate 3D tomographical images at a selected inclusion-WEC interaction. The sample was tilted by 54° so that the cross-sectional face prepared by standard metallography was perpendicular to the ion beam to allow perpendicular milling. Platinum deposition was used to reduce curtaining artefacts. After rough milling the cross section was polished with a low beam of 30 kV: 4 nA until almost all milling artefacts had been removed and the microstructure over an area 40 µm wide by about 15 µm below the cross section surface was visible. 30 nm thick slices were then milled with a 30 kV: 1 nA beam and images were taken every third slice using the InLens secondary electron detector at 3 kV: 10 nA. The FIB tomography model in this study therefore have an effective slice thickness of 90 nm and ~400 slice images were obtained. Images were acquired with tilt correction.

3.6 Transmission electron microscopy (STEM/TEM)

Scanning transmission electron microscopy (STEM) using the Zeiss NVission system was conducted on a thinned lamella using 30 kV and a combination of bright and dark field imaging modes. Transmission electron microscopy (TEM) using model Joel 3010 and EDS using Oxford Inca 100 at 300 kV using a double axis tilt holder has been used in this study for the highest in-depth microstructural characterisation. As electrons pass through the thin specimen, they are separated into those that pass through unaffected (called direct beam) and those that are scattered by some angle. Therefore a non-uniform distribution of electrons emerge from the exit of the specimen, where this non-uniform scattering contains all the structural, chemical and other information about the material [192]. TEM is able to display the non-uniform distribution of scattered electrons in two ways, by either spatial distribution which is observed as contrast in images, or by angular distribution of scattering, which is viewed as diffraction patterns.

3.7 3D crack reconstruction

Several 3D crack reconstructions have been conducted in this study to aid understanding of crack formation. The different procedures and software used are detailed in the following.

3.7.1 WEC network 3D reconstruction

A 3D model of a WEC was created from the images obtained during the serial sectioning process. The optical microscopy images at 200X magnification were aligned to form a stack of images using Photoshop CS3. The image stack was imported into Aviso 6.3 software and the crack + WEA segmented at each slice manually using a stylus on a touch screen tablet. 3D models were subsequently constructed using Aviso 6.3 and VGStudio MAX software. The Z resolution was set at 5 μm to represent the approximate slice thickness. Animations of the 3D models were constructed utilising a combination of the in-built functions in modelling software's and Image J.

3.7.2 FIB butterfly and inclusion-WEC 3D crack reconstruction

Two 3D crack reconstruction models have been made from the tomographical images obtained during the two FIB milling investigations.

FIB investigation 1 – butterfly: Once the milling and imaging of all 50 slices was completed, the images were aligned as a 3D stack using the landmark registration tool in Fiji (Image J) with the surface fiducial markers. The image stack was then imported into VGStudio MAX 2.1 graphics software to create a virtual stack volume. The software's region growing tool based on linear interpolation at grey scale thresholds was used to determine the main crack volume. The other areas of interest such as voids, spherical M_3C carbides and WEA were manually defined and interpolated to a volume in a similar manner.

FIB investigation 2 – inclusion-WEC interaction: The 403 images acquired were already aligned with the FIB software. The 3D models were constructed in the same way as described in the 3D WEC reconstruction (section 3.7.1), however only the inclusions and cracks themselves were segmented and not the associated WEA.

4. TE-74S test results – non-hydrogen charged

4.1 Introduction

In this chapter the results of the non-hydrogen charged RCF tests are presented. As there were no known conditions from literature that would enable creation of WECs on two-roller machines, the effect of different tribological conditions on enabling WEC formation were investigated following the strategy outlined in chapter 2. In addition to the standard metallographic analysis described in chapter 3 performed on all tests, a serial sectioning analysis has also been conducted on test 7b*. The damage features that were found to form in the test rollers were analysed by optical microscopy and SEM. Fig 4.1.1 shows the thesis work flow chart.

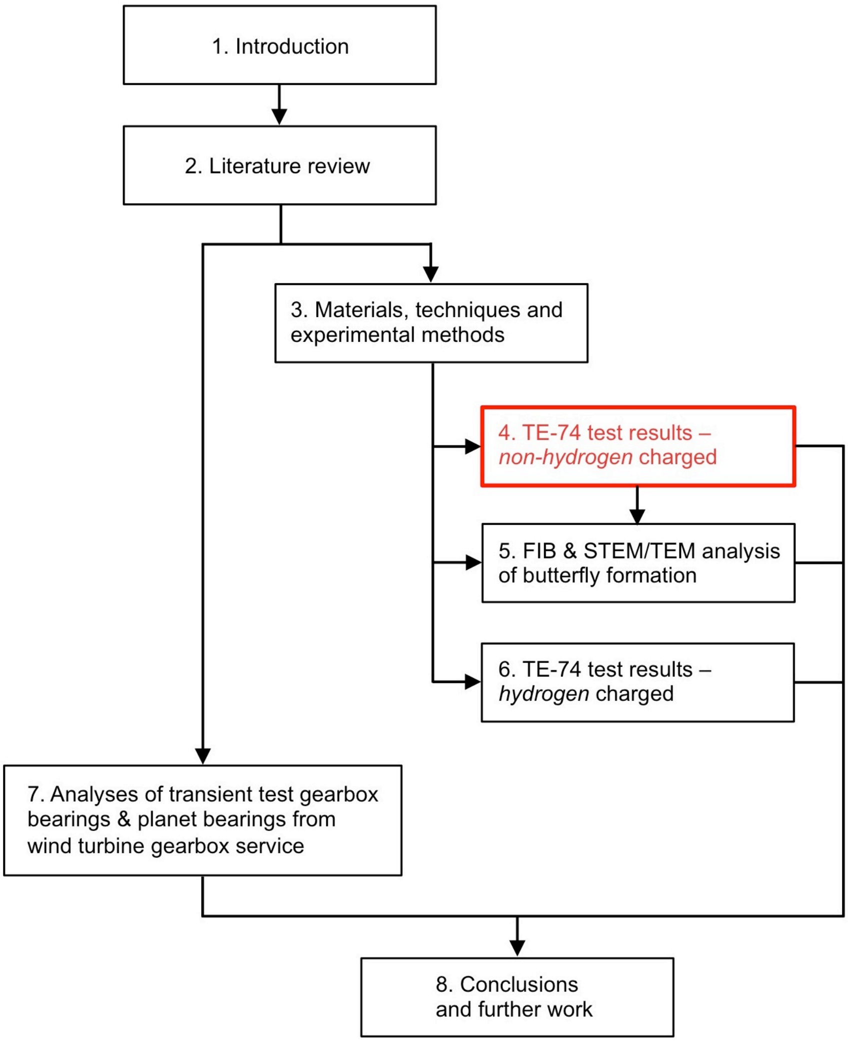

Figure 4.1.1: Thesis work flow chart.

4.2 Results & Discussion

4.2.1 RCF tests

The RCF tests were terminated either when the designed test duration had elapsed (tests 1a – 6a, 1b and 5b – 7b), when mechanical problems occurred on the test rig (tests 2b and 3b) or when a roller spalled causing an automatic stop of the test from a safety trip vibration threshold (tests 7a – 10a and 4b) (see Table 4.2.1).

Table 4.2.1: Non-hydrogen charged RCF tests (phases 1 – 3).

Test	**Test type**	**P_{max} [GPa]**	**Slave speed [rpm]**	**Slave cycles [rpm]**	**Base oil + additives**	**Oil temp [°C]**	**Test stop**	**Butterflies in central plane of contact**	**WEC**
40v40 mm tests (phase 1/2)									
1a	Speed transient	4	0 – 2970	5.9E6	PAO-4 + ZDDP AW	52	**Manual**	**None**	**None**
2a	Load transient	3 – 4.5	2970	5.0E6	PAO-4 + ZDDP AW	50	**Manual**	**None**	**None**
3a	Constant	3	2970	10E6	PAO-4 + ZDDP AW	60	**Manual**	**None**	**None**
4a	Load transient	3 – 4	2970	10E6	PAO-4 + ZDDP AW	60	**Manual**	**None**	**None**
5a	Constant	3	2970	10E6	PAO-4 + ZDDP AW	60	**Manual**	**None**	**None**
6a	Load transient	3 – 4.5	2970	10E6	PAO-4 + ZDDP AW	60	**Manual**	**None**	**None**
7a	Load/speed/slip transient	0 – 5	0 – 2970	9.8E6	PAO-4 + ZDDP AW	65	**Spall**	**None**	**None**
8a	Load/speed/slip transient	0 – 5	0 – 2970	0.5E6	PAO-4 + ZDDP AW	65	**Spall**	**None**	**None**
9a	Load/speed/slip transient	0 – 5	0 – 2970	25E6	PAO-4 + ZDDP AW	65	**Spall**	**None**	**None**
10a	Load/speed/slip transient	0 – 5	0 – 2970	14E6	PAO-4 + ZDDP AW	65	**Spall**	**None**	**None**
26v52 mm tests (phase 3)									
1b	Load/speed/slip transient	2 – 5	0 – 6000	42E6	PAO-4 + Sulphide EP	$70/90^{+}$	**Manual**	***Few (<25)***	**None**
2b	Load/slip transient	2 – 5	6000	26E6	PAO-4 + Sulphide EP	70	**Rig stop**	***Few (<25)***	**None**
3b	Load transient	2 – 5	0 – 6000	75E6	PAO-4 + Sulphide EP	70	**Rig stop**	***Few (<25)***	**None**
4b	Constant slip	4	3000	2.5E6	PAO-4 + Sulphide EP	77	**Spall**	**None**	**None**
5b	Constant slip	2	480	10E6	PAO-4 + Mo EP/AW + Ca S	70	**Manual**	**None**	**None**
6b*	Load/speed/slip transient	1.2 – 4	200 – 5000	50E6	PAO-4 + Mo EP/AW + Ca S	70	**Manual**	***Few (<25)***	**None**
7b*	Speed/slip transient	2	100 – 6000	99E6	PAO + Mo EP/AW + Ba/Na/Ca S	90	**Manual**	***~30***	**None**

PAO-4 base additives: Sulphide EP is type dialkyl polysulphide, Mo EP/AW is type molybdenum dithiocarbamate at 1 wt.%, Ca S is corrosion inhibitor calcium sulfonate at 2 wt.%.

PAO base additives: Mo EP/AW is type molybdenum dithiocarbamate, Ba/Na/Ca S is corrosion inhibitors barium, sodium and calcium sulfonate.

* Rough surface finish rollers.

+: The first 24 hours of the test used an inlet oil temperature of 90 °C, this being dropped to 70 °C for the remainder of the test.

4.2.2 Subsurface identification and quantification of damage features

40v40 mm roller tests (phase 1/2)

Tests 1a – 6a (pure rolling) showed that even with high loads and moderate numbers of stress cycles, only surface wear ranging from minor to severe was generated and no butterfly or WECs were found in the subsurface of the samples after standard metallographic analysis. The reason was likely to be the insufficient numbers of rolling cycles. It was also unfortunately found that cracks were developed around sample removal holes, extending through and up to the sample surface (see Fig. 4.2.1). These acted as stress release points and were assumed to reduce the chance of WEC formation in subsurface, perhaps due to change in residual stress state.

Test 7a – 10a were multi-transient tests that were inherently different from tests 1a – 6a (pure rolling) as slip was induced in the contact by operating both drive shafts independently. Transients in load, speed, standstills and slip were used. Metallographic analysis revealed that no butterflies or WECs formed in these tests from the sections analysed. Spalls occurred on all tests over a wide range of rolling cycle number. However, as explained on at least 3 out of 4 of the tests, metallographic analysis revealed that the sample removal holes initiated through cracking to the surface, causing these spalls. A dark etching region (DER) formed in test 9a, as this test experienced high contact pressures and moderate numbers of stress cycles (see later in section for an example).

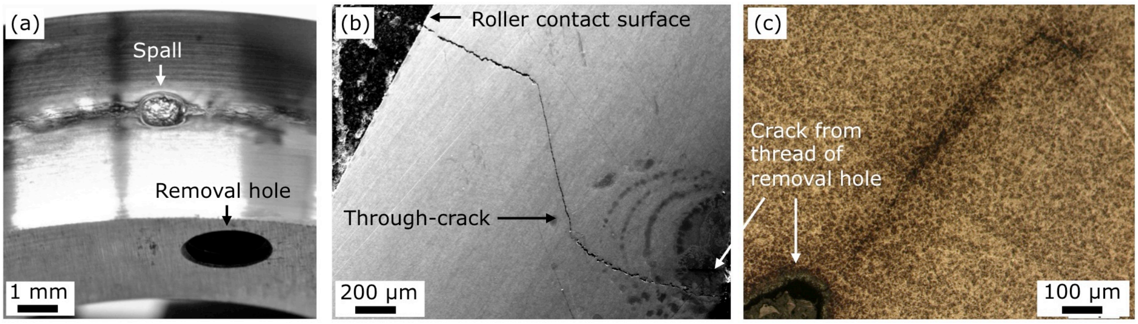

Figure 4.2.1: Through cracking in 40 mm sample from sample removal holes. (a) Optical microscopy image showing contact surface spall and location above removal hole. (b) SEM image of circumferential section showing through-crack from removal hole to roller contact surface. (c) Optical microscopy image in etched condition of circumferential section showing crack initiation at thread part of removal hole.

Therefore a change in sample design from the manufactures original design was required to ensure crack initiation did not occur from sample removal holes. Also, to enable a large number of rotational cycles to be generated within suitable timescales, it was decided also to change the sample diameter ratio from 40v40 to 26v52 for future testing. The contact geometries were also changed to crown-on-flat. The results of these tests are shown in the following section.

26v52mm roller tests (phase 3)

The 26v52 mm tests 1b – 7b* were exploratory and conditions were made severe to increase the chance of the formation of WECs. Despite the severe tribological conditions, metallographic analysis revealed that no WECs formed. The premature spall on the 52 mm roller of test 4b was deduced to be surface initiated from metallographic analyses (shallow cracks extending from surface into the sample) and presumed to be caused by the high slip in the test. Apart from this spall, no evidence of surface cracking was observed that would suggest that this is a mechanism of WEC formation.

A possible reason for the lack of WECs was that there was insufficient hydrogen diffusion into the steel during the RCF tests. This could have been due to a lack of wear induced nascent surfaces to allow the tribochemical reactions necessary for hydrogen release to take place. A lack of events which could cause wear induced nascent surfaces may be because several operating conditions in wind turbine gearbox bearing operation that could cause wear (e.g. vibrations, impact loading, torque reversals, slip between element-race, water contamination, etc.) are not possible on the TE-74S.

Butterflies were however found to have formed in low quantities in several of the rollers. Examples of butterflies that formed in these tests are shown in Fig. 4.2.2. The characteristics of the butterflies were typical, i.e. butterfly wing geometries at orientations of ~0 – 60°, initiation at non-metallic inclusions and double wing length (tip to tip) below 50 µm. The likely reason why butterflies were found in tests 1b – 3b and 6b* – 7b* only is due to high numbers of rolling cycles or a combination of moderate numbers of rolling cycles and a high transient load. This is because both the magnitude of the shear stresses acting and number of stress cycles drive crack growth from material imperfections.

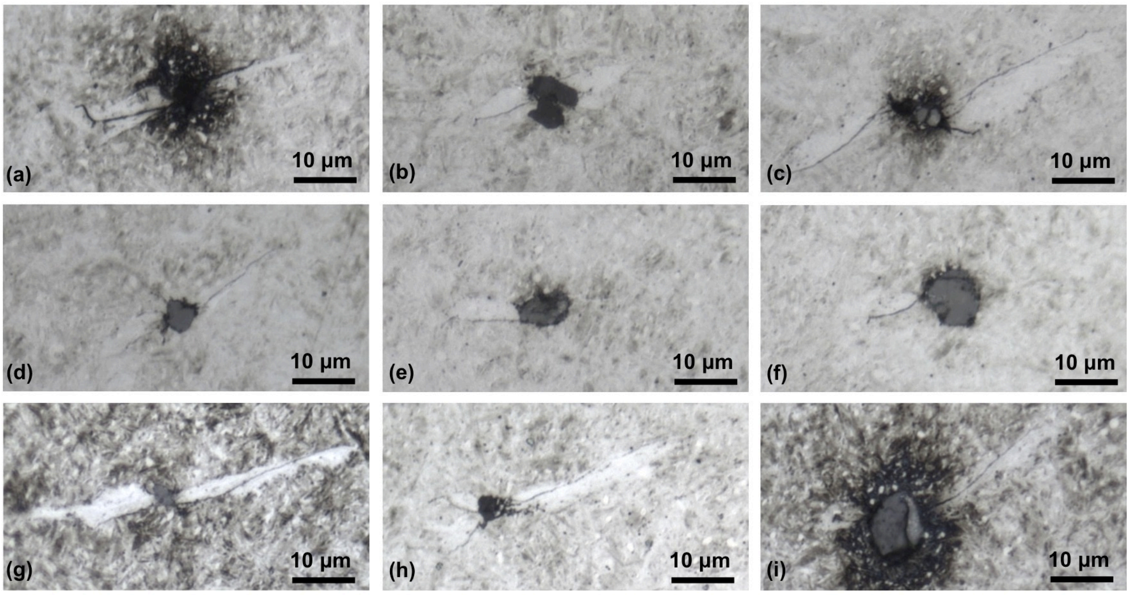

Figure 4.2.2: Optical images showing examples of butterflies created in the test rollers. Images show circumferential sections with over-rolling direction left to right.

In addition to standard metallographic analysis, the partial wear zone serial sectioning process (see chapter 3) was conducted on the rollers from test 7b*. The results of the analysis are shown in Fig. 4.2.4. The plot maps every observed butterfly in the sections analysed. Butterflies observed were mapped according to their double wing length (tip to tip) and the depth of the non-metallic inclusion associated. In case of a single wing butterfly, the wing length also includes the length of the inclusion. A schematic showing the methods for butterfly quantification is given in Fig. 4.2.3 to help interpretation of the details presented in Figs. 4.2.4. The plot includes the data of both rollers for the test (colour coded).

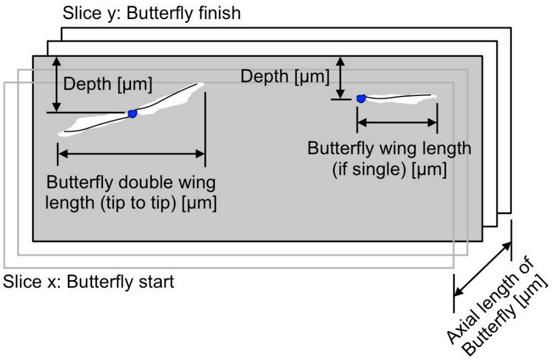

Figure 4.2.3: Schematic showing how butterfly measurements are obtained from the serial sectioning process for the mapping plots. See permission [3.1].

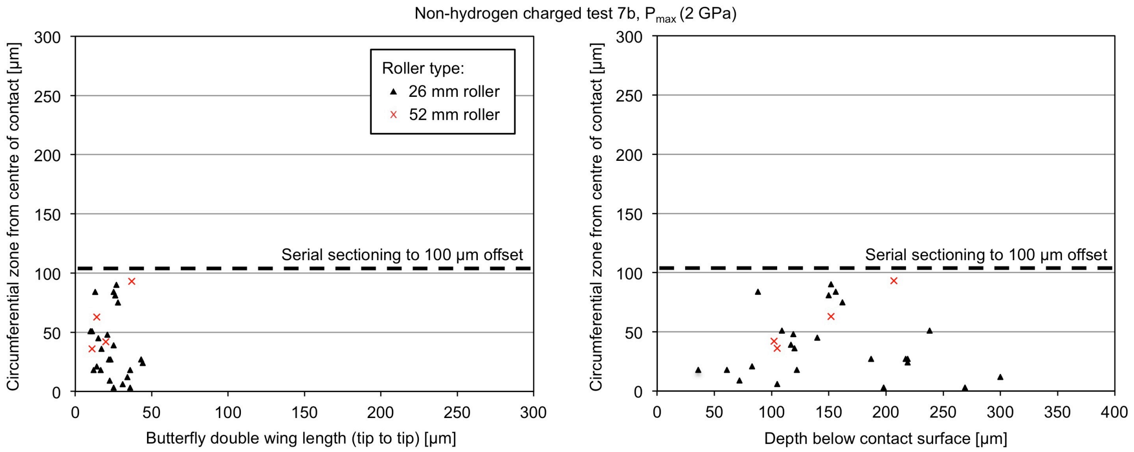

Figure 4.2.4: Butterfly formations in the non-hydrogen charged test 7b.

Fig. 4.2.4 reveals that about 30 butterflies combined were observed in the sections from the 26 mm and 52 mm rollers of test 7b. Only 4 butterflies were found in the 52 mm roller, as opposed to ~20 butterflies in the 26 mm roller. Several other sections from the rollers of test 7b at different offset positions from the centre were also analysed where similar results to the above were found. It can be seen that the butterflies all formed at depths of less than 300 µm and with wing lengths (tip to tip) below 50 µm.

A dark etching region (DER) formed in tests 9a, 1b – 3b and 6b*, as these tests experienced high contact pressures and moderate numbers of stress cycles. Fig. 4.2.5 shows the DER that formed in the 26 mm roller from test 1b.

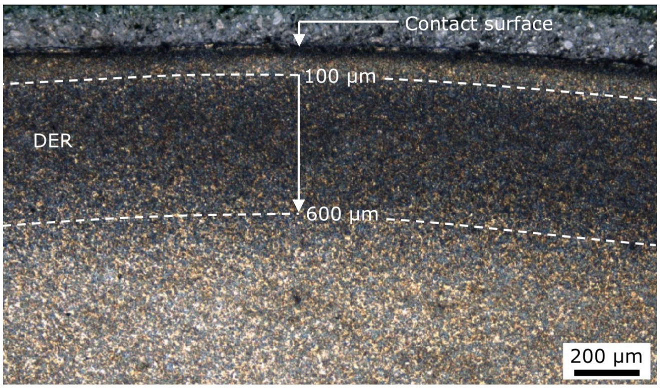

Figure 4.2.5: Dark etching region (DER) in a 26 mm roller circumferential section in centre of contact from test 1b. Sample etched with Nital 2%.

It can be seen that the DER occupies a region from ~100 µm to ~600 µm below the contact surface. Referring to chapter 2, DERs are zones that are visually dark after etching because slip motions have occurred in the martensitic structure. With increased number of slip motions in the martensite, the darker the DERs become. The position and darkness of the DER zone reveals information about the heaviest stressing which has occurred subsurface. The upper boundary is sharp whilst the lower one is diffuse. The upper boundary correlates quite well with 2 GPa base load shear stresses ($\tau_{o,max}$ depth = 107 μm, τ_{max} depth = 178 μm), which with traction in the contact would be raised towards the surface for considerable durations in the test. The lower boundary is more diffuse, and gradually starts to decrease from ~500 μm towards disappearance at 700 μm, therefore 600 μm has been marked at the approximate lower boundary. At 5 GPa contact pressure, $\tau_{o,max}$ depth = 267 μm and τ_{max} depth = 446 μm, where in this case it can be seen that the unidirectional shear stress (τ_{max}) appears to be predominately initiating the plastic deformation at the deeper depths, rather than orthogonal shear stress (τ_o) which would have low magnitudes at these depths.

4.3 Conclusions

Some 17 RCF tests were conducted using two sample geometries. Despite inducing the most severe tribological conditions that the TE-74S test machine can operate with, no WECs were formed in the test rollers. Limited numbers of butterflies and also DER were however created in some of the tests. It is suggested that one reason why no WECs formed in these tests was that there was insufficient hydrogen diffusion into the steel during the RCF tests. This could have been due to insufficient operating conditions used on the test machine that cannot replicate those of actual wind turbine gearbox service conditions.

5. FIB & STEM/TEM analysis of butterfly formation

5.1 Introduction

Butterflies are cited [22] as potentially being an initiator of white etching cracks (WECs). This chapter presents a study on a butterfly formed in 100Cr6 bearing steel subject to non-hydrogen charged RCF testing as detailed in chapter 4. Analysis by FIB tomography, STEM/TEM and 3D reconstruction techniques has been performed to further understanding of butterfly crack formation, microstructural change and spherical carbide dissolution.

It is currently contested whether the microcrack initiating at a defect forms prior to WEA microstructural change [18, 23, 25, 26, 39, 115, 117] or whether cracks and wings form cooperatively [24], as is why WEA only forms at one side of the cracks. In addition, the mechanisms of butterfly crack formation are not fully established. The involvement of voids and cavities has been proposed [27], however little evidence has been offered to support this mechanism. It is cited that dislocation generation and movement (glide) from the interface of the defect/matrix [39, 115] lead to repeated interaction between dislocations and carbide precipitates thus causing temper carbide dissolution, and spherical M_3C carbide elongation, deformation, break-up and dissolution [21, 23, 25, 27, 29, 39, 41, 45, 46]. Spherical carbide dissolution in WEA adjacent to larger RCF cracks has been observed previously by TEM [25], however spherical carbide dissolution in butterflies and how this relates to the WEA microstructural change in the butterfly wings is not well understood.

Section 5.3 of this chapter includes two videos that aid in understanding of butterfly crack WEA wing formation. These can be accessed as supplementary material and are listed in the following:

- **Video 5.3.1:** Video showing all the slices from the FIB tomography of a butterfly wing.
- **Video 5.3.2:** Video showing 360 degrees rotation of the 3-D model of a butterfly wing.

Fig. 5.1.1 shows the thesis work flow chart.

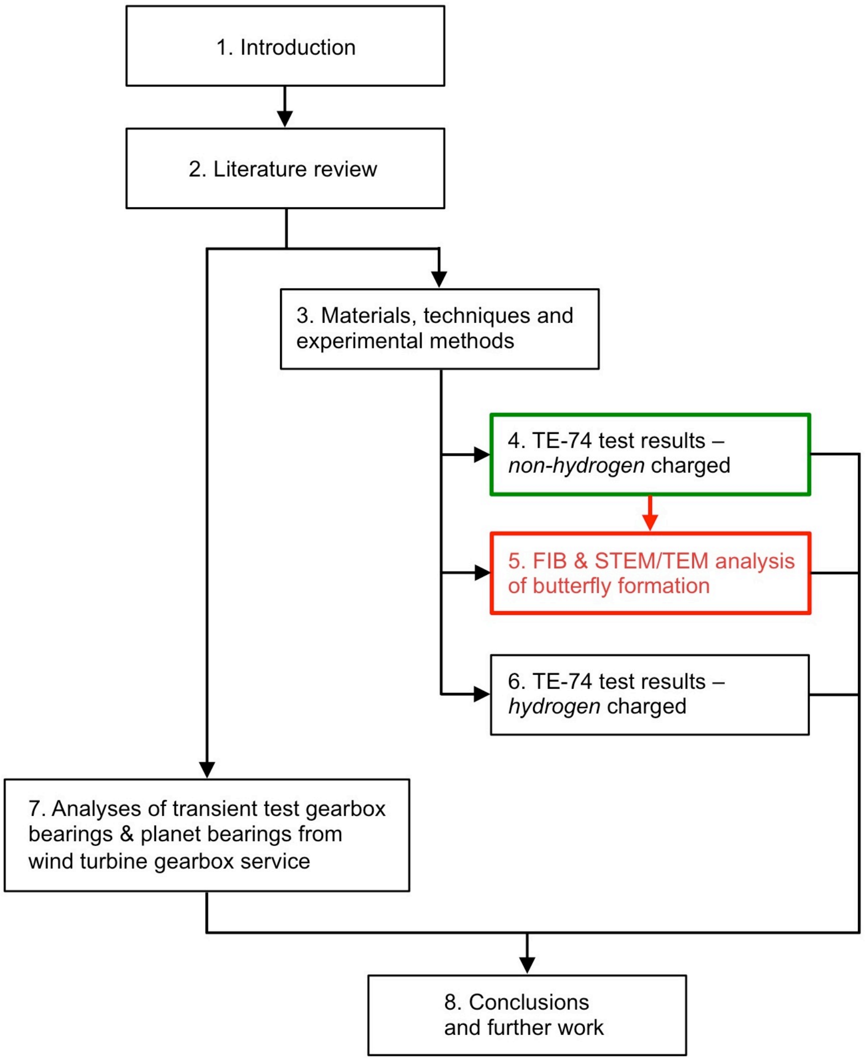

Figure 5.1.1: Thesis work flow chart.

5.2 RCF Experiments

5.2.1 RCF testing

Details of the test that created the butterfly from chapter 4 are shown in Table 5.2.1.

Table 5.2.1: Non-hydrogen charged test (phase 3 test).

#	Step type	Step time (s)	Ramp time (s)	Load (GPa)	52mm (rpm)	26mm (rpm)	26mm CoF - µ (Avg), [Max]
1	Run-in	1800	-	2	3000	6000	-
2	Base	5	1	2	3000	6000	(0.02), [0.1]
3	Load	3.4	3	**5**	3000	6000	[0.075]
4	Base	5	-	2	3000	6000	(0.02), [0.1]
5	Deceleration	10	5	2	0	0	[0.03, 0.06]
6	Standstill	5	-	2	0	0	-
7	Acceleration	10	5	2	3000	6000	[0.08]
8	Slip (5%)	10	1	2	2857	6000	(0.03)

See permission [3.3].

5.2.2 Roller surface and subsurface inspection

After RCF testing, the 26 mm roller was inspected to investigate butterfly formation and microstructural changes in the material. Standard metallographic preparation of the 26 mm roller was made after RCF testing so that a circumferential section (parallel to rolling direction) in the centre of the wear scar (see Fig. 5.2.1) could be analysed by optical microscopy and subsequently SEM.

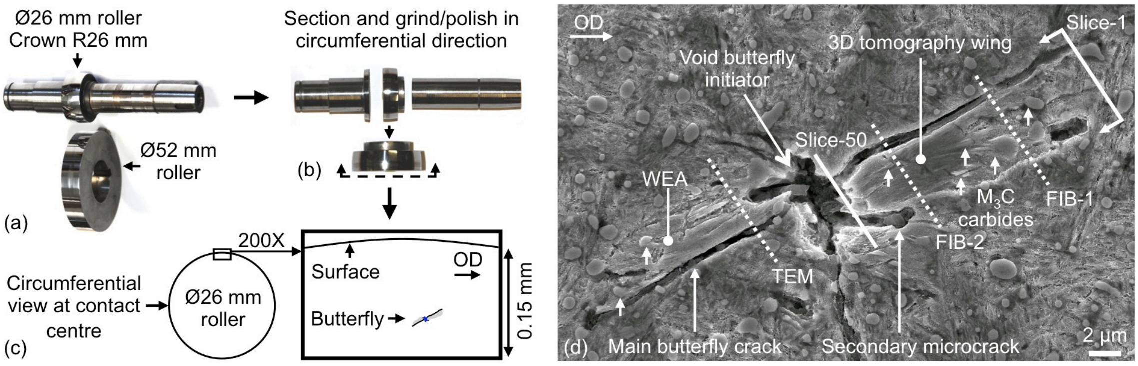

Figure 5.2.1: Images showing the butterfly analysed in this study and its location in the 26 mm roller. (a) – (c) location of circumferential section at a position in the centre of contact. (d) SEM image of the butterfly in the as-etched condition with mark-up of analysis positions. Over-rolling direction marked as OD. See permission [3.3].

FIB was used to generate 3D tomographical images at a selected butterfly crack. Slices from within the butterfly were sputtered to expose the tip (slice 1 in Fig. 5.2.1) of the butterfly crack. Secondary electron images were taken at regular intervals during sputtering, resulting in over 50 slices at approximately 350 nm slice thickness being captured up to the centre at the void. Gallium ion beam images were also captured at select locations shown in Fig. 5.2.1. Once the milling and imaging of all 50 slices was completed, the images were aligned as a 3D stack and imported into graphics software to create a 3D model of the butterfly features. FIB was also used to remove a cross-sectional lamella for STEM/TEM analysis from the remaining butterfly wing (see Fig. 5.2.1 for location).

5.3 Results & Discussion

5.3.1 SEM/EDS

A total of 12 butterflies were found to have formed in the circumferential centre plane of contact of the 26 mm roller, the depth ranging from 30 – 800 μm from the contact surface. Many of these were very small (~5 μm wing length) where often the crack was well developed compared to the comparatively small WEA. All WEAs were observed with the presence of a crack.

One of the well-developed butterflies that formed at a depth of 110 μm from the contact surface was chosen for detailed analysis (Fig. 5.2.1). Energy dispersive X-ray spectrography (EDS) of the hole area showed the butterfly to have initiated from a void in the steel, and not a non-metallic inclusion removed by metallographic preparation due to the lack of increased levels of typical elements for inclusions in 100Cr6 steel such as Si, Ti, Mn, S, Al, O and Ca (see Table 5.3.1).

The length of the butterfly was ~40 μm (wing tip to wing tip). The butterfly cracks formed at an orientation of 30° and 150° relative to the over-rolling direction, which agrees with the findings in other studies [23-28, 39, 44]. The number of spherical M_3C carbides in the WEA appeared to be much lower than that in the matrix, and the positions of deformed spherical carbides (marked with white arrows) and shear flow appeared to be in the direction of the main crack. These observations agree with previous findings [18, 21, 23, 26-28, 39, 44-46].

Table 5.3.1: The chemical composition of the void butterfly initiator by EDS analysis. Values are displayed in wt.%.

Si	**Mn**	**P**	**S**	**Cr**	**Mo**	**Al**	**Ca**	**Ti**	**O**	**Fe**
0.29	0.58	0.20	0.16	2.42	0.06	0.31	0.48	0.01	4.38	90.91

Carbon content was excluded from the analysis. See permission [3.3].

5.3.2 FIB

Selected InLens images through the cross-section FIB milling of the wing are shown in Fig. 5.3.1 (see Video 5.3.1 for all slices). The images are numbered according to consecutive milling of 50 slices from the wing tip to the central void initiator at an average slice thickness of 350 nm (see Fig. 5.2.1). The main crack extends from the top of the surface protected by a carbon deposition layer vertically downwards into the matrix, where rolling direction is approximately into the page. The WEA is distinguishable to the left of the crack as a fine phase compared to that of the matrix (see Fig. 5.3.1c dashed line). Spherical M_3C carbides appear as spherical dark grey features in the matrix (see Fig. 5.3.1b).

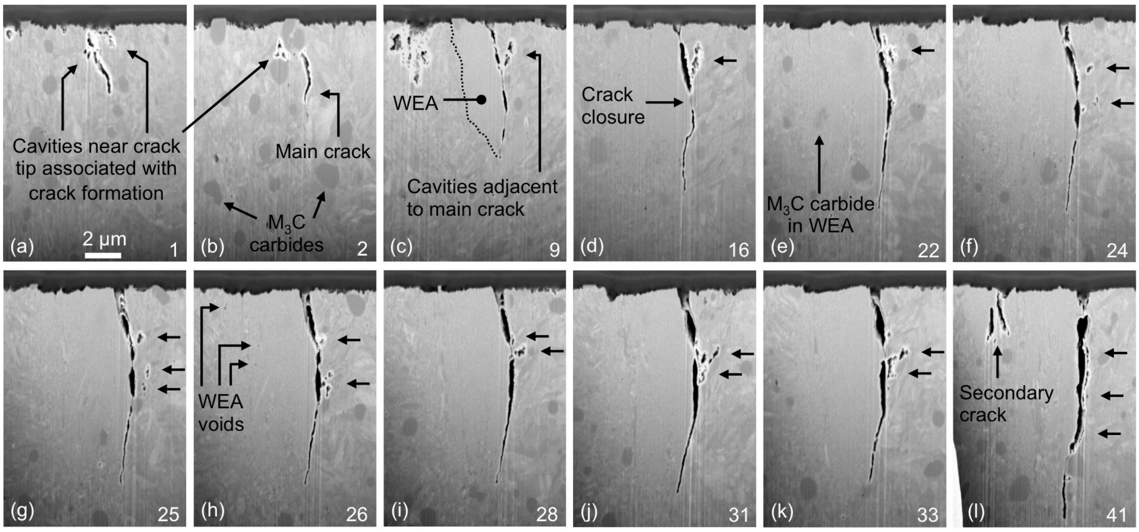

Figure 5.3.1: FIB InLens images of cross-sections of the butterfly wing. Single unlabelled arrows point to voids and cavities on the non-WEA side of the main crack. See Video 5.3.1 for all FIB slices. See permission [3.3].

Voids were found within the WEA (see Fig. 5.3.1h), which was also reported in other studies [18, 27, 29, 44, 116]. In these studies it was proposed that voids form in WEA as a result of microstructural changes due to high cyclic stresses during RCF [28]. A secondary crack can be observed in Fig. 5.3.1l), where the WEA is seen to have extended to the far left in the image due to the microstructural change driven by the secondary crack. Deformed/indistinct spherical carbides were infrequently observed in the WEA (see Fig. 5.3.1e). This supports previous theories that dislocation emission from defects and the subsequent repeated interaction of these dislocations with carbide precipitates can cause spherical M_3C carbide elongation and deformation at an early stage followed by spherical carbide break-up and dissolution [21, 23, 27, 29, 39, 41, 45]. Cavities are observed around the main crack at the wing tip (Fig. 5.3.1a and Fig. 5.3.1b) as well as immediately adjacent to main crack on the non-WEA side (Fig. 5.3.1c to Fig. 5.3.1l).

Two of the slices (positions shown in Fig. 5.2.1 labelled as FIB-1 and FIB-2) were also imaged with the FIB gallium ion beam giving higher contrast to distinguish different phases (see Fig. 5.3.2). The WEA in FIB-1 (highlighted by a dashed line) clearly shows a fine granular structure. In FIB-2, apart from the large WEA to the left of the main crack, a small WEA is observed near the secondary crack. Cavities adjacent to the main crack observed in previous images are visible in both images. In addition, portions of high contrast microstructure are shown within the large WEA in FIB-2 (marked by arrows).

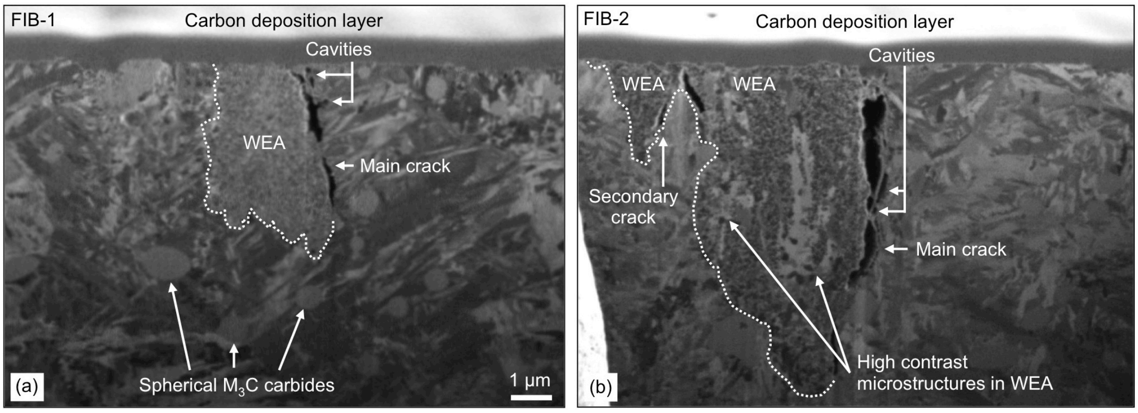

Figure 5.3.2: FIB Ga^+ beam images of two slices marked as FIB-1 and FIB-2 in Fig. 5.2.1. See permission [3.3].

The 3D reconstruction of the butterfly wing is shown in Fig. 5.3.3. Video 5.3.2 presents 360 degrees rotation of the 3D model. Different colours are assigned to differentiate the various phases existing in the wing. The main crack is shown in red, spherical M_3C carbides inside WEA or those on the boundary of WEA in yellow, voids or cavities on the WEA side in blue, cavities on the non-WEA side of the main crack in green, and WEA in white. The WEA has been made semi-transparent to enable partial viewing of phases within WEA such as voids and spherical carbides. The front view of the tip of the wing is shown in Fig. 5.3.3a, where voids/cavities and portions of the main crack are present (also refer to Fig. 5.3.1a and Fig. 5.3.1b). Fig. 5.3.3b shows a side view of the wing along the main crack (the wing tip is on the left), illustrating the voids/cavities in the non-WEA side of the main crack.

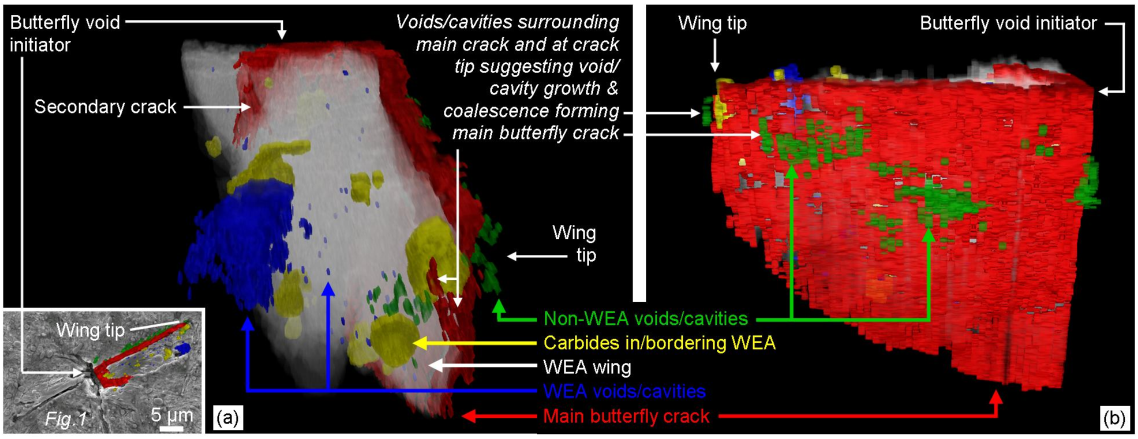

Figure 5.3.3: A 3D reconstruction of the butterfly wing. (a) View from tip of wing looking towards butterfly initiating void. (b) View at side profile of the main crack showing its variable length and highlighting the non-WEA cavities coloured in green. The insert in (a) shows the 3D reconstruction top view laid on original SEM image shown in Fig. 5.2.1. See Video 5.3.2 for 360 degrees rotation of the 3D model. See permission [3.3].

The voids/cavities and portions of main crack at the tip of the wing appear to intersect through a spherical M_3C carbide (see Fig. 5.3.3a). A large cavity is also present on the left side in Fig. 5.3.3a. Since the cavity is located far from the main crack, but still in the WEA, it is either part of the microstructural changes occurring as cited in previous studies [27], present in the microstructure from manufacture, or introduced by a particle being removed during sample preparation.

Void/cavity coalescence theory for butterfly crack formation:

In agreement with a previous study [27], Fig. 5.3.1 to Fig. 5.3.3 show non-WEA cavities adjacent to the main crack, which appeared to be independent of the main crack itself. It has been cited that the decohesion of defects/inclusions from the matrix lead to the nucleation of voids that can lead to formation of cavities [27, 129]. Under continued straining, the cavities grow and coalesce into a central crack propagating away from the defect into the matrix along localised shear planes at 45° with respect to the contact surface [98]. The observed non-WEA cavities adjacent to the crack in this study support this mechanism. It is assumed that the voids/cavities observed did not constitute towards creation of the main crack itself, the crack taking a different path. Fig. 5.3.1a and Fig. 5.3.1b further supports this due to the scattered presence of cavities associated with the crack formation near the crack tip. From a fracture mechanics approach, crack initiation and short crack growth from inclusions/butterflies is governed by Mode I loading [120]. A tensile stress must exist around an inclusion for positive stress intensity factors to prevail at the crack tips, therefore as the residual tensile stress field around the inclusion eventually diminishes with distance away from the inclusion, the mode I crack would eventually arrest at a crack size determined by the mode I threshold stress intensity factor [120]. The transition from mode I to II cracking in butterflies is expected to be aided by microstructural discontinuities (voids and cavities) that are created near the vicinity of the extending crack and on the boundaries of the WEA microstructural change [120].

A number of spherical carbides are distributed either around the WEA boundary, or occasionally inside the WEA. The depths of the main crack appear to reduce from the centre of the butterfly to the wing tip (see Fig. 5.3.3b). This suggested that this particular butterfly crack was a feature that revolves in a plane around its initiator as previously cited [25, 39].

5.3.3 STEM/TEM

FIB was also used to remove a lamella for TEM analysis from the remaining butterfly wing (see Fig. 5.2.1 for location). A FIB gallium ion image of the TEM lamella prior to final thinning is shown in Fig. 5.3.4 indicating the areas where TEM analyses has been carried out (TEM-A and STEM-B). TEM-A encompasses the general WEA region, main crack and banding microstructures, whereas STEM-B focuses on an area that was suspected to be a spherical M_3C carbide in the WEA. The WEA (encircled by a dashed line) is distinguishable on the left-hand side of the main crack. Voids are observed adjacent to the main crack on the WEA side and are believed to follow the void/cavity crack formation theory discussed previously. Portions of high contrast band microstructure are also seen in the WEA similar to those shown in Fig. 5.3.2b.

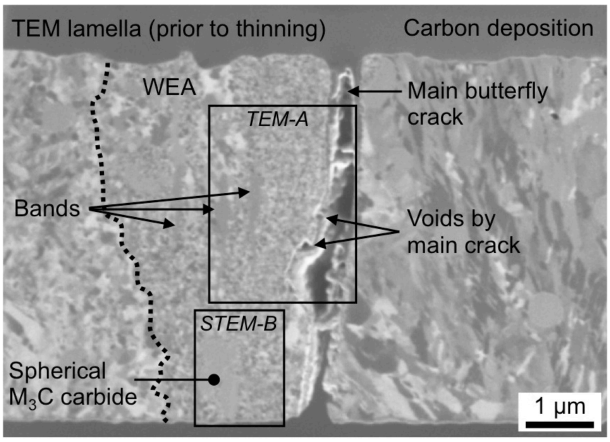

Figure 5.3.4: FIB Ga$^+$ image of TEM lamella labelled in Fig. 5.2.1 showing the locations of the two areas used for STEM/TEM analyses; TEM-A and STEM-B. See permission [3.3].

Fig. 5.3.5 shows the TEM images, selected area diffraction patterns (SADP) (A, B & C) and bright-field (BF) images at the TEM-A location. A layer of re-deposition material is present on the right-hand side of the main crack due to gallium re-deposition from FIB preparation and the portion of white space to the right-hand side of this layer is the crack space (the crack width opened up upon thinning of the lamella). Two bands (marked as Band-1 and Band-2 in TEM-A image) show apparent different microstructures from the WEA, where Band-1 can be seen in higher detail in image BF-1. While the SADP B and C are similar, diffraction pattern A is different due to overlap with Band-2. Indexing of the diffraction patterns using the BCC iron unit cell (2.861 Å) confirms that the WEA consists of BCC ferrite nanocrystalline grains as previously cited [25, 27-29, 44, 48].

Fig. 5.3.5 also shows a bright field image (BF-2) showing the grain size distribution inside the WEA, ranging from ~10 – 60 nm. Compared with some previous observations that observed increasing grain size towards the butterfly wing boundary [25, 27], in this study no observable systematic relations to the position within a wing were found, which agrees with the findings by Osterlund, et al. [39]. However it must be noted that the lamella in this study did not spread the whole width of the wing, therefore the grain size in the near vicinity of the wing boundary was not observed.

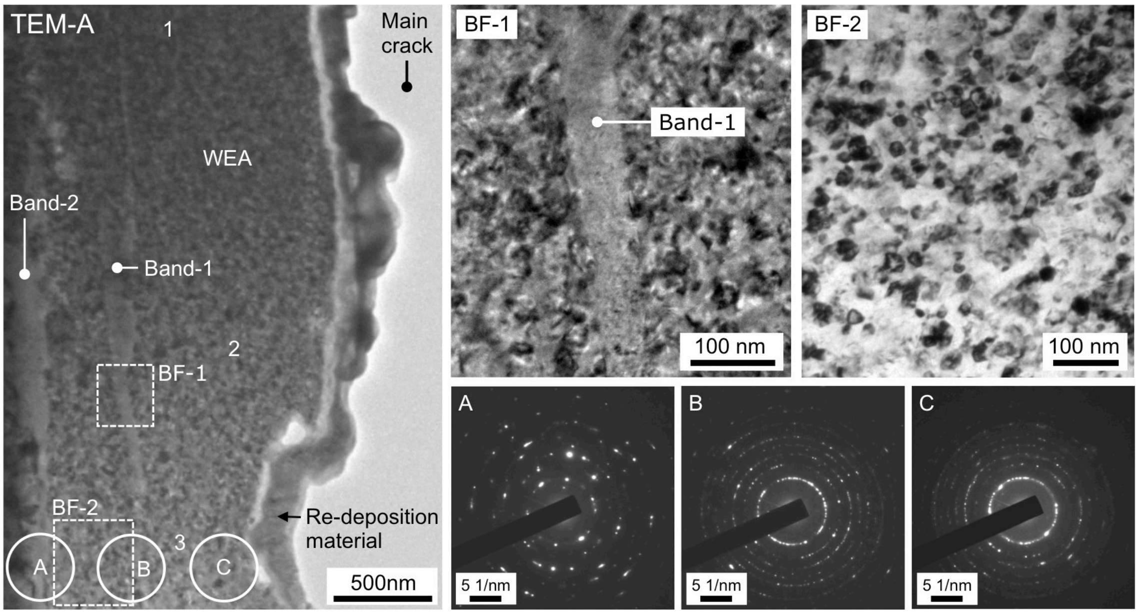

Figure 5.3.5: Selected area diffraction patterns (A, B & C), bright field image (marked BF-1) and a bright field image (marked BF-2) referring to TEM-A location in Fig. 5.3.4. Numbers 1 – 3 in the TEM-A image show the positions of EDS analysis. See permission [3.3].

To further investigate the suspected spherical M_3C carbide in the WEA, STEM/TEM analysis was carried out for the area STEM-B marked in Fig. 5.3.4, see STEM/TEM images shown in Fig. 5.3.6. The STEM image of the whole area is shown in Fig. 5.3.6a together with two insert images X & Y showing diffraction patterns at the two areas marked in the main image. During the sample thinning process, one small area was polished through and is marked 'hole' in Fig. 5.3.6a. In the STEM-B image, it can be seen that the microstructure appears to differ significantly, containing 'smooth and dark contrast areas' and 'light contrast areas with visible grain structures'. Diffraction patterns at X and Y show that, in both cases the pattern is different from those obtained in TEM-A. The thick halo ring that occurred in the diffraction patterns in the 'smooth and dark contrast areas' indicated an amorphous type structure, which is different from the nanocrystalline structure found in the areas in TEM-A. This was confirmed by tilting of the specimen, showing very few grains inside these areas.

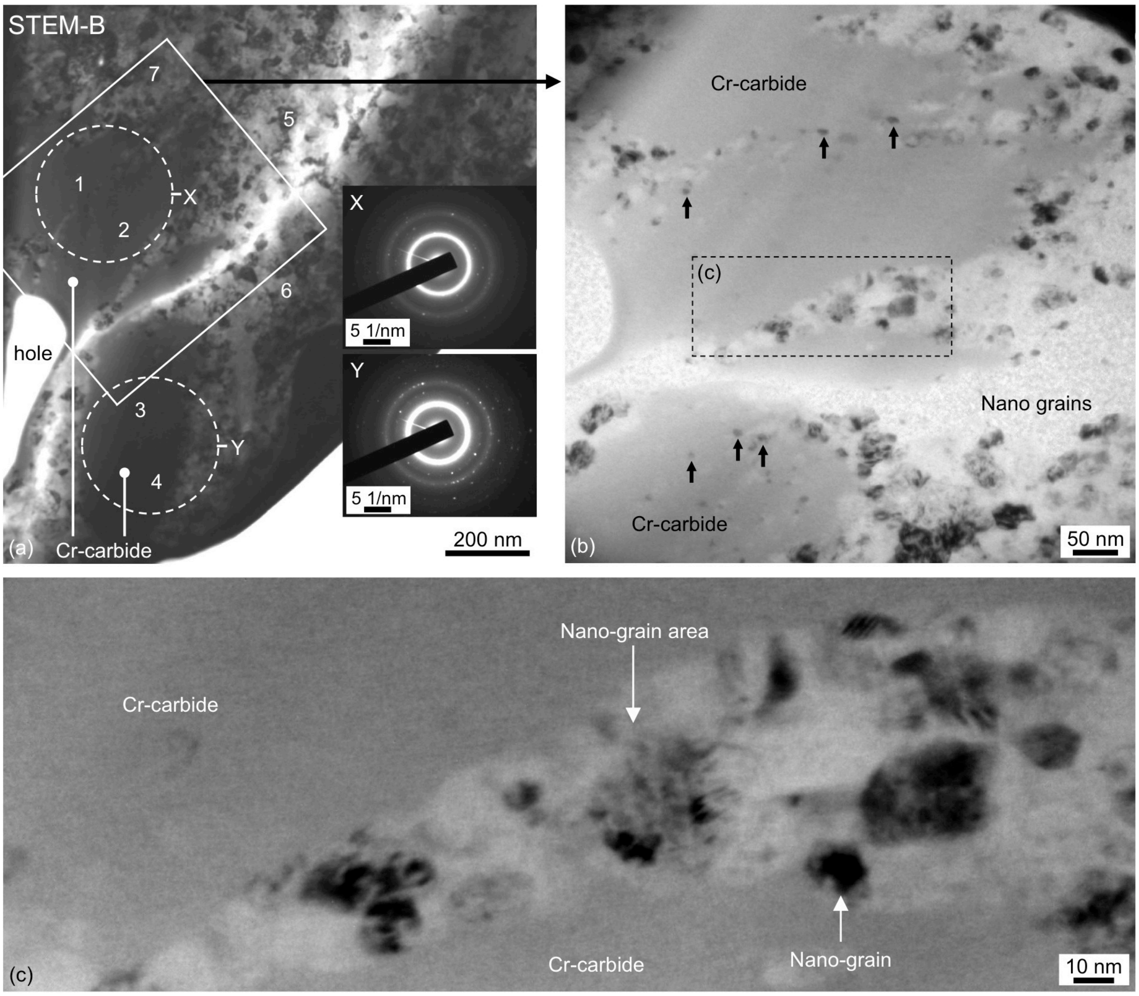

Figure 5.3.6: STEM/TEM images of STEM-B location in Fig. 5.3.4. (a) A STEM image of STEM-B with two diffraction patterns X & Y (locations are marked in the main image). Numbers 1 – 7 in the STEM-B image show the positions of EDS analysis. (b) A TEM bright field image of the tilted specimen for the area highlighted in (a), where arrows point to nano grains. (c) Higher magnification TEM bright field image of area marked in (b). See permission [3.3].

To verify the chemical composition of the suspected amorphous spherical M_3C carbide as well the general WEA and other features contained within, EDS analysis was conducted for the locations in TEM-B marked as 1 – 7 in Fig. 5.3.6a, in TEM-A labelled 1 – 3 in Fig. 5.3.5, and Band-1 and Band-2 in Fig. 5.3.5. The chemical composition in weight percentage of these positions in the WEA is shown in Table 5.3.2. The content of carbon is regarded as a qualitative value and is therefore not presented. It was found in STEM-B positions 1 – 4 that the carbon and chromium (average 8.14 wt.% Cr) contents are greatly increased (carbon was 6X and chromium 3X) from that of the miscellaneous WEA measurements 1 – 3 in TEM-A (average 2.70 wt.% Cr), which is expected for the suspected spherical M_3C carbide (iron-chromium type) and therefore confirms that it is an iron-chromium carbide. Compared with the chemical composition of the 100Cr6 rollers (as received, see Table 3.3.1 in Chapter 3) the chromium content in TEM-A positions 1 – 3 is found to be an average of 2.7 wt.%, which is higher than the ~1.5 wt.% in the 100Cr6 matrix. EDS measurements 5 – 7 were also made on the granular areas surrounding the smooth areas, which showed carbon and chromium contents comparable to those of miscellaneous WEA measurements 1 – 3 in TEM-A. The increased chromium content is thought to be a result of the chromium from the dissolving spherical M_3C carbide diffusing into the adjacent WEA. Previous studies [48] also found that the level of manganese and chromium slightly increased in transformed regions of white etching cracks (WEC) in JIS SUJ2 steel matrix (similar to 100Cr6), caused by cementite going into solution. However, other studies found that the average level of alloying elements (particularly chromium) in a butterfly WEA region was the same as that of the matrix [39, 41]. In this study, EDS showed Band-1 and Band-2 to have similar levels of alloying elements as that of TEM positions 1 – 3. Referring to Fig. 5.3.2b, it is postulated that the high contrast band microstructures (marked with arrows) are either elongated and deformed spherical carbides, other non-metallic inclusions, or portions of the original tempered martensitic matrix that have not changed to a fine granular structure.

Table 5.3.2: The chemical composition of areas in TEM-A and STEM-B by EDS analysis. Values are displayed in wt.%.

Position	Cr	Si	P	Mn	S	Mo	Fe
TEM-A							
Pos. 1-3 Avg	2.70	0.30	0.13	0.12	0.09	0.17	96.74
Band-1 Avg	1.74	0.41	-	0.24	0.05	0.01	97.86
Band-2 Avg	2.52	0.18	-	0.39	0.02	-	97.11
STEM-B							
Pos. 1-4 Avg	8.14	0.24	0.06	1.10	0.16	0.19	90.36
Pos. 5-7 Avg	2.53	0.42	0.06	0.62	0.11	-	96.88

Carbon content was excluded from the analysis. See permission [3.3].

In Fig. 5.3.6b it can be seen that the iron-chromium carbide has fingers of what appears to be nano-grain areas intruding inside its structure. Fig. 5.3.6c at higher magnification shows that super fine nano-grains (~3 – 15 nm diameter) exist within the spherical M_3C carbide (marked with black arrows in Fig. 5.3.6b). It is proposed that this evidence shows the early formation of nano-grains that eventually replace the spherical carbide. Therefore in this study it is also proposed that spherical carbide dissolution was occurring in Fig. 5.3.1e and also Fig. 5.3.1b/Fig. 5.3.4a from the observation of the cavities and crack tip intersecting through a spherical carbide. Formation of WEA by the structural breakdown of the matrix associated with carbide dissolution is expected to be cooperative with the propagation of the main crack, and the associated high stresses induced in the near vicinity of the crack. From the evidence of nano-grain formation eventually replacing spherical carbides in this study, it is suggested that grain refinement is gradual and the formation mechanisms are akin to those proposed in references [25, 28, 39, 44]. Spherical carbide dissolution as part of the WEA formation is supported by previous TEM studies [25] that provided evidence for partial spherical M_3C carbide dissolution with fine grain replacement adjacent to RCF cracks. Spherical carbides which are thought to be located in areas of early WEA formation have also been observed with dislocations, these dislocations indicting decay of the carbides [29].

5.4 Summary

In this investigation, butterfly formations in standard 100Cr6 bearing steel under transient RCF conditions have been studied using SEM, FIB and STEM/TEM techniques. The techniques used allowed further information to be gained regarding formation mechanisms of butterfly cracks, WEA microstructural change and spherical M_3C carbide dissolution. The following observations are made:

1. The combined evidence supports that the mechanism for butterfly crack and WEA formation is cooperative. This is supported by the in-depth analysis of a butterfly by FIB tomography analysis and that sometimes small cracks (<5 μm length) were found initiating at inclusions without the WEA microstructural change, however it was not observed that a WEA exists around an inclusion without the presence of a crack.
2. The FIB 3D tomography proved to be a powerful tool for revealing the features of a butterfly within a steel matrix. WEA was confirmed to be a BCC nanocrystalline ferrite structure. The WEA was also found to contain different phases such as inclusions or spherical carbides with a randomly distributed ferrite grain size varying between ~10 – 60 nm.
3. The extensive presence of voids/cavities immediately adjacent to the main crack on the non-WEA side and also at crack tip provides evidence for a void/cavity coalescence theory for initial butterfly crack formation at defects.
4. An iron-chromium carbide was observed inside the butterfly wing WEA identified from its amorphous structure and increased chromium/carbon composition. The spherical M_3C carbide appears deformed and dissolving, where fingers of nanocrystalline grains intersect the spherical carbide containing super-fine nano-grains of 3 – 15 nm. This is evidence of the early formation of nano-grains associated with the WEA formation mechanism as spherical M_3C carbides dissolve.

This page is intentionally left blank

6. TE-74S test results – *hydrogen charged*

6.1 Introduction

No WECs were created on the two-roller RCF test machine using transient testing (non-hydrogen charged) conditions as shown in chapter 4. Therefore to investigate the influence of diffusible hydrogen on the initiation, propagation and thresholds of WSF formation, a number of RCF tests using hydrogen charged rollers have been conducted. The hydrogen charging process aims to replicate hydrogen entry into bearings by the bulk diffusion mechanism at wear induced nascent surfaces. With this technique the test rollers contain various quantifiable concentrations of diffusible hydrogen at the onset of RCF testing, however local concentrations of diffusible hydrogen are unknown.

Previous WSF investigations have used limited metallographic analyses that have led to incomplete conclusions on WSF initiation and propagation mechanisms. Suggested WEC initiation mechanisms are surface initiation at cracks [106] and subsurface initiation at non-metallic inclusions [22] or adiabatic shear banding caused by impact events between elements/raceways in bearings [70]. To fully understand the 3D structure of WECs, this investigation has applied a serial sectioning technique to map subsurface wear volumes of test specimens from laboratory for the first time. This has allowed viewing of entire independent WECs and investigation of initiation points and propagation mechanisms of WSF. The WEC/WEA formation propensity is quantified using the serial sectioning technique while FIB tomography and 3D crack reconstruction techniques have been used to confirm WEC initiation and propagation mechanisms.

This chapter is split into three sections. Section 6.2 details the analysis conducted to determine the concentration of diffusible hydrogen in the test rollers after the hydrogen charging process and also after aging. Section 6.3 details the analysis and results used to establish the thresholds of concentration of diffusible hydrogen, load and rolling cycles for the formation of white etching features. Section 6.4 specifically concerns the results from the investigation of the initiation and propagation mechanisms of WECs.

Section 6.4 of this chapter includes six videos that aid in understanding of crack initiation and formation. These can be accessed as supplementary material and are listed in the following:

- **Video 6.4.1:** Video of the FIB tomography slices of an inclusion-WEC interaction.
- **Video 6.4.2:** Video showing 360 degrees rotation of the 3-D model of the inclusion-WEC interaction. The 3-D model is formed from 2D segmentation of the inclusions and crack portion from the FIB tomography. The WEA portion was not segmented or modelled.
- **Video 6.4.3:** Video showing all the 2D crack + WEA segmentations from the serial sectioning process of WEC-9.

- **Video 6.4.4:** Video showing an orthoslice sweep of the 2D crack + WEA segmentations from the serial sectioning process of WEC-9 in-situ with the 3-D model. The orthoslices are in the circumferential plane (the plane of material removal during serial sectioning).
- **Video 6.4.5:** Video showing 360 degrees rotation of the 3-D model of WEC-9.
- **Video 6.4.6:** Video showing a virtual orthoslice sweep of the 3-D model of WEC-9 in the axial plane (the plane perpendicular to that of material removal during serial sectioning).

Fig. 6.1.1 shows the thesis work flow chart.

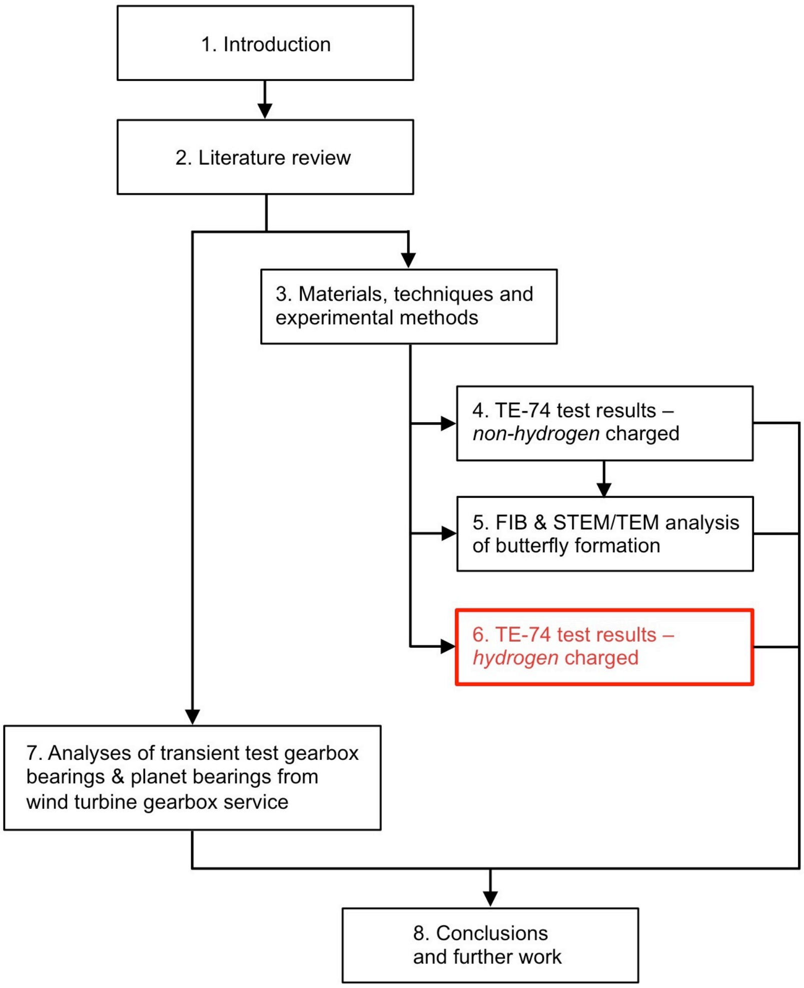

Figure 6.1.1: Thesis work flow chart.

6.2 Diffusible hydrogen concentration analysis

The RCF tests were conducted under differing concentrations of diffusible hydrogen, which was achieved by hydrogen charging prior to testing under different conditions 1 wt.% – 20 wt.% NH_4SCN aqueous solutions. Therefore to deduce the concentration of diffusible hydrogen in the actual test rollers during RCF testing, the concentration of diffusible hydrogen in model rollers under five NH_4SCN hydrogen charge concentrations was measured at a number of effusion times. See section 3.2.4 in chapter 3 for details on the hydrogen charging process and hydrogen measurement technique. Average values from the TDA hydrogen measurements are shown in Fig. 6.2.1 and Table 6.2.1. Compared with the control specimen (without hydrogen charging) which had 0.04 ppm diffusible hydrogen, all hydrogen charged specimens contained much higher concentrations of diffusible hydrogen at zero effusion time, with hydrogen generally increasing with an increase in NH_4SCN charge concentration.

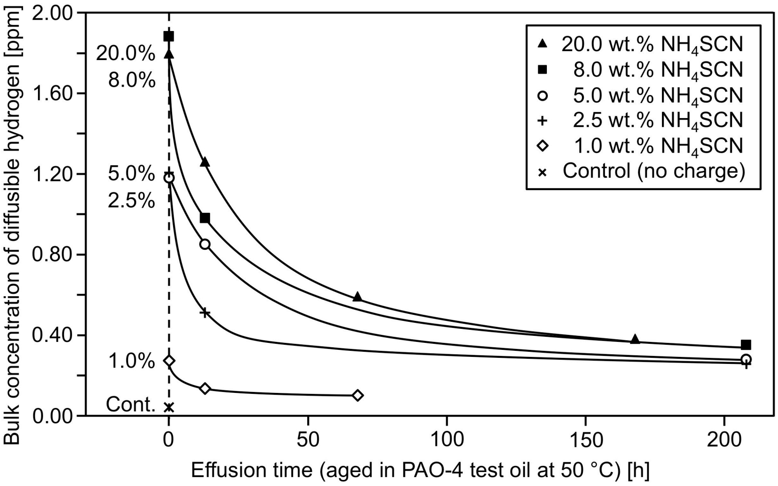

Figure 6.2.1: Diffusible hydrogen concentration effusion curve in model 26 mm specimens. See permission [3.1].

Table 6.2.1: Average concentration of diffusible hydrogen in ppm in the model 26 mm specimens for a range of hydrogen charge concentrations. Values displaying a ± value are obtained from 2 to 4 measurements and single values represent single measurements.

Effusion time [h]‡	**NH_4SCN hydrogen charge concentrations**					
	20 wt.%	**8 wt.%**	**5 wt.%**	**2.5 wt.%**	**1 wt.%**	**No charge**
0	1.80 ± 0.03	1.90 ± 0.29	1.18 ± 0.18	1.20 ± 0.10	0.27 ± 0.07	0.04
13	1.26 ± 0.09	0.98 ± 0.21	0.85 ± 0.11	0.51 ± 0.06	0.14 ± 0.02	-
68	0.59	-	-	-	0.10	-
168	0.38	-	-	-	-	-
208	-	0.35	0.28	0.26	-	-

‡ Samples held in PAO-4 test oil at 50 °C. See permission [3.1].

In all cases the concentration of diffusible hydrogen in the steel continuously decreased with effusion time. The concentration of diffusible hydrogen for all charging concentrations reduced to below 0.4 ppm after ~200 hours indicating that the RCF test rollers contained some diffusible hydrogen throughout the duration of the RCF test. Evidence showing the differences in concentration of diffusible hydrogen in the steel between the different charge levels is most apparent at the 13-hour effusion interval. This is important when comparing the formation of white etching features between tests under differing charge conditions, as it is not immediately apparent at 0-hour effusion time what differences in hydrogen concentration exist. Since fatigue crack initiation and propagation in the test rollers is expected to occur during the entire RCF test duration, an understanding of the concentration of hydrogen in the RCF test rollers is important over the range of the test duration.

TDA measurements were made on three sets of real RCF test rollers (see Table 6.2.2). Differences were seen when comparing the concentrations of diffusible hydrogen between the 26 mm and 52 mm RCF test rollers from the same hydrogen charge (8 wt.% NH_4SCN). Differences are also apparent when comparing the measurements on the 26 mm RCF test rollers in Table 6.2.2 with the measurements on model 26 mm specimens in Table 6.2.1 under the same charging conditions (8 wt.% NH_4SCN) and effusion times (0 hours). In this case the hydrogen concentration is slightly lower in the actual 26/52 mm RCF test rollers (average 1.47 ppm) than the model 26 mm specimens (average 1.90 ppm). It would seem that the concentration of diffusible hydrogen in the RCF test rollers is lower than that measured in the model 26 mm specimens due to geometrical differences, variations and uncertainties in the hydrogen charging process. Therefore the effusion curves displaying concentration of diffusible hydrogen show the differences between the charge concentrations, and therefore should be regarded as indicative and not fully representative of actual concentrations in the RCF test rollers.

Table 6.2.2: Average concentration of diffusible hydrogen in ppm in test roller sections pre-charge and post RCF test for varying hydrogen charge concentrations. Values displaying a ± value are made over a range of 2 to 3 measurements and single values are single measurements.

Test roller analysis type	NH_4SCN charge concentrations	26 mm test roller	52 mm test roller
0 hours effusion time	8 wt.%	1.37 ± 0.24	1.54 ± 0.18
Post 208 hour test (test 8)	8 wt.%	0.26	0.32
Post 208 hour test (test 9)	5 wt.%	0.37	0.40 ± 0.01

See permission [3.1].

Table 6.2.2 also shows the post RCF test TDA results using the 8 wt.% and 5 wt.% NH_4SCN charges. It can be seen that the concentration of diffusible hydrogen in the test rollers after the 208 h RCF test is similar to that of the model specimens (~0.3 – 0.4 ppm). Additional hydrogen has not diffused into the steel during the RCF test from lubricant breakdown.

6.3 Thresholds for white etching feature formation

6.3.1 Introduction

This section focuses on establishing the influence and thresholds of the concentrations of diffusible hydrogen, contact pressure and rolling contact cycles on white etching feature formation in the subsurface of hydrogen charged test rollers.

6.3.2 RCF tests and serial sectioning analysis

The RCF tests are displayed in Table 6.3.1. The maximum contact pressure was varied between 1.2 – 2 GPa and the rolling cycles between 0.5 x 10^6 – 125 x10^6 cycles. The RCF tests were terminated either when the designed test duration had elapsed (tests 2H and 4H – 12H) or when a roller spalled (tests 1H and 3H) causing an automatic stop once vibration exceeded a threshold.

Table 6.3.1: Details of RCF tests (phase 4 testing).

Test	26 mm [rpm]	52 mm [rpm]	SRR	Traction coefficient	P_{max} [GPa]	26 mm [cycles]	52 mm [cycles]	Time [h]	Stop type	WEC ?
20 wt.% NH_4SCN hydrogen charge										
1H	4000	2040	0.02	0.042	2.0	70 x 10^6	36 x 10^6	295	Spall	**Yes**
2H	4000	2000	0	0.008	2.0	50 x 10^6	25 x 10^6	208	Manual	**Yes**
3H	4000	2040	0.02	0.047	2.0	36 x 10^6	19 x 10^6	152	Spall	**Yes**
4H	4000	2000	0	0.009	2.0	7.5 x 10^6	3.8 x 10^6	31	Manual	**No**
5H	4000	2000	0	0.008	2.0	1.0 x 10^6	0.5 x 10^6	4.2	Manual	**No**
6H	4000	2000	0	0.022	1.5	50 x 10^6	25 x 10^6	208	Manual	**Yes**
7H	4000	2000	0	0.028	1.2	50 x 10^6	25 x 10^6	208	Manual	**No**
8 wt.% NH_4SCN hydrogen charge										
8H	4000	2000	0	0.008	2.0	50 x 10^6	25 x 10^6	208	Manual	**Yes**
5 wt.% NH_4SCN hydrogen charge										
9H	4000	2000	0	0.008	2.0	50 x 10^6	25 x 10^6	208	Manual	**Yes**
2.5 wt.% NH_4SCN hydrogen charge										
10H	4000	2000	0	0.008	2.0	125 x 10^6	65 x 10^6	465	Manual	**No**
1 wt.% NH_4SCN hydrogen charge										
11H	4000	2040	0.02	0.031	2.0	125 x 10^6	65 x 10^6	465	Manual	**No**
12H	4000	2000	0	0.007	2.0	50 x 10^6	25 x 10^6	208	Manual	**No**

See permission [3.1].

The white etching features in the RCF test rollers were identified and quantified using serial sectioning. For the partial wear zone analysis the length for polishing was either 300 μm or 100 μm offset from the centre of the wear track depending on the amount of white etching features observed (see Fig. 6.3.1). The material removal interval was ~3 μm.

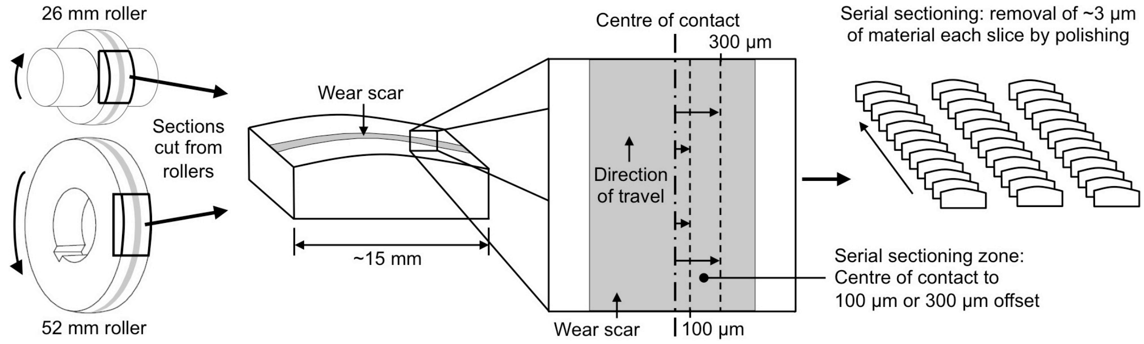

Figure 6.3.1: Partial wear zone serial sectioning analysis. See permission [3.1].

6.3.3 Results

Contact surface inspection

Optical images of typical portions of the wear tracks on the rollers in tests 1H – 12H are shown in Fig. 6.3.2. On the wear tracks corresponding to test 10H, surface pitting has occurred in some areas. An optical and SEM image of the WSF failure on the 26 mm roller in test 3H is shown in Fig. 6.3.3a and Fig. 6.3.3b. The flaking failure covers the whole width of the wear track. Surface cracking on the edge of the wear track in the rollers from test 1H and 3H occurred and is shown in Fig. 6.3.3c and Fig. 6.3.3d SEM images.

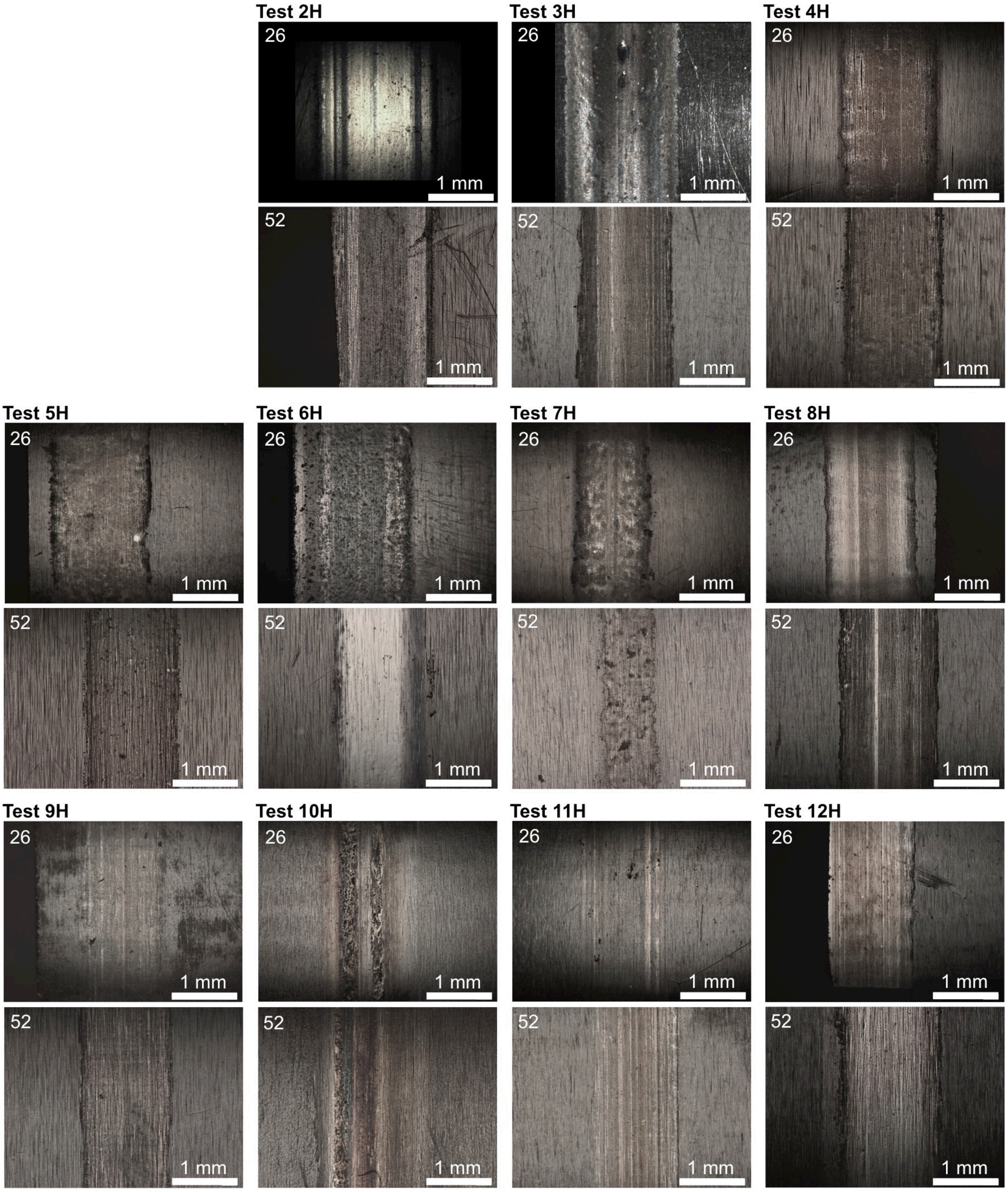

Figure 6.3.2: Optical images of wear tracks in the 26 mm and 52 mm rollers from tests 2H – 12H.

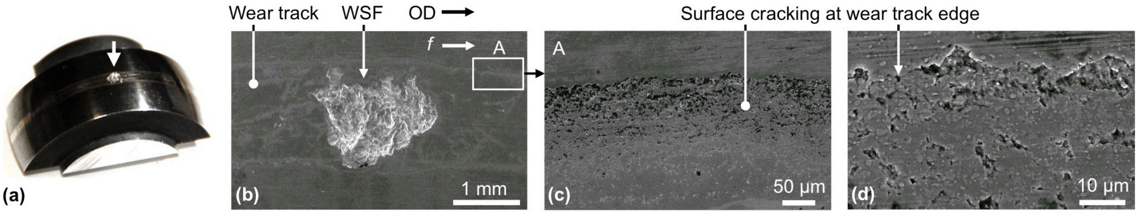

Figure 6.3.3: Surface images of the 26 mm roller in test 3H. (a) Optical image showing WSF failure. (b) SEM image of the flaking. (c) and (d) SEM images showing evidence of surface cracking at the edges of the wear scar. The directions of over-rolling direction (OD) and friction force (*f*) are from left to right. See permission [3.2].

Subsurface identification and quantification of white etching features

Typical examples of well-developed WECs from tests 1H – 3H, 6H and 8H are shown in Fig. 6.3.4.

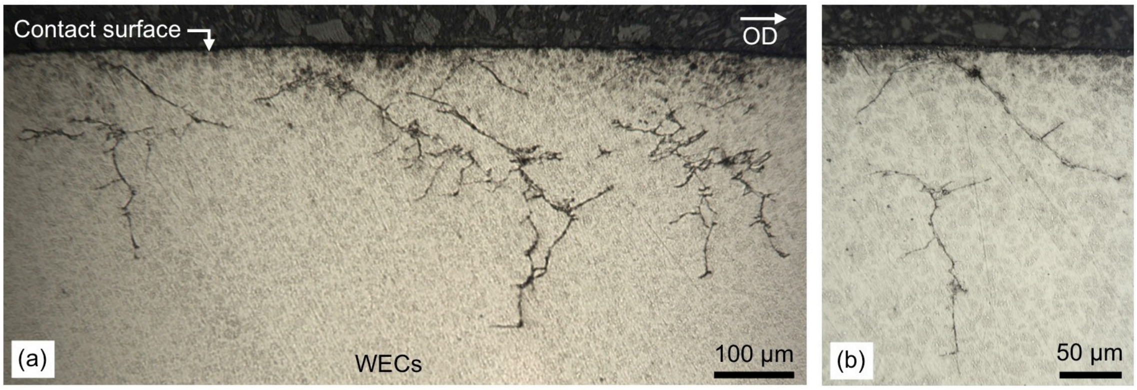

Figure 6.3.4: Optical images in the etched condition of typical well-developed WEC networks observed in the cross sections of the RCF test rollers in tests 2H, 3H, 6H and 8H. Circumferential sections, over-rolling direction left to right. See permission [3.1].

In tests 2H, 6H and 8H, a large number of WEA/WECs formed very near to the contacting surface (<25 μm in depth). Examples of these are shown in Fig. 6.3.5, where arrows highlight very small WEA features. Butterflies, or micro-cracking at inclusions with associated WEA microstructural changes, were also frequently observed in almost all test rollers; SEM images of typical formations are shown in Fig. 6.3.6. The orientations of all the butterflies/micro-cracking agree with the characteristics found in previous studies, i.e. the angle that the butterfly wings or cracks make with the tangent of the contact surface ranges between ~0 – 60° with respect to the over-rolling direction [23, 25, 26, 39]. Details of the type of inclusion, the depth and the over-rolling direction (OD) are indicated in each of the images.

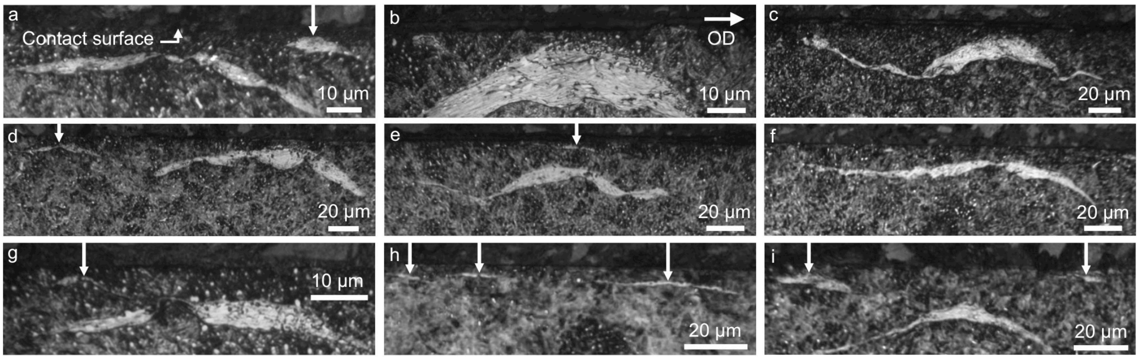

Figure 6.3.5: Optical images in the etched condition of very near surface WEA/WECs in tests 2H, 3H, 6H and 8H. White arrows point to very small WEA formations. Circumferential sections, over-rolling direction left to right. See permission [3.1].

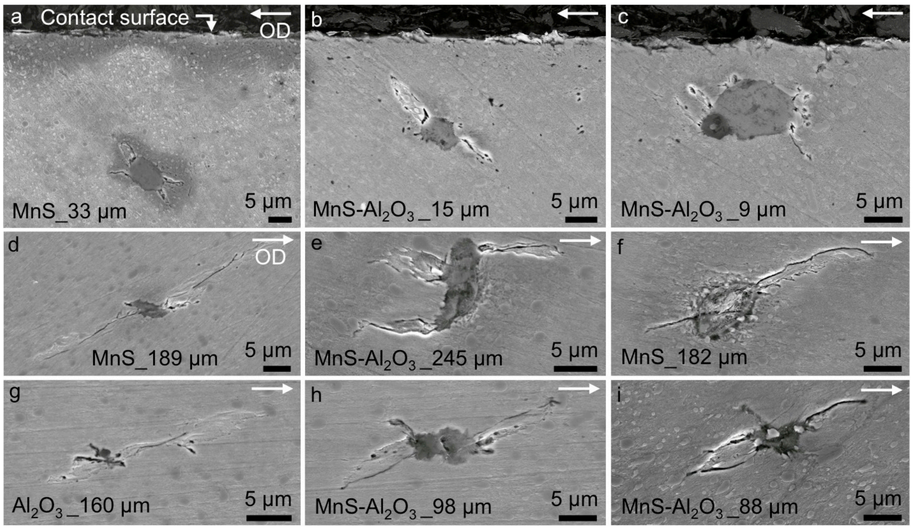

Figure 6.3.6: SEM images of typical butterflies that formed in the RCF tests. (a) to (c) (over-rolling direction right to left). (d) to (f) (over-rolling direction left to right). The lettering at the bottom of each image reveals the inclusion composition and depth below the contact surface. See permission [3.1].

The significant number of white etching features observed and details of their formation such as size and position are displayed in Figs. 6.3.8 – 6.3.16. Two schematics showing the methods for butterfly and WEA/WEC quantification are given in Fig. 6.3.7 to help interpretation of the details presented in plots Figs. 6.3.8 – 6.3.16. The plots map every observed independent white etching feature in the sections analysed. An 'independent white etching feature' refers to an entire white etching feature, usually spanning multiple slices, that is independent of other white etching features in the roller. The plots detail the maximum length of the white etching features in the circumferential direction of the roller (viewing plane, x-axis), the maximum depth from the contacting surface and the maximum length in the axial direction of the roller (polishing plane, y-axis). A single line represents the length of an independent white etching feature in the axial direction (i.e. over multiple slices). The maximum depths of the white etching features are identifiable by the style of the lines. Butterflies are mapped according to their double wing length (tip to tip) and the depth of the non-metallic inclusion associated (see Fig. 6.3.7). In case of a single winged butterfly, the wing length also includes the length of the inclusion. The total length of polishing was either 300 µm or 100 µm (starting from the centre of wear line, see Fig 6.3.1) as shown in the y-axis in Figs. 6.3.8 – 6.3.16. Each figure includes the data of both rollers for the test (colour coded). As can be seen, tests 4H, 7H and 10H – 12H only have butterfly formations while the rest of the tests produced both butterflies and WEA/WECs.

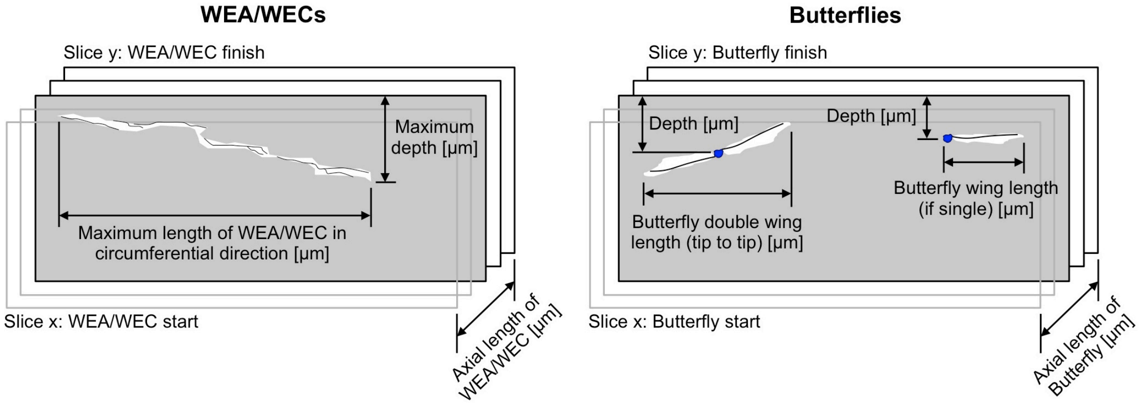

Figure 6.3.7: Schematic showing how white etching area measurements are obtained from the serial sectioning process for the mapping plots. See permission [3.1].

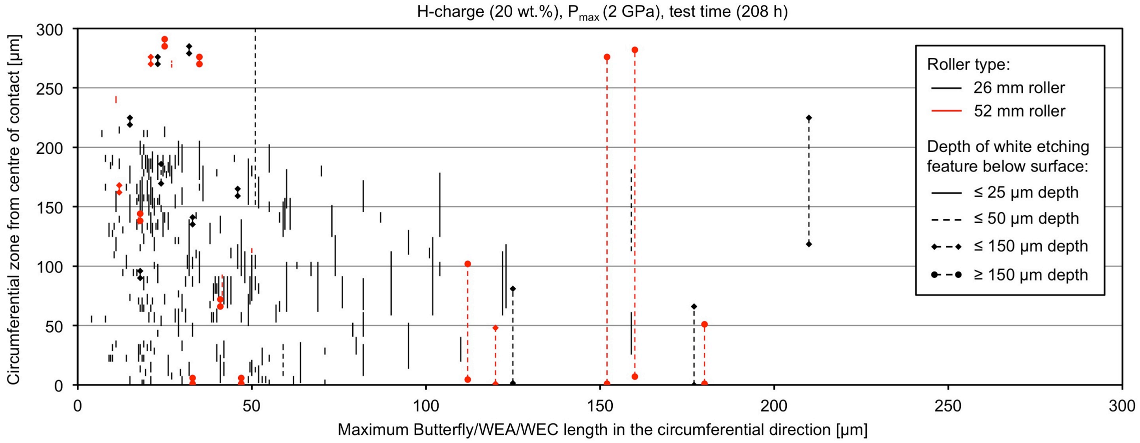

Figure 6.3.8: White etching feature formations (complete independent formations) in test 2H (20 wt.% charge). See permission [3.1].

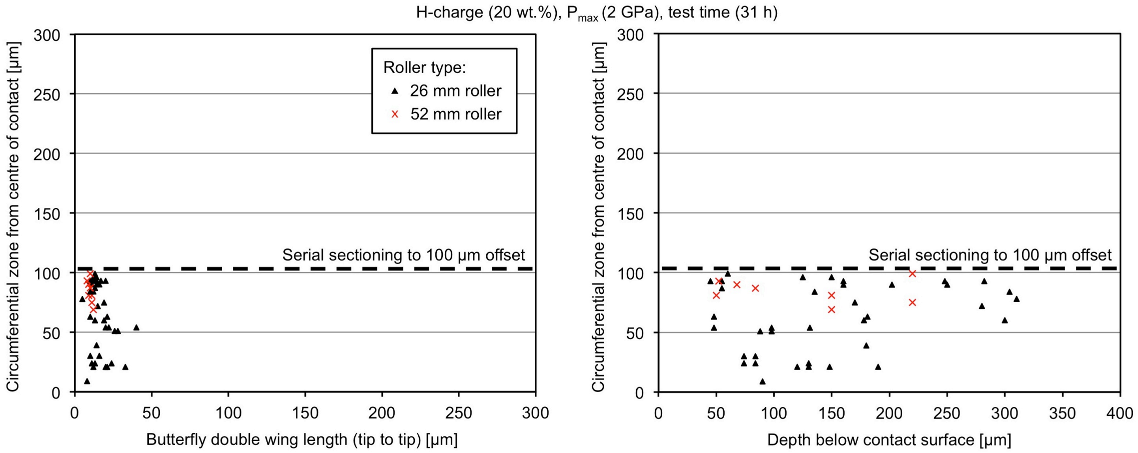

Figure 6.3.9: Butterfly formations in test 4H (20 wt.% charge). See permission [3.1].

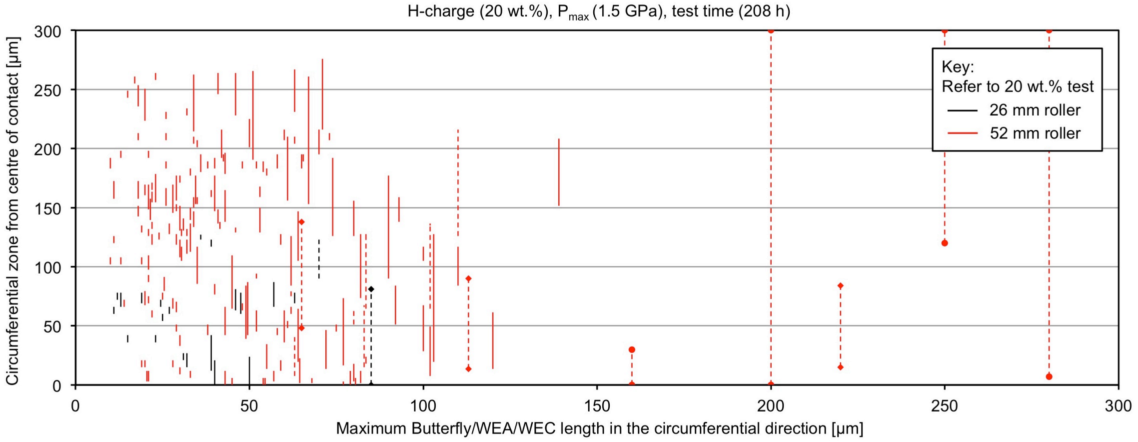

Figure 6.3.10: White etching feature formations (complete independent formations) in test 6H (20 wt.% charge). See permission [3.1].

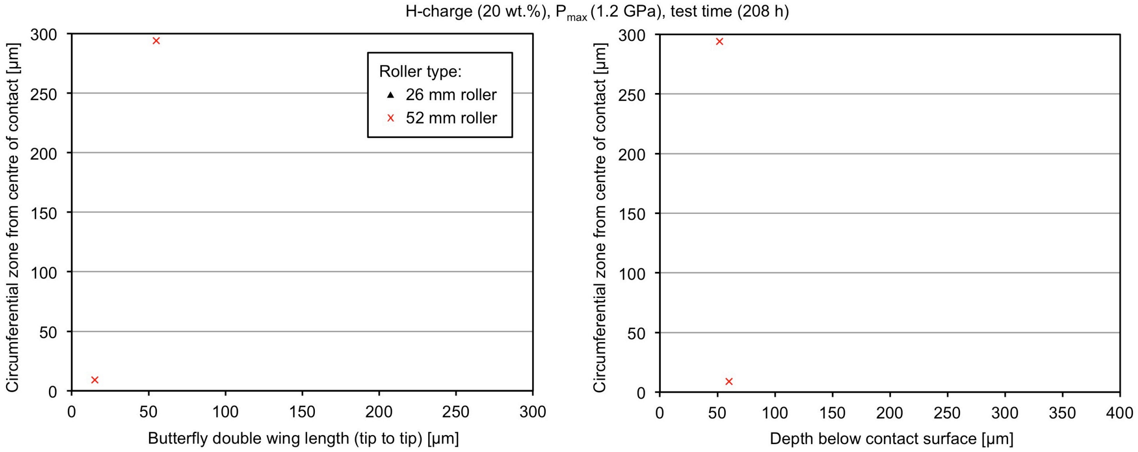

Figure 6.3.11: Butterfly formations (complete independent formations) in test 7H (20 wt.% charge). See permission [3.1].

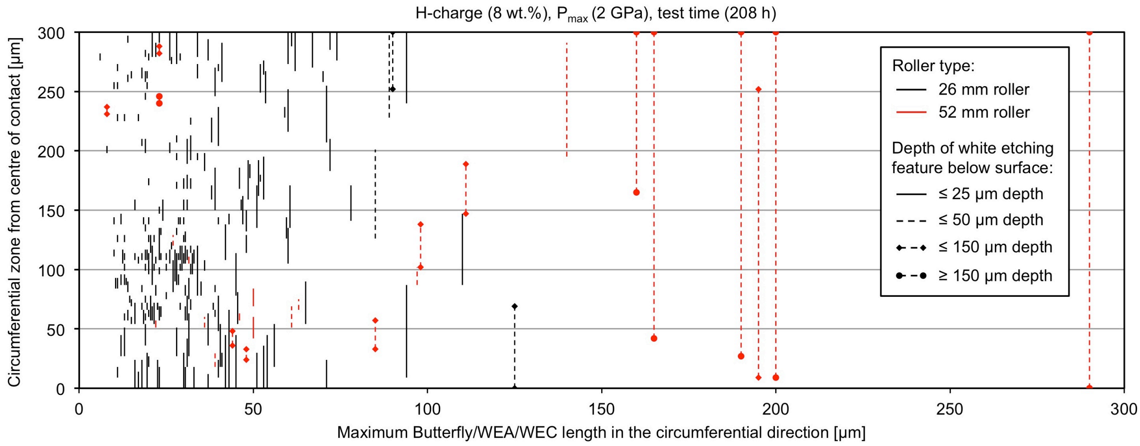

Figure 6.3.12: White etching feature formations (complete independent formations) in test 8H (8 wt.% charge). See permission [3.1].

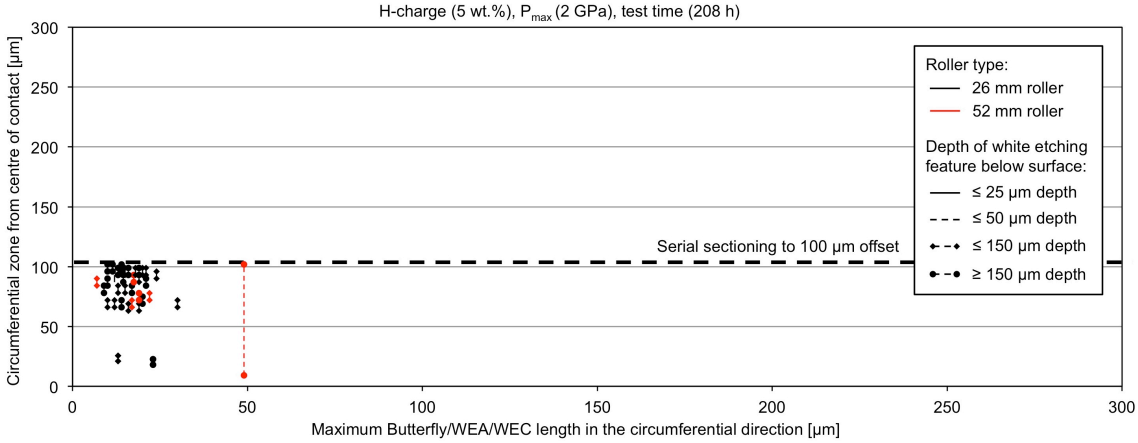

Figure 6.3.13: White etching feature formations (complete independent formations) in test 9H (5 wt.% charge). See permission [3.1].

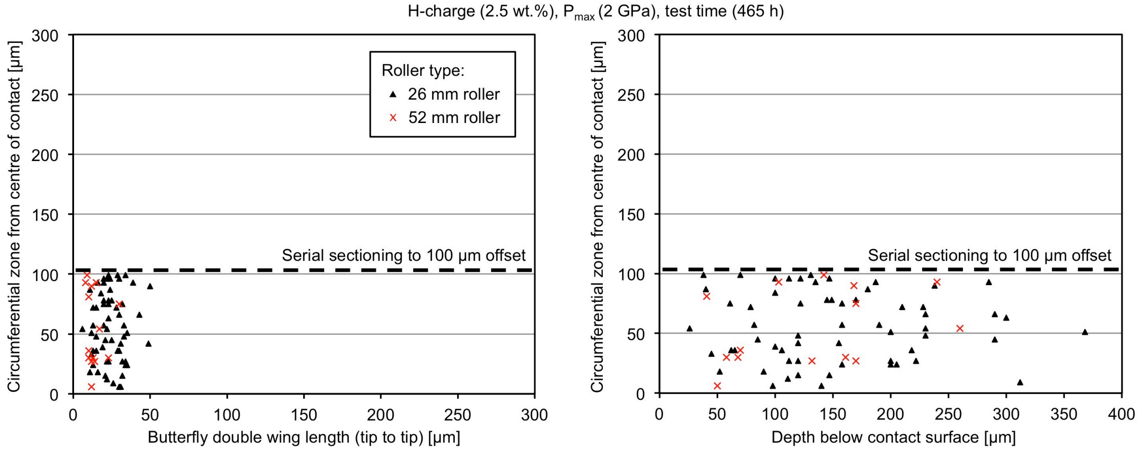

Figure 6.3.14: Butterfly formations in test 10H (2.5 wt.% charge). See permission [3.1].

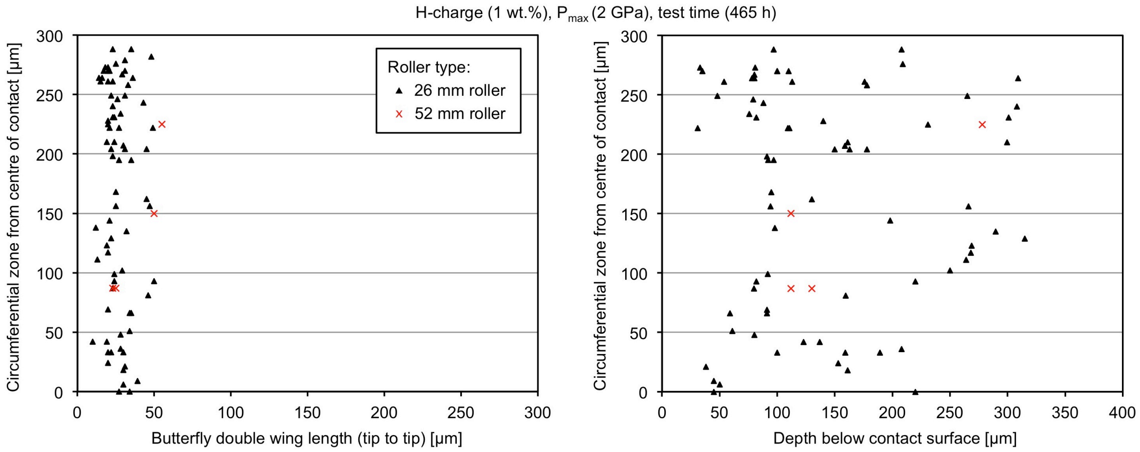

Figure 6.3.15: Butterfly formations in test 11H (1 wt.% charge). See permission [3.1].

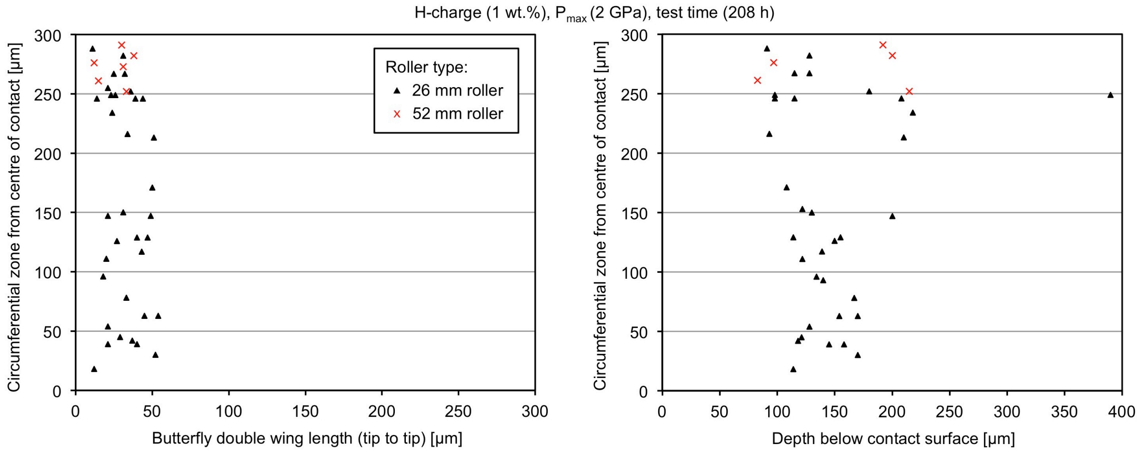

Figure 6.3.16: Butterfly formations in test 12H (1 wt.% charge). See permission [3.1].

Table 6.3.2 displays a summary of the results from 10 of the RCF tests. To summarise the large amount of information an index of 0 – 5 has been given to reflect the amount of both butterfly and WEA/WEC formations in the rollers. Detailed definitions of the indices (0 being the lowest and 5 being the highest) are also given in Table 6.3.2. It can be seen that tests under higher concentrations of diffusible hydrogen (hydrogen charges 5 – 20 wt.% NH_4SCN) allow production of WECs, whereas tests with lower concentrations of diffusible hydrogen (hydrogen charges 1 – 2.5 wt.% NH_4SCN) only created butterflies. Under the highest hydrogen charge (20 wt.% NH_4SCN), WECs were created under contact pressures of 1.5 GPa and above and rolling contact cycles of ~10 x 10^6 cycles.8

Table 6.3.2: Butterfly & WEA/WEC formation indexes in the RCF tests, number of sections analysed and contact zones analysed.

Test no.	**NH_4SCN charge concentration**	**P_{max} [GPa]**	**Test time [h]**	**Butterfly index 26 mm / 52 mm**	**WEA/WEC index 26 mm / 52 mm**	**Sections analysed 26 / 52 mm**
2H	20 wt.%	2.0	208	2 / 2	5 / 3	I / I
$3H^{0.02}$	20 wt.%	2.0	152	- / -	- / 5	- / I
4H	20 wt.%	2.0	31	4 / 2	0 / 0	I / I
5H	20 wt.%	2.0	4.2	0 / 0	0 / 0	I / I
6H	20 wt.%	1.5	208	1 / 1	2 / 5	I / I
7H	20 wt.%	1.2	208	0 / 1	0 / 0	I / I
8H	8 wt.%	2.0	208	2 / 2	5 / 3	I / II[a]
9H	5 wt.%	2.0	208	3 / 1	0 / 1[b]	II* / II[b]
10H	2.5 wt.%	2.0	465	5 / 2	0 / 0	II* / III*
$11H^{0.02}$	1 wt.%	2.0	465	3 / 1	0 / 0	II[c] / II*
12H	1 wt.%	2.0	208	2 / 1	0 / 0	I / I

Formation indexes 0 to 5: 0 = no formations, 1 = minimum amounts of formations (<5), 5 = maximum amounts of formations (~100+)

- = Not recorded

0.02: = 0.02 slide to roll ratio (SRR) in the test.

a = No butterflies or WEA/WECs found in one of the 52 mm roller sections, whereas many found in the other section (the later used for the formation plots in the Figs. 6.3.8 – 6.3.16).

b = Only one single WEC formation observed in one of the 52 mm roller sections, whereas none found in the other section (the section with the single WEC formation used for the formation plots in Figs. 6.3.8 – 6.3.16).

c = ~3X more butterflies found in one of the 26 mm roller sections (this section used for the formation plots in Figs. 6.3.8 – 6.3.16).

* = Only minor differences in amounts of white etching feature formations between the sections.

See permission [3.1].

It must be noted that there could be an element of misclassification between butterflies and WEA in Table 6.3.2, as smaller WEAs observed without inclusion interactions (because they were missed) were not classified as butterflies. This is because many inclusions found to interact with butterflies/WEAs were very small (<3 μm), so with the slice thickness of ~3 μm during serial sectioning, inclusions could be fully removed between slices and therefore missed. In tests where several sections are analysed, a single section has been chosen for mapping in the plots in Figs. 6.3.8 – 6.3.16. If there was little difference between the sections then a section was chosen at random for mapping, however if a large variance was observed between sections then the section containing the highest amount of white etching features was chosen (details of the sections chosen can be seen in the last column of Table 6.3.2).

Residual stress development

The subsurface residual stress distribution in the 52 mm rollers post RCF testing in test 2H and 3H at the centre and edge of the wear track is shown in Fig. 6.3.17. In Fig. 6.3.17a and Fig. 6.3.17b little change in the residual stresses were seen for test 2H and no sharp peak in compressive residual stress developed (e.g. see Fig 2.3.5 in chapter 2). However in test 3H significant compressive residual stress in the axial direction in both the centre and edge zones developed from the surface to an approximate depth of 1 mm in Fig. 6.3.17c and Fig. 6.3.17d.

Only minor compressive or tensile variations in the residual stresses in the circumferential direction are present for this case.

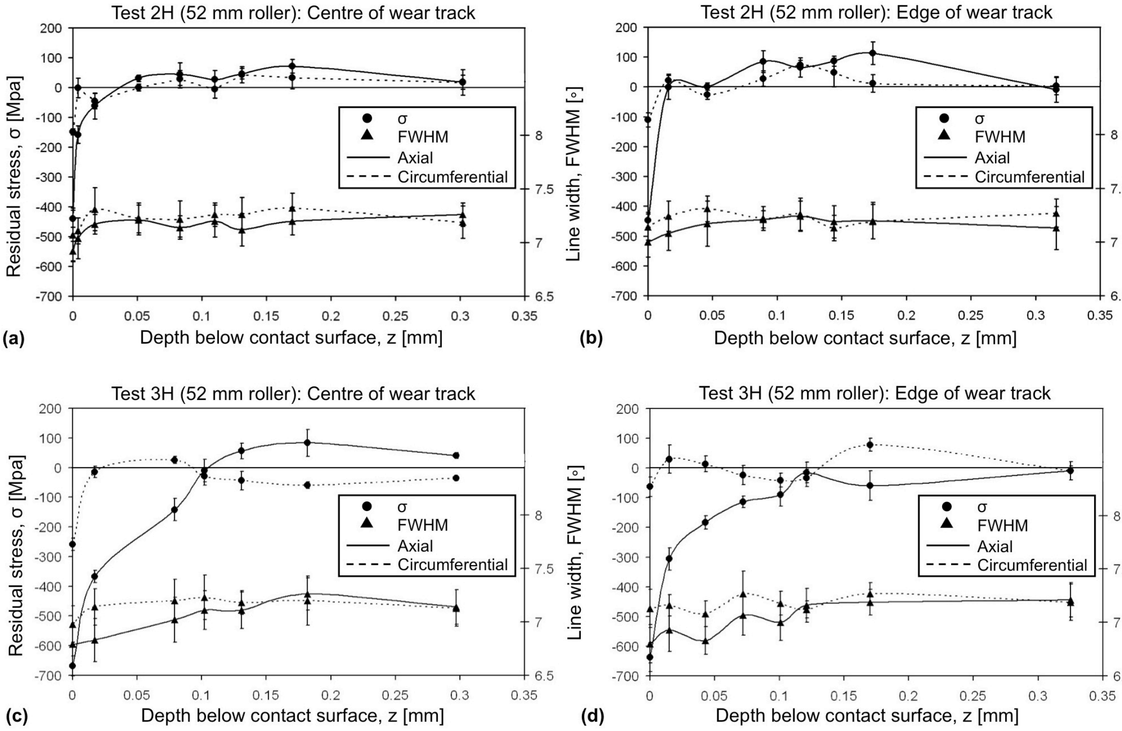

Figure 6.3.17: Residual stress and FWHM plots in the 52 mm roller of test 2H and test 3H. (a) Test 2H at centre of wear track, (b) Test 2H at edge of wear track, (c) Test 3H at centre of wear track, (b) Test 3H at edge of wear track. See permission [3.2].

6.3.4 Discussion

Contact surface inspection and RCF tests

Only the 26 mm roller of test 1H and 3H spalled due to WSF. This could be an influence of the higher concentration of hydrogen (20 wt.% NH_4SCN charge) and increased traction from the 0.02SRR in test 1H and 3H. Metallographic analysis at the vicinity of the spall area has confirmed that the surface spall was a result of the white etching features formed in the immediate subsurface region. The fact that the flaking failure occurred in the shallow surface also agrees with the typical characteristics of WSF failure.

It is proposed that the presence of surface cracking found at the edges of the wear track on the test rollers of test 1H and 3H is due to boundary lubrication and the enhanced tensile stresses at the edges of the contact ellipse [152] caused by the 0.02SRR and increased traction in these tests. However this phenomenon did not occur in test 11H under a 1.0 wt.% NH_4SCN charge which also experienced a 0.02SRR. Therefore the combination of SRR and a much higher concentration of hydrogen is the likely cause of surface cracking at the edges of the wear track.

This surface cracking could have been an initiation point for WECs, however no evidence was found that this was the case.

The surface pitting on the wear tracks of test 10H under a 2.5 wt.% NH_4SCN charge could have been caused by the high number of stress cycles experienced in this test compared to most other tests. However this surface pitting did not occur in test 11H under a 1.0 wt.% NH_4SCN charge that experienced the same number of stress cycles. Therefore it is proposed that a combination of the increased number of stress cycles and slightly higher concentration of hydrogen caused the micropitting. Again it could be thought that cracks could start at this surface damage, however no evidence was found that this occurred in the test from a detailed serial sectioning analysis in the aim of deducing this aspect specifically.

Propensity of butterfly formations

From the butterfly indices in Table 6.3.2 it can be seen that, except in test 5H and in the 26 mm roller of test 7H, butterflies were observed in all other rollers. No direct relationship between butterfly formations and concentration of diffusible hydrogen was found (when comparing tests at 208 hours or higher duration under a P_{max} of 2 GPa). Contact pressure was shown to strongly control the formation of butterflies/micro-cracking at inclusions. Comparing tests 2H, 6H and 7H under the same hydrogen charging conditions and rolling cycle numbers, when the contact pressure decreased from 2 GPa to 1.5 GPa to 1.2 GPa, the butterfly index also reduced from 2/2 to 1/1 to 0/1. Only two butterflies were found in the 52 mm roller of test 7H (1.2 GPa), and none in the 26 mm roller. The depths the two butterflies formed (~65 μm) in this threshold test were found to be near those of maximum shear stress ($\tau_{o,max}$ of 256 MPa at 63 μm depth, τ_{max} of 388 MPa at 105 μm depth). This suggests that 1.2 GPa is near the threshold for butterfly formation (under a 20 wt.% NH_4SCN charge and 208 h test duration). An orthogonal shear stress (τ_o) of ~400 – 500 MPa has been previously cited [22, 24] as a threshold for butterfly formation in steel without the presence of diffusible hydrogen. It can be seen that $\tau_{o,max}$ is well below this at 256 MPa under a P_{max} of 1.2 GPa in these tests. In addition two other studies reported thresholds of 1.3 GPa and 1.4 GPa as threshold maximum contact pressures for butterfly formations [118, 143]. These findings suggest that the reason why only a couple of butterflies were created under 1.2 GPa in this study is insufficient shear stress for crack propagation from inclusions. Rolling cycle number is also an important parameter, where it can be seen that a step change in butterfly formations occurred between test 5H (4.2 h) and test 4H (31 h). However, once a threshold number of rolling cycles has been experienced, a relationship of increasing formation with increasing cycle number did not exist (e.g. compare tests 2H, 3H and 4H, and also tests 11H and 12H).

Propensity of WEA/WEC formation and formation thresholds

From Table 6.3.2 it can be seen that the rollers from tests 2H, 3H, 6H and 8H showed high quantities of WEA/WECs with indexes ranging from (2) to (5). However, no WEA/WECs were found in either roller from tests 4H, 5H, 7H, 10H, 11H and 12H, or in the 26 mm roller of test 9H.

- Influence of diffusible hydrogen concentration

  Tests 2H, 3H, 6H & 8H, which are either at the 20 wt.% or 8 wt.% charge levels, revealed a high amount of WEA/WEC formations. Comparing tests 2H, 8H, 9H and 12H, where the contact pressure and test time were constant and the concentration of NH_4SCN hydrogen charge reduced from 20 wt.% to 1 wt.%, the WEA/WEC index reduced from the maximum (5) down to no formations (0). A step change in WEA/WEC formation occurred between the 8 wt.% and 5 wt.% charges in tests 8H and 9H respectively. In test 9H with 5 wt.% NH_4SCN hydrogen charge, two sections for both the 26 mm and 52 mm rollers were analysed. Only a single WEC formation was found to have occurred in one of the 52 mm roller sections, with no WECs found in the remaining sections. Therefore test 9H is a threshold test for concentration of diffusible hydrogen. Since test 10H at the 2.5 wt.% NH_4SCN charge showed no WEA/WEC formation in any of the sections analysed, even after an extended testing time of 465 hours, suggests that the threshold for WEA/WEC formation is between the 2.5 wt.% and 5 wt.% NH_4SCN hydrogen charges at a P_{max} of 2 GPa with the test configuration in this study. Based on measurements from model samples this corresponds to an initial hydrogen concentration of ~1.20 ppm in the 5 wt.% and 2.5 wt.% NH_4SCN hydrogen charges, which decreased to ~0.85 ppm and ~0.51 ppm after 13 hours respectively. Since the concentration in the actual RCF test rollers was found to be slightly lower than that in the equivalent model rollers (see Table 6.2.1 & Table 6.2.2), a conservative estimate for WEC formation with the test configuration in this study is given as an initial concentration of diffusible hydrogen at the start of RCF testing of ~1 ppm. This concentration has been previously cited a possible threshold for WSF [42].

- Influence of maximum contact pressure

  Comparing tests 2H, 6H and 7H under the same hydrogen charging conditions and test durations, when the maximum contact pressure was kept at 2 GPa and 1.5 GPa, reasonably large quantities of WEA/WECs were found in the rollers. However no WEA/WECs were found in the rollers when the pressure decreased to 1.2 GPa as in test 7H. This indicates that the contact pressure threshold for WEA/WEC formation is between 1.2 GPa and 1.5 GPa.

- Influence of cycle number or test duration

  Comparing tests 2H – 5H under the same hydrogen charge conditions and contact pressure, when the test duration was decreased from 208 h, 152 h, 31 h to 4.2 h, the WEA/WEC index also reduced from maximum (5) to no formations (0). A step change is seen between test 3H (152 hours) and test 4H (31 hours). When comparing rolling cycle numbers directly irrespective of roller type, WEA/WECs apparently form between 7.5 x 10^6 cycles (test 4H, 26 mm roller) and 19 x 10^6 cycles (test 3H, 52 mm roller). Therefore an estimate of the cycle number at which WEA/WECs form is ~10 x 10^6 cycles, under a P_{max} of 2 GPa and 20 wt.% NH_4SCN hydrogen charge and the test configuration in this study.

- Combined threshold for WEA/WEC formation

  From the above, it can be seen that the influences of diffusible hydrogen, contact pressure and rolling cycles on the formation of WEA/WECs are inter-related. When the hydrogen charge is below 5 wt.% NH_4SCN, even under the highest contact pressure of 2 GPa and the highest number of rolling cycles at 125 x 10^6 (465 hours), no WEA/WEC formations were found (see tests 10H – 12H). Also when the number of rolling cycles is low (between 7.5 x 10^6 to 19 x 10^6 cycles), and the rollers contain the highest concentration of diffusible hydrogen (20 wt.% NH_4SCN charge) with the highest test contact pressure (P_{max} 2 GPa), no WEA/WEC were found (see tests 4H and 5H). The threshold for WEA/WEC formation can be estimated as a combination of a ~1 ppm concentration of diffusible hydrogen (initial concentration at the start of RCF test), rolling cycle number of >10 x 10^6 and maximum contact pressure of >1.2 GPa.

White etching feature depth characteristics

For the lower duration tests and those with lower concentration of diffusible hydrogen (1 wt.% – 5 wt.% charges), few butterflies formed at depths close to the contact surface (<50 µm), but rather scattered around the depths of maximum shear stress ($\tau_{o,max}$ depth of 107 µm, τ_{max} depth of 178 µm). This is in contrast to the high amounts of white etching features that formed at depths very near surface (<25 µm) in the tests with higher concentrations of diffusible hydrogen (8 wt.% and 20 wt.% charges). An explanation for the lack of butterflies at depths <25 µm in the 1 wt.% – 5 wt.% tests could be that the increased concentration of diffusible hydrogen present in the steel for the 8 wt.% and 20 wt.% tests enabled crack initiation and propagation at shallower depths where magnitudes of shear stresses are lower. The reason why no near surface butterflies were found to form in the lower duration tests (e.g. test 4H) could be due to insufficient stress cycles for butterfly formation at these lower shear stress zones.

Uniformity of white etching feature distribution in rollers

To confirm the uniformity of the white etching feature formations around the rollers, repeated analyses on multiple sections from same roller were conducted for a number of tests, e.g. tests 8H – 11H. This process revealed some variability in the distribution of white etching features. In most cases the variability between sections is small, as seen in tests 9H, 10H and 11H (52 mm roller only for test 11H). However, in other cases, large variability has been observed. For example in test 8H two sections of the 52 mm roller were analysed where one of the sections was found to contain many white etching features (see Fig. 6.3.12), whereas in the other section no white etching features were found. In test 11H, where two sections of the 26 mm roller were analysed, one was found to contain approximately three times more butterflies than the other (see Fig. 6.3.15). This shows that it is extremely important to examine multiple locations in test rollers/bearings to ensure a representative analysis. False conclusions regarding WEC formation may arise after incomplete metallographic examination. Although some tests in this study did not have multiple sections analysed, the tests at the threshold for formation of butterflies or WEA/WECs had multiple sections analysed to confirm observations. The differences in white etching feature formation in the same test rollers may be due to variability in the distribution of diffusible hydrogen concentrations in the sections, local diffusible hydrogen concentration and variability in non-metallic inclusions in the rollers. The variability in concentration of diffusible hydrogen in different sections of a roller has been shown in Table 6.2.1 and Table 6.2.2. However, the variability of the inclusion type/distributions was not investigated in this study.

Residual stress development

No peak in subsurface compressive residual stress such as those shown in Fig. 2.3.5 in chapter 2 was found in the 52 mm rollers in both tests. This was expected as there is evidence that these peaks do not develop at contact stresses below 2.4 GPa [32, 104, 107]. However the development of the compressive residual stresses in the ~0 – 0.1 mm subsurface zone in the axial direction in test 3H with slip in the contact are unusual. Since this did not occur in test 2H with pure rolling it was investigated if this phenomenon could be explained due to slip in the contact in test 3H increasing subsurface shear stresses in magnitude and shifting these towards the surface causing retained austenite decay to martensite with its associated volumetric expansion inducing compressive residual stresses. However retained austenite measurements were made at depths of 0.011 mm and 0.052 mm at the centre of contact and this indicated no retained austenite decay to have occurred.

Gegner [106] reports on a similar distribution of compressive residual stress in the circumferential direction (as opposed to axial in this study) in various service bearings (profiles in each direction are expected to be similar in the absence of vibrations [106]). Evidence of residual stress profiles that have monotonically increasing curves from the contact surface to a depth of ~0.1 to 0.15 mm are shown, where these are termed type A residual stress profiles (see Fig. 33b, Fig. 34 and Fig. 54 in [106]). Gegner reports that type A residual stress profiles are caused by the impact of vibrations during service, however clearly vibrations such as these were not existent with the RCF tests in this study.

The development of the axial near surface compressive residual stress in the 52 mm roller of test 3H in this study is not completely clear, but could be due to the influence of hydrogen in the steel. Further work is required to elucidate the mechanism behind the observed phenomenon.

6.3.5 Conclusions

This section focuses on establishing the influence and thresholds of the concentrations of diffusible hydrogen, contact pressure and rolling contact cycles on white etching feature formation in the subsurface of hydrogen charged test rollers. The hydrogen charging process aims to replicate hydrogen entry into bearings by the bulk diffusion mechanism at wear induced nascent surfaces. With this technique the test rollers contain various quantifiable concentrations of diffusible hydrogen at the onset of RCF testing, however local concentrations are unknown. The application of serial sectioning has been used to successfully map the subsurface white etching features formed in sections of the RCF test rollers. It was found that:

1. Butterfly formation was independent of the concentration of diffusible hydrogen at durations of more than 208 hours and maximum contact pressures of 2 GPa. At pressures in the range of 1.2 – 2 GPa, butterfly formation increased with pressure and with the number of rolling cycles to a threshold.
2. WEA/WEC formation thresholds were found to be: i) A concentration of diffusible hydrogen between the 5 – 2.5 wt.% NH_4SCN hydrogen charges under a maximum contact pressure of 2 GPa. ii) A maximum contact pressure in excess of 1.2 GPa under a 20 wt.% NH_4SCN charge. iii) Approximately 10 x 10^6 rolling cycles under a maximum contact pressure of 2 GPa and 20 wt.% NH_4SCN charge.
3. Comparison of several sections from the same roller revealed there is variability in the white etching feature distribution. It is therefore important to examine multiple locations, especially in large bearings, to ensure a representative analysis is conducted, as false conclusions on white etching feature formation may be made based on incomplete metallographic examinations.

4. No formation of dark etching region (DER), peak compressive residual stress at a depth corresponding to the maximum material stressing or retained austenite decay was found to have occurred in the test rollers. However near surface compressive residual stress development in the axial direction was found to have developed in the test with slip in the contact that is currently not fully understood.

6.4 Initiation and propagation of white etching features

6.4.1 Introduction

This section focuses on elucidating the initiation and propagation mechanisms of WECs in hydrogen charged test rollers. Numerous WECs have been mapped in their entirety by serial sectioning and one WEC has been modelled in 3-D. FIB tomography has been used to verify initiators and construct 3-D crack models.

6.4.2 Serial sectioning analysis

In addition to gaining crack initiation information throughout the partial wear zone serial sectioning analysis in section 6.3 of this chapter, a full wear zone serial sectioning analysis was conducted on the 52 mm roller of test 3H only. Sectioning over approximately 300 slices corresponding to a distance of ~1200 μm was conducted (~600 μm either side of the centre of contact, see Fig. 6.4.1). The material removal interval was ~5 μm.

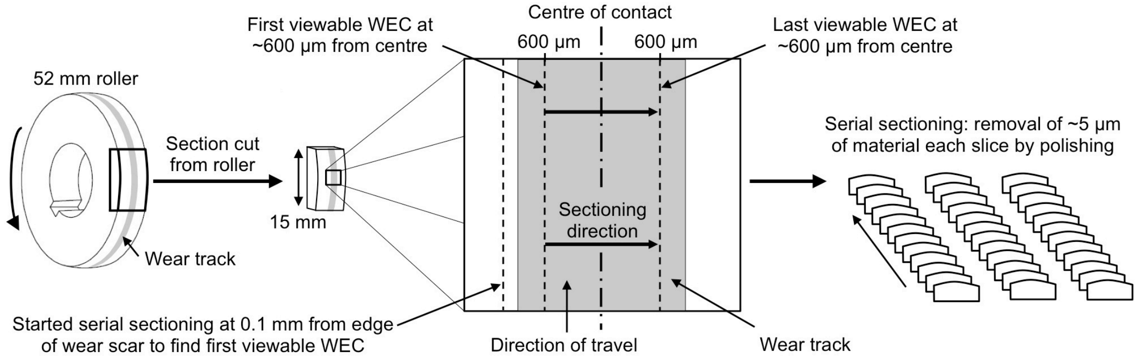

Figure 6.4.1: Full wear zone serial sectioning analysis. See permission [3.2].

6.4.3 Results

Full wear zone serial sectioning analysis

In total 15 independent WECs were mapped during the serial sectioning and these varied in size, shape, orientation and location in the 52 mm roller section of test 3H. Table 6.4.1 summarises the features of all the 15 WECs mapped. The WECs circumferentially spanned a length ranging from 0.2 – 1.3 mm, a length in the axial direction ranging from about 0.15 – 0.9 mm and the WECs extended to a depth below the contact surface of 0.15 – 0.55 mm. Only two of the 15 WECs (WEC-3S and WEC-4S) made a connection with the surface. Information on independent butterflies that are not connected to these 15 WECs is also included (only butterflies that had crack lengths ≥10 μm are listed).

Table 6.4.1: Inclusions interacting with WECs 1 – 15 and independent extended butterflies.

Circumferential plane in contact zone [mm]	**Separate extended butterflies**	**WEC 1**	**WEC 2**	**WEC 3-*S***	**WEC 4-*S***	**WEC 5**	**WEC 6**
		S, D mm 0.3, 0.2	S, D mm 0.35, 0.2	S, D mm 0.2, 0.15	S, D mm 0.25, 0.15	S, D mm 0.4, 0.55	S, D mm 1.3, 0.55
-0.550 to -0.600				▨		▨	▨
-0.500 to -0.550							
-0.450 to -0.500	$A^{*(21),22}$						D^{*1_91}
-0.400 to -0.450	$D_{Dup}^{(15),8}$			$D_{sulf}^{*2,2}$			
-0.350 to -0.400	$D_{cas}^{(65),40}$	▨		▨			
-0.300 to -0.350	$X^{*(12),192}$, $D^{*(30),8}$				▨	A^{*2_83}	$D_{Dup}^{1\_118}$
-0.250 to -0.300	$D^{*(18),112}$				A^{1_53}	A^{1_82}, $D_{sulf}^{1\_130}$ A^{*3_488}	D^{*2_137}
-0.200 to -0.250		▨					
-0.150 to -0.200							$D_{sulf}^{*3\_200}$, F^{2_142}
-0.100 to -0.150							
-0.050 to -0.100	$D^{*(15),146}$						
0.000 to -0.050						F^{3_250}	$D_{Dup}^{1\_70}$
0.000 to 0.050			▨				
0.050 to 0.100					▨		D^{1_10}
0.100 to 0.150	$A/D_{Dup}^{(100+),21}$						X^{*1_48}, $D_{cas}^{1\_149}$ $D_{DupTi}^{3\_130}$, F^{1_73}
0.150 to 0.200	$D_{Dup}^{*(18),x}$					$D_{Dup}^{1\_120}$	F^{2_48}, X^{*2_77}
0.200 to 0.250							C^{1_39}, F^{1_39}, F^{3_81}, F^{1_56}
0.250 to 0.300	$D_{sulf}^{*(18),18}$, $D^{*(32),20}$						
0.300 to 0.350	$D_{sulf}^{(10),14}$, $A/D_{Dup}^{*(20),16}$						D^{1_157}, $D_{sulf}^{1\_41}$
0.350 to 0.400			▨				$D_{sulf}^{2\_155}$
0.400 to 0.450							
0.450 to 0.500						▨	$D_{sulf}^{*1\_127}$
0.500 to 0.550							▨
0.550 to 0.600							
NMI Total (type)		-	-	1^2	1^1	3^1, 1^2, 2^3	13^1, 5^2, 3^3
NMI Total	13	-	-	1	1	6	21

Circumferential plane in contact zone [mm]	**WEC 7**	**WEC 8**	**WEC 9**	**WEC 10**	**WEC 11**	**WEC 12**	**WEC 13**	**WEC 14**	**WEC 15**
	S, D mm 0.45, 0.3	S, D mm 0.45, 0.25	S,D mm 0.65, 0.4	S, D mm 0.35, 0.3	S, D mm 0.35, 0.35	S, D mm 0.8, 0.45	S, D mm 0.3, 0.15	S, D mm 0.55, 0.5	S, D mm 0.45, 0.3
-0.550 to -0.600									▨
-0.500 to -0.550									
-0.450 to -0.500					▨	▨	▨		
-0.400 to -0.450				▨			$D_{Dup}*^{1\_42}$		D^{2_127}
-0.350 to -0.400									
-0.300 to -0.350								▨	
-0.250 to -0.300			▨	$D_{Dup}^{3\_87}$		$X*^{2\_110}$, $D_{cas}^{3\_321}$	A^{2_79}		
-0.200 to -0.250	▨	▨		$A*^{2\_200}$		$A/D_{Dup}*^{2\_311}$	▨		
-0.150 to -0.200					$D_{Dup}^{1\_57}$				
-0.100 to -0.150					A^{2_37}			$D_{Dup}^{1\_102}$	
-0.050 to -0.100				▨		$X*^{2\_52}$			
0.000 to -0.050	F^{2_87}				$A*^{2\_91}$	F^{1_91}, F^{2_49}, F^{2_100}		$D_{cas}^{1\_50}$	▨
0.000 to 0.050	$X*^{2\_63}$, F^{2_118}				$D_{cas}^{2\_115}$	$X*^{3\_131}$		$D_{Dup}^{1\_70}$, $D*^{1\_129}$	
0.050 to 0.100			F^{1_132}		$D_{sulf}*^{3\_93}$, $D_{Dup}^{1\_101}$				
0.100 to 0.150									
0.150 to 0.200	$D_{cas}^{1\_151}$	$D_{sulf}*^{1\_26}$			▨				
0.200 to 0.250		A^{1_23}, A^{1_29}	$D_{sulf}^{1\_81}$			$D_{Dup}^{1\_177}$			
0.250 to 0.300						$D_{cas}^{1\_100}$, $D_{Dup}^{2\_96}$			
0.300 to 0.350		▨	$A*^{3\_230}$					$A*^{1\_68}$	
0.350 to 0.400			$A/D_{sulf}^{1\_87}$						
0.400 to 0.450	▨							▨	
0.450 to 0.500			▨			▨			
0.500 to 0.550									
0.050 to 0.600									
NMI Total (type)	1^1, 3^2	3^1	3^1, 1^3	1^2, 1^3	2^1, 3^2, 1^3	3^1, 6^2, 2^3	1^1, 1^2	5^1	1^2
NMI Total	4	3	4	2	6	11	2	5	1

KEY: WEC inclusions

See Fig. 6.4.3 for KEY to WEC table data entries.

KEY: Extended butterfly column

Superscript (#), #: (length of longest crack from inclusion), depth of inclusion.

Inclusion type:

A: manganese sulfide or sulfide duplex, C: silicate, D: globular oxide, D_{sulf}: globular sulfide, D_{Dup}: globular duplex inclusion (e.g. globular manganese and/or calcium sulfide surrounding aluminate), D_{cas}: globular calcium sulfide, D_{DupTi}: globular sulfide with Ti(C,N), F: iron oxide and iron-chromium oxide type, X: unknown (e.g. inclusion pull-out), *: Assumed inclusion composition based on appearance in optical microscopy as not analysed in with SEM/EDS.

Other:

- The information of WEC length in the axial direction can be viewed under each WEC-# as shaded cells, indicating the first view and end view of the WEC during the serial sectioning process.
- WEC circumferential crack length span, and length of WEC in depth direction, can be viewed as the (S, D mm) data column located under each WEC-#.

S, D mm under the WEC-# columns are: S = maximum circumferential span of WEC in [mm], D = maximum depth of WEC in [mm]. E.g. 0.2, 0.3 corresponds to 0.2 mm maximum circumferential span and 0.3 mm maximum depth.

See permission [3.2].

In total, 67 inclusions were found to interact with 15 independent WECs. Table 6.4.1 includes information on the inclusion type, location in the roller/WEC and likelihood of its initiation of the WECs (the later as a ranking from 1 to 3). A rank of 1 or 2 has been used for those inclusions that appear to have been involved in the initiation of the WEC, whereas a rank of 3 has been used when this did not appear to be the case. Inclusions were judged to be crack initiators from the inclusions chemical composition, depth below the contact surface and crack continuity in the near vicinity of the inclusion. Short type A sulfide inclusions, MnS associated inclusions (D_{sulf}, D_{cas} and D_{Dup}), and type D inclusions were the inclusions that were found to interact the most with the extended butterflies and WECs and the maximum length/diameters were 20 – 30 µm (type A) and 7 – 10 µm (type D). Examples of inclusions/butterflies interacting with the WECs can be viewed in Fig. 6.4.2b and Fig. 6.4.3. The key above the images in Fig. 6.4.3 illustrates each parameter used in the SEM images and explains the ranking system used to judge crack initiation. Inclusions interacting with the 15 WECs are summarised in Fig. 6.4.4 showing their spatial distribution in the circumferential plane and depth below the contact surface. Inclusions that initiated extended butterflies are also shown.

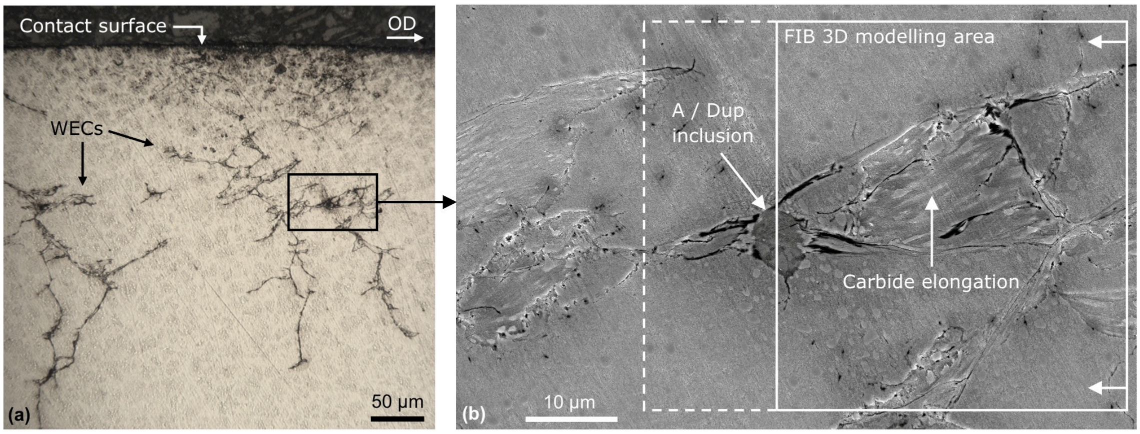

Figure 6.4.2: Images showing an example of a inclusion-WEC interaction. Test 3H, 52 mm roller circumferential section, over-rolling direction (OD) left to right. (a) Optical image. (b) SEM image. The inclusion was identified by EDS as MnS type lying at depth of 145 μm beneath the contact surface at a distance of 0.40 mm from the centre of the contact. Solid lined box represents the FIB tomography area used for 3D modelling, the dashed line represents the total area milled by FIB tomography. See permission [3.2].

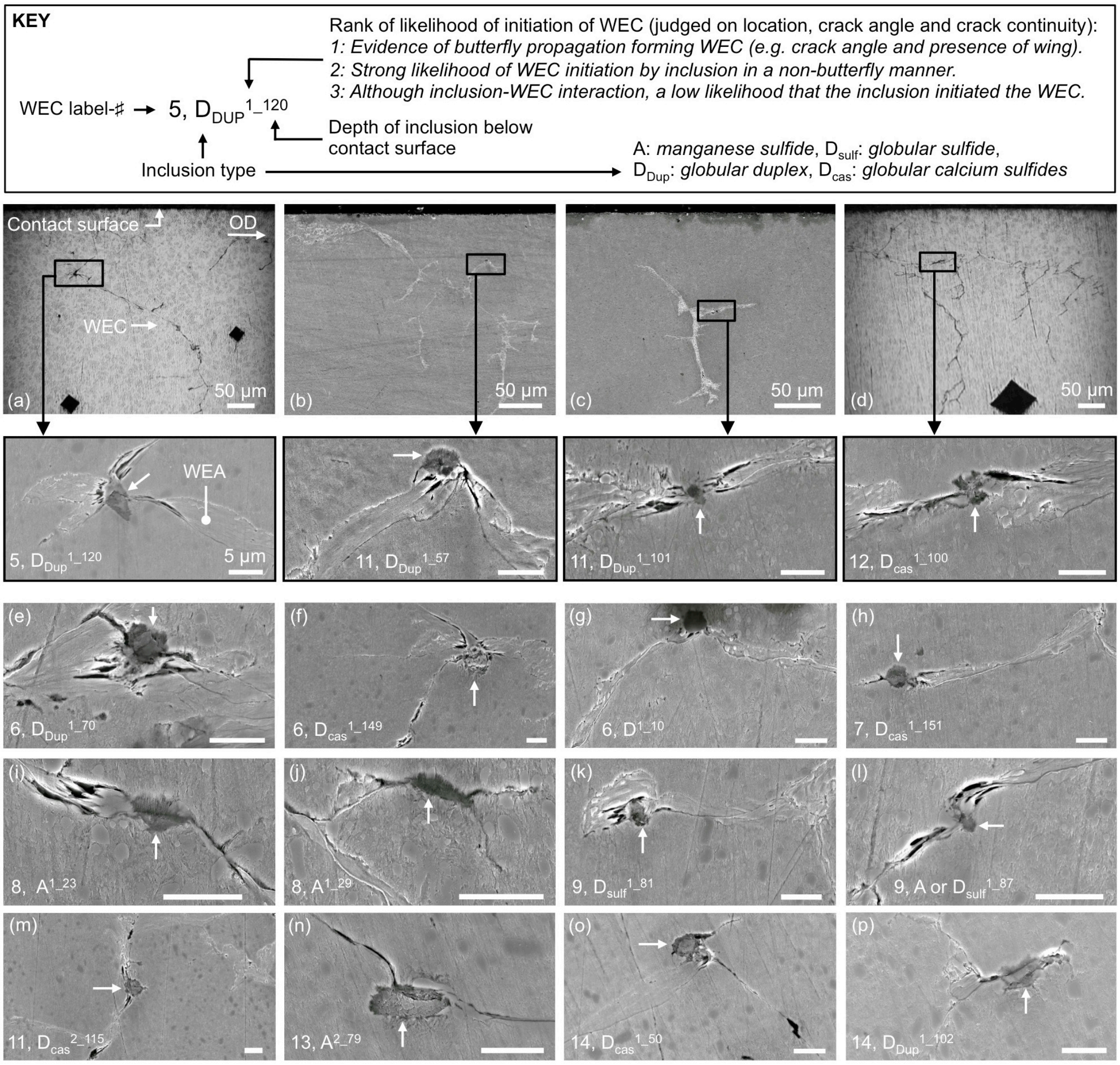

Figure 6.4.3: Examples of inclusion-WEC interactions. Test 3H, 52 mm roller circumferential sections, over-rolling direction (OD) left to right. The high magnification SEM images all have 5 µm scale bars and the small arrows highlight the inclusion. See permission [3.2].

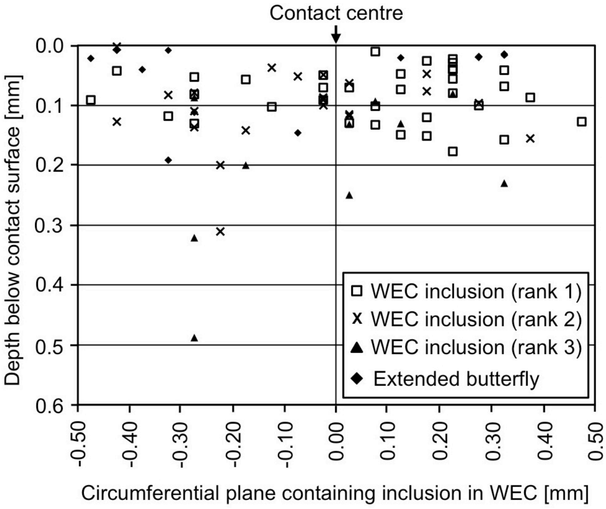

Figure 6.4.4: Spatial distribution and depth of inclusion-WEC interactions and inclusions that initiated extended butterflies. See permission [3.2].

Similar observations of butterflies and WECs were observed in the less extensive serial sectioning process of the 26 mm roller from test 3H. Two explicit examples of butterflies initiated from type A + oxide (Duplicate) or D_{Dup} inclusions with large crack extensions are shown in Fig. 6.4.5.

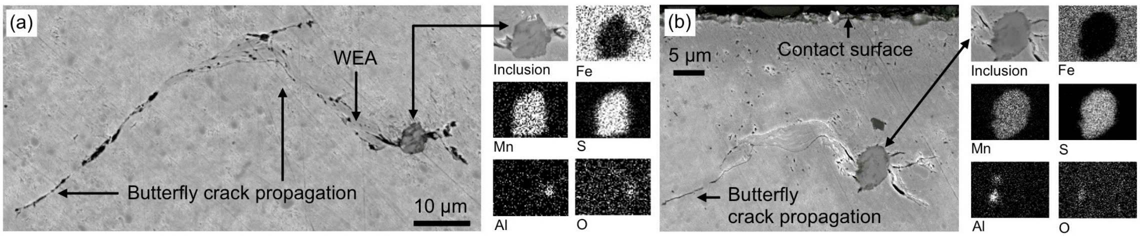

Figure 6.4.5: SEM images and EDS mapping of butterfly crack propagation from the 26 mm roller in test 3H. (a) Crack propagation to 70 μm+ initiated at an inclusion of MnS type with Al_2O_3 encapsulation (type Duplicate or D_{Dup}) confirmed with EDS analysis. The inclusion lies at a depth of 75 μm beneath the contact surface at a distance of 0.49 mm from the centre of the contact. (b) Inclusion composition is MnS with Al_2O_3 encapsulation (type Duplicate or D_{Dup}) at the crack initiation points, lying at a depth of 25 μm beneath the contact surface at a distance of 0.59 mm from the centre of the contact. See permission [3.2].

Partial wear zone serial sectioning analysis

Throughout the partial wear zone serial sectioning analysis inclusions were often found to interact with the white etching features, where large WECs sometime interact with a number of inclusions. EDS analysis showed that butterflies or micro-cracking at inclusions predominately initiated at MnS (D_{sulf}), MnS + Al oxide (D_{Dup}) and oxide (type D) inclusions, all of which are globular (aspect ratios <3). A few examples are given in Fig. 6.4.6 for near surface WEA/WECs and Fig. 6.4.7a for the only WEC that was found to occur in test 9H, which was found to be a threshold test for WECs to form at the 5 wt.% NH_4SCN charge (see details in section 6.3).

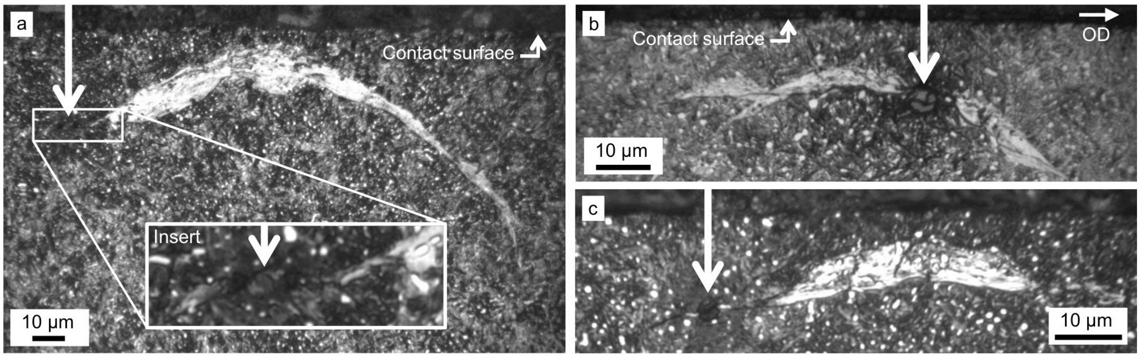

Figure 6.4.6: Optical images in the etched condition of circumferential cross sections showing inclusions associated with near surface white etching features in tests 2H, 3H, 6H and 8H. Over-rolling direction left to right. See permission [3.2].

The inclusions in these examples are highlighted with arrows. From the crack orientation and continuity over multiple slices, it was deduced that the white etching features were likely crack extensions originated at inclusions. Very occasionally evidence was also found for cracks initiating at carbides. A number of white etching features were found to interact with inclusions, but did not connect with the contact surface upon close examination and tracking over multiple slices. This suggests that white etching features are initiated at inclusions. On the other hand, a few microcracks/WEA were also seen to initiate from inclusions located at the contact surface (see Fig. 6.4.8). In general the types of inclusions interacting with WEA/WECs were also found to be globular types of MnS, MnS + oxide and oxide inclusions.

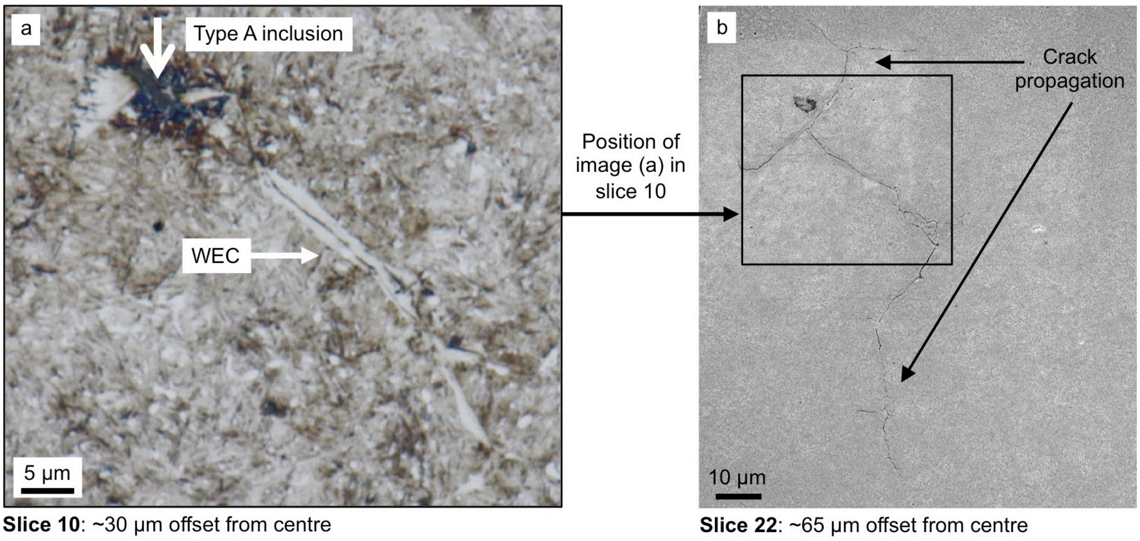

Slice 10: ~30 μm offset from centre **Slice 22**: ~65 μm offset from centre

Figure 6.4.7: WEC appearing to initiate from a type A inclusion in the 52 mm roller of the 5 wt.% test (test 9H). (a) Optical image at slice 10 in the etched condition. (b) SEM image at slice 22 in the etched condition. Over-rolling direction left to right. See permission [3.1].

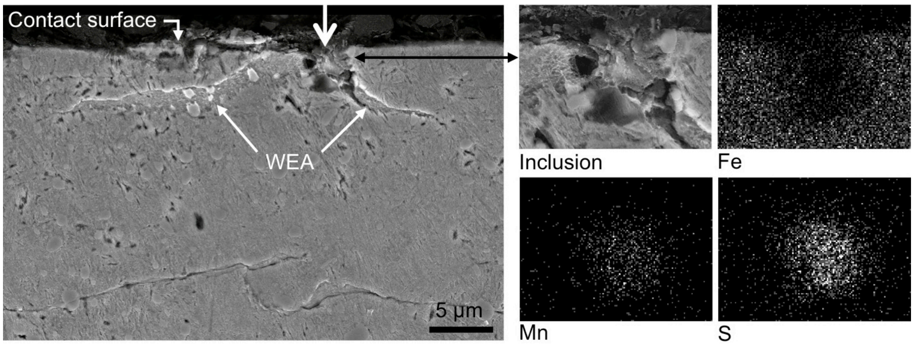

Figure 6.4.8: SEM circumferential cross section in the etched condition showing an inclusion at the contact surface which has initiated a WEA and microcrack. EDS revealed the inclusion is of MnS type. Over-rolling direction left to right. See permission [3.1].

FIB tomography of inclusion-WEC interaction

The inclusion-WEC interaction chosen for FIB tomography is shown in Fig. 6.4.2 and Fig. 6.4.9. FIB InLens images of four slices are shown in Fig. 6.4.9a to Fig. 6.4.9d, whilst positions of the slices are shown in Fig. 6.4.9e. Two inclusions were found to interact with the WEC network (main inclusion shown in Fig. 6.4.9c and Fig. 6.4.9d, secondary inclusion shown in Fig. 6.4.9a and Fig. 6.4.9b). See Video 6.4.1 for all FIB slices. FIB EDS confirmed that the main inclusion was Duplicate type due to the concealed Al_2O_3 encapsulated within the MnS part. Fig. 6.4.9f and Fig. 6.4.9g shows 3D models of the crack portions only (i.e. excluding the WEA microstructural change) from the 403 images acquired in the FIB tomography process (see Video 6.4.2). In the FIB InLens images and two 3D models, the cracks are labelled A – C; A being the main crack connected to the main inclusion, crack B being connected to the secondary inclusion and crack C being independent. Fig. 6.4.9h and Fig. 6.4.9i show 3D models of the two inclusions showing the cracking through their centres.

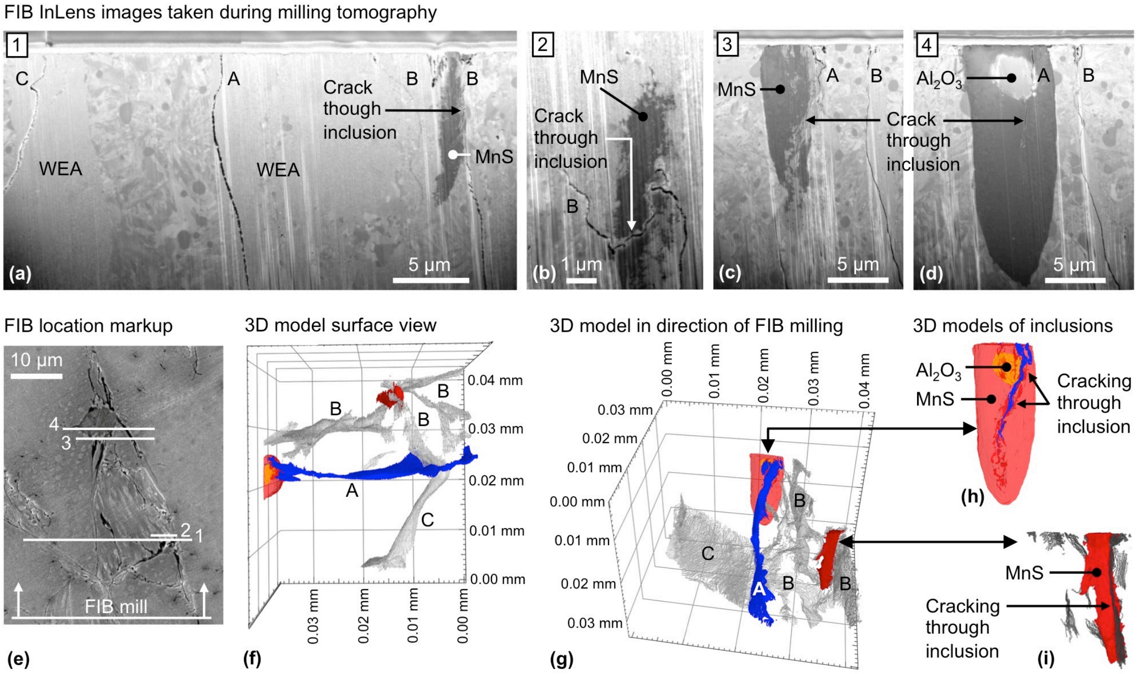

Figure 6.4.9: FIB tomography of inclusion-WEC interaction from the 52 mm roller in test 3H (also shown in Fig. 6.4.2). (a) – (d) show FIB InLens images of slices in the tomography process (see Video 5 for all FIB slices). (e) shows the location of the FIB milling and mark-up of images shown in (a) – (d). (f) and (g) show 3D models of the 403 slices obtained during FIB milling (see Video 6.4.2). The FIB InLens and 3D model images label the cracks A – C, A being the assumed main crack initiated at the main inclusion, crack B being initiated from the secondary inclusion and crack C being independent. (h) and (i) show 3D models of cracking which was present through both inclusions. See permission [3.2].

Each side of the main Duplicate inclusion appears to have double cracks connecting to the inclusion (Fig. 6.4.10), however as shown in Fig. 6.4.9, Video 6.4.1 and Video 6.4.2, one of the two cracks diminishes and stops a short distance from the main inclusion. This also occurs on the opposite side of the inclusion. Therefore the crack on each side that continues and does not diminish is judged as the main crack connecting to the main inclusion (e.g., crack A in Fig. 6.4.9). The left side of the inclusion (slice-1) has the WEA located above the main crack, and the right side of the inclusion (slice-2) has the WEA located below the main crack.

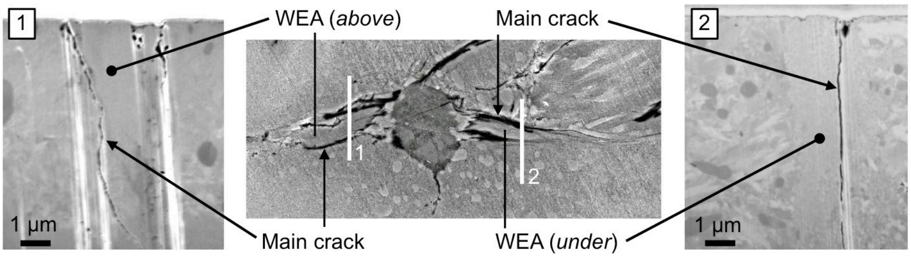

Figure 6.4.10: FIB InLens images showing WEA microstructural change on specific sides of the main cracks connected to the main Duplicate inclusion shown in Fig. 6.4.9. Over-rolling direction was left to right. On the left side in FIB slice-1, the WEA is located above the main crack connecting to the inclusion, whereas on the right side in FIB slice-2, the WEA is located below the main crack connecting to the inclusion. White streaks on the left side image are due to differential milling and curtaining effects in the FIB milling process. See permission [3.2].

3D modelling of WECs

Out of the 15 WECs observed from the full wear zone serial sectioning analysis in the 52 mm roller section from test 3H, WEC-9 (see Table 6.4.1) was chosen for 3D modelling as shown in Fig. 6.4.11. This particular WEC was chosen as the crack at each slice was contained within the field of view under 200X magnification, which made aligning and stacking images easier. Fig. 6.4.11a shows an example of a circumferential slice imaged during the serial sectioning process and Fig. 6.4.11b shows the 2D segmentation of the WEC at this slice. See Video 6.4.3 for all 2D segmentation images of the crack + WEA and Video 6.4.4 for a 2D segmentation orthoslice sweep in the 3D model. Fig. 6.4.11c shows an aerial view of the 3D model (observing directly down onto the raceway surface). Fig. 6.4.11d shows an isometric view of the 3D model (see Video 6.4.5 for a 360 degree rotation of the 3D model). The positions of four inclusions that interacted with the WEC are labelled 1 – 4 in both views of the 3D model. SEM images of inclusions 2 and 4 are shown in Fig. 6.4.3k and Fig. 6.4.3i respectively.

The shape of WECs differed depending on the direction of sectioning. Circumferential sections showed vertically branching networks whereas axial sections showed much more parallel networks. Fig. 6.4.12 shows axial views of the 3D model of WEC-9 with virtual axial orthoslices highlighted in black (see Video 6.4.6 for an axial orthoslice sweep in the 3D model).

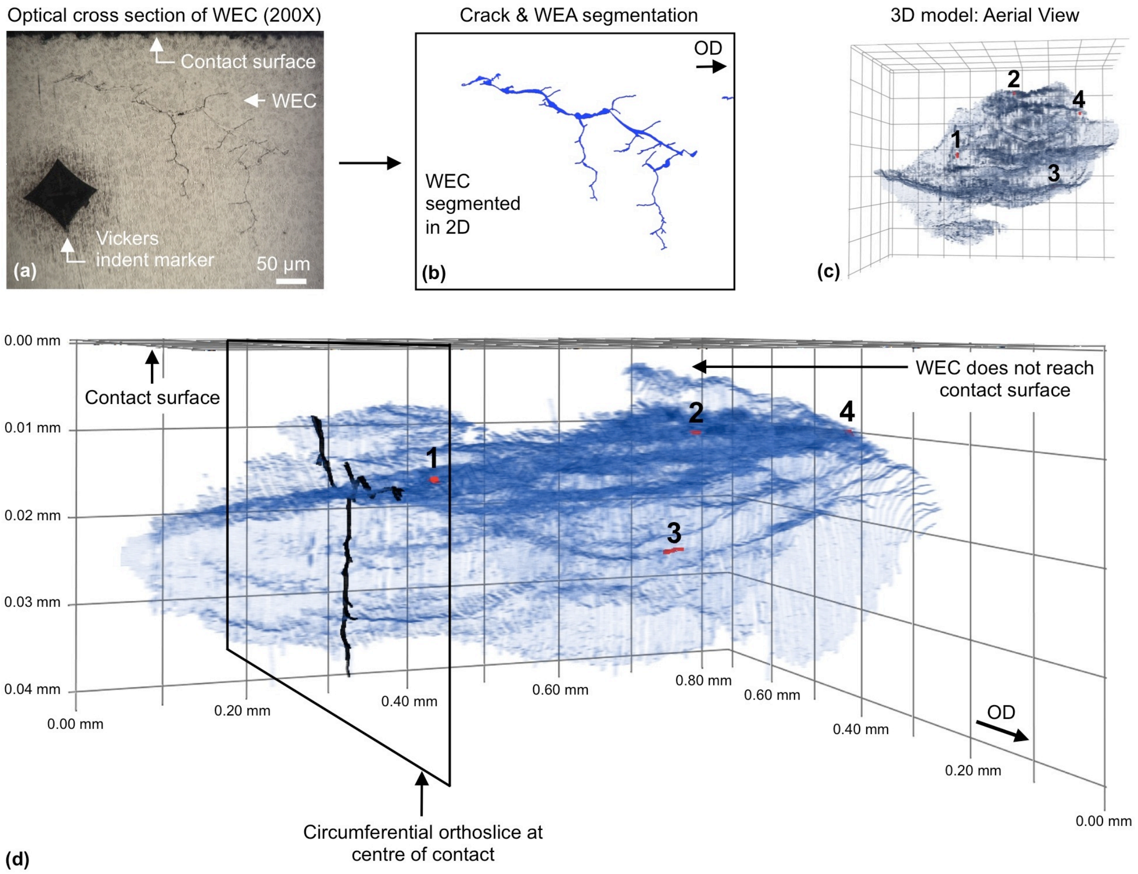

Figure 6.4.11: Process of image segmentation and 3D modelling of WEC-9. (a) Example circumferential slice from WEC-9 showing the WEC and the Vickers indent marker. (b) 2D WEC segmentation from (a). (c) and (d) show 3D models of WEC-9, where (d) highlights the 2D circumferential orthoslice at a position in the centre of the contact. Non-metallic inclusions interacting with the WEC are labelled 1 – 4 in the models where inclusions 2 and 4 are shown in Fig. 6.4.3k and Fig. 6.4.3i respectively. See Videos 6.4.3, 6.4.4 & 6.4.5 for all of the 2D segmentation images, a 2D segmentation orthoslice sweep in the 3D model and a 360 degrees rotation of the 3D model respectively. See permission [3.2].

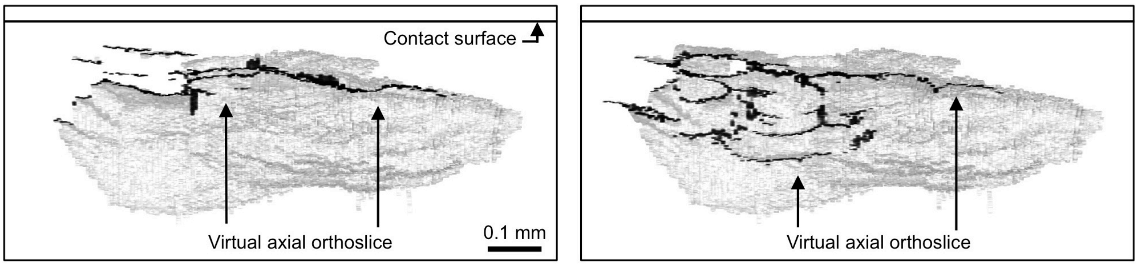

Figure 6.4.12: Virtual orthoslice examples in the axial direction. WECs tend towards more parallel orientations without extensive vertical branching as seen in the circumferential direction (see Video 6.4.6 for an axial orthoslice sweep in the 3D model). See permission [3.2].

6.4.4 Discussion

WEC characteristics

The size, shape and location of the WECs varied considerably as detailed in Table 6.4.1 and also Figs. 6.3.8 – 6.3.16 in section 6.3. The direction of the plane of sectioning has been found to be important in observing the WECs. Sectioning in the circumferential plane typically show vertically branching networks that span a large area (see Fig. 6.4.11 and Videos 6.4.3, Video 6.4.4 and Video 6.4.5), whereas sections in the axial direction show more parallel type WECs with less branching (see Fig. 6.4.12 and Video 6.4.6).

Initiation and propagation of WEA/WECs

Strong evidence is presented that WECs can be initiated from non-metallic inclusions. It is proposed that the WECs in this study were created from a network of cracking initiated from inclusions, where the higher the density of inclusions able to initiate a crack, the higher the probability of WEC formation and size of the WECs. A ranking system has been used to rank the likelihood of the inclusion being involved in the initiation of the WEC. This has been judged by crack orientation, crack continuity over multiple slices either side of the inclusion-WEC interaction and location of the inclusion in the 3D WEC network. Although the ranking system is qualitative, it is useful for designating whether inclusions are likely WEC initiators. For a crack/WEA with the typical butterfly crack/wing orientation it is suggested that the butterflies propagated to form WECs. If this relationship was not observed then it is suggested that the inclusions initiated cracks that eventually became WECs.

The *full wear zone* analysis test 3H 52 mm roller showed that 13 of the 15 WECs mapped did *not* make any interaction with the contact surface, thus dismissing surface crack initiation. The two WECs that were connected to the surface could have initiated from cracking at the surface, however each of these WECs also interacted with an inclusion. For those WECs with little or no inclusion interactions it is likely that some inclusion interactions were missed during serial sectioning as the process of 5 μm material removal at each slice was approximate and sometimes more material was removed due to differential polishing. Therefore these WECs could have contained inclusion-WEC interactions that were missed. 67 non-metallic inclusions were found to interact with the 15 WECs mapped in the 52 mm roller section of test 3H, and 57 of these inclusions were ranked with a high likelihood for crack initiation (rank 1 or 2). It was found that the number of inclusions interacting with a WEC is related to the size of the WEC, e.g. large WECs such as WEC-6 and WEC-12 had 21 and 11 inclusion interactions respectively compared to smaller WECs which had fewer inclusion interactions. The location below the contact surface of the majority of inclusion-WEC interactions and inclusions that initiated extended butterflies lie at 0 – 0.15 mm depth (see Fig. 6.4.4). Therefore the depth below the contact surface and axial range (i.e. close to the centre of contact) of the inclusion-crack interactions are consistent with the location of high subsurface shear stressing from rolling contact, this further supporting WEC initiation at inclusions.

An example of the propagation of a WEC from an inclusion is shown from Fig. 6.4.7a to Fig. 6.4.7b. This is the single WEC that formed in the 52 mm roller of the 5 wt.% test (test 9H). The WEC was first observed at an offset axial distance of ~12 μm from the centre of the contact and continued until termination of the serial sectioning process at ~100 μm offset. Fig. 6.4.7a shows a slice at ~30 μm offset from centre of the contact and Fig. 6.4.7b at ~65 μm offset. The inclusion that appears to initiate the WEC is observed at ~30 μm offset from the centre (Fig. 6.4.7a). This inclusion was located at a depth of 90 μm below the contact surface and was type A with a length of ~30 μm. The size of the WEC at ~30 μm offset (Fig. 6.4.7a) is relatively small; however, when comparing this to the slice at ~65 μm offset (Fig. 6.4.7b), the WEC has propagated to a much larger size. This was commonly observed with other WECs in the serial sectioning process. It is proposed that this WEC initiated at the inclusion near the centre of the contact zone then propagated in a direction away from the centre of the contact. It should be noted that the inclusion shown in Fig. 6.4.7a ended through the slices and in Fig. 6.4.7b a different inclusion is shown that did not interact with the WEC.

From the FIB tomography process, considering the location of the WEA in relation to the main cracks on either side of the main Duplicate inclusion (Fig. 6.4.10), the evidence suggests that this is a butterfly connected to a WEC. This is because butterflies that form in bearing steels typically have certain features such as the WEA being located in particular orientations with respect to the butterfly crack. In addition, it can be seen from Fig. 6.4.9 that cracking has occurred through both the main Duplicate inclusion and the smaller MnS inclusion, which both interact with WECs. Cracking through these inclusions was either part of the initiation process of butterflies/WECs from these inclusions, or from WECs propagating through the steel and through inclusions cracking them in the process. Recent research [106, 118] suggests that the initiation mechanism of butterflies from MnS type inclusions under RCF differ from that of oxide type inclusions. It is suggested that cracks through MnS type inclusions (induced by RCF) open up and propagate out into the matrix. MnS type inclusions were found to be predominately cracked in the zone of subsurface material stressing, and that for a butterfly to exist at an MnS inclusion, the inclusion was always cracked in the direction of the major axis. From Fig. 6.4.9 it can be seen that indeed both MnS-Al_2O_3 / MnS type inclusions exhibit through cracking in the direction of the major axis, therefore this provides evidence that the inclusions themselves were initiators of cracks/butterflies that propagated to form WECs.

The white etching features in this study have been found to be predominately initiated at short type A sulfide inclusions, MnS associated inclusions (D_{sulf}, D_{cas} and D_{Dup}), and type D inclusions. Duplicate inclusions were not found to have many WEC interactions, however some of the assumed type A inclusions recorded could be Duplicate type as the oxide part may only be a small part attached to the sulfide and could therefore have been removed entirely between slices. The following explanation is offered. Different inclusions will have different coefficients of thermal expansion (CTE) compared with a typical bearing steel. Sulfide inclusions will have larger CTEs than oxide inclusions. Compressive and tensile stresses are thus induced around these inclusions respectively [123]. A tensile residual stress also exists at sulfides + oxides where the oxide part makes contact with the matrix [120, 123]. Therefore inclusions having initiated at MnS + oxide (D_{Dup}) and oxide (type D) inclusions is expected due to the induced tensile residual stresses, the hardness and elastic modulus mismatch with the tempered martensite matrix and poor coherence/debonding between the oxide part and matrix [22, 28, 115]. The maximum length of any type A (or Duplicate) inclusion found to interact with the WECs was only ~20 – 30 μm and the largest globular type D inclusion was ~7 – 10 μm in diameter with aspect ratios <3 in nearly all cases. In this study it can be seen that it is the small globular inclusions that are predominately crack initiators as opposed to elongated type inclusions (type A). As the inclusions interacting with the WECs were relatively small in length or diameter, steel cleanliness standards focusing on the density of small inclusions then become more applicable than those that estimate maximum lengths.

WEA microstructural change

The inspection of WEA using serial sectioning and FIB observed in many cases that spherical carbide deformation or dissolution in the WEA was occurring (see Fig. 6.4.2, Fig. 6.4.9 and Video 6.4.1). This is due to the severe plastic deformation, dislocation interactions and grain refinement occurring in the local region. More in-depth details about WEA microstructural changes has been presented in chapter 5.

6.4.5 Conclusions

This section focuses on elucidating the initiation and propagation mechanisms of WECs in hydrogen charged test rollers. Numerous WECs have been mapped in their entirety by serial sectioning and one WEC has been modelled in 3-D. FIB tomography has been used to verify initiators and construct 3-D crack models. It was found that:

1. One of the WECs mapped was modelled in 3D for the first time. Standard cross-sections and the 3D modelling of a WEC showed that the sectioning direction was influential on the shape of the WECs; in the circumferential direction WECs appear highly vertically branched,

whereas in the axial direction WECs tend to often appear more parallel with less vertical crack branching.

2. The extensive serial sectioning of WECs revealed their varying size, shape and orientation and also initiators such as non-metallic inclusion interactions or contact surface connections. The vast majority of WECs were contained in the subsurface wear zone and did not make any connection with the surface, thus dismissing surface initiation.
3. Strong evidence was found that WEA/WECs were initiated at inclusions. In the full wear zone analysis in test 3H, a total of 67 non-metallic inclusions were found to interact with the 15 WECs mapped and 57 of these inclusions were ranked with a high likelihood for crack initiation. Inclusions were also often found to interact with the WECs in the other RCF tests. Serial sectioning and FIB tomography provided evidence that butterflies can propagate to form WECs. It is proposed that one mechanism of WEC formation is due to multiple linking of extended butterflies or small WECs in the subsurface to form larger WEC networks that eventually propagate to the surface resulting in WSF.
4. The white etching features in this study initiated predominately at short type A sulfide inclusions, MnS associated inclusions (D_{sulf}, D_{cas} and D_{Dup}) and type D inclusions. The maximum length of any type A inclusion found to interact with the WECs was only ~20 – 30 µm and the largest type globular type D inclusion was ~7 – 10 µm in diameter. Small globular inclusions predominated as crack initiators as opposed to elongated sulfide/duplicate type inclusions (type A).
5. As small/short sized inclusions predominated as crack initiators the data suggests that steel cleanliness standards analysing inclusion density (as opposed to maximum inclusion lengths) are more relevant in understanding butterfly/WEC initiation. However steel cleanliness standards used should be able to differentiate pure sulfides from sulfides + oxide encapsulations and record inclusions that are only a couple of micrometer's in length/diameter.
6. The larger WECs that formed in the tests are similar or identical to those observed in actual wind turbine gearbox bearings. However it must be considered that hydrogen charging could change the initiation and propagation mechanisms of WECs. Therefore Chapter 7 aims to investigate and provide verification of the mechanisms proposed in this chapter.

This page is intentionally left blank

7. Analyses of transient test gearbox bearings & planet bearings from wind turbine gearbox service

7.1 Introduction

The investigation in this chapter aimed to reveal information about WEC initiators (non-metallic inclusions, butterfly interactions and surface cracking) by the application of serial sectioning to map WEC networks in wind turbine gearbox bearings for the first time. The analysis aimed to understand if a difference in WEC initiation and propagation mechanisms occurs under non-hydrogen charged RCF conditions compared to the hydrogen charged results presented in chapter 6.

A large-scale transient test rig designed to simulate conditions to wind turbine gearbox bearing service was used to test actual high-speed wind turbine gearbox bearings (non-hydrogen charged conditions). The serial sectioning process has been conducted on two different wind turbine gearbox bearing inner rings; 1) the bearing used on the large-scale transient test rig, and 2) a planet bearing from a 3 MW wind turbine that spalled in service. Fig. 7.1.1 shows the thesis work flow chart.

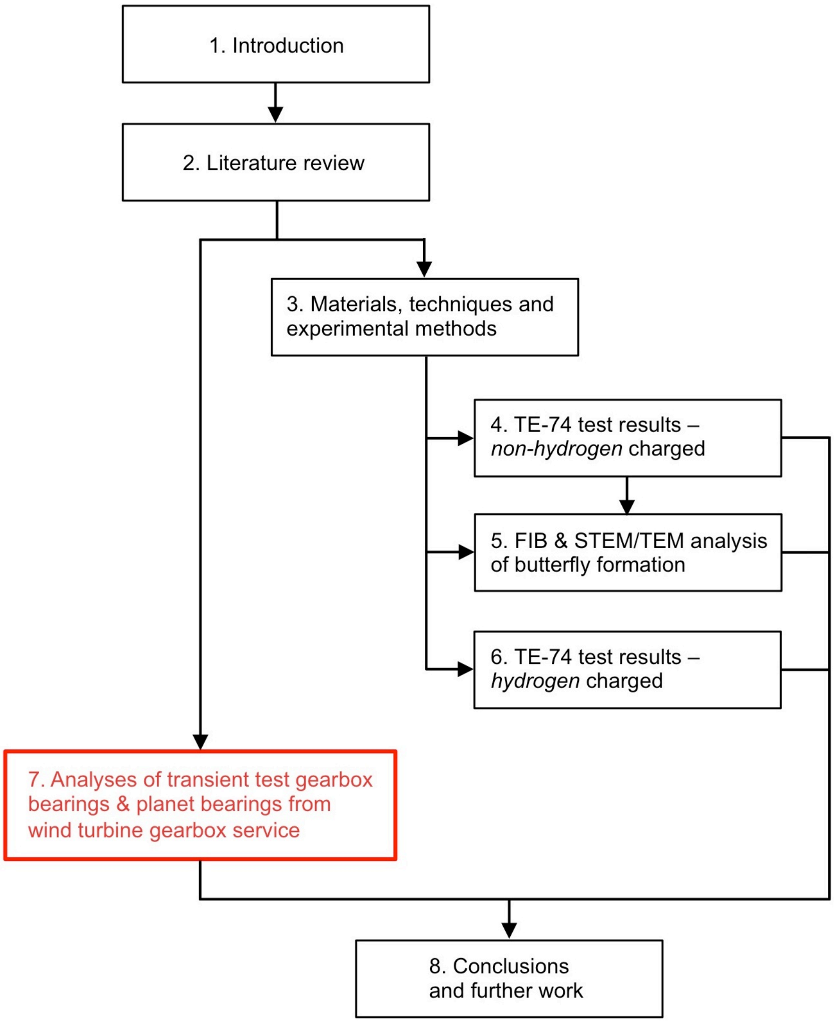

Figure 7.1.1: Thesis work flow chart.

7.2 Techniques and experimental methods

7.2.1 Transient test gearbox bearing operating conditions

A large-scale transient test rig designed to simulate conditions to wind turbine gearbox bearing service was used to test actual high-speed wind turbine gearbox bearings. Four double-row spherical roller bearings with 150 mm inner bore diameter were tested simultaneously. Mechanical spindles statically loaded each bearing continuously during the test. A run-in period of roughly 2 hours was conducted, with the inner ring of the bearings experiencing a maximum contact pressure of 1.5 GPa in the centre of the contact

After the run-in period, transient speed operation with load dynamics was used throughout the remainder of the test. The set of four bearings were driven by a static shaft and also a dynamic shaft (a resonance being induced in this shaft from the dynamic motor). Torsional dynamics (speed dynamics) was achieved by inducing a resonance in the dynamic shaft at a high frequency, where load dynamics was achieved by a second independent resonance system generating a high frequency dynamic radial loading. Overlaid frequencies are sine shaped in both cases. Information on the frequencies used is not revealed due to proprietary sensitivity. The four bearings are aligned side-by-side in a row of four, resulting in one bearing being located adjacent to the static shaft, one bearing adjacent to the dynamic shaft and two bearings being located between these two end bearings. The loads experienced in the inner ring during operation were a mean contact pressure of 1.9 GPa and a maximum contact pressure of 2.15 GPa. The test cycle was designed with transients so that the bearings ran at base-speed for about 5 minutes, followed by a transient drop to low-speed for about 1 minute. The base-speed rpm replicated typical upper high-speed gearbox bearing operation of ~1500 rpm, and the low-speed rpm was ~20X lower than the base-speed. When operating at the low-speed portions, in combination with the speed dynamics, standstill is almost reached. The time of the transients to ramp the bearing speed up and down was about 20 seconds in each case.

The bearings experienced 130% of their basic rating life (L_{10} life), this equating to about 1400 x 10^6 stress cycles (over-rolling's at any one point on the inner ring raceway) before the test was manually stopped. Each bearing was supplied independently with lubrication during testing. The oil used was a commercially available ISO VG 320 water-soluble PAG fully formulated wind turbine gearbox oil. The bearing temperature measured at the outer ring was about 85 – 90 °C during the test. The Kappa value (Eq. 7.2.1) is the ratio of the actual viscosity of the oil under operating conditions (pressure and temperature) to the minimum calculated viscosity required for adequate lubrication (i.e. EHL).

$$k_{kappa} = v/v_1 \tag{7.2.1}$$

Where,
k_{kappa} = viscosity ratio (kappa value)
v = operating viscosity of the lubricant [mm^2/s]
v_1 = rated viscosity depending on the bearing mean diameter and rotational speed [mm^2/s]

Kappa values in the range of about 2 to 4 are required for optimum bearing life, where a Kappa value in excess of about 4 equates to full-film operation. A kappa value of 1 equates to boundary/mixed lubrication. The predicted kappa values during the following operation conditions are as follows; base-speed (5 min portion): ~10, and low-speed (1 min portion): <1.

As the bearings are of spherical roller type, a phenomena called Heathcote slip would occur during periods of operation, which is a geometrical constraint suffered by all spherical roller bearings. This is where sliding occurs between the roller and centre of the raceway. When the rollers rotate through the loaded zone, no gross slip occurs at the roller-raceway interfaces due to roller-raceway traction, however when the rollers rotate through the unloaded zone, the rollers may experience gross slip due to roller-raceway contact area reduction and consequent roller-raceway traction loss [1]. Computer simulations have shown that for spherical roller bearings in an intermediate shaft location of a wind turbine gearbox, moderate sliding (3–10% slide to roll ratio) at roller–raceway contacts in the unloaded zone occurs continuously [176]. In the test in this study, it is also expected that additional slip between the rolling elements and the bearing rings would have been induced during the acceleration/deceleration speed transients and at the low-speed sequences of the test cycle. Estimation of slip in wind turbine gearbox spherical roller bearings during acceleration transients has been calculated by Kang, et al. [176]. SRRs ranging between 30 – 110% were calculated to have been experienced at various points in the acceleration transient depending on the load applied to the bearing. This was however modelled for a much smaller change of bearing speeds and also a longer transient ramp time compared with the test in this study. Therefore it is expected that the bearings experienced more severe slip during portions of the acceleration transient in this study.

7.2.2 Operating conditions of the planet bearing from service

The planet bearing is of double-row spherical roller bearing type with inner bore diameter of 300 mm and an inner ring that is stationary. The operating life history of the planet bearing from service is generally unknown, however compared to the transient gearbox bearing test, the typical operating conditions do differ considerably. The maximum contact pressure in the centre of the inner ring raceway was calculated as ranging between 1.3 GPa and about 1.8 GPa as an extreme maximum value. However these are estimates, as it is not known whether this gearbox was running under calculated conditions due to different site conditions, manufacturing tolerances, etc. In general the speed of the planet service bearing would be about 30 – 50 rpm (about 50 – 30X lower than the base-speed of the transient test gearbox bearing). During operation the Kappa and lambda values are expected to be about 1, this equates to boundary/mixed lubrication. The number of stress cycles would also be lower than that for a high-speed bearing in the same gearbox.

7.2.3 Serial sectioning and microscopy

To better understand possible initiation points of WECs, a serial sectioning approach was used (see Fig. 7.2.1a). A polishing material removal interval of ~3 µm was used for each slice. This approach maximised detection of possible initiators of WECs, e.g. inclusions, butterflies and surface cracking.

In the transient gearbox bearing test, only one of the four bearings showed evidence of flaking, where two small white structure flaking areas developed in the bearing that was directly adjacent to the dynamic shaft. Therefore the inner ring sectioning locations of the transient test gearbox bearing were chosen in the local vicinity of the two small flaking areas on the raceway (Fig. 7.2.1b), as these were the locations most likely to contain WECs. Sections in an axial plane (perpendicular to rolling direction) were cut at the edges of these spalls. These sections were then hot mounted in bakelite resin mounts, then prepared by standard metallography techniques to enable viewing of the cross sections. WECs were found beneath the white structure flaking shown in Fig. 7.2.1c (designated as WEC-B1) and adjacent to the larger white structure flaking shown in Fig. 7.2.1d (designated as WEC-B2). As the flaking areas and WECs were relatively small, it was assumed that a high percentage of the WECs volume could be mapped in the process.

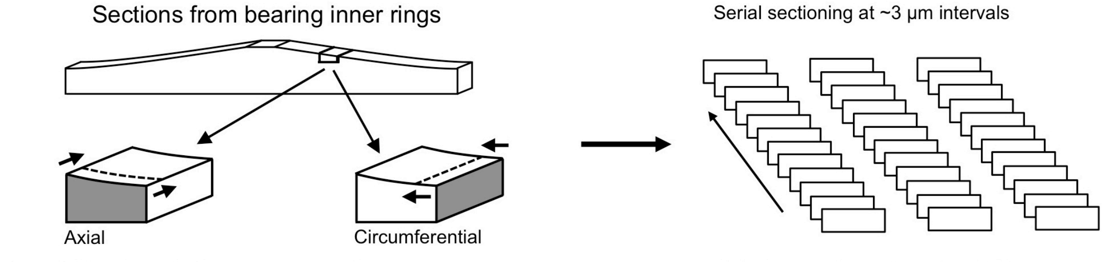

(a) Different sectioning planes depending on specimen

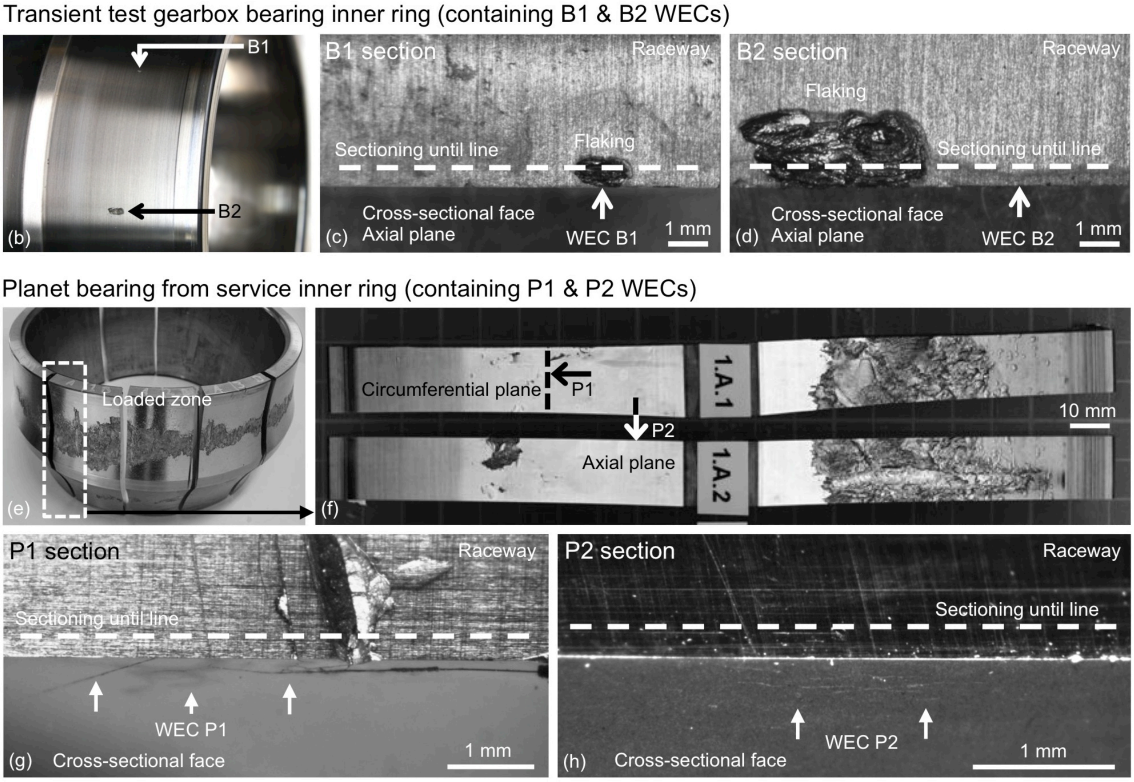

Figure 7.2.1: Schematics of bearing sectioning and optical microscopy images of the two bearing inner rings under investigation. (a) Schematic showing the sectioning method and location on the bearing inner rings. (b) The transient test gearbox bearing overview showing two spalls. (c) and (d) show the location of the WEC's B1 and B2 and starting plane of their analysis, where WEC-B1 lies under the shallow flaking. (e) Shows the planet bearing inner ring overview showing the extensive flaking on the raceway. (f) Two sections were cut, where the locations of the WECs P1 and P2 are labelled and shown in (g) and (h). WEC-P1 has a surface interaction and WEC-P2 appears to be contained within the subsurface. Dotted lines in (c), (d), (g) and (h) mark the end point of the serial sectioning process. See permission [7.4].

The planet bearing from service analysis locations were chosen from the loaded zone of the stationary inner ring, as this is where extensive flaking had occurred during service. Sections across the whole raceway were cut in both the circumferential and axial planes. WECs were observed in the near surface zone (up to 1.5 mm depth below contact surface) across most of the sections. Two WECs from the planet bearing were chosen for serial sectioning analysis. These WECs were chosen, as they were located in the raceway that did not contain heavy flaking. One of the WECs (designated WEC-P1) (Fig. 7.2.1g) was part of a large subsurface crack, and also connected to the contact surface. Another WEC (designated WEC-P2) (Fig. 7.2.1h) was chosen, as it appeared it was contained in the subsurface and was found to be relatively small in comparison to other WECs across the sections.

In the serial sectioning process, 125 slices were polished and imaged, which equates to about 375 μm distance (see Fig. 7.2.1a). Vickers indents were made in the near vicinity of the WECs during the serial sectioning. These Vickers indents acted as reference markers to track WECs during the process. WECs were imaged optically at a magnification 25X or 50X at each slice so that the WECs were imaged as well as the position of the Vickers indents in relation to the WECs. Some WECs spanned a large area; therefore to map the individual WECs at a particular slice, several 25X images were sometimes required. This process allowed accurate tracking of the WECs. Any inclusion interactions with the WECs were located using 200X magnification and were then imaged optically at 500X and 1000X.

7.3 Material characterisation

The inner ring of the transient test gearbox bearing was made of a variant of standard 100Cr6 bearing steel, and the inner ring of the planet bearing from service was made of 100CrMo7-4 steel according to the grade B7 in the standard ISO 683-17. Both the inner rings were bainitically through hardened with a hardness of 60 HRC.

7.3.1 Steel cleanliness

The cleanliness of the bearing steels was analysed using the ISO 4967-B standard [87], which measures the density of inclusions. The analysis was carried out at the Dr. Sommer Werkstofftechnik GmbH lab. Sections of the steel are polished at planes in the direction of rolling/deformation of the steel billets; hence some types of inclusions in this viewing plane may have elongated features (e.g. sulfides). The process used computer software for automatic detection of inclusion type, size and count. Each field of view (magnification 100X equating to an observed area of 0.5 mm^2) is compared to pre-determined charts in the standard and a particular severity index given to the inclusions present. The results are displayed in Table 7.3.1.

The total index for each inclusion type (i_{total}), the mean index for each inclusion type (i_{mean}) and the global cleanliness index (C_i) for the steels were calculated using the procedures and weighting factors described in the standard. Since the areas of analysis differ between the steel types (251.3 mm^2 and 880.0 mm^2), it is more relevant to look at the mean index (i_{mean}) and global cleanliness index (C_i), which are calculated dependant on the area analysed.

It can be seen that sulfide associated inclusions (type A) were the most recorded inclusion type across the two bearing steels, where a higher number with increased severity was recorded in the planet service bearing (i_{mean}: 0.0877) as opposed to the transient test gearbox bearing (i_{mean}: 0.0438). Because some type A inclusions were found in field 1.0, the inclusions measured between 127 to 261 μm in length, which is consistent with these sulfide type inclusions being elongated in the inclusion elongation direction. No aluminates or silicates were found in either steel, which is consistent with silicates being rare in modern bearing steels. Some globular oxides (type D and DS) were found in the planet service bearing, but not the transient test gearbox bearing, where type DS having a diameter ≥ 13 μm may be critical to RCF life if found in the highly stressed zone. The transient test gearbox bearing has a C_i of 9.0 and the planet service bearing has a C_i of 19.2.

Table 7.3.1: ISO 4967-B steel cleanliness data.

Field	**A**		**B**		**C**		**D**		**DS**
	Fine	Thick	Fine	Thick	Fine	Thick	Fine	Thick	Count
Transient test gearbox bearing inner ring									
0.5	35	4	-	-	-	-	-	-	-
1	3	0	-	-	-	-	-	-	-
1.5	-	-	-	-	-	-	-	-	-
2	-	-	-	-	-	-	-	-	-
2.5	-	-	-	-	-	-	-	-	-
3	-	-	-	-	-	-	-	-	-
i_{total}	20.5	2	-	-	-	-	-	-	-
i_{mean}	0.0438	0.0043	-	-	-	-	-	-	-
No. fields = 468 , Area = 251.3 mm^2									
C_i, global cleanliness index = 9.0									
Planet service bearing inner ring									
0.5	265	45	-	-	-	-	-	5	1
1	10	1	-	-	-	-	-	-	-
1.5	-	-	-	-	-	-	-	-	-
2	-	-	-	-	-	-	-	-	-
2.5	-	-	-	-	-	-	-	-	-
3	-	-	-	-	-	-	-	-	-
i_{total}	142.5	23.5	-	-	-	-	-	2.5	0.5
i_{mean}	0.0877	0.0145	-	-	-	-	-	0.0015	0.0003
No. fields = 1625, Area = 880.8 mm^2									
C_i, global cleanliness index = 19.2									

Group A (sulfide type), group B (aluminate type), group C (silicate type), group D (globular type, usually oxide), group DS (single globular type with diameter ≥ 13 μm).

i_total = total index for each inclusion type.

i_mean = mean index for each inclusion type.

Ci, global cleanliness index, is calculated using the suggested weighting factor as described in the standard.

See permission [7.4].

7.4 Results

In the transient gearbox test, butterflies and WECs were found in the metallurgical screening process in the bearing that showed flaking. In the following, the results from the subsurface examination by serial sectioning for both the transient test gearbox bearing and planet bearing from service are presented.

7.4.1 Subsurface serial sectioning

Fig. 7.4.1a & Fig. 7.4.1b show example images of the WECs investigated from the transient test gearbox bearing in the axial sectioning plane, and Fig. 7.4.1c & Fig. 7.4.1d from the planet bearing from service in the circumferential and axial sectioning planes. WEC-B1 is located beneath the small flaking region and does not appear to directly connect to the surface in this particular plane/image. WEC-B2 is contained within the subsurface in this plane/image. WEC-P1 spans a much larger area than the other WEC's, where a connection with a large subsurface crack and interaction with surface flaking is apparent. WEC-P2 is a WEC that is contained within the subsurface within this plane/image.

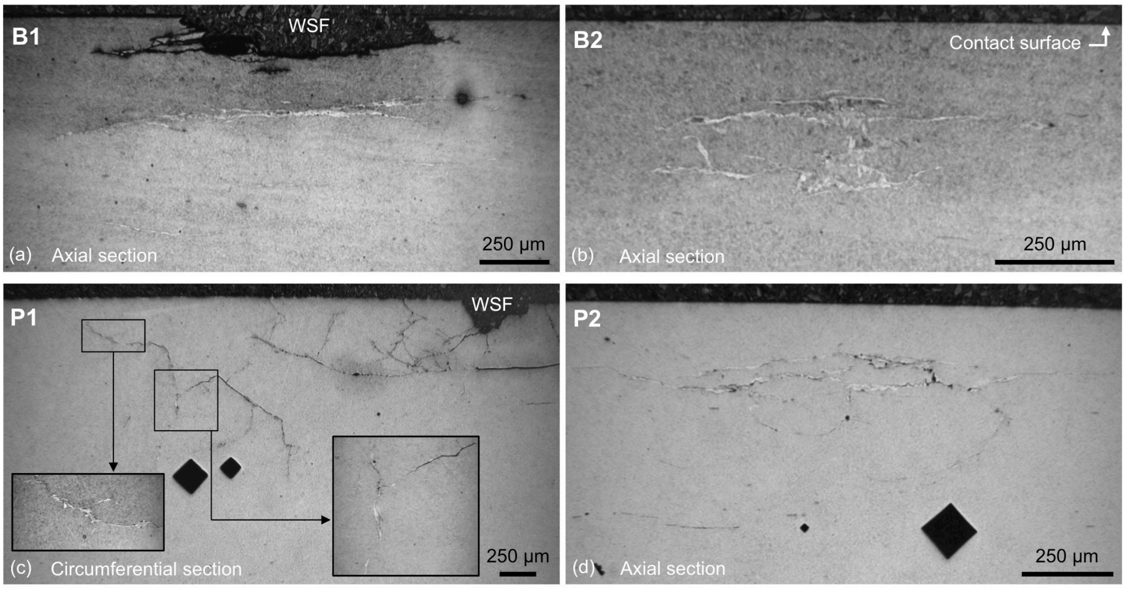

Figure 7.4.1: Example optical images of the four WECs investigated in the etched condition, where B1 and B2 are axial sections from the transient test gearbox bearing inner rings, and P1 and P2 are circumferential and axial sections respectively from the planet service bearing inner rings. (a) WEC is located below the small flaking. (b) WEC appears to be contained in the subsurface. (c) Large WEC with connection to the contact surface. (d) Relatively small WEC in the subsurface. See permission [7.4].

In both bearing inner rings analysed it was observed in many cases that non-metallic inclusions and also what appeared to be butterflies interacted with the WECs. In total, 76 inclusions were found to interact with the four independent WECs in the volume of steel analysed. Many non-metallic inclusions were observed in the process which did not interact with the WECs and hence were not recorded. Examples of inclusions and/or possible butterflies associated with WECs can be viewed in Fig. 7.4.2. The optical images all have the same scale as the first image. A key above the images in Fig. 7.4.2 illustrates each parameter used in the image label fields. Inclusion lengths in the plane of material removal were estimated. The entire combined data from the process, including the information on the inclusion type, inclusion interaction location in the section/WEC, likelihood of inclusion initiation of the WECs and details of the crack length span for each WEC can be found in Table 7.4.1. Inclusions were judged to be crack initiators from the inclusions chemical composition, depth below the contact surface and crack continuity in the near vicinity of the inclusion. A rank of 1 or 2 has been used for those inclusions that appear to have been involved in the initiation of the WEC, whereas a rank of 3 has been used when this did not appear to be the case. Where a WEC is thought to pass through an inclusion (i.e. the inclusion did not initiate the WEC), the inclusion-WEC interactions were given a likelihood rank of initiation of 3 (see Fig. 7.4.2 for an example). It was found that the number of inclusion-WEC associations was as follows; B1 had 9 interactions (8 inclusions at rank 1 or 2), B2 had 3 interactions (2 inclusions at rank 1 or 2), P1 had 41 interactions (23 inclusions at rank 1 or 2) and P2 had 23 interactions (18 inclusions at rank 1 or 2). Except for WEC-B2, the three remaining WECs were found to contain many inclusion-WEC interactions that appeared to be likely crack initiators (ranked 1 or 2). A total of 51 inclusions of rank 1 or 2 were found to interact with the four WECs.

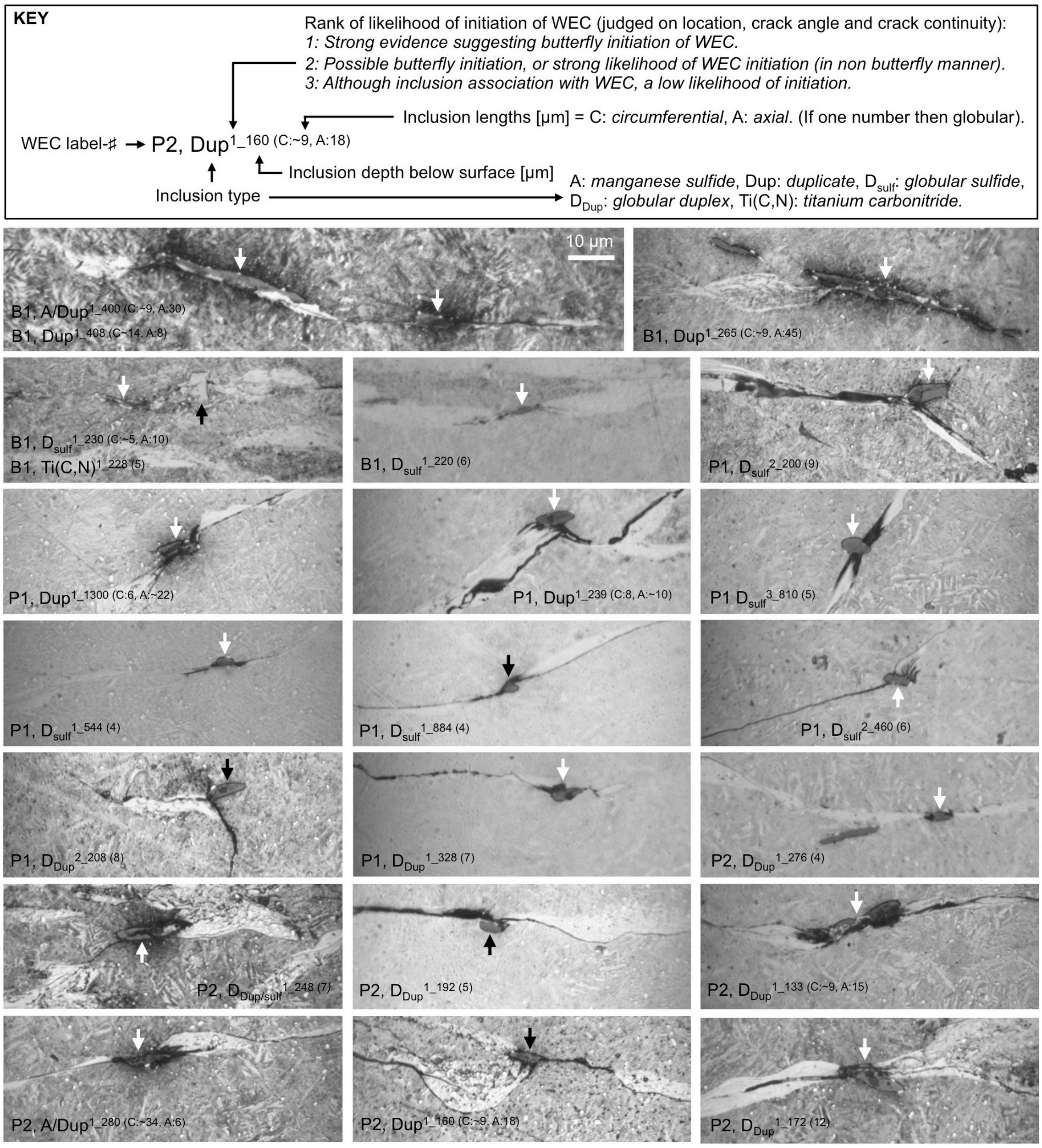

Figure 7.4.2: Examples of inclusion-WEC interactions in B1, P1 and P2 WECs. The optical images all have the same scale as the first image, and the small arrows highlight the inclusions. Many interactions suggest an inclusion initiation of WECs or a butterfly crack extension mechanism forming the WECs. See permission [7.4].

Table 7.4.1: Non-metallic inclusions interacting with the four WECs B1, B2, P1 and P2.

Circumferential tomography zone	**B1** (axial section)	**B2** (axial section)	**P1** (circumferential section)	**P2** (axial section)
	Axial span: 1.8 mm Max depth: 0.8 mm	Axial span: 1 mm Max depth: 0.4 mm	Circumferential span: 3.5 mm Max depth: 1.5 mm	Axial span: 1.7 mm Max depth: 0.45 mm
0 – 15 µm		$D^{3\_220\,(4)}$	$D_{Dup}^{2\_208\,(8)}$, $D_{sulf}^{2\_200\,(9)}$	$D_{sulf}^{3\_328\,(3)}$, $Dup^{1\_160\,(C:\sim9,\,A:18)}$
15 – 30 µm	$D_{Dup}^{2\_360\,(5.5)}$, $D_{sulf}^{3\_220\,(2)}$		$D_{sulf}^{3\_520\,(9)}$	$Dup^{1\_240\,(C:\sim9,\,A:22)}$, $D_{sulf}^{1\_236\,(4.5)}$
30 – 45 µm	$A/Dup^{1\_400\,(C:\sim9,\,A:30)}$ $Dup^{1\_408\,(C:\sim14,\,A:8)}$		$Dup^{3\_760\,(C:11,\,A:\sim13)}$	$D_{Dup}^{1\_276\,(4)}$, $D_{Dup/sulf}^{1\_248\,(7)}$, $D_{sulf}^{2\_300\,(7)}$
45 – 60 µm			$Dup^{1\_214\,(C:9,\,A:\sim13)}$, $D_{sulf}^{1\_464\,(5)}$	$Dup^{1\_640\,(C:\sim6,\,A:30)}$, $Dup^{2\_640\,(C:\sim6,\,A:18)}$, $D_{Dup}^{1\_192\,(5)}$
60 – 75 µm	$Dup^{1\_265\,(C:\sim9,\,A:45)}$	$Dup^{2\_205\,(C:\sim21,\,A:12)}$	$Dup^{1\_1300\,(C:6,\,A:\sim22)}$, $Dup^{2\_1090\,(C:8.5,\,A:\sim25)}$	$D_{Dup}^{1\_564\,(C:\sim6,\,A:12)}$, $D_{Dup}^{3\_428\,(C:\sim12,\,A:30)}$, $D_{sulf}^{1\_309\,(5)}$
75 – 90 µm			$A/Dup^{3\_1120\,(C:3,\,A:\sim19)}$, $D_{sulf}^{3\_1430\,(2)}$	$D_{sulf}^{1\_396\,(9)}$, $A/Dup^{1\_280\,(C:\sim34,\,A:6)}$
90 – 105 µm	$D^{1\_285\,(40)}$		$A^{2\_640\,(C:13,\,A:\sim10)}$, $Dup^{1\_239\,(C:8,\,A:\sim10)}$, $D_{sulf}^{1\_544\,(4)}$	$D_{Dup}^{1\_172\,(12)}$
105 – 120 µm			$D_{sulf}^{3\_824\,(4)}$, $D_{sulf}^{1\_884\,(4)}$, $D_{Dup}^{3\_1040\,(6)}$	$D_{sulf}^{1\_271\,(9)}$
120 – 135 µm			$A/Ti(C,N)^{3\_1000\,(C:14,\,A:\sim27)}$, $D_{Dup}^{3\_1028\,(6)}$	$D_{Dup/sulf}^{3\_192\,(6)}$
135 – 150 µm			$D_{sulf}^{2\_460\,(6)}$, $D_{sulf}^{2\_168\,(8)}$, $D_{Dup}^{1\_328\,(7)}$	
150 – 165 µm				$D_{sulf}^{3\_137\,(5)}$
165 – 180 µm				$D_{sulf}^{1\_162\,(3)}$
180 – 195 µm				
195 – 210 µm			$D_{sulf}^{3\_312\,(7)}$	
210 – 225 µm			$Dup^{3\_291\,(C:11,\,A:\sim19)}$, $Ti(C,N)^{1\_289\,(C:5,\,A:\sim19)}$	$D_{Dup}^{1\_133\,(C:\sim9,\,A:15)}$, $D_{Dup/sulf}^{1\_238\,(C:\sim6,\,A:10)}$
225 – 240 µm			$D_{sulf}^{3\_990\,(12)}$	
240 – 255 µm			$D_{sulf}^{3\_810\,(5)}$, $D_{sulf}^{3\_795\,(6)}$, $D_{sulf}^{2\_320\,(7)}$	$D_{Dup/sulf}^{3\_100\,(6)}$
255 – 270 µm				
270 – 285 µm			$D_{Dup}^{3\_965\,(8)}$, $D_{sulf}^{1\_550\,(2)}$, $D_{sulf}^{2\_212\,(6)}$, $D_{sulf}^{2\_815\,(5)}$	
285 – 300 µm			$D_{sulf}^{3\_810\,(6)}$, $D_{sulf}^{3\_600\,(9)}$, $D_{sulf}^{3\_635\,(9)}$, $D^{1\_542\,(5)}$	
300 – 315 µm	$D_{sulf}^{1\_230\,(C:\sim5,\,A:10)}$ $Ti(C,N)^{1\_228\,(5)}$		$D_{sulf}^{2\_1070\,(5)}$	
315 – 330 µm			$A/Ti(C,N)^{3\_640\,(C:10,\,A:\sim13)}$	
330 – 345 µm		$D^{2\_200\,(20)}$		
345 – 360 µm			$D_{sulf}^{2\_632\,(C:17,\,A:\sim6)}$	
360 – 375 µm	$D_{sulf}^{1\_220\,(6)}$		$D_{Dup}^{1\_575\,(7)}$, $D_{Dup}^{1\_1172\,(7)}$	
NMI Total (type)	$7^1, 1^2, 1^3$	$2^2, 1^3$	$12^1, 11^2, 18^3$	$16^1, 2^2, 5^3$
NMI Total	9	3	41	23

See Fig. 7.4.2 for KEY to data entries. See permission [7.4].

An observation is that the number of inclusions in a WEC is related to the size of the WEC. For example between each type of bearing, the larger WEC in each case had more inclusion interactions than the smaller WEC (WEC-B1 (the larger WEC) = 9, WEC-B2 = 3 and WEC-P1 (the larger WEC) = 41, WEC-P2 = 23). See Table 7.4.1 for sizes of WECs.

From the screening process of the planet bearing sections, an explicit example of an inclusion-WEC interaction that appears to have been a butterfly that extended to form a WEC is shown (Fig. 7.4.3a). The inclusion was type A + oxide (Duplicate). Fig. 7.4.3b shows a large globular type D inclusion measuring 39 μm that initiated a butterfly, and Fig. 7.4.3c shows a similar large globular type D inclusion measuring 40 μm that was found to interact with the WEC-B1. These findings alone provide strong evidence that butterfly cracks could possibly extend to form WECs, or that WECs could be initiated from crack extension at inclusions.

Similarly, the shape of the WECs appeared to differ depending on the direction of sectioning. Circumferential section (P1) showed vertically branching networks whereas axial sections (B1, B2 and P2) showed much more parallel networks (see Fig. 7.4.1).

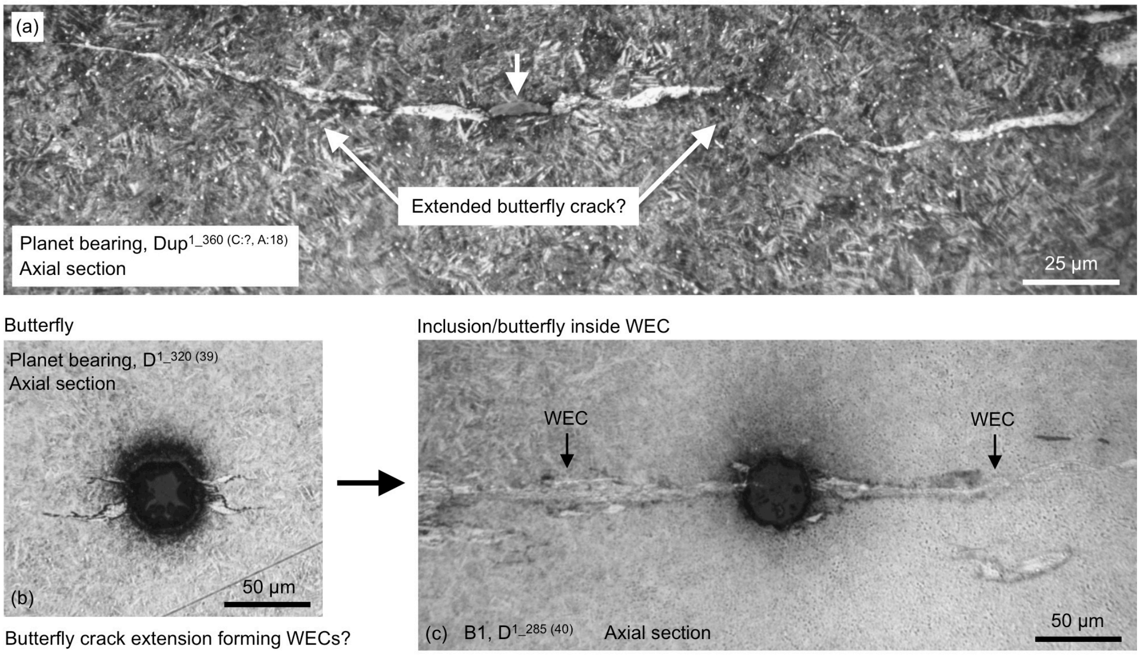

Figure 7.4.3: Optical images showing the possible mechanism of WEC formation by butterfly crack extension. (a) Example of apparent extended butterfly crack from a Duplicate inclusion forming a WEC in a miscellaneous axial section of the planet service bearing. (b) Butterfly formation initiated from a large oxide inclusion in a miscellaneous axial section of the planet service bearing. (b) A similar large oxide located in the B1-WEC that suggests the inclusions role in the WEC initiation process is either by a butterfly crack extension mechanism or by a crack extension mechanism in a non-butterfly manner. See permission [7.4].

7.4.2 Size of inclusions interacting with WECs

It was found that D_{sulf}, D_{Dup}, Duplicates and type D inclusions were those that interacted the most with the WECs. Fig. 7.4.4 shows the inclusion size/lengths interacting with the WECs (initiation likelihood rank 1 and 2 only) in the axial and circumferential directions for both bearing types analysed. In the transient test gearbox bearing data, the maximum length of inclusions interacting with WECs in the circumferential/axial directions was 40 – 45 µm and the average inclusion size was 13.5 µm and 18.2 µm in the circumferential and axial directions respectively. In the planet bearing from service data, the maximum length of inclusions interacting with WECs in the circumferential/axial directions was 30 – 35 µm and the average inclusion size was only 7.6 µm and 9.7 µm in the circumferential and axial directions respectively. The average length of inclusions interacting with the WECs (likelihood of initiation rank 1 or 2) in both the circumferential/axial directions was quite small for the transient test gearbox bearing (less than 20 µm) and especially so for the planet bearing from service (less than 10 µm).

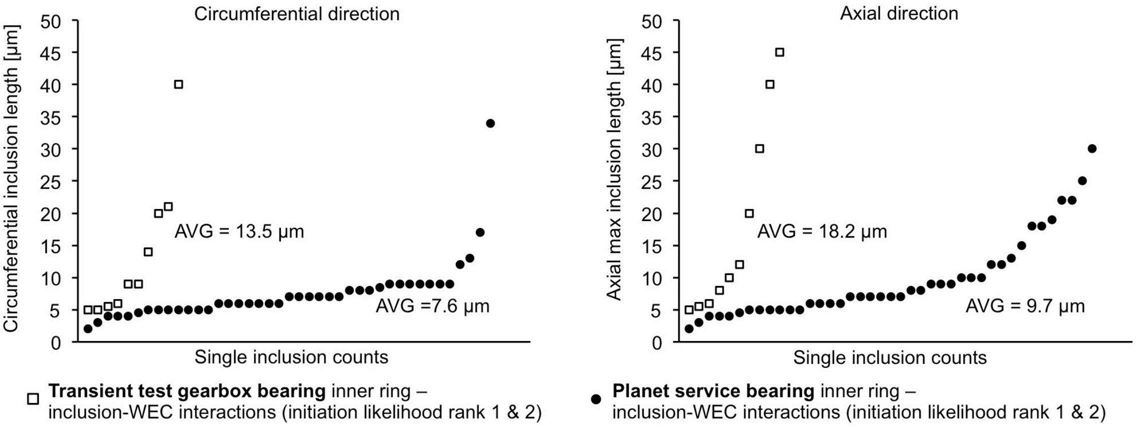

Figure 7.4.4: The inclusion lengths, as determined by maximum size in either the axial or circumferential directions, interacting with the WECs (initiation likelihood rank 1 and 2 only) for both bearing inner rings. Axial direction is that in which inclusions are elongated in the steels for both bearings. See permission [7.4].

7.5 Discussion

7.5.1 Transient gearbox bearing tests

The transient gearbox bearing test successfully created butterflies and WECs using upper realistic maximum contact pressures experienced in service of ~2.15 GPa. The other tribological test conditions on the transient gearbox bearing test were deemed quite aggressive, which enabled the creation of WECs. It is therefore possible that the aggressive tribological conditions caused hydrogen liberation and diffusion into the bearing steel during operation, which enabled the WEC creation leading to flaking. This may have occurred from damage being caused to the tribofilm on the raceways, exposing nascent surfaces and entry roots of hydrogen ions into the steel. However no thermal desorption hydrogen analysis was conducted to confirm this.

The transient gearbox bearing test ran for 130% of its L_{10} life equating to 1400 x 10^6 stress cycles (over-rollings at any one point on the inner ring raceway) with only two small white structure flaking areas being present. The time the flaking occurred is unknown as the flaking was not detected by the condition monitoring instruments. Bearings in service typically run for 6 – 24 months before WSF occurs. Wind turbine gearbox high-speed bearings would accumulate about 100 x 10^6 to 1000 x 10^6 cycles in this time. Hence the transient gearbox bearing test replicates the service life of a multi-MW intermediate and high-speed wind turbine gearbox bearings.

7.5.2 Dark etching region (DER)

No dark etching region (DER) was found to exist in either of the two bearing inner rings. The lack of a DER (subsurface material decay from subsurface shear stressing) is perhaps expected due to the low-moderate contact pressures used in the transient gearbox bearing test and those predicted during operation in the planet service bearing.

7.5.3 Non-metallic inclusions as WEC initiators

The volume of steel mapped in the two bearings analysed in this study (125 slices at ~3 μm per slice equal to 375 μm slicing distance) actually equates to an extremely small volume compared to the total stressed volume in the entire bearings. Hence the finding of many inclusion-WEC interactions that appeared to be initiators in such a small volume offers evidence that one mechanism of WEC formation in wind turbine gearbox bearings is due to subsurface WEC initiation from inclusions, either in a butterfly manner or non-butterfly manner; where these small WECs link together to form larger WEC networks, these eventually propagating to the surface resulting in WSF. This is supported by the observation that the number of inclusions interacting with a WEC (rank 1 or 2) is related to the size of the WEC, and also that the inclusions predominately appearing to initiate the butterflies/WECs were D_{sulf}, D_{Dup}, Duplicates and type D inclusions which is expected as these are likely crack initiators. Most of the inclusions interacting with the WECs that appear to be WEC initiators were relatively small in length or diameter. It is suggested that butterfly cracks could extend to form WECs. This is supported by the evidence in Fig. 7.4.2, the large globular type D inclusion measuring 39 µm that initiated a butterfly in the planet service bearing (Fig. 7.4.3b) and the similar large globular type D inclusion measuring 40 µm that was found to interact with the transient test gearbox bearing B1-WEC (Fig. 7.4.3c). The two ~40 µm globular type D inclusions found to exist in the stressed contact zone are both very severe in terms of likelihood for crack initiation and driving stress for further crack extension from the cyclic stresses from rolling contact.

Little inclusion-WEC interactions were found in WEC-B2, which may be because of the following reasons. 1) The WEC was in the early formation stages and therefore networking of smaller cracks from inclusions was minimal. 2) Only portions (375 µm) of the WECs in both bearings were mapped, therefore possibly the portion of WEC-B2 mapped happened to not contain many inclusion-WEC associations, these being located elsewhere in the WEC not mapped. 3) It is also possible that occasionally some small whole inclusions (globular types) were removed between slices, and were therefore lost and not recorded.

As only portions of the WECs in the bearings in this study were analysed, it is not possible to confirm whether surface initiation occurred or not. However it appeared for the transient test gearbox bearing that no surface cracking was visible on the raceway surface, for example as shown in Fig. 7.2.1. Even though visible surface crack connection was made in the WEC-P1 and possibly WEC-B1 (which was located directly beneath a small surface flaking area), it is suggested that these WECs may have initiated from inclusions due to the evidence of inclusion interactions found.

It is however difficult to judge whether observed inclusions interacting with the WECs are due to the inclusions having initiated the WECs, or whether the WECs initiated elsewhere and happened to propagate through the inclusions. Although there will be some uncertainty, the system devised to rank the likelihood of the inclusions for WEC initiation, based on inclusion type, crack orientation and depth location in the WEC, helps identification of probable inclusion initiators.

The direction in which the inclusion length is elongated is in the axial direction (transverse to direction of travel/over-rolling) for the two bearing inner rings in this study. Bearings in wind turbine gearboxes can either have inclusion elongation in the axial direction, circumferential direction or with no definitive elongation direction depending on the manufacturing techniques used. Whether the inclusion elongation is aligned in direction of travel/over-rolling may be quite influential on crack initiation, however serial sectioning investigations are yet to be conducted on the bearings with this property.

7.5.4 Steel cleanliness analysis

The proposition from this study is that WECs were created from a network of cracking initiated from inclusions and the higher the density of inclusions able to initiate a crack, the higher the propensity and size of the WECs. In regards to steel cleanliness standards, the finding that relatively small/short inclusions were those that appeared to be WEC initiators suggests that measurements that assess the density of inclusions are much more relevant than those that estimate maximum inclusion lengths for butterfly/WEC formation. However the evidence from this study suggests that cleanliness standards in relation to wind turbine gearbox bearings steels should be able to differentiate pure sulfides from sulfides + oxide encapsulations (type A) and record inclusions that are only a couple of micrometer's in length/diameter. This is because in the ISO 4967-B steel cleanliness standard for example, the minimum inclusion size rating for recording of type A inclusions is 37 μm for index 0.5, therefore any type A inclusions less than 37 μm length are not recorded. Hence there will have likely been many short length sulfides with oxide encapsulation (Duplicates) which were not recorded in the data. This is important as Duplicate inclusion lengths below 37 μm could still be likely to initiate a crack (the maximum lengths of inclusions interacting with the WECs in the bearings in this study being only being 20 – 40 μm). In addition, the greater global cleanliness index, C_i, of the planet service bearing compared to the transient test gearbox bearing would infer that the planet bearing from service is dirtier. However, for example due to the minimum inclusion size rating for type A inclusions in the ISO 4967-B standard, it is not known how many inclusions below that threshold existed in either steel, making such conclusions invalid in relation to small/short inclusions.

7.5.5 WEC comparison with the two-roller hydrogen charged tests

Correlation of the results from the extensive analyses of WECs in hydrogen-charged two-roller tests (chapter 6) and the transient gearbox bearing tests (non-hydrogen charged) and wind turbine gearbox bearings from service from this chapter is apparent.

The WECs in both the two-roller hydrogen charged tests and transient gearbox bearing tests were created under service realistic maximum contact pressures. This shows that it is not necessary to apply high loads to create WECs.

The larger WECs in the two-roller hydrogen charged tests presented in chapter 6 have a morphology that appears similar or identical to the WECs found in the bearings in this chapter. The influence of sectioning direction (circumferential or axial) on the orientation of WECs also shows the same relationship.

Both chapters showed that non-metallic inclusions often interacted with the WEC networks. In all cases small length/diameter inclusions interacted with the WECs rather than larger inclusions often focused on in steel cleanliness standards. The combined evidence strongly suggests that *one* mechanism of WEC initiation and propagation is from inclusions and butterflies in the subsurface of the wear zone.

7.6 Conclusions

Butterflies, WECs and WSF have been successfully reproduced in the inner ring of a transient test gearbox bearing that used conditions aiming to mimic conditions faced by bearings in wind turbine gearboxes. In-depth analysis on a transient test gearbox bearing and planet bearing from service has been conducted by the application of serial sectioning (removal of ~3 μm of material per slice by fine grinding and polishing) to map WEC networks in wind turbine gearbox bearings for the first time. This process has revealed critical information about possible WEC initiators. The WECs that formed in the bearing analysed in this chapter are compared to those formed in the two-roller hydrogen charged tests in chapter 6. The analysis aimed to understand if a difference in WEC initiation and propagation mechanisms occurs under non-hydrogen charged RCF conditions compared to hydrogen charged conditions.

1. It was found during metallographic sectioning in both the circumferential/axial directions that the WECs orientation differs considerably depending on the sectioning direction. In the circumferential direction, WECs appear highly vertically branched, whereas in the axial direction, WECs tend to often appear more parallel with less vertical crack branching.
2. Two WECs in both a transient test gearbox bearing and a planet bearing from service were mapped, where in total 76 non-metallic inclusions were found to interact with the four WECs mapped. Based on the 76 inclusion-WEC interactions found, a system devised to rank the likelihood of the inclusions for WEC initiation, based on inclusion type, crack orientation and location in the WEC was used. It was found that many of the inclusion interactions appeared to be WEC initiators (51 of the inclusions had a high likelihood of initiation rank 1 or 2). Evidence was also found that butterflies could propagate to form WECs.
3. MnS associated inclusions (D_{sulf} and D_{Dup}), Duplicates and type D inclusions were the inclusions that interacted the most with the four WECs mapped in the inner rings of the bearings. The average length of inclusions interacting with the WECs (likelihood of

initiation rank 1 or 2) in both the circumferential/axial directions was quite small for the transient test gearbox bearing (less than 20 µm) and especially the planet bearing from service (less than 10 µm). The maximum inclusion lengths in the axial direction were only approximately 30 – 40 µm in the bearings. Therefore the data suggests that steel cleanliness standards analysing inclusion density (as opposed to maximum inclusion lengths) are more relevant in understanding butterfly/WEC initiation in wind turbine gearbox bearings. However steel cleanliness standards used should be able to differentiate pure sulfides from sulfides + oxide encapsulations and record inclusions that are only a couple of micrometer's in length/diameter.

4. Correlation of the results from the analyses of WECs in hydrogen-charged two-roller tests (chapter 6) and the transient gearbox bearing tests (non-hydrogen charged) and wind turbine gearbox bearings from service from this chapter is apparent. The larger WECs in the two-roller hydrogen charged tests have morphology and orientation similar or identical to the WECs found in the bearings in this chapter. Both chapters showed that non-metallic inclusions often interacted with the WEC networks. In all cases small length/diameter inclusions interacted with the WECs rather than larger inclusions often focused on in steel cleanliness standards. The combined evidence strongly suggests that *one* mechanism of WEC initiation and propagation is from inclusions and butterflies in the subsurface of the wear zone.

This page is intentionally left blank

8. Conclusions and further work

8.1 Introduction

This chapter provides an overview of the main novelties and conclusions from the study and how future work in specific areas can expand the outputs from this project. In the future work section a focus is made specifically on RCF testing methods, 3D mapping of damage features and methods for analysing diffusible hydrogen in steels. Fig. 8.1.1 shows the thesis work flow chart.

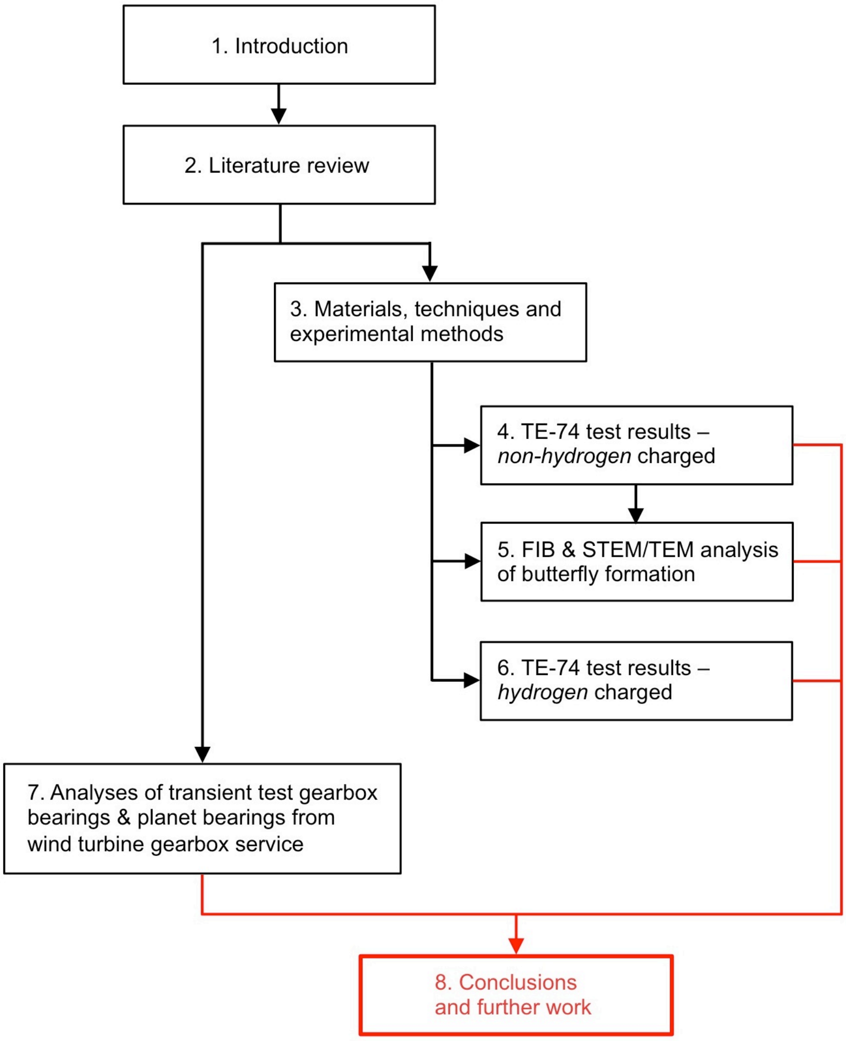

Figure 8.1.1: Thesis work flow chart.

8.2 Conclusions

8.2.1 Overview

This study focused on investigating the formation drivers and mechanisms of white etching features (butterflies and WEA/WECs) in bearing steels that are resulting in a significant amount of premature gearbox failures in wind turbines. Hydrogen diffusion into the bearing steel during service and transient operating conditions have been suggested as drivers of white etching features (butterflies, WEA and WECs). However the initiation and propagation mechanisms as well as the thresholds for WEC formation are not well understood. This is due to the difficulties of creating WECs repeatedly under laboratory conditions and the lack of a method established for mapping WECs in detail or 3-dimensions as typically only limited metallographic analyses are conducted over several cross-sections.

A series of RCF tests have been conducted in this study to investigate the formation drivers and formation mechanisms of butterflies and WECs using a two-roller RCF machine. 100Cr6 martensitic bearing steel rollers were used as test specimens. Following a large number of RCF tests under transient conditions without any success in reproducing WECs (though butterflies were created in the rollers), a hydrogen-charging strategy was adopted to enable WEC creation under lab conditions. This strategy has been used to replicate the bulk diffusion mechanism of hydrogen at wear induced nascent surfaces on bearing raceways that is suggested to occur during operation. This study also conducted a detailed microstructural analysis of a butterfly formed in 100Cr6 bearing steel under RCF on the laboratory two-roller test rig under the transient operating conditions (non-hydrogen charged). Analysis was conducted using focused ion beam (FIB) tomography, 3D reconstruction and transmission electron microscopy (STEM/TEM) methods to further understanding of crack formation mechanisms and carbide dissolution as part of the WEA microstructural change. In the hydrogen charged tests a focus was made on investigating the influence of the concentration of diffusible hydrogen, the magnitude of the contact load and the number of rolling cycles on the formation of white etching features under service realistic loading conditions.

RCF testing (non-hydrogen charged) was also conducted on a large-scale transient test rig with bainitic high-speed wind turbine gearbox bearings. Testing was designed to replicate severe bearing operating conditions in wind turbine gearboxes.

Metallography was extensively used in this project to view cross-sections of the wear zones subject to RCF and any damage features contained within. A metallographic serial sectioning technique was developed to map wear zones subject to RCF in 3-dimensions. This technique has allowed quantitative analysis of white etching feature formation under RCF in both the two-roller lab scale testing, transient test gearbox bearings and wind turbine gearbox bearings obtained from service. This approach maximised detection of possible initiators of WECs, e.g., non-metallic inclusions, butterflies and surface cracking. Mapping of wear zones also gives information concerning the 3-dimensional nature of WEC formation and has been used to generate a virtual model of a WEC for the first time.

The main novelties in this study are:

WECs and WSF have been successfully created on a two-roller RCF machine using hydrogen-charged test rollers under low-moderate concentrations of diffusible hydrogen (~1 ppm) and service realistic loads (P_{max} 1.5 – 2 GPa). Also for the first time WECs and WSF have been created in high-speed wind turbine gearbox bearings on a large-scale transient test rig under severe transient and non-hydrogen charged conditions.

RCF wear zones in test rollers and wind turbine gearbox test bearings and bearings from the field have been quantitatively mapped with a serial sectioning process for the first time. Serial sectioning enabled WECs to be mapped in their entirety and modelled in 3-dimensions, revealing initiation and propagation mechanisms, morphology and orientation relationships. The combination of controlled RCF testing and the serial sectioning process enabled the quantitative investigation of the influence the concentration of diffusible hydrogen, load and rolling cycles to butterfly and WEC formation and thresholds for these parameters on WEC formation.

A butterfly formed under the two-roller transient tests (non-hydrogen charged) was analysed in detail by SEM, FIB tomography and STEM/TEM to further understanding of crack formation mechanisms and carbide dissolution as part of the WEA microstructural change. Based on the evidence a void/cavity coalescence theory for initial butterfly crack formation and iron-chromium carbide dissolution as part of the WEA formation mechanism was proposed.

Based on the serial sectioning analysis across various test specimens and bearings, the evidence showed that *one* mechanism of WEC formation is due to multiple linking of extended butterflies or small WECs in the subsurface to form larger WEC networks that eventually propagate to the surface resulting in WSF. Small/short sized inclusions also predominated as crack initiators suggesting that steel cleanliness standards analysing inclusion density (as opposed to maximum inclusion lengths) are more relevant in understanding butterfly/WEC initiation.

The main conclusions from this study are summarised in the following four sections.

8.2.2 White etching cracks

WECs were successfully created on a two-roller RCF machine using a hydrogen charging technique under low-moderate concentrations of diffusible hydrogen (~1 ppm) and service realistic loads (P_{max} 1.5 – 2 GPa). WECs and WSF have also been successfully reproduced in high-speed wind turbine gearbox bearings in a large-scale transient test rig under severe transient, non-hydrogen charged and service realistic loading conditions (P_{max} 2.15 GPa). The conclusions of the RCF testing and serial sectioning analysis are as follows:

- The serial sectioning technique that was established in this study has proved to be extremely powerful in mapping WECs in 3-dimensions and elucidating initiation and propagation mechanisms, morphology and orientation relationships. Standard metallographic cross-sections and the 3D modelling of a WEC showed that the sectioning direction was influential on the shape of the WECs; in the circumferential plane WECs appeared highly vertically branched, whereas in the axial plane WECs tended to often appear more parallel with less vertical crack branching.
- In the hydrogen charged two-roller tests WECs were found to initiate and propagate in the subsurface. This was confirmed by the mapping of numerous WECs in their entirety and observing that the vast majority of WECs were contained in the subsurface wear zone and did not make any connection with the surface, thus dismissing surface initiation.
- Serial sectioning of both the two-roller lab scale testing, transient test gearbox bearings and wind turbine gearbox bearings obtained from service showed that WECs often interacted with inclusions that were judged to be crack initiators from the inclusions chemical composition, depth below the contact surface and crack continuity in the near vicinity of the inclusion. Evidence was also found that butterfly cracks could propagate to form WECs and FIB tomography verified the initiation mechanisms. Small/short sized sulfide inclusions, globular manganese sulfide + oxide inclusions and small globular oxide inclusions between ~1 – 20 μm in diameter/length predominated as crack initiators. The combined evidence strongly suggests that *one* mechanism of WEC initiation and propagation is from inclusions and butterflies in the subsurface of the wear zone.
- The data suggests that steel cleanliness standards analysing inclusion density (as opposed to maximum inclusion lengths) are more relevant in understanding butterfly/WEC initiation in wind turbine gearbox bearings. However steel cleanliness standards used should be able to differentiate pure sulfides from sulfides + oxide encapsulations and record inclusions that are only a couple of micrometer's in length/diameter.
- This study has for the first time established the thresholds of diffusible hydrogen, load and rolling cycles on white etching feature formation under the hydrogen charged two-roller testing. Butterfly formation was independent of the concentration of diffusible hydrogen at

durations of more than 208 hours and maximum contact pressures of 2 GPa. At pressures in the range 1.2 – 2 GPa butterfly formation increased with pressure and with the number of rolling cycles to a threshold. WEA/WEC formation thresholds were found to be: i) A concentration of diffusible hydrogen between the 5 – 2.5 wt.% NH_4SCN hydrogen charges under a maximum contact pressure of 2 GPa. ii) A maximum contact pressure in excess of 1.2 GPa under a 20 wt.% NH_4SCN charge. iii) Approximately 10 x 10^6 rolling cycles under a maximum contact pressure of 2 GPa and 20 wt.% NH_4SCN charge.

- Comparison of several sections from the same roller revealed there is variability in the white etching feature distribution, which highlights the importance of examining multiple locations in bearings.

8.2.3 Butterfly crack formation mechanisms

Butterfly formations were analysed in both non-hydrogen charged and hydrogen charged test rollers, test bearings and bearings from service.

- The combined evidence supports that the mechanism for butterfly crack and WEA formation is cooperative. This is supported by the in-depth analysis of a butterfly by FIB tomography analysis and that sometimes small cracks (<5 μm length) were found initiating at inclusions without the WEA microstructural change, however it was not observed that a WEA exists around an inclusion without the presence of a crack.
- WEA was confirmed to be a BCC nanocrystalline ferrite structure. The WEA was also found to contain different phases such as inclusions or spherical carbides with a randomly distributed ferrite grain size varying between ~10 – 60 nm.
- Based on the evidence obtained from the SEM, FIB tomography and STEM/TEM analysis, a void/cavity coalescence theory for initial butterfly crack formation and iron-chromium carbide dissolution as part of the WEA formation mechanism was proposed.

8.2.4 WEC initiation and propagation mechanisms

One of the most important conclusions from this study concerns the proposition of an initiation and propagation mechanism of WECs. Prior to the commencement of this study, WEC formation had mostly been attributed to hydrogen embrittlement and there was little information in the literature concerning initiation and propagation mechanisms of WECs. However, since then several hypotheses have been recently suggested. The mechanisms proposed are WEC initiation from surface cracks [37, 106], from inclusions or butterflies in the subsurface [22, 32, 37], or by adiabatic shear banding from impact events [70]. However these WSF investigations have typically been based on a small number of metallographic analyses that has provided little evidence to confirm the proposed mechanisms. The in-depth quantitative analysis of the formation of WECs in this study has for the first time elucidated their initiation and propagation mechanisms. The combined evidence strongly suggests that *one* mechanism of WEC initiation and propagation is from inclusions and butterflies in the subsurface of the wear zone. Fig. 8.2.1 shows a schematic of the proposed steps of WEC formation from the start of rolling contact until WSF occurs.

The *first stage* is crack initiation and short crack growth at inclusions, which is governed by Mode I loading from a fracture mechanics approach [120]. A residual tensile stress field must exist around inclusions in order that the overall compressive stress arising from rolling contact can develop positive stress intensity factors at inclusion-initiated crack tips [120]. These residual tensile stresses are cited to enable initial crack growth relatively easily when combined with the overall cyclic shear stress field from rolling contact. Hence as the residual tensile stress field around an inclusion diminishes moving away from the inclusion, the mode I crack would eventually arrest at a crack size determined by the mode I threshold stress intensity factor [120]. Therefore in general, type D (oxides) and type A (with oxide parts) inclusions are those most likely to initiate cracks and the evidence from this study strongly supports this. These inclusions are most likely to initiate cracks because different inclusions will have different coefficients of thermal expansion (CTE) compared with typical bearing steel microstructures. Sulfide inclusions will have larger CTEs than oxide inclusions. Compressive and tensile stresses are thus induced around these inclusions respectively [123]. A tensile residual stress also exists at sulfides + oxides where the oxide part makes contact with the matrix [120, 123]. Therefore inclusions having initiated at MnS + oxide (D_{Dup}) and oxide (type D) inclusions is expected due to the induced tensile residual stresses, the hardness and elastic modulus mismatch with the tempered martensite matrix and poor coherence/debonding between the oxide part and matrix [22, 28, 115]. In this study the effect of hydrogen on WEA/WEC formation has been shown to be critical in controlling whether WECs will form. Hydrogen is thought to diffuse into the bearing steel at wear induced nascent surfaces [32, 51]. Although hydrogen embrittlement theories do not fully explain the effects of hydrogen in bearing steels [164], hydrogen's role in the steel would be to enhance slip deformation and localisation of plasticity at the fatigue crack tip [149, 151] and to decrease mode I/II stress limits for crack growth and propagation [120, 149]. As WECs have been found to initiate predominately at small/short sized inclusions, the effect of hydrogen is proposed to allow crack initiation at inclusion sizes that are usually regarded as sub-critical. Additional factors such as impact events may also contribute to crack initiation at inclusions.

The *second stage* is further growth of the cracks, which would be governed by Mode II/III shear loading from the high cyclic shear stress field induced during rolling contact if the Mode II/III threshold stress intensity factor were exceeded [120]. Cracks are suggested to be able to propagate from butterflies to form WECs [22, 32, 120], in addition to the crack propagation from inclusions that occurs in a non-butterfly manner. The critical effect of diffusible hydrogen within the steel would be to facilitate the transition of cracking from the initial Mode I to Mode II/III which would not usually occur. Additional mechanical stress drivers such as impact events may also contribute to continued crack propagation.

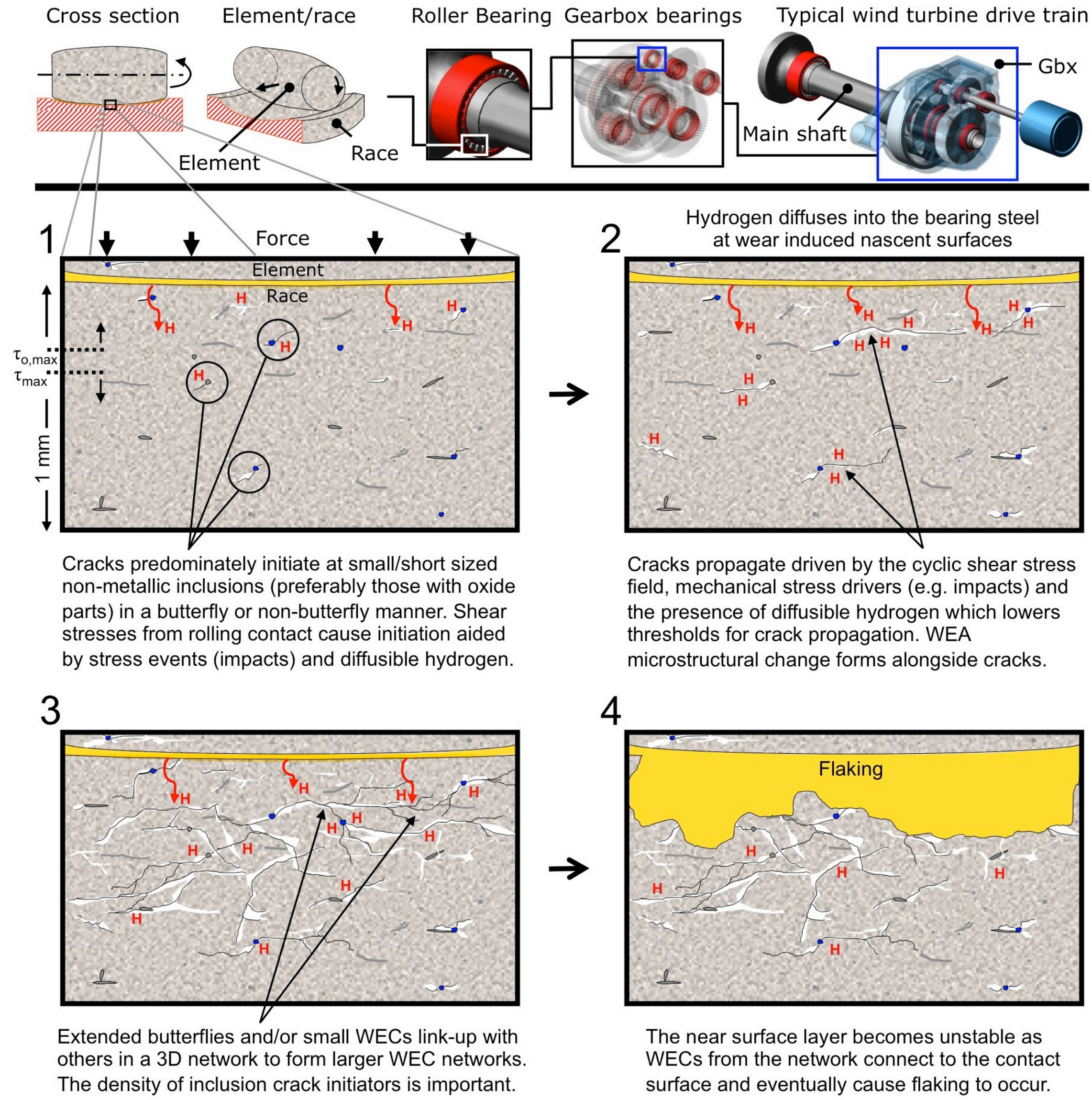

Hydrogen diffuses into the bearing steel at wear induced nascent surfaces

Cracks predominately initiate at small/short sized non-metallic inclusions (preferably those with oxide parts) in a butterfly or non-butterfly manner. Shear stresses from rolling contact cause initiation aided by stress events (impacts) and diffusible hydrogen.

Cracks propagate driven by the cyclic shear stress field, mechanical stress drivers (e.g. impacts) and the presence of diffusible hydrogen which lowers thresholds for crack propagation. WEA microstructural change forms alongside cracks.

Extended butterflies and/or small WECs link-up with others in a 3D network to form larger WEC networks. The density of inclusion crack initiators is important.

The near surface layer becomes unstable as WECs from the network connect to the contact surface and eventually cause flaking to occur.

Figure 8.2.1: The proposed initiation and propagation mechanisms of WEA/WECs.

The *third stage* is the link-up of multiple extended butterflies and/or small WECs to form large 3D WEC networks beneath the contact surface. Therefore it can be expected that the higher the density of inclusions in the bearing steel, the higher the likelihood that the small cracks which initiate at these inclusions will propagate and link with others in the local vicinity to form large WEC networks. This supports the notion that steel cleanliness standards that assess the density of inclusions are more relevant in understanding WEC formation than those that estimate the maximum length of inclusions by statistical methods. However the steel cleanliness standards should be able to record inclusions that are small/short (i.e. from ~3 µm and above), as these inclusions are expected to initiate cracks.

The *fourth stage* is where multiple cracks from the WEC network connect to the contact surface causing the near surface layer to become unstable. Lubricant may enter cracks that connect to the contact surface resulting in a hydraulic crack opening mechanism as over-rolling occurs [92]. Traction in the contact will also cause tensile crack opening. Tensile residual stresses in bearing rings may enable subsurface initiated and propagated cracks to turn upwards towards the surface creating axial hairline cracks. These mechanisms lead to the near surface layer becoming unstable followed by small particle break off until flaking of the steel eventually occurs.

8.3 Future work

8.3.1 RCF testing to elucidate WEC formation drivers and develop solutions

TE-74 two-roller RCF testing

A condition was not established which would enable WEC formation in the TE-74 two-roller testing without the use of hydrogen charging. However operating conditions may exist that would enable this, which would allow further investigation into the formation drivers of WSF. This would allow changes in the test program to pinpoint the effect of individual parameters.

A change in operating condition (e.g. load, slip, speed), roller surface finish or oil type may be required to enable WSF without hydrogen charging. Other techniques that have previously been used to enable WEC formation include adding water to the lubricant in the test. These could be further explored to try and enable WEC formation.

Transient gearbox bearing testing

In chapter 7, a first of its kind RCF test was detailed that allowed creation of WSF in large scale gearbox bearings. The test parameters were chosen to maximise the chance of creating

WECs on the first test run. The operating conditions were complex involving transients in the constant speed and high frequency speed and radial load transients. The bearing type used was spherical roller bearings as these are known to operate with inherent slip in the contact. The lubricant used was a highly surface-active oil known to increase the chance of WSF.

There is a large scope for future tests that can be conducted on this test rig to further understanding of the tribological drivers of WSF. Changes in the test program can be made to pinpoint the effect of individual parameters such as high frequency radial impact loading, high frequency speed transients and the application of an axial load in combination with radial loading. Different oils and additives can be screened and different bearing types and bearing steel materials tested to try and find solutions to the failure mode.

Testing using different RCF machines

During this PhD project a couple of non-public domain studies have surfaced which detail test rigs and conditions that allow creation of WECs without the use of hydrogen charging.

One of the test rigs uses thrust washer rolling element bearings with roughened contact surfaces in combination with automotive transmission oil that is known to highly increase the chance for WECs to form. The dynamics of the elements on the thrust washer set-up has been suggested to cause nascent surface generation on the contact surfaces and a route for hydrogen entry into the bearing steel. However it should be noted that these dynamics are probably not realistic to those of wind turbine gearbox bearings. Another RCF machine tests small deep groove ball bearings that are driven by belts that have resonance induced inside the belts. This in turn introduces high frequency vibrations and impact loading on the test bearings.

A combination of tests on these RCF machines could be beneficial in rapidly and relatively cheaply assessing drivers of WSF and investigating lubrication, steel and coating solutions.

8.3.2 Serial sectioning analysis

Chapter 7 detailed the serial sectioning analysis of WECs in transient test gearbox bearings and planet bearings from service. However the analysis conducted only involved a fraction of the total WEC, therefore even though strong evidence was observed for a subsurface initiation mechanism at non-metallic inclusions it was not possible to confirm this. Hence it would be highly beneficial to map numerous WECs in their entirety to gain more understanding of whether WECs definitely initiate subsurface or whether other mechanisms can occur. It would also be useful to compare between planet, intermediate and high-speed bearings as the mechanisms of WEC initiation and propagation may differ due to different operating conditions.

Further work by the author and coworkers in the research group has already begun to conduct serial sectioning analyses on the rolling elements of a thrust washer bearing (mentioned in previous paragraph) that contained WECs from testing under *non*-hydrogen charged conditions. The analysis shows that although WECs can interact with the surface, many small/short inclusions also typically interact with the WECs that appear to be crack initiators. This already provides further evidence that inclusions can be involved in WEC initiation and/or propagation. Full details of this work will be released in a future publication.

8.3.3 Crack initiation mechanisms and WEA microstructural change

The crack initiation mechanisms of butterflies and WECs at inclusions/voids requires further characterisation to confirm how the crack forms and how the WEA microstructural change is associated with crack formation. The evidence presented in chapter 5 for a void/cavity coalescence theory for initial butterfly crack formation at defects requires verification by further FIB tomography investigations of crack initiation at different types of inclusions/defects, as the initiation mechanisms may differ. The evidence from this project and some literature support a cooperative mechanism of crack formation and WEA microstructural change. This aspect also requires further work for verification.

8.3.4 Measurements of the concentration of diffusible hydrogen

A limited number of thermal desorption analysis (TDA) investigations have been conducted on specimens/bearings with WEC formation immediately after RCF testing. The specimens/bearings must be removed from the RCF test machine as quickly as possible and frozen in LIN until the time of TDA. Analyses such as these on the bearings from the tests mentioned in section 8.3.1 would give critical information on confirming whether diffusible hydrogen is present in the bearing steel during rolling contact. Ideally TDA would also be performed on actual wind turbine gearbox bearings that have operated in the field. However it seems that the impracticality of doing so has prevented this type of analysis from taking place.

A new technique by KircTech GmbH for online or offline measurement of diffusible hydrogen in steel has recently surfaced [193]. The technique involves spot welding a probe to the surface of the steel to be analysed. Diffusible hydrogen that may enter the steel will eventually travel to the probe that acts as a sink where it is trapped and collected. The probe is then linked to a sensor instrument that measures the concentration of hydrogen in the probe. By solving the underlying physical equations (Fick's laws), the concentration of diffusible hydrogen in the steel sample can be determined.

If the surface the probe is attached to is static (e.g. the stationary outer ring of a rolling element bearing) then the probe can be kept linked to the sensor instrument and an online measurement can be made throughout the bearing operation or test. If the surface the probe is attached to is dynamic, then a reference measurement can be made at the start of operation, then the probe left welded on to the surface without a link to the sensor instrument, followed by a final link-up and measurement at the end of the bearing operation or test.

The accuracy of the sensor has been stated as between 0.05 – 0.1 ppm depending on if the measurement if online or offline. A constant test temperature and no electromagnetic interference results in the highest accuracy. A source of error is that one of the input parameters is the diffusion coefficient of hydrogen in the steel at the temperature of operation, which may not be precisely known.

This method has been qualified in a thrust washer bearing set-up where the component being analysed is a thin (~2 – 5 mm thick) steel washer that is static. Because the washer is thin it is an ideal set-up as any hydrogen diffusing into the steel will relatively quickly diffuse through the thickness of the steel. However how the method could work for placement on bearing rings in cylindrical/spherical/taper roller bearings that are much thicker has yet to be established. Nonetheless, this is a promising method that requires further efforts to establish its usefulness in measuring diffusible hydrogen in bearing operation or tests.

8.3.5 Non-destructive analysis of WECs

The serial sectioning technique used to map white etching feature formations in the test specimens and bearings in this study is a powerful method but is inherently destructive and time consuming. It would be highly informative for a technique to be used that could map WEC formations non-destructively. If sufficient resolution were obtainable this could be a highly time saving process compared to serial sectioning for mapping WEC formations after bearing operation or tests. In addition crack formation could be monitored in test specimens/bearings at intervals of the RCF tests to provide further information on the initiation and propagation mechanisms of WECs. Non-public domain studies have shown that high frequency submersed ultra-sound is able to detect subsurface crack networks but lacks the ability to map WECs in 3D in any level of detail. On the other hand an X-ray method at a synchrotron facility could perhaps provide the necessary penetration power and resolution required to detect and map WECs.

9. Appendix

9.1 Appendix

This appendix chapter details the calculations used for determining the maximum contact pressures and shear stresses during rolling contact in the 26v52 mm roller testing.

9.1.1 Theoretical overview of elliptical contact parameters

The calculations in the following section has been taken from Dieter (1986) [98], Johnson (1985) [99] and Stachowiak & Batchelor (2006) [92]. An elliptical contact is formed in a contact when two solid bodies have different principle relative radii of curvature in orthogonal planes. This is the case for the 26v52 mm contact. The contact ellipse dimensions are described by 'a' and 'b', the semimajor and semiminor axes respectively. Table 9.1.1 below show the formula for calculating the main contact parameters in elliptical contacts along with definition of unidirectional and orthogonal shear stresses.

Table 9.1.1: Formulae for contact parameters between to elastic bodies forming elliptical contacts.

Contact area dimensions	Maximum contact pressure	Average contact pressure	Maximum deflection	Maximum unidirectional shear stress	Maximum orthogonal shear stress
$a = k_1\left(\frac{3NR'}{E'}\right)^{1/3}$ $b = k_2\left(\frac{3NR'}{E'}\right)^{1/3}$ 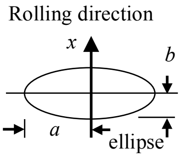 	$P_{max} = \frac{3N}{2\pi ab}$	$P_{average} = \frac{N}{\pi ab}$	$\delta = 0.52k_3\left(\frac{N^2}{E'^2 R'}\right)^{1/3}$	$\tau_{max} = k_4 P_{max}$ $z_{max} = k_5 b$	$\tau_{o,max} = P_{max}\frac{(2t^* - 1)^{1/2}}{2t^*(t^* + 1)}$ $z_o = \zeta^* b \;,\; x_o = \pm\xi^* b$ $t^* = 1 + 0.16\cosh\frac{\left(R_y/R_x\right)^{2/\pi}}{2}$ $\zeta^* = \frac{1}{\left(t^* + 1\right)\left(2t^* - 1\right)^{1/2}}$ $\xi^* = \frac{t^*}{t^* + 1}\left(\frac{2t^* + 1}{2t^* - 1}\right)^{1/2}$

Where:

a	is the semimajor axis of the contact ellipse [m];
b	is the semiminor axis of the contact ellipse [m];
E’	is the reduced Young’s Modulus [Pa];
δ	is the total deflection at the centre of the contact (i.e. $\delta = \delta_A + \delta_B$; where '$\delta_A$' and '$\delta_B$' are the maximum deflections of body 'A' and 'B', respectively) [m];
N	is the normal load [N];
P	is the contact pressure (Hertzian stress) [Pa];
τ_{max}	is the maximum unidirectional shear stress acting at ±45° below the centre of the contact at depth z_{max} [Pa];
$\tau_{o,max}$	is the maximum orthogonal shear stress acting parallel and normal to the surface below the contact at depth z_o [Pa];
z_{max}	is the depth under the surface where the maximum unidirectional shear stress (τ_{max}) acts [m];

z_o	is the depth under the surface where the maximum orthogonal shear stress ($\tau_{o,max}$) acts [m];
x_o	is position where $\tau_{o,max}$ acts in the x-direction (i.e. y=0) [m];
$k_0, k_1, k_2, k_3, k_4, k_5$	are the contact coefficients which are determined by equations and charts;
R'	is the reduced radius of curvature [m];
R_x	is the reduced radii of curvature in x-direction [m];
R_y	is the reduced radii of curvature in y-direction [m].

$$\frac{1}{R'} = \frac{1}{R_x} + \frac{1}{R_y} = \left(\frac{1}{R_{ax}} + \frac{1}{R_{bx}}\right) + \left(\frac{1}{R_{ay}} + \frac{1}{R_{by}}\right)$$

Where:

R_{ax}	is the radius of curvature of body 'A' in the 'x' direction [m];
R_{ay}	is the radius of curvature of body 'A' in the 'y' direction [m];
R_{bx}	is the radius of curvature of body 'B' in the 'x' direction [m];
R_{by}	is the radius of curvature of body 'B' in the 'y' direction [m].

Convention:

The arrangement of 'x' and 'y' coordinates plays an important role in the calculation of contact parameters, and must therefore be defined so that the following condition is fulfilled:

$$\left(\frac{1}{R_x} \geq \frac{1}{R_y}\right)$$

Then the 'x' coordinate determines the direction of the semiminor axis and 'y' coordinate the direction of the semimajor axis.

$$k_0 = \frac{\left[\left(\frac{1}{R_{ax}} - \frac{1}{R_{ay}}\right)^2 + \left(\frac{1}{R_{bx}} - \frac{1}{R_{by}}\right)^2 + 2\left(\frac{1}{R_{ax}} - \frac{1}{R_{ay}}\right)\left(\frac{1}{R_{bx}} - \frac{1}{R_{by}}\right)\cos 2\phi\right]^{\frac{1}{2}}}{\left(\frac{1}{R_{ax}} + \frac{1}{R_{ay}} + \frac{1}{R_{bx}} + \frac{1}{R_{by}}\right)}$$

Where:

ϕ	is the angle between the plane containing the minimum principle radius of curvature of body 'A' and the plane containing the minimum principle radius of curvature of body 'B'. In the 26v52 mm contact, $\Phi = 0$.

9.1.2 Calculation of general contact parameters for the 26v52 mm contact

26 mm roller: R_{ax} = 13 mm, R_{ay} = 26 mm (crown)
52 mm roller: R_{ax} = 26 mm, $R_{ay} = \infty$ (flat)
100Cr6 steel: Young's Modulus, E = 213 x 10^9 Pa, Poisson's ratio, $\nu = 0.29$

Reduced radius of curvature:

$$\frac{1}{R_x} = \frac{1}{R_{ax}} + \frac{1}{R_{bx}}$$ **R_x = 0.009 [m]**

$$\frac{1}{R_y} = \frac{1}{R_{ay}} + \frac{1}{R_{by}}$$ **R_y = 0.026 [m]**

Convention $\left(\frac{1}{R_x} \geq \frac{1}{R_y}\right)$ must be satisfied, which in this case it is, therefore coordinate directions are kept.

$$\frac{1}{R'} = \frac{1}{R_x} + \frac{1}{R_y} = \left(\frac{1}{R_{ax}} + \frac{1}{R_{bx}}\right) + \left(\frac{1}{R_{ay}} + \frac{1}{R_{by}}\right)$$ **R' = 0.0065 [m]**

Reduced Young's Modulus:

$$E' = \left(\frac{E}{1-\upsilon^2}\right)$$ **E' = 2.326x10^{11} [Pa]**

Contact coefficients:

$$k_0 = \frac{\left[\left(\frac{1}{R_{ax}} - \frac{1}{R_{ay}}\right)^2 + \left(\frac{1}{R_{bx}} - \frac{1}{R_{by}}\right)^2 + 2\left(\frac{1}{R_{ax}} - \frac{1}{R_{ay}}\right)\left(\frac{1}{R_{bx}} - \frac{1}{R_{by}}\right)\cos 2\phi\right]^{\frac{1}{2}}}{\left(\frac{1}{R_{ax}} + \frac{1}{R_{ay}} + \frac{1}{R_{bx}} + \frac{1}{R_{by}}\right)}$$ **k_0 = 0.50**

In the 26 mm vs. 52 mm contact, $\Phi = 0$.

Using k_0 = 0.50, k_1, k_2, k_3, k_4 and k_5 can be found from Fig. 9.1.1. **k_1 = 1.49, k_2 = 0.73**

k_3 = 1.88, k_4 = 0.33

k_5 = 0.64

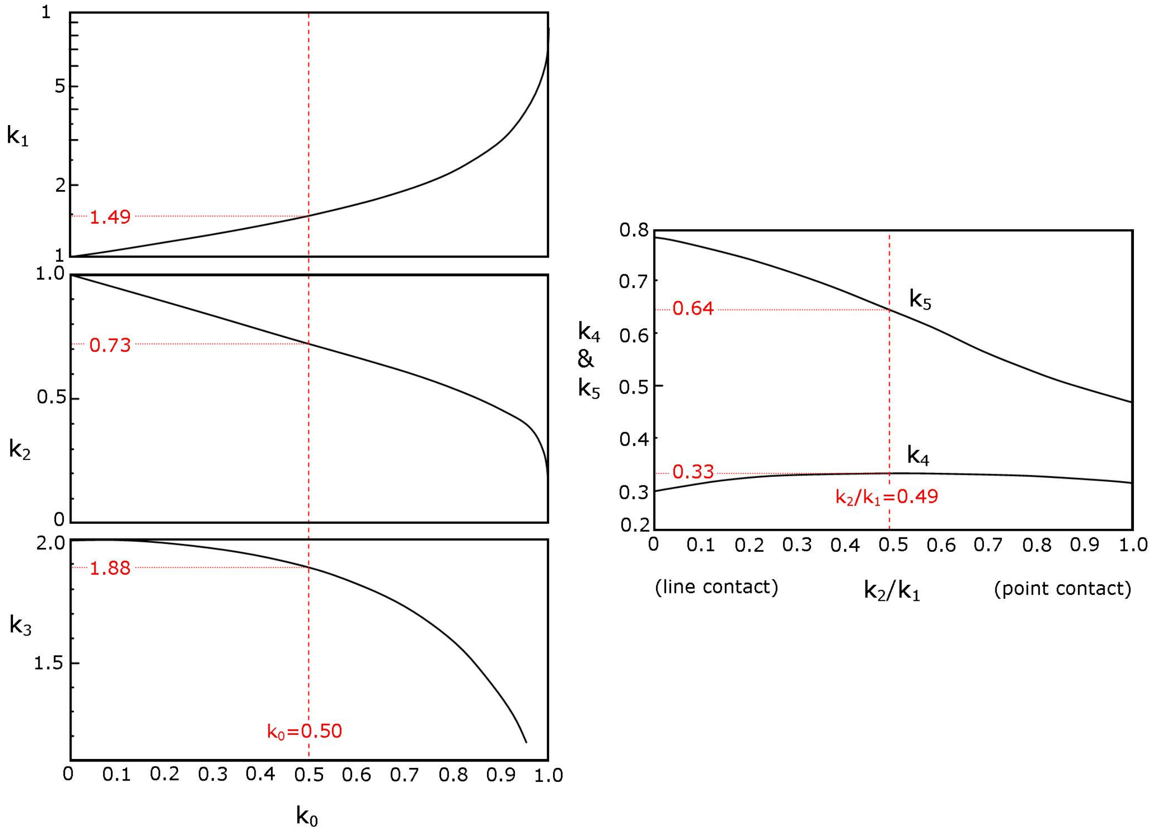

Figure 9.1.1: Contact coefficient charts.

9.1.3 Example calculation of contact parameters for P_{max} = 2 GPa

<u>Contact area dimensions:</u>

N = 665 N

$$a = k_1\left(\frac{3NR'}{E'}\right)^{1/3}$$ **a = 0.57 [mm]**

$$b = k_2\left(\frac{3NR'}{E'}\right)^{1/3}$$ **b = 0.28 [mm]**

<u>Maximum & average contact pressure:</u>

$$P_{max} = \frac{3N}{2\pi ab}$$ **P_{max} = 2 [GPa]**

P_{avg} = 2/3P_{max} = 1.3 [GPa]

<u>Maximum deflection:</u>

$$\delta = 0.52k_3\left(\frac{N^2}{E'^2 R'}\right)^{1/3}$$ **δ = 10.55 [μm]**

Maximum unidirectional shear stress, τ_{max}:

$$\tau_{max} = k_4 P_{max}$$

τ_{max} = 660 [MPa]

$$z_{max} = k_5 b$$

z_{max} = 178 [µm]

Maximum orthogonal shear stress, $\tau_o = (\tau_{zx})_{max}$:

$$t^* = 1 + 0.16 \cosh \frac{\left({R_y}/{R_x} \right)^{2/\pi}}{2}$$

t^* = 1.248

$$\zeta^* = \frac{1}{\left(t^* + 1\right)\left(2t^* - 1\right)^{1/2}}$$

ζ^* = 0.383

$$\xi^* = \frac{t^*}{t^* + 1}\left(\frac{2t^* + 1}{2t^* - 1}\right)^{1/2}$$

ξ^* = 0.849

$$\tau_o = \left(\tau_{zx}\right)_{max} = P_{max} \frac{(2t^* - 1)^{1/2}}{2t^*(t^* + 1)}$$

τ_o = 436 [MPa]

$$z_o = \zeta^* b$$

z_o = 107 [µm]

$$x_o = \pm \xi^* b$$

x_o = ±237 [µm]

9.1.4 Table of calculated contact parameters for P_{max} 1.2 – 5 GPa

Table 9.1.2: Calculated parameters for P_{max} 1.5 – 5 GPa used in 26v52mm roller testing.

P_{max}	**[GPa]**	**1.2**	**1.5**	**2.0**	**3.0**	**4.0**	**5.0**
$P_{average}$	[GPa]	0.78	1.0	1.3	2.0	2.7	3.3
Normal load [N]	[N]	135	280	665	2245	5320	10390
a (semimajor axis of contact ellipse)	[mm]	0.335	0.427	0.569	0.854	1.138	1.423
b (semiminor axis of contact ellipse)	[mm]	0.164	0.209	0.279	0.418	0.558	0.697
δ (maximum deformation in centre of contact)	[µm]	3.6	5.9	10.6	23.7	42.2	66.0
Unidirectional shear stress, τ_{max}							
τ_{max}	[MPa]	388	495	660	990	1320	1650
z_{max} (depth of τ_{max})	[µm]	105	134	178	268	357	446
Orthogonal shear stress, $\tau_{o,max}$							
$\tau_{o,max}$	[MPa]	256	327	436	654	872	1090
z_o (depth of $\tau_{o,max}$)	[µm]	63	80	107	160	214	267
x_o (pos. of $\tau_{o,max}$ in x-plane (rolling direction = x) (y=0))	[µm]	139	177	237	355	473	592

References

[1] M.N. Kotzalas, G.L. Doll, Tribological advancements for reliable wind turbine performance, Phil. Trans. R. Soc. A, 368 (2010) 4829-4850.
[2] W.M. Needelman, M.A. Barris, L.G. L., Contamination control for wind turbine gearboxes, Power Engineering, 2009.
[3] K. Ihata, T. Shiga, A. Umeda, Rolling bearing assembly having magnet to prevent brittle flaking, Denso Corporation, US, 2009.
[4] S. Tanaka, N. Mitamura, Y. Murakami, Influence of sliding and chromium content in the steel on the white structural change under rolling contact, Proceedings of the Global Powertrain Conference, Dearborn, MI, 2004, pp. 6-13.
[5] K. Iso, A. Yokouchi, H. Takemura, Research work for clarifying the mechanism of white structure flaking and extending the life of bearings, SAE World Congress, SAE International, Detroit, MI, 2005.
[6] J. Luyckx, W. Broeders, J. Geertsom, Method for increasing the fatigue strength of a predominantly steel mechanical part of a wind turbine and/or for reducing the tendency to form what are called "white etching cracks" or "brittle flakes" in such steel mechanical parts, Hansen Transmissions International, US, 2009.
[7] Northwest Laboratories of Seattle, Inc., 2007.
[8] J. Barry, G. Byrne, TEM study on the surface white layer in two turned hardened steels, Metall. Mater. Trans. A, 325 (2002) 356–364.
[9] A. Ramesh, S. Melkote, L. Allard, L. Riester, T. Watkins, Analysis of white layers formed in hard turning of AISI 52100 steel, Mater. Sci. Eng., A, 390 (2005) 88-97.
[10] D. Schwach, Y. Guo, A fundamental study on the impact of surface integrity by hard turning on rolling contact fatigue, Int. J. Fatigue, 28 (2006) 1838-1844.
[11] G. Baumann, K. Knothe, H.-J. Fecht, Surface modification, corrugation and nanostructure formation of high speed railway tracks, Nanostruct. Mater., 9 (1997) 751-754.
[12] R. Carroll, J. Beynon, Rolling contact fatigue of white etching layer: Part 1 crack morphology, Wear, 262 (2007) 1253-1266.
[13] I.M. Widiyarta, F.J. Franklin, A. Kapoor, Modelling thermal effects in ratcheting-led wear and rolling contact fatigue, Wear, 265 (2008) 1325-1331.
[14] G. Baumann, H.J. Fecht, S. Liebelt, Formation of white-etching layers on rail treads, Wear, 191 (1996) 133-140.
[15] H. Yokoyama, S. Mitao, S. Yamamoto, Y. Kataoka, T. Sugiyama, High strength bainitic steel rails for heavy haul railways with superior damage resistance, NKK Technical Review, 84 (2001) 44-51.
[16] T.W. Wright, The physics and mathematic of adiabatic shear bands, Cambridge University Press, Cambridge, UK, 2002.
[17] S.M. Walley, Shear localization: A historical overview, Metall. Mater. Trans. A, 38 (2007) 2629-2654.
[18] H. Schlicht, E. Schreiber, O. Zwirlein, Effects of material properties on bearing steel fatigue strength, in: J.J.C. Hoo (Ed.) Effect of steel manufacturing processes on the quality of bearing steels, ASTM, Philadelphia, 1988, pp. 81-101.
[19] A.P. Voskamp, R. Österlund, P.C. Becker, O. Vingsbo, Gradual changes in residual stress and microstructure during contact fatigue in ball bearings, Met. Technol., (1980) 14-21.
[20] I.A. Polonsky, L.M. Keer, On white etching band formation in rolling bearings, J. Mech. Phys. Solids, 43 (1995) 637-669.
[21] H. Swahn, P.C. Becker, O. Vingsbo, Martensite decay during rolling contact fatigue in ball bearings, Metall. Trans. A, 7 (1976) 1099-1110.
[22] T.B. Lund, Subsurface initiated rolling contact fatigue - influence of non-metallic inclusions, processing conditions, and operating conditions, J. ASTM Int., 7 (2010) 1-12.
[23] K. Sugino, K. Miyamoto, M. Nagumo, K. Aoki, Structural alterations of bearing steels under rolling contact fatigue, ISIJ Int., 10 (1970) 98-111.

[24] A. Grabulov, Fundamentals of rolling contact fatigue, University of Belgrade, Serbia, 2010, pp. 153.
[25] P.C. Becker, Microstructural changes around non-metallic inclusions caused by rolling contact fatigue of ball-bearing steels, Met. Technol., 8 (1981) 234–243.
[26] K. Hiraoka, M. Nagao, T. Isomoto, Study on flaking process in bearings by white etching area generation, J. ASTM Int., 3 (2006) 1-7.
[27] A. Grabulov, U. Ziese, H.W. Zandbergen, TEM/SEM investigation of microstructural changes within the white etching area under rolling contact fatigue and 3-D crack reconstruction by focused ion beam, Scripta Mater., 57 (2007) 635-638.
[28] A. Grabulov, R. Petrov, H.W. Zandbergen, EBSD investigation of the crack initiation and TEM/FIB analyses of the microstructural changes around the cracks formed under Rolling Contact Fatigue (RCF), Int. J. Fatigue, 32 (2010) 576-583.
[29] H. Harada, T. Mikami, M. Shibata, D. Sokai, A. Yamamoto, H. Tsubakino, Microstructural changes and crack initiation with white etching area formation under rolling/sliding contact in bearing steel, ISIJ Int., 45 (2005) 1897-1902.
[30] D. Scott, B. Loy, G.H. Mills, Metallurgical aspects of rolling contact fatigue, P. I. Mech. Eng., 181 (1966) 94-103.
[31] T. Endo, D. Dong, Y. Imai, Y. Yamamoto, Study on rolling contact fatigue in hydrogen atmosphere - improvement of rolling contact fatigue life by formation of surface film, in: D. Dowson, M. Priest, G. Dalmaz, A. Lubrecht (Eds.) Life Cycle Tribology, 31st Leeds-Lyon Tribology Symposium, Elsevier, Trinity and All Saints College, Leeds, UK, 2004, pp. 343-350.
[32] R.H. Vegter, J.T. Slycke, The role of hydrogen on rolling contact fatigue response of rolling element bearings, J. ASTM Int., 7 (2009) 1-12.
[33] Y. Imai, T. Endo, D. Dong, Y. Yamamoto, Study on rolling contact fatigue in hydrogen environment at a contact pressure below basic static load capacity, Tribol. T., 53 (2010) 764-770.
[34] P. Xiangduo, Y. Shimizu, N. Mitamura, Long life bearing technologies on material aspect, in: J. Luo, Y. Meng, T. Shao, Q. Zhao (Eds.) Advanced Tribology, Springer Berlin Heidelberg, 2010, pp. 932-933.
[35] S. Fujita, N. Mitamura, Y. Murakami, Research of new factors affecting rolling contact fatigue life, World Tribology Congress III, ASME, Washington, DC, 2005, pp. 1-2.
[36] Y. Matsumoto, Y. Murakami, M. Oohori, Rolling contact fatigue under water-infiltrated lubrication, in: J.M. Beswick (Ed.) Bearing Steel Technology, ASTM International, West Conshohocken, PA, 2002, pp. 226-243.
[37] H. Uyama, H. Yamada, H. Hidaka, N. Mitamura, The effects of hydrogen on microstructural change and surface originated flaking in rolling contact fatigue, Tribology Online, 6 (2011) 123-132.
[38] K. Hiraoka, T. Fujimatsu, N. Tsunekage, A. Yamamoto, Generation process observation of micro-structural change in rolling contact fatigue by hydrogen-charged specimens, Jpn. J. Tribol., 52 (2007) 673-683.
[39] R. Österlund, O. Vingsbo, L. Vincent, P. Guiraldenq, Butterflies in fatigued ball bearings - formation mechanism and structure, Scand. J. Metall., 11 (1982) 23-32.
[40] W.J. Davies, K.L. Day, Surface fatigue in ball bearings, roller bearings, and gears in aircraft engines, Symposium: Fatigue in Rolling Contact, Instn. Mech. Engrs., Instn. Mech. Engrs., London, UK, 1963, pp. 23-40.
[41] Y. Murakami, M. Naka, A. Iwamoto, G. Chatell, Long life bearings for automotive alternator applications, International Congress and Exposition, SAE International, Detroit, MI, 1995, pp. 1-14.
[42] N. Kino, K. Otani, The influence of hydrogen on rolling contact fatigue life and its improvement, JSAE Rev., 24 (2003) 289-294.
[43] K. Tamada, H. Tanaka, Occurrence of brittle flaking on bearings used for automotive electrical instruments and auxiliary devices, Wear, 199 (1996) 245-252.
[44] J.A. Martin, S.F. Borgese, A.D. Eberhardt, Microstructural alterations of rolling bearing steels undergoing cyclic stressing, Trans. ASME J. Basic Eng., 88 (1966) 555-567.

[45] J.L. O'Brien, A.H. King, Electron microscopy of stress-induced structural alterations near inclusions in bearing steels, Trans. ASME J. Basic Eng., (1966) 568-572.
[46] J. Buchwald, H.W. Heckel, An analysis of microstructural changes in 52100 steel bearings due to cyclic stressing, Trans. ASM, 61 (1968) 750-756.
[47] D. McVittie, Wind turbine gearbox reliability, 2006.
[48] A. Muroga, H. Saka, Analysis of rolling contact fatigued microstructure using focused ion beam sputtering and transmission electron microscopy observation, Scripta Metall. Mater., 33 (1995) 151-156.
[49] H.W. Walton, The influence of residual stresses on the susceptibility to hydrogen embrittlement in hardened steel components subjected to rolling contact conditions, SAE International Off-Highway Congress, SAE International, Las Vegas, Nevada, 2002, pp. 1-6.
[50] NSK, Long life bearings for engine accessories, Motion & Control, NSK, 2004, pp. 1-10.
[51] M. Kohara, T. Kawamura, M. Egami, Study on mechanism of hydrogen generation from lubricants, Tribol. T., 49 (2006) 53-60.
[52] T. Kawamura, H. Mikami, Development of NA103A long-life grease for automotive components, NTN Technical Review, 75 (2007) 116-123.
[53] H. Mikami, T. Kawamura, Influence of electrical current on bearing flaking life, SAE Technical Paper, SAE International, 2007.
[54] K. Iso, H. Miyajima, K. Denpou, Y. Toda, M. Yamazaki, M. Naka, Y. Fujita, Rolling bearing, rolling bearing for fuel cell, compressor for fuel cell system and fuel cell system, NSK, US, 2007.
[55] H. Nakashima, Trends in materials and heat treatments for rolling bearings, NTN Technical Review, 2008, pp. 10-17.
[56] S. Tanaka, Y. Murakami, Rolling bearing, NSK, US, 2008.
[57] A. Umeda, T. Shiga, K. Ihata, Rolling bearing incorporated in auxiliary device for internal combustion engine, Denso Corporation, US, 2009.
[58] J. Beswick, A.A. Gabelli, S. Ioannides, J.H. Tripp, A.P. Voskamp, Rolling bearing life models and steel internal cleanliness, in: J. Mahaney (Ed.) Advances in the production and use of steel with improved internal cleanliness, ASTM, West Conshohocken, PA, 1999, pp. 12-31.
[59] H. Harada, Y. Ono, Toroidal continuously variable transmission and method for producing torque transmitting member thereof, Koyo Seiko Co, US, 2009.
[60] National Renewable Energy Laboratory (NREL), Gearbox Reliability Collaborative.
[61] International Standards Organisation (ISO), Rolling bearings: dynamic load ratings and rating life, 281:2007, Geneva, Switzerland, 2007.
[62] W. Musial, S. Butterfield, B. McNiff, Improving wind tubine gearbox reliability, EWEA 2007, U.S. Department of Commerce, Milan, Italy, 2007, pp. 1-10.
[63] International Standards Organisation (ISO), Wind turbines - Part 4. Design and specifications of gearboxes, 81400-4, Geneva, Switzerland, 2005.
[64] ANSI/AGMA/AWEA, Design and specification of gearboxes for wind turbines, 6006-A03, American National Standards Institute/American Gear Manufacturers Association/American Wind Energy Association, Washington, DC, 2003.
[65] F. Rasmussen, K. Thomsen, T.J. Larsen, The gearbox problem revisited, Risø National Laboratory, Roskilde, DK, 2004, pp. 1-8.
[66] P.J. Tavner, J. Xiang, F. Spinato, Reliability analysis for wind turbines, Wind Energy, 10 (2007) 1-18.
[67] T. Hamilton, A more durable wind turbine, Technology Review, MIT, 2009.
[68] Northern Power, The Gearbox Problem, 2009.
[69] J. Broehl, Gearbox performance probe sparks legal fears, Windpower Monthly Magazine, 2010.
[70] J. Luyckx, Hammering Wear Impact Fatigue Hypothesis WEC/irWEA failure mode on roller bearings, Wind Turbine Tribology Seminar, Renaissance Boulder Flatiron Hotel Broomfield, CO, USA, 2011.
[71] S.E. Thor, 57th IEA Topical Expert Meeting, Jyväskylä, Finland, 2008.
[72] J. Rosinski, D. Smurthwaite, Troubleshooting wind gearbox problems, Gear Solutions, 2010, pp. 22–33.

[73] R.J.K. Wood, A.S. Bahaj, S.R. Turnock, L. Wang, M. Evans, Tribological design constraints of marine renewable energy systems, Philosophical Transactions of the Royal Society A: Mathematical, Physical and Engineering Sciences, 368 (2010) 4807-4827.
[74] E.J. Terrell, W.M. Needelman, J.P. Kyle, Tribological challenges to the system, ASME/STLE Int. Joint Tribology Conference, ASME/STLE, Memphis, TN, US, 2009, pp. 26-30.
[75] H. Siebert, Wind turbines power up with oil, Lubrication & Fluid Power, 2006.
[76] A. Heege, Y. Radovcic, J. Betran, Fatigue load computation of wind turbine gearboxes by coupled structural, mechanism and aerodynamic analysis, DEWI Magazine, 2006, pp. 61-68.
[77] T. Burton, D. Sharpe, N. Jenkins, E. Bossanyi, Wind energy handbook, John Wiley and Sons, New York, 2001.
[78] E. Vries, Wind turbine gearboxes and the effort to improve their reliability, Windpower Monthly, 2010.
[79] M. Perez, C. Sidoroff, A. Vincent, C. Esnouf, Microstructural evolution of martensitic 100Cr6 bearing steel during tempering: From thermoelectric power measurements to the prediction of dimensional changes, Acta Mater., 57 (2009) 3170-3181.
[80] H.K.D.H. Bhadeshia, Steels for bearings, Prog. Mater Sci., 57 (2012) 268-435.
[81] T.A. Harris, M.N. Kotzalas, Rolling bearing analysis - Essential concepts of bearing technology, 5th ed., Taylor & Francis, Boca Raton, FL, US, 2007.
[82] H.K.D.H. Bhadeshia, H. Bhadeshia, R.W.K. Honeycombe, Steels: microstructure and properties, 3 ed., Butterworth-Heinemann, 2006.
[83] A. Olver, The Mechanism of Rolling Contact Fatigue: An Update, P. I. Mech. Eng. J-J. Eng., 219 (2005) 313-330.
[84] A. Stiénon, A. Fazekas, J.Y. Buffière, A. Vincent, P. Daguier, F. Merchi, A new methodology based on X-ray micro-tomography to estimate stress concentrations around inclusions in high strength steels, Mater. Sci. Eng., A, 513-514 (2009) 376-383.
[85] A.P. Voskamp, E.J. Mittemeijer, State of residual stress induced by cyclic rolling contact loading, Mater. Sci. Technol., 13 (1997) 430-438.
[86] J.J.C. Hoo, Bearing Steels: Into the 21st Century, Issue 1327, ASTM International, West Conshohocken, PA, US, 1998.
[87] International Standards Organisation (ISO), Steel - determination of content of nonmetallic inclusions - micrographic method using standard diagrams, ISO 4967, ISO, Geneve, Switzerland, 1998.
[88] ASTM International, Standard practice for extreme value analysis of non-metallic inclusions in steel and other microstructural features, ASTM E 2283-08, ASTM International, West Conshohocken, PA, 2008, pp. 1-11.
[89] J.A. Eckel, P.C. Glaws, J.O. Wolfe, B.J. Zorc, Clean engineered steels - progress at the end of the twentieth century, in: J. Mahaney (Ed.) Advances in the production and use of steel with improved internal cleanliness, ASTM, West Conshohocken, PA, US, 1999, pp. 1-12.
[90] Y. Murakami, T. Toriyama, K. Tsubota, K. Furumura, What happens to the fatigue limit of bearing steel without nonmetallic inclusions Fatigue strength of electron beam remelted super clean bearing steel., in: J.J.C. Hoo, W.B. Green (Eds.) Bearing steels: Into the 21st century, ASTM, West Conshohocken, PA, 1998, pp. 87-105.
[91] Y. Murakami, S. Beretta, Small defects and inhomogeneities in fatigue strength: experiments, models and statistical implications, Extremes, 2 (1999) 123-147.
[92] G.W. Stachowiak, A.W. Batchelor, Engineering Tribology, 3rd ed. ed., Elsevier Butterworth-Heinemann, Oxford, UK, 2006.
[93] H.H. Hertz, Hertz's miscallaneous papers, MacMillan, London, 1896.
[94] J. Tao, T.G. Hughes, H.P. Evans, R.W. Snidle, N.A. Hopkinson, M. Talks, J.M. Starbuck, Elastohydrodynamic lubrication analyses of gear tooth surfaces from micropitting tests, J. Tribol-T. ASME, 125 (2003) 267-274.
[95] F. Sadeghi, B. Jalalahmadi, T.S. Slack, N. Raje, N.K. Arakere, A review of rolling contact fatigue, J. Tribol-T. ASME, 131 (2009) 1-15.
[96] G. Lundberg, A. Palmgren, Dynamic capacity of rolling bearings, Acta Polytech. Scand., Mech. Eng. Ser, 1 (1947) 6-9.

[97] R.L. Widner, Failures of rolling element bearings: failure analysis and prevention, Metals Handbook, ASM International, 1986.
[98] G.E. Dieter, Mechanical metallurgy, 3 ed., McGraw-Hill, 1986.
[99] K.L. Johnson, Contact mechanics, Cambridge University Press, 1985.
[100] F.B. Oswald, E.V. Zaretsky, J.V. Poplawski, Interference-fit life factors for roller bearings, Tribol. T., 52 (2009) 415-426.
[101] F.B. Oswald, E.V. Zaretsky, J.V. Poplawski, Interference-fit life factors for ball bearings, Tribol. T., 54 (2010) 1-20.
[102] A.P. Voskamp, Fatigue and material response in rolling contact, in: J.J.C. Hoo, W.B. Green (Eds.) Bearing Steels: Into the 21st Century ASTM, West Conshohocken, PA, 1998, pp. 152-166.
[103] O. Zwirlein, H. Schlicht, Rolling contact fatigue mechanisms - accelerated testing versus field performance, in: J.J.C. Hoo (Ed.) Rolling Contact Fatigue Testing of Bearing Steels - ASTM STP 771, ASTM International, West Conshohocken, PA, 1982, pp. 358-379.
[104] A.P. Voskamp, Material response to rolling contact loading, J. Tribol-T. ASME, 107 (1985) 359–366.
[105] R. Robert, L. Snyder, Defect and Microstructure Analysis by Diffraction, Oxford University Press, Oxford, UK, 1999.
[106] J. Gegner, Tribological Aspects of Rolling Bearing Failures, in: C.-H. Kuo (Ed.) Tribology - Lubricants and Lubrication, InTech, 2011, pp. 33-94.
[107] R.H. Vegter, J.T. Slycke, The role of hydrogen in rolling contact fatigue response of ball bearings, 8th ASTM international symposium on bearing steel technologies, ASTM International, Vancouver, BC, Canada, 2009.
[108] J. Muller, R. Errichello, Oil cleanliness in wind turbine gearboxes, Machinery Lubrication Magazine, Noria Corporation, 2002.
[109] R. Gohar, H. Rahnejat, Fundamentals of Tribology, Imperial College Press, London, UK, 2008.
[110] G. Lundberg, A. Palmgren, Dynamic Capacity of Rolling Bearings, Acta Polytech. Scand., Mech. Eng. Ser, 2 (1952).
[111] A.B. Jones, Effect of structural changes in steel on fatigue life of bearings, Steel, 119 (1946) 68-70:97-100.
[112] B.G. Mellor, Discussion on WEA, 2010.
[113] H. Swahn, P.C. Becker, O. Vingsbo, Electron-microscope studies of carbide decay during contact fatigue in ball bearings, Metal Science, 10 (1976) 35-39.
[114] R. Tricot, J. Monnot, M. Lluansi, How microstructural alterations affect fatigue properties of 52100 steel, Metals Eng. Quart., 12 (1972) 39-47.
[115] A. Vincent, G. Lormand, P. Lamagnère, L. Gosset, D. Girodin, G. Dudragne, R. Fougères, From white etching areas formed around inclusions to crack nucleation in bearing steels under rolling contact fatigue, in: J.J.C. Hoo, W.B. Green (Eds.) Bearing Steels: Into the 21st Century, ASTM, West Conshohocken, PA, 1998, pp. 109-123.
[116] R.S. Hyde, Microstructural changes from contact fatigue, ASM Handbook - Vol 19 Fatigue and Fracture, ASM International, OH, 1996, pp. 1749-1780.
[117] K. Böhm, H. Schlicht, O. Zwirlein, R. Eberhard, Nonmetallic inclusions and rolling contact fatigue, Bearing Steels: The Rating of Nonmetallic Inclusions, ASTM, Boston, MA, US, 1974, pp. 96-113.
[118] M. Brückner, J. Gegner, A. Grabulov, W. Nierlich, J. Slycke, Alternative butterfly formation mechanisms in rolling contact fatigue, 5th International Conference on Very High Cycle Fatigue, Berlin, Germany, 2011, pp. 138-151.
[119] R.F. Johnson, J.R. Blank, Fatigue in rolling contact: some metallurgical aspects, P. I. Mech. Eng., (1963) 95-102.
[120] M.N. Lewis, B. Tomkins, A fracture mechanics interpretation of rolling bearing fatigue, P. I. Mech. Eng. J-J. Eng., 226 (2012) 389-485.
[121] O. Umezawa, K. Nagai, Effects of test temperature on internal fatigue crack generation associated with nonmetallic particles in austenitic steels, Metall. Mater. Trans. A, 29 (1998) 3017-3028.

[122] H. Mayer, W. Haydn, R. Schuller, S. Issler, M. Bacher-Höchst, Very high cycle fatigue properties of bainitic high carbon–chromium steel under variable amplitude conditions, Int. J. Fatigue, 31 (2009) 1300-1308.
[123] D. Brooksbank, K.W. Andrews, Stress fields around inclusions and their relation to mechanical properties, J. Iron Steel Inst. (London), 210 (1971) 246-255.
[124] K. Furumura, Y. Murakami, T. Abe, Development of long life bearing steel for full film lubrication and for poor and contaminated lubrication, Motion & Control, 1 (1996) 30-36.
[125] A. Kerrigan, J.C. Kuijpers, A. Gabelli, E. Ioannides, Cleanliness of bearing steels and fatigue life of rolling contacts, in: J.M. Beswick (Ed.) Bearing Steel Technology - Advances and State of the Art in Bearing Steel Quality Assurance ASTM International, West Conshohocken, PA, 2006, pp. 101-106.
[126] K. Hashimoto, T. Fujimatsu, N. Tsunekage, K. Hiraoka, K. Kida, E.C. Santos, Study of rolling contact fatigue of bearing steels in relation to various oxide inclusions, Materials & Design, 32 (2011) 1605-1611.
[127] K. Hashimoto, T. Fujimatsu, N. Tsunekage, K. Hiraoka, K. Kida, E.C. Santos, Effect of inclusion/matrix interface cavities on internal-fracture-type rolling contact fatigue life, Materials & Design, 32 (2011) 4980-4985.
[128] D. Ray, L. Vincent, B. Coquillet, P. Guirandenq, Hydrogen embrittlement of a stainless ball bearing steel, Wear, 65 (1980) 103–111.
[129] S. Suresh, Fatigue of Materials, Cambridge University Press, Cambridge, 1991.
[130] J. Gegner, W. Nierlich, Frictional surface crack initiation and corrosion fatigue driven crack growth, Wind Turbine Tribology Seminar, Renaissance Boulder Flatiron Hotel Broomfield, CO, USA, 2011.
[131] A. Greco, S. Sheng, J. Keller, A. Erdemir, Material wear and fatigue in wind turbine systems, Wear, (2013).
[132] K. Hono, M. Ohnuma, M. Murayama, S. Nishida, A. Yoshie, T. Takahashi, Cementite decomposition in heavily drawn pearlite steel wire, Scripta Mater., 44 (2001) 977–983.
[133] Y. Ivanisenko, W. Lojkowski, R.Z. Valiev, H.-J. Fecht, The mechanism of formation of nanostructure and dissolution of cementite in a pearlitic steel during high pressure torsion, Acta Mater., 51 (2003) 5555-5570.
[134] Y. Todaka, M. Umemoto, A. Ohno, M. Suzuki, Y. Kawabata, K. Tsuchiya, Dissolution of cementite in carbon steels by ball drop deformation and laser heating, J. Alloys Compd., 434-435 (2007) 497-500.
[135] S. Ohsaki, K. Hono, H. Hidaka, S. Takaki, Characterization of nanocrystalline ferrite produced by mechanical milling of pearlitic steel, Scripta Mater., 52 (2005) 271-276.
[136] Y. Xu, Z.G. Liu, M. Umemoto, K. Tsuchiya, Formation and annealing behavior of nanocrystalline ferrite in Fe-0.89C spheroidite steel produced by ball milling, Metall. Mater. Trans. A, 33 (2002) 2195-2203.
[137] N. Min, W. Li, H. Li, X. Jin, Atom probe and mossbauer spectroscopy investigations of cementite dissolution in a cold drawn eutectoid steel, J. Mater. Sci. Technol., 26 (2010) 776-782.
[138] V. Gavriljuk, Comment on 'cementite decomposition in heavily drawn pearlite steel wire', Scripta Mater., 46 (2002) 175-177.
[139] A. Taniyama, T. Takayama, M. Arai, T. Hamada, Structure analysis of ferrite in deformed pearlitic steel by means of X-ray diffraction method with synchrotron radiation, Scripta Mater., 51 (2004) 53-58.
[140] X. Sauvage, A. Chbihi, X. Quelennec, Severe plastic deformation and phase transformations, J. Phys.: Conf. Ser., 240 (2010) 1-8.
[141] C. Först, J. Slycke, K. Van Vliet, S. Yip, Point defect concentrations in metastable Fe-C alloys, Phys. Rev. Lett., 96 (2006) 175501.
[142] MATTER, Havovy Cama, released under CC BY-NC-ND 2.0 license.
[143] H. Takemura, Y. Matsumoto, Y. Murakami, Development of a new life equation for ball and roller bearings, Motion & Control, 11 (2001) 1-10.
[144] L. Grunberg, D.T. Jamieson, D. Scott, Hydrogen penetration in water-accelerated fatigue of rolling surfaces, Philos. Mag., 8 (1963) 1553-1568.

[145] J.A. Ciruna, H.J. Szieleit, The effect of hydrogen on the rolling contact fatigue life of AISI 52100 and 440C steel balls, Wear, 24 (1973) 107-118.

[146] T. Imran, B. Jacobson, A. Shariff, Quantifying diffused hydrogen in AISI-52100 bearing steel and in silver steel under tribo-mechanical action: Pure rotating bending, sliding–rotating bending, rolling–rotating bending and uni-axial tensile loading, Wear, 261 (2006) 86–95.

[147] Y. Matsubara, H. Hamada, A novel method to evaluate the influence of hydrogen on fatigue properties of high strength steels, J. ASTM Int., 3 (2006) 1-14.

[148] L. Hong, L. Midan, Z. Tiancheng, C. Wuyang, Hydrogen-enhanced dislocation emission, motion and nucleation of hydrogen-induced cracking for steel, Sci. China. Ser. E, 40 (1997) 530-538.

[149] S. Fujita, S. Matsuoka, Y. Murakami, G. Marquis, Effect of hydrogen on mode II fatigue crack behavior of tempered bearing steel and microstructural changes, Int. J. Fatigue, 32 (2010) 943-951.

[150] Y. Murakami, H. Matsunaga, The effect of hydrogen on fatigue properties of steels used for fuel cell system, Int. J. Fatigue, 28 (2006) 1509-1520.

[151] Y. Murakami, T. Kanezaki, Y. Mine, S. Matsuoka, Hydrogen embrittlement mechanism in fatigue of austenitic stainless steels, Metall. Mater. Trans. A, 39 (2008) 1327-1339.

[152] H. Hamada, Y. Matsubara, The influence of hydrogen on tension-compression and rolling contact fatigue properties of bearing steel, NTN Technical Review, NTN, 2006, pp. 54-61.

[153] M. Nagumo, M. Nakamura, K. Takai, Hydrogen thermal desorption relevent to delayed-fracture susceptibility of high-strength steels, Metall. Mater. Trans. A, 32 (2001) 339-347.

[154] M. Nagumo, Hydrogen related failure of steels – a new aspect, Mater. Sci. Technol., 20 (2004) 940-950.

[155] K. Takai, H. Shoda, H. Suzuki, M. Nagumo, Lattice defects dominating hydrogen-related failure of metals, Acta Mater., 56 (2008) 5158-5167.

[156] J.P. Hirth, Effects of hydrogen on the properties of iron and steel, Metall. Trans. A, 11 (1980) 861-890.

[157] T. Otsuka, H. Hanada, H. Nakashima, K. Sakamoto, M. Hayakawa, K. Hashizume, M. Sugisaki, Observation of hydrogen distribution around non-metallic inclusions in steels with tritium microautoradiography, Fusion Sci. Tech., 48 (2005) 708-711.

[158] H.W. Walton, Ubiquitous Hydrogen, in: S.J. Midea, G.D. Pfaffmann (Eds.) 19th ASM heat treating society proceedings including steel heat treating in the new millennium, ASM, Cincinnati, Ohio, US, 1999, pp. 558-563.

[159] M. Enomoto, D. Hirakami, T. Tarui, Thermal Desorption Analysis of Hydrogen in High Strength Martensitic Steels, Metall. Mater. Trans. A, 43 (2012) 572.

[160] D. Park, I.S. Maroef, A. Landau, D.L. Olson, Retained austenite as a hydrogen trap in steel welds, Weld. J., (2002) 27-35.

[161] G.M. Pressouyre, A classification of hydrogen traps in steel, Metall. Trans. A, 10 (1979) 1571-1573.

[162] R.A. Oriani, Hydrogen - the versatile embrittler, Corrosion, 43 (1987) 390-397.

[163] H.K. Birnbaum, P. Sofronis, Hydrogen-enhanced localized plasticity - a mechanism for hydrogen related failure, Mater. Sci. Eng., A, 176 (1994) 191-202.

[164] B.A. Szost, P.E.J. Rivera-Díaz-del-Castillo, Unveiling the nature of hydrogen embrittlement in bearing steels employing a new technique, Scripta Mater., 68 (2012) 467–470.

[165] R.D. Evans, G.L. Doll, C.H. Hager, J.Y. Howe, Influence of steel type on the propensity for tribochemical wear in boundary lubrication with a wind turbine gear oil, Tribology Letters, 38 (2010) 25-32.

[166] M. Reichelt, T.E. Weirich, J. Mayer, T. Wolf, J. Loos, P.W. Gold, M. Fajfrowski, TEM and nanomechanical studies on tribological surface modifications formed on roller bearings under controlled lubrication conditions, Journal of Materials Science, 41 (2006) 4543-4553.

[167] S.M. Hsu, R.S. Gates, Effect of materials on tribochemical reactions between hydrocarbons and surfaces, J. Phys. D: Appl. Phys., 39 (2006) 3128-3137.

[168] T. Sakamoto, H. Uetz, J. Föhl, M.A. Khosrawi, The reaction layer formed on steel by additives based on sulphur and phosphorus compounds under conditions of boundary lubrication, Wear, 77 (1982) 139–157.

[169] G.T.Y. Wan, H. Lankamp, A.d. Vries, E. Ioannides, The effect of extreme pressure (EP) lubricants on the life of rolling element bearings, P. I. Mech. Eng. J-J. Eng., 208 (1994) 247-252.
[170] J. Fitch, How water causes bearing failure, Machinery Lubrication Magazine, 2008.
[171] L.J. Taylor, H.A. Spikes, Friction-enhancing properties of ZDDP antiwear additive: Part I - friction and morphology of ZDDP reaction films, Tribol. T., 46 (2003) 303-309.
[172] A. Thompson, I.M. Bernstein, The role of metallurgical variables in hydrogen-assisted environmental fracture, in: M.G. Fontana, R.W. Staehle (Eds.) Advances in Corrosion Science and Technology, Plenum Press, NY, 1980, pp. 53-175.
[173] P. Schatzberg, Inhibition of water-accelerated rolling-contact fatigue, J. Lubric. Tech-T. ASME., 70 (1971) 231-233.
[174] L. Grunberg, The formation of hydrogen peroxide on fresh metal surfaces, Proc. Phys. Soc. London, Sect. B, 66 (1953) 153-161.
[175] P.J.L. Fernandes, C. McDuling, Surface contact fatigue failures in gears, Eng. Fail. Anal., 4 (1997) 99-107.
[176] Y.S. Kang, R.D. Evans, G.L. Doll, Roller-raceway slip simulations of wind turbine gearbox bearings using dynamic bearing model, STLE/ASME 2010 International Joint Tribology Conference, ASME, San Francisco, CA, US, 2010, pp. 407-409.
[177] P. Johansson, S. Bengtsson, S. Dizdar, RCF-testing of selectively densified rollers of p/m materials for gear applications, Advances in Powder Metallurgy & Particulate Materials, 5 (2002) 180-192.
[178] J. Lord, R. Larsson, Effects of slide-roll ratio and lubricant properties on elastohydrodynamic lubrication film thickness and traction, P. I. Mech. Eng. J-J. Eng., 215 (2001) 301-308.
[179] D.M. Nuruzzaman, M.A.A. Sheikh, EHL oil film thickness under rolling-sliding contact, Journal of Mechanical Engineering, 38 (2007) 58-60.
[180] S. Tanaka, K. Yamamura, M. Oohori, Excellent stainless bearing steel (ES1), Motion & Control, 8 (2000) 23-26.
[181] B.A. Szost, R.H. Vegter, P.E.J. Rivera-Díaz-del-Castillo, Developing bearing steels combining hydrogen resistance and improved hardness, Mater. Des., 43 (2013) 499-506.
[182] R.D. Evans, C.H. Hager, R.D. Logsdon, Friction and wear performance of candidate surface treatments for wind turbine gearbox bearings in high slip contacts, ASME/STLE 2009 International Joint Tribology Conference, Memphis, TN, 2009, pp. 491-493.
[183] TheEngineer, New coating for cylindrical roller bearings reduces gearbox failures in wind turbine applications, 2009.
[184] Schaeffler, Protective materials and coatings for extreme environments, 2010.
[185] G. Plint, TE 74 two roller machine, 2011.
[186] B.J. Hamrock, D. Dowson, Isothermal elastohydrodynamic lubrication of point contacts, part III - Fully flooded results, J. Tribol-T. ASME, 99 (1977).
[187] B.J. Hamrock, D. Dowson, Ball bearing lubrication: the elastohydrodynamics of elliptical contacts, John Wiley, New York, 1981.
[188] F.T. Barwell, Bearing Systems, Principles and Practice, Oxford University Press, 1979.
[189] B.J. Hamrock, B.E. Brewe, Simplified Solution for Stresses and Deformations, J. Lubric. Tech-T. ASME., 105 (1983) 171-177.
[190] S. Takagi, Y. Toji, Application of NH4SCN Aqueous Solution to Hydrogen Embrittlement Resistance Evaluation of Ultra-high Strength Steels, ISIJ Int., 52 (2011) 329–331.
[191] L.A. Giannuzzi, F.A. Stevie, Introduction to focused ion beams: instrumentation, theory, techniques, and practice, Springer, NY, 2005.
[192] D.B. Williams, C.B. Carter, Transmission Electron Microscopy: A Textbook for Materials Science, Springer, NY, 2009.
[193] R. Kirchheim, A. Kirchheim, Hydrogen sensor: non-destructive measurement of diffusible hydrogen in metals, in: KircTec (Ed.) http://www.kirctec.com, 2012.

Permissions

[2.1] Reprinted, with permission, from the *ASTM STP 987*, copyright ASTM International, 100 Barr Harbor Drive, West Conshohocken, PA 19428.
[2.2] Reprinted, with permission, from the *ASTM STP 1327*, copyright ASTM International, 100 Barr Harbor Drive, West Conshohocken, PA 19428.
[2.3] Springer and Metallurgical Transactions A, 7, 1976, Pg. 1101-1102, Martensite Decay During Rolling Contact Fatigue in Ball Bearings, H. Swahn, et. al., Figs. 2 & 4, with kind permission from Springer Science+Business Media B.V.
[2.4] Reprinted from International Journal of Fatigue, 32, A. Grabulov, et. al., EBSD investigation of the crack initiation and TEM/FIB analyses of the microstructural changes around the cracks formed under rolling contact fatigue RCF, 576-583, Copyright (2009), with permission from Elsevier.
[2.5] Reprinted, with permission, from the *ASTM STP 1327*, copyright ASTM International, 100 Barr Harbor Drive, West Conshohocken, PA 19428.
[2.6] Havovy Cama, released under CC BY-NC-ND 2.0 license. http://core.materials.ac.uk/
[2.7] Copyright (2005) by the American Nuclear Society, La Grange Park, Illinois. T. Otsuka, H. Hanada, H. Nakashima, K. Sakamoto, M. Hayakawa, K. Hashizume and M. Sugisaki: Fusion Sci. Tech., 2005, 48, (1), 708-711.
[2.8] Reprinted from Engineering Failure Analysis, 4, P.J.L Fernandes and C. McDuling, Surface contact fatigue failures in gears, Pg. 100, Copyright (1997), with permission from Elsevier.
[2.9] Springer and Tribology Letters, 38, 2010, Pg. 29 & 32, Influence of steel type on the propensity for tribochemical wear in boundary lubrication with a wind turbine gear oil, R.D. Evans, et. al., Figs. 3 & 7, with kind permission from Springer Science and Business Media.
[3.1] Reprinted from Wear, In Press (http://dx.doi.org/10.1016/j.wear.2013.03.008), M.-H. Evans, et al., Effect of hydrogen on butterfly and white etching crack (WEC) formation under rolling contact fatigue (RCF), pp. 1-16, Copyright (2013), with permission from Elsevier.
[3.2] Reprinted from Tribology International, In Press (http://dx.doi.org/10.1016/j.triboint.2013.03.022), M.-H. Evans, et al., White etching crack (WEC) investigation by serial sectioning, focused ion beam and 3-D crack modelling, pp. 1-15, Copyright (2013), with permission from Elsevier.
[3.3] Reprinted from Materials Science and Engineering: A, 570, M.-H. Evans, et al., A FIB/TEM study of butterfly crack formation and white etching area (WEA) microstructural changes under rolling contact fatigue in 100Cr6 bearing steel, pp. 127-134, Copyright (2013), with permission from Elsevier.
[7.4] Reprinted from Wear, 302, M.-H. Evans, et al., Serial sectioning investigation of butterfly and white etching crack (WEC) formation in wind turbine gearbox bearings, pp. 1573-1582, Copyright (2012), with permission from Elsevier.